

University of Twente (UT)  
Faculty of Applied Mathematics (AM)  
Department of Applied Analysis and Mathematical Physics (AAMP)

Date: October 11, 2007

# The STN-GPe-network - a bifurcation analysis

Sanne SMIT

Prof. dr. S.A. (Stephan) VAN GILS  
Dr. H.G.E. (Hil) MEIJER  
Dr. Ir. T. (Ciska) HEIDA



## Abstract

This report discusses the conductance-based network model, described in [1], of the interactions of the external segments of the globus pallidus (GPe) with the subthalamic nucleus (STN) in the basal ganglia (BG). Analysis of this important network in the BG can lead to a better understanding on correlated synchronous rhythmic activity of the network, which is a major characteristic of Parkinson's Disease (PD).

A codim-1 bifurcation analysis is applied to each individual model which represents a certain type of neuron within the STN or GPe. The STN- and GPe-models consist of the same type of currents but the difference in constant parameter values cause their behaviour to differ. The parameter which is varied is the applied current,  $I_{app}$ , to the specific neuron. This current simulates the synaptic input to the neuron. Bifurcation analysis gives a detailed division of the parameter line in different regions, bounded by transition/bifurcation points. Within these regions the specific model-neuron, behaves qualitatively different from other regions. Values for  $I_{app}$  at which transitions between spiking and quiescent states are present can therefore be indicated accurately.

Simulations of the behaviour of the two neuron-models show the spiking characteristics described in literature. We find that the STN-model represents a STN-neuron which is unable to generate plateau potentials. Such a neuron is present in the STN but represents the least interesting one when networks of STN- and GPe-neurons are considered. With and without input the STN- and GPe-models show the correct behaviour. Both models miss the pronounced slow part of the afterhyperpolarization (AHP) though. Comparison of the fi-curves of both models with ones from experimental literature, shows that the parameter  $I_{app}$  needs scaling. The parameter range in which all essential events take place is simply too small for both models. Although much is uncertain on the *exact* behaviour-characteristics of the two neurons in vivo, some improvements for future modelling are considered.

A codim-2 equilibrium bifurcation analysis is applied to the two-cell reciprocally connected STN-GPe network-model. This network is too small and too tightly connected to really resemble the network in vivo or provide us with further knowledge on synchronization properties of the network. A complete understanding of the results from the simulations and bifurcation analysis of this small network, is necessary though to extend the network to larger sizes with different architecture. The codim-2 *equilibrium* bifurcation analysis showed that the model-network will never be quiescent in the physical parameter regime and the solution of the coupled system of ODEs will always converge to a stable limit cycle. Because a codim-2 *limit cycle* bifurcation analysis has not been performed, knowledge on the possible bistable regions, or on the transitions between different types of spiking of this network has not been gained.

Analysis of larger STN-GPe-network models with different architectures can give us more insight in PD-related phenomena as synchronized bursting, of the network. When MatCont, the bifurcation software in Matlab, is linked to Simulink the bifurcation analysis, described in this report, can be easily extended to larger networks. Neurons can then be added to the network by a click of the mouse.



# Acknowledgements

I would like to thank some people who have been of great importance to me during this final project. First and most of all I would like to thank my main supervisor Stephan van Gils. He helped me not only with mathematics, but also during difficult times, when I found it difficult to get anything on paper. He never got angry or upset, but was able to motivate me again and bring back my enthusiasm for this subject. He increased my motivation, because I was, and still am, greatly interested in this field of mathematics where solutions to systems can do such great and strange things. Thanks for transmitting your enthusiasm to me, it works contagious! And of course thanks for your kind words the last year when I needed them so much.

I would also like to thank Hil Meijer, who came to work here in Enschede and immediately was assigned to help me with the use of MatCont. He was of great help when certain errors showed-up on the screen, which did not ring any bells to me. In the period of absence of Stephan in the last month, Hil was my supervisor. This was in a period I was stressed out because 12 October was approaching fast. Hil helped me by giving me small assignments, which I could finish without actually stressing. In the last month we found nice bifurcations, which made us both happy. Thanks for all the help even when you had many other things to do. I do not know what 'marsepein' is in English but you will get a large piece!

Although I had less contact with Ciska Heida, than with the mathematicians, she was of great help to me, for the physiological part of the research. Although I hardly knew anything to say about the various methods used for obtaining results from experiments, she never gave me the idea I made weird or even stupid remarks on these methods (which I definitely did!). She was also of great importance for improving my writing skills and bringing more scientific structure into my report. Thanks for all the help!

Also I would like to thank my parents who took care of me during the last two weeks, to let me finish my report in silence (although with four dogs it is not quiet that often...). They forced me to go to bed when I was still busy in the middle of the night, and made me remember to eat and drink. They just took great care of me, and I could not have finished my report without them.



# Contents

<b>1</b>	<b>Introduction</b>	<b>1</b>
1.1	Introduction to the subject . . . . .	2
1.1.1	Neurophysiology . . . . .	2
1.1.2	Neurodynamics . . . . .	13
1.2	Motivation . . . . .	20
1.3	Problem definition and approach . . . . .	21
1.4	Structure of the report . . . . .	22
<b>2</b>	<b>The STN-neuron</b>	<b>25</b>
2.1	Literature . . . . .	25
2.1.1	Experimentally found results . . . . .	26
2.1.2	The STN-model . . . . .	34
2.2	Analysis . . . . .	38
2.2.1	Bifurcation analysis . . . . .	38
2.2.2	Simulations . . . . .	53
2.3	Discussion . . . . .	69
2.3.1	Summary of the results . . . . .	70
2.3.2	Evaluation . . . . .	74
<b>3</b>	<b>The GPe-neuron</b>	<b>79</b>
3.1	Literature . . . . .	79
3.1.1	Experimentally found results . . . . .	79
3.1.2	The GPe-model . . . . .	82
3.2	Analysis . . . . .	82
3.2.1	Bifurcation analysis . . . . .	83
3.2.2	Simulations . . . . .	94
3.3	Discussion . . . . .	98
<b>4</b>	<b>The STN-GPe network</b>	<b>101</b>
4.1	Literature . . . . .	102
4.1.1	Computational and experimental results . . . . .	103
4.1.2	The two-cell model . . . . .	107
4.2	Analysis . . . . .	113
4.2.1	Equilibrium bifurcation analysis . . . . .	114
4.2.2	Simulations . . . . .	121
4.3	Discussion . . . . .	127
<b>5</b>	<b>Conclusion</b>	<b>129</b>

<b>6 Recommendations</b>	<b>131</b>
<b>References</b>	<b>136</b>
<b>Appendices</b>	<b>136</b>
<b>A Model constants</b>	<b>137</b>
<b>B Some M-files</b>	<b>139</b>
<b>C Possible bifurcations</b>	<b>149</b>
C.1 Possible codim-1 bifurcations . . . . .	149
C.1.1 Bifurcations of a stable equilibrium . . . . .	149
C.1.2 Bifurcations of a stable limit cycle . . . . .	151
C.2 Possible codim-2 equilibrium bifurcations . . . . .	153
<b>D Pulse-coupled models</b>	<b>157</b>

# Chapter 1

## Introduction

The title of this report and the subject of this MSc-research is:

The STN-GPe-network - *a bifurcation analysis*

Which will not ring any bells to people who do not work in the area of neurodynamics. This chapter is for that reason devoted to explain this title and thereby to explain the subject of this research.

To be able to clearly explain the subject of this research, the various uncertainties in the neurodynamical research field of the STN-GPe-network (see title) will first have to be explained. The STN-GPe-network is a subnetwork of the ‘Basal Ganglia’ (BG) which on its turn is a part of the brain. Thus to be able to explain these various uncertainties, the basic *neurophysiological* aspects of the brain, and the BG need to be explained first. These concepts can be found in Section 1.1.1. Because in this research neurodynamical methods (mathematical instead of experimental methods) are used to look at the STN-GPe-network, the concepts of *neurodynamics* need a short explanation as well and can be found in Section 1.1.2. The interested reader is referred to [2] for more information on the physiology of the brain and to [3] for the neurodynamical approach to describe the brain’s behaviour.

After the short introduction to the subject the various uncertainties and unanswered questions in the research field of the BG, and in particular of the STN-GPe-network, can be listed and will naturally lead to the motivation to conduct this specific research. This motivation can be found in Section 1.2.

In Section 1.3 the formal problem definition for this research is given. In short, the aim is to learn more about the STN-GPe-network by using mathematical techniques as bifurcation theory on an already present computational model of the network. Although it is called a ‘problem definition’ it is more a description of the aim of this research based on the motivation given in Section 1.2. The delimitation of the problem for this research is given and the division of this problem into subproblems defines the approach to this research.

The definition of this approach in Section 1.3 also defines the structure of the report, which consists of different parts in which the different sub-problems are discussed. The structure of this report is given in Section 1.4 for the reader who wants to be able to skip to the relevant chapter or section instantly.

## 1.1 Introduction to the subject

This section gives an introduction to the subject of this research by first explaining some general neurophysiological concepts of the brain in the beginning of Section 1.1.1. The physiological arrangement of the various nuclei within the BG and their type of connections is also described. Parkinson's Disease (PD) originates in the BG, but it is still uncertain where and how the various tremor frequencies, related to this disease, exactly originate. This is one of the strong motivations for this and other research of the BG. The knowledge present at the moment on PD and on its quite successful treatment for symptom-reduction (Deep Brain Stimulation (DBS)) is described in Section 1.1.1 as well. All information given in Section 1.1.1 is derived from [2].

In Section 1.1.2 the role mathematics can play in brain science is explained and discussed. This application of mathematics on neuroscience is called neurodynamics. The various concepts of the conductance-based Hodgkin-Huxley (HH) type of models and the powerful tool bifurcation theory can play in their analysis are explained.

### 1.1.1 Neurophysiology

The brain consists of many functionally different parts. For example the sensory information (visual, auditory, touch) 'travels' through sensory pathways to specific nuclei of the thalamus and then to regions of the cerebral cortex that are specific to each sensory system: the visual system, the auditory system, and the somatosensory system. To control movement the brain has several parallel systems of muscle control. The motor system controls the voluntary muscle movement and is aided by the motor cortex, the cerebellum, and the basal ganglia. The motor system eventually projects to the spinal cord and then out to the muscle neurons.

To perform all these tasks the human brain consists of about  $10^{11}$  neurons which project altogether to  $10^{14}$  other neurons (there are  $10^{14}$  synapses). Given the diversity of functions performed by neurons in different parts of the nervous system, there is, as expected, a wide variety in the shape, size, and electrochemical properties of neurons. Although this is the case, all neurons have certain anatomical and morphological similarities: they all consist of a soma (cell body with the nucleus of the cell), axons and dendrites (see Figure 1.1).

The soma is usually about 10-25  $\mu\text{m}$  in diameter and often is not much larger than the cell nucleus it contains. The smallest soma is 4  $\mu\text{m}$  in diameter and the largest 100  $\mu\text{m}$ .

The axon is the 'output road' through which the generated signal of the neuron can travel almost undisturbed and undiminished to its end-points (axon terminals) and eventually innervate other neurons by projecting on *their* dendrites. This process of innervation is explained later. The part of the axon which is closest to the soma is called the axon hillock and is important for the neuron's action potential generation.

Dendrites are the main 'input roads' to the neuron. The majority of information arrives there. Other neurons project to the dendrites of the specific neuron and innervate it. Projections are also possible on the soma or axon, but are less often encountered. Axons and dendrites in the brain are typically only about 1  $\mu\text{m}$  thick.

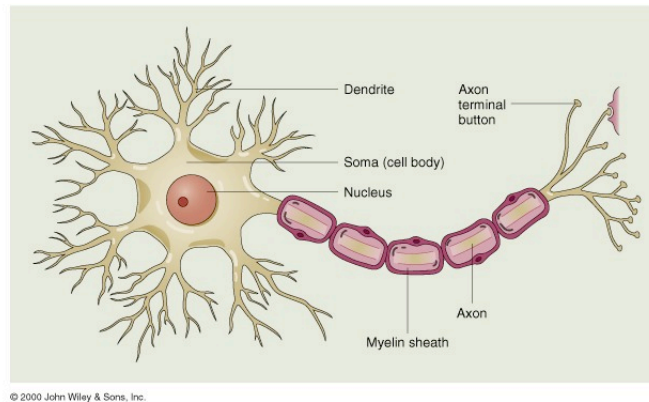


Figure 1.1: The anatomy of a neuron. All neurons consist of a soma with several dendrites and a branched axon.

Differences in neurons can be described in many ways. One way is to distinguish between neurons by looking at their direction of projection:

1. *Afferent neurons* convey information *from* tissues and organs *into* the central nervous system. They are also called sensory neurons.
2. *Efferent neurons* transmit signals *from* the central nervous system *to* the effector cells (which control muscles) and are also called motor neurons.
3. *Interneurons* connect neurons within specific regions of the central nervous system.

The longest axon in the nervous system, of a human motor neuron, can be over 1 m long, reaching from the base of the spine (location motor neuron) to the muscles of the toes which the neuron innervates. Sensory neurons have axons that can reach over 1.5 m in adult humans. These specific sensory neurons run from the toes to the spinal cord.

The neuron's intracellular fluid is separated from the extracellular fluid by its membrane. The extracellular fluid consists of concentrations of various ion types such as sodium ( $\text{Na}^+$ ), potassium ( $\text{K}^+$ ), calcium ( $\text{Ca}^{2+}$ ), chloride ( $\text{Cl}^-$ ) and other cations (positively charged ions) and anions (negatively charged ions). The neuron's intracellular fluid consists of the same *type* of ions. The concentrations differ though and due to the difference in ion concentrations, between the intra- and extracellular fluid, a potential difference  $V = V_{in} - V_{out}$  is present across the neuron's membrane.  $V$  is almost always less than zero. Ions in- and outside the membrane tend to flow across the membrane due to:

- The concentration gradient present between the in- and outside of the neuron for the specific type of ion.
- The potential difference, which results in an electrical force on the charged ions.

The membrane consists of channels made out of proteins. These channels are permeable to a certain type of ion and can open or close dependent on the change in voltage (voltage-gated channels) or dependent on the intracellular

concentration of a specific type of ion (ligand-gated). When the channels are open (or partly open) ions of the specific type can flow through the channels, resulting in a membrane current. When positive ions flow out (into the extracellular fluid), the current is called ‘outward’ and indicated as positive (+). This current makes the membrane potential more negative, and is called a *hyperpolarizing* current. When positive ions flow into the cell the current is called ‘inward’ and is indicated as negative (-). This current makes the membrane potential more positive and is called a *depolarizing* current. The flow of negative ions such as  $\text{Cl}^-$  for example into the cell, is therefore indicated as an outward and positive current (influx of negative ions has the same effect as an efflux of positive ions). A small note has to be made about this convention: When the membrane potential gets more positive ( $V = -80 \text{ mV} \rightarrow -30 \text{ mV}$  for example), we call this an ‘increase’ in membrane potential, while others (as in Figure 1.2) see this as a decrease, because the difference  $V = V_{in} - V_{out}$  indeed decreases. This may be confusing in the beginning.

*Voltage-gated* channels are opened and closed by activation and inactivation gates. Some channels only have activation gates (resulting in persistent currents), some have both (transient currents), and some channels do not have any gates (are thus independent on  $V$ ) and are always in an open state (ohmic leak currents). For every voltage-gated channel, for a specific ion-type  $C$ , an equilibrium (Nernst)-potential  $E_C$  can be defined. When the membrane potential  $V$  is equal to  $E_C$ , the in- and efflux of these ions is zero. When  $V = E_C$  the diffuse forces (due to the concentration gradient) and the electrical forces (due to the membrane potential difference  $\Delta V$ ) working on ions from type  $C$  balance each other. The value of the equilibrium potential  $E_C$  is defined by the Nernst-equation given in (1.1).

$$E_C = \frac{RT}{zF} \ln \frac{[C]_{out}}{[C]_{in}} \quad (1.1)$$

With  $E_C$  the equilibrium potential of the specific ion in mV,  $T$  the absolute temperature in K,  $z$  the valence of the ion (for example  $-1$  for  $\text{Cl}^-$ ),  $F$  the Faraday constant ( $96485.3 \text{ C/mol}$ ), and  $R$  the ideal gas constant ( $8.31451 \text{ J mol}^{-1} \text{ K}^{-1}$ ).  $[C]_{out}/[C]_{in}$  is the ratio between the extracellular and intracellular concentration of the specific ion.

If only one ion type  $C$  were present in the intracellular and extracellular fluid, the resting membrane potential RMP would be given by the Nernst potential of this ion  $E_C$ . Because many types can be found in both fluids, which all have different concentrations and Nernst potentials, the RMP will be a weighed average of all equilibrium potentials with the weights for each  $E_C$  given by the conductance of the membrane to ion-type  $C$  (often indicated by  $g_C$ ). The conductance  $g_C$  is the reciprocal of the resistance  $R_C$  of the membrane with respect to a flux of ions of type  $C$  (see (1.2)) and is dependent on the number of  $C$ -channels present in the membrane.

$$g_C = \frac{1}{R_C} \quad (1.2)$$

This gives the Goldman equation for the calculation of the RMP of a certain neuron. In the following the Goldman equation for a neuron with only three types of ions is given:

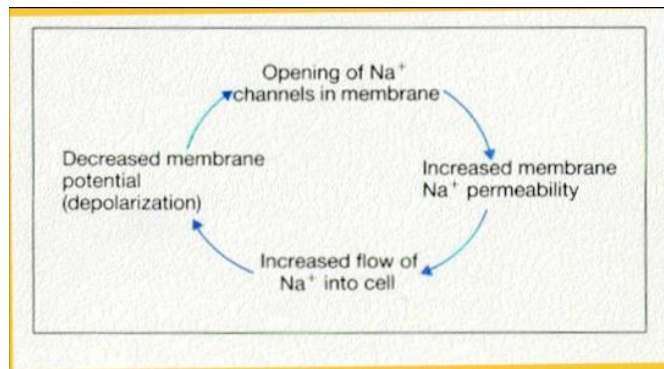


Figure 1.2: The regenerative process of increase in membrane potential which opens up sodium-channels (top), which causes an influx of positive sodium-ions (bottom) and increases the membrane potential even more. This process repeats itself until the membrane potential is near  $E_{Na}$  and  $K^+$ -channels open up.

$$RMP = \frac{g_{Na}E_{Na} + g_K E_K + g_{Cl}E_{Cl}}{g_{Na} + g_K + g_{Cl}}$$

It is clear that with only channels present for  $Na^+$ ,  $RMP = E_{Na}$ . When the membrane gets de- or hyperpolarized and tends to return to its RMP this process is called repolarization. Because  $V_{eq} \neq E_C$  for every ion-type  $C$ , in- and efflux of ions of every type  $C$  is present (of course when channels permeable to ion-type  $C$  are open) to cause  $V_{eq} \rightarrow E_C$ , which will never completely succeed.

The *voltage-gated* channels (in comparison to the ligand-gated ones) are mainly responsible for action potential generation, the major neuron characteristic to communicate with others. Before explaining this phenomenon the influence of changes in voltage on channel dynamics is explained. A de- or hyperpolarization of the membrane might bring the potential in a range in which certain channels become activated, deactivated, inactivated or deinactivated (dependent on the voltage-dependence of the specific gates). This alters the opening of the channel and thereby influence the magnitude of certain ion fluxes. These fluxes effect the membrane potential again and might cause other channels to open or close, which changes the potential again, etc etc. This causes the membrane potential to behave dynamically after the occurrence of an event.

Dependent on the channel-type the (de)activation (or possible (in)activation) can be anything in between fast and slow. In most neurons sodium ( $Na^+$ ) contributes the most to the generation of action potentials. Now assume some event (discussed later) depolarizes the neuron's membrane, at a certain location, causing an increase in  $V$ . After such a depolarization, sodium-channels open, causing an influx of sodium-ions, which increases the membrane potential even more, causing more gates to open etc etc. This could lead to a regenerative process (depending on the threshold above which the membrane potential should come to trigger this process) which increases the potential extremely fast until it almost approaches  $E_{Na} \approx 50$  mV. The threshold for this process is the lowest at the axon hillock. The regenerative process is graphically shown in Figure 1.2.

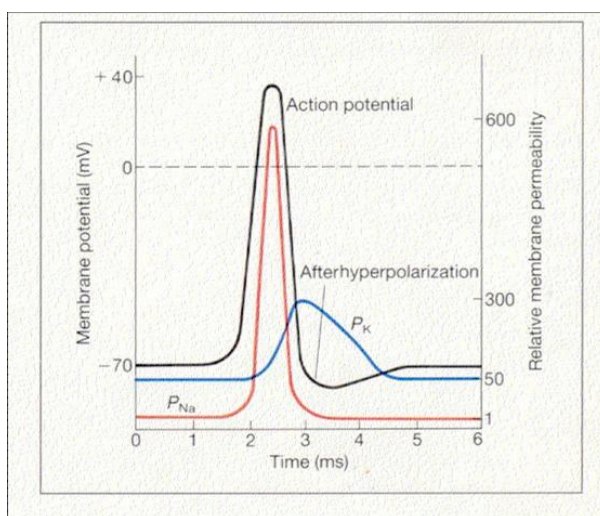


Figure 1.3: The time diagram of the membrane potential  $V$  (in black) shows an action potential. The red and blue curves represent the sodium-conductance  $P_{Na}$  and the potassium conductance respectively, both dependent on  $V$  and thus on  $t$ . The slow dynamics of  $P_K$  is clear.

This is called action potential generation. During the rising phase of the action potential, potassium ( $K^+$ ) channels are activated. This activation is much slower than the activation of  $Na^+$ -channels. This generates an outward, and thus hyperpolarizing, current which repolarizes the membrane back to RMP. This inactivates the sodium channels as well. Due to the slow response of the potassium channels to changes in potential, the potential hyperpolarizes below RMP until the potassium channels are all deactivated. This part after the generation of an action potential is called the *afterhyperpolarization* (AHP). During this phase and the subsequent slow depolarizing phase toward RMP the sodium channels are still inactivated and can not respond to a new event. This is called the absolute refractory period. It is followed by a relative one in which an increased stimulus is needed to generate an action potential again. A time diagram of an action potential is shown in Figure 1.3 with the dynamical behaviour of the conductances for sodium (indicated in the figure by the red curve  $P_{Na}$ , often called  $g_{Na}$ ) and potassium (the blue curve  $P_K = g_K$ ), both dependent on  $V$ , drawn as well. The dynamical behaviour of the conductances show the slow activation and deactivation of the potassium current, leading to the AHP, which can be seen in the time diagram of  $V$ .

There are many different channels with one or two types of gates and their own dynamical behaviour. Some channels, and therefore currents, are activated at hyperpolarized levels, others such as sodium are activated at higher potentials. Their speed of (in)activation determines their influence on the dynamics of the membrane potential. Time scales of variables are therefore very important.

But which events can trigger the neuron to start this regenerative process and generate an action potential? The firing of other cells which project to the specific neuron are such events, which will be described later. When neuron 1 receives input from neuron 2 at a certain time instant, neuron 1 is called the

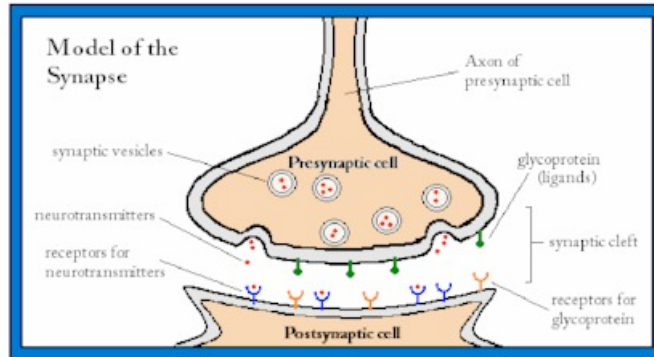


Figure 1.4: When the generated action potential of the presynaptic neuron arrives at the synaptic terminal, the synaptic vesicles release neurotransmitter molecules in the synaptic cleft between the pre- and postsynaptic neuron. These molecules bind to receptor channels on the membrane of the postsynaptic cell. On the right side of the picture an example with the neurotransmitter glycoprotein is shown.

postsynaptic neuron and neuron 2 the presynaptic neuron. This is indicated in Figure 1.4.

Beside the different ion-types present in the presynaptic neuron, other molecules, with a totally different function, are present as well. Every neuron keeps these neurotransmitter molecules such as dopamine, glutamate, serotonin or  $GABA_A$  within the synaptic vesicles of the synaptic terminal (see Figure 1.4). These neurotransmitters can bind to ligand-gated receptor channels, specific for the neurotransmitter, in the postsynaptic cell membrane. Through ligand-gating these channels, permeable to a certain ion-type, open up. Small de- or hyperpolarizing effects can then be seen in the postsynaptic cell. The type of neurotransmitter of the presynaptic neuron therefore classifies this neuron in another way: by looking at how they exactly change the membrane potential of the postsynaptic neuron they project on. This leads to the following classification:

1. *Excitatory neurons* excite their target (postsynaptic) neurons (increase their membrane potential). Excitatory neurons are often glutamatergic. The STN-neuron in this research is such an excitatory neuron.
2. *Inhibitory neurons* inhibit their target neurons. Inhibitory neurons are often interneurons. The output of some brain structures (neostriatum, globus pallidus, cerebellum) are inhibitory. The primary inhibitory neurotransmitters are GABA (A and B) and glycine. The GPe-neuron in this research is such an inhibitory  $GABA_A$ -inhibitory neuron.
3. *Modulatory neurons* evoke more complex effects, called neuromodulation, in the postsynaptic neuron. These neurons use such neurotransmitters as dopamine, acetylcholine, serotonin and others.

Although this is a good classification, it is not the neurotransmitter that decides excitatory or inhibitory action, but rather it is the postsynaptic receptor that is responsible for the action of the neurotransmitter.

When the presynaptic neuron fires an action potential at the axon hillock (due to another event occurring on *its* membrane), this action potential ‘travels’ through the axon to its synaptic terminal. Due to the good isolation of the axon the amplitude of the action potential does not decrease during the ‘trip’. When the action potential arrives in the synaptic terminal the increase in membrane potential there opens channels permeable to  $\text{Ca}^{2+}$ , which results in an inward current increasing  $V$  even more. This triggers the release of neurotransmitter molecules in the synaptic cleft by the synaptic vesicles. These molecules bind to receptor channels, specific for this neurotransmitter, in the membrane of the postsynaptic cell. Due to this binding-process these channels, which are permeable to a certain ion, open up. An influx of these specific ions is the result, and it leads to a postsynaptic membrane response many times smaller than an action potential. In the case of an influx of cations (often  $\text{Na}^+$ -ions) an excitatory postsynaptic potential (EPSP) is the result. In the case of an influx of anions (often  $\text{Cl}^-$ -ions) an inhibitory postsynaptic potential (IPSP) can be seen. In the case of binding of  $\text{GABA}_A$ -neurotransmitter (released by for example the GPe-cell) to receptor-channels in the postsynaptic cell (in that case the STN-membrane), an influx of  $\text{Cl}^-$ -ions into the postsynaptic cell follows after the opening of the channels. This hyperpolarizes the membrane resulting in a decrease in probability that the postsynaptic cell will fire an action potential. In the case of binding of glutamate by the STN-neuron to receptor-channels of, in this case, the GPe-neuron, an influx of calcium-ions results, which depolarizes the membrane and increases the chance of action potential generation in the GPe-neuron.

Because many aspects of a neuron clearly show dynamical behaviour (as the membrane potential, the channel gates and ion concentrations), and these processes are often coupled, the behaviour of a neuron or a network of neurons, exciting and inhibiting each other, can be naturally captured in a mathematical nonlinear dynamical model. This description of the dynamical behaviour of a network of neurons is described in the next section. Now the anatomy and functional arrangement of a special part of the brain, called the Basal Ganglia (BG), is discussed. A sub-network of the Basal Ganglia consisting of two coupled nuclei, the subthalamic nucleus (STN) and the external segments of the globus pallidus (GPe) receive special attention as this network is the main subject for this research.

## The Basal Ganglia

The Basal Ganglia (or basal nuclei) are a group of nuclei located deeply in the brain which are interconnected with the cerebral cortex, the thalamus and brainstem. In humans the basal ganglia are associated with a variety of functions among which motor control, cognition, emotions and learning are the most important. The location of the BG in the brain is shown in Figure 1.5, in a horizontal cross section of the brain at ear height.

The five individual nuclei that make up the primate basal ganglia (see Figure 1.5), along with their major subdivisions, are:

1. The *striatum*, which consists of:

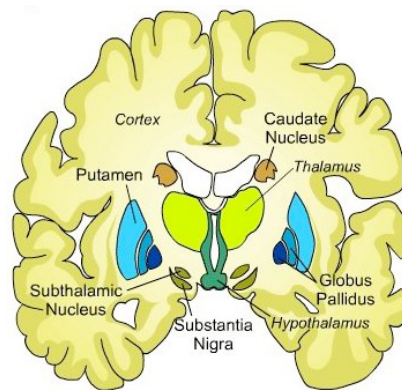


Figure 1.5: The location of the BG is shown in a horizontal cross section of the brain at ear height. The different nuclei of the BG, which come in pairs mirrored in the two hemispheres, are indicated in the figure.

- The putamen
  - The caudate nucleus
  - The nucleus accumbens (not indicated in Figure 1.5)
2. The external segment of the globus pallidus (GPe) (the outer part of the GP in Figure 1.5)
  3. The internal segment of the globus pallidus (GPi) (the inner part of the GP in Figure 1.5)
  4. The subthalamic nucleus (STN)
  5. The substantia nigra (SN), which consists of:
    - The substantia nigra pars compacta (SNc)
    - The substantia nigra pars reticulata (SNr)
    - The substantia nigra pars lateralis (SNl)

There are 2 sets of basal ganglia in the brain, mirrored in the left and right hemispheres as can also be seen in Figure 1.5.

In Figure 1.6 the different nuclei of the BG are shown with their interconnections with each other and with other parts of the brain.

The blue square in Figure 1.6 indicates the nuclei of the BG. The cortex and thalamus project to the basal ganglia, and the output nuclei are the GPi and SNr. Indicated are the excitatory (purple), inhibitory (blue) and dopaminergic (can be excitatory and inhibitory) connections (green) between the nuclei.

The striatum is the main input zone for other areas of the brain to connect with the BG. Via the striatum, the basal ganglia receives input from the cortex. The circuitry (see Figure 1.6) of the basal ganglia is often divided into two major pathways, the direct and the indirect pathway (when the connection is inhibitory a '-' can be seen above the projection arrow, when is it excitatory a '+');

1. The *direct* pathway: striatum  $\xrightarrow{-}$  GPi/SNr  $\xrightarrow{-}$  thalamus  $\xrightarrow{+}$  cortex.
2. The *indirect* pathway: striatum  $\xrightarrow{-}$  GPe  $\xrightarrow{-}$  STN  $\xrightarrow{+}$  GPi/SNr  $\xrightarrow{-}$  thalamus  $\xrightarrow{+}$  cortex

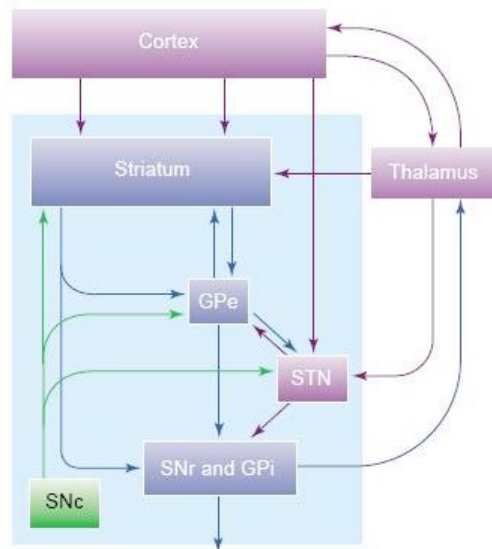


Figure 1.6: Schematic view of the Basal Ganglia, with connections present between the nuclei. Excitatory (glutamatergic) connections in purple, inhibitory (GABAergic) connections in blue and dopaminergic connections in green [4].

It is thought that the cortex, exciting the striatum in the indirect pathway, *inhibits* the thalamus while via the direct pathway it *excites* the thalamus.

Dopamine from the SNc stimulates all of the dopamine receptors in the BG, but because the different pathways express different receptor channels ( $D_1$  and  $D_2$ ), which express different effects, the following effects of dopamine can be observed: dopamine activates the direct pathway through  $D_1$ -receptor channels and inhibits the indirect pathway through  $D_2$  receptor channels. In this way dopamine excites the thalamus by ‘choosing’ the direct pathway instead of the indirect pathway.

### The STN-GPe-network

The focus of this research lies on the STN-GPe-network, which is a part of the indirect pathway of the BG. The STN-neurons are glutamatergic and therefore excitatory. The GPe-neurons are GABAergic ( $GABA_A$ ) and therefore inhibitory. The following characteristics of the network have been described in [4, 5]:

- The STN-GPe-network is innervated by the principal afferent of the BG, the cortex through the *direct* pathway, and through striatal neurons or thalamic neurons in the *indirect* pathway.
- The network has the most extensive connections with the output nuclei of the BG, the GPi and SNr. In this way the STN-GPe-network has a major influence on the communication between the BG and the rest of the brain.
- With their strong interconnections the two nuclei constitute a feedback system called a Central Pacemaker Generator (CPG), which means it can keep itself active (non-quiescent) without external input. Striatal inhibition only *modulates* the firing of the network [4].

- The network behaves differently in *normal* compared to *parkinsonian* states:
  - During *normal* information processing the firing of the various STN- and GPe-neurons is uncorrelated and displays a difficult spatiotemporal pattern.
  - In *parkinsonian* states, the pattern of firing of the network seems highly correlated and synchronous. The neurons seem to fire synchronically at low frequencies associated with the resting tremor frequency (0.4–1.8 Hz [5]), and the mechanisms, underlying this synchronized bursting, are uncertain:
  - There are contradictory results on the origin of synchronized behaviour seen in the STN-GPe-network and other nuclei of the BG. Three hypotheses:
    1. The synchronous rhythms start in the thalamus and are transferred through the thalamus to the GP (external and internal segments) [4].
    2. Rhythmic activity of the cortex drives the synchronized bursting in the STN-GPe-network [4]. This hypothesis is contradicted by results in [5] which show that cortical lesion does not abolish synchronized oscillatory bursting in the different nuclei.
    3. Synchronized oscillatory bursts are generated *within* the basal ganglia and specifically in the STN-GPe feedback system. [5] states that together with striatal modulation this CPG network generates oscillatory correlated bursting which is transferred to the other nuclei of the BG. Lesion of this STN-GPe-network abolishes the synchronized bursting behaviour.

Parkinson's Disease (PD), which originates in the BG, has been mentioned in the list above, and its characteristics with their link to the STN-GPe-network are discussed now.

### Parkinson's Disease

Parkinson's Disease (PD) is a movement disorder which originates in the BG. It is caused by a decreased stimulation of the motor cortex by the BG. This on its turn is caused by a decrease in formation and action of dopamine of the SNC, due to the loss of these cells. Due to the decrease in dopamine-secretion by the SNC, the indirect pathway gets less inhibited while the direct pathway gets less excited (see the end of the BG-section). The thalamus (and thus the cortex) therefore gets more inhibited and less excited which leads to for example muscle rigidity (stiffness), a tremor in muscles (of about 4–7 Hz), a difficulty to start/stop movement (akinesia), a slowing of physical movement (bradykinesia) and postural instability. Also cognitive disfunction, mood disturbances and language problems can be the result of this disease. It is a chronic and progressive disease.

The disinhibition of the indirect pathway can be seen as follows (the classical view): due to the loss of SNC-cells, the striatum over-inhibits the GPe, which therefore is unable to inhibit the STN. These become overactive and overexcite the output nuclei of the BG. They then overinhibit the thalamus and therefore the cortex.

The behaviour of the STN-GPe-network changes due to the over-inhibition of the GPe by the striatum. In normal states, the neurons within the network fire irregularly and show difficult uncorrelated spatiotemporal patterns, which possibly encodes information efficiently. In parkinsonian states the STN shows rhythmic correlated behaviour which leads to rhythmic and synchronous bursting in the output nucleus GPi that negatively affects thalamic cell responsiveness to sensorimotor depolarizing signals. It also could encode received and transferred information less efficiently [1].

Although the follow-up of events in the indirect pathway due to the over-activity of the striatum can be understood quite well, the influence of loss of dopamine on the generation of synchronous and correlated behaviour in the STN-GPe-network (and therefore also in the GPi), while *with* dopamine, it was uncorrelated and irregular, is not yet understood. Also the origin of the synchronized bursting behaviour in the different nuclei is uncertain (see the list in the previous section).

Because the PD-patient lacks dopamine molecules in the BG, medicines as L-DOPA, which is converted into dopamine in the brain of the PD-patient, can treat the PD-patient. Unfortunately only 1–5% of L-DOPA effectively enters the dopaminergic neurons in the SNC, and beside this drawback the medicine becomes counterproductive after a while due to the tolerance the patient develops to the drug.

Beside medicinal treatment, surgical treatments become more common. Deep Brain Stimulation of the STN has proven to be an effective treatment for the motor symptoms of PD. It dramatically alleviates motor symptoms and decreases dependence on dopaminergic drugs as L-DOPA. After the implantation of the electrode it typically sends high-frequency pulses ( $> 100$  Hz) to the STN [6]. It is clear that DBS works, but how does DBS actually modulate the activity in the target areas? Many neurosurgeons do not have the slightest idea [7]. One theory is that DBS *suppresses* the firing of the STN when the electrode is placed on the soma of a STN-neuron. This treatment then mimicks the effect of the lesion of the STN. If this is the case it then leads to less excitation of the output nuclei and therefore less inhibition of the thalamus and cortex. An opposite theory on the other hand states that DBS *enhances* activity of the STN when the electrode is placed on the axons of the neuron. This does not resemble the effect of a lesion of the STN at all and should inhibit the thalamus by the GPi even further [7]. How can *enhancement* of STN-activity oppose the PD-inhibition of the thalamus, *caused* by the overactive STN? The hypothesis is that in this case DBS modulates periodic high-frequency tonic firing of the BG (higher frequency than of normal irregular firing and of pathological bursting [8]) to “mask” the pathological firing patterns (synchronized rhythmic bursting) that characterize the parkinsonian state [6, 9].

There are some negative aspects to DBS. Because little is known on the exact role DBS plays in reducing the synchrony between neurons it could cause serious complications and side-effects. The effects of the high-frequency pulses on other neurons in the brain is also unsure.

Lesioning of the STN or GPi is another surgical treatment of PD but is less often applied than DBS at the moment.

### 1.1.2 Neurodynamics

After the description of some general concepts of neurophysiology and describing the physiology behind PD and DBS, the field of neurodynamics will be explained, a field which applies mathematical (nonlinear) dynamical systems theory on problems and questions arising from neuroscience. First some reasons will be given why mathematics can be of great importance for the community of neuroscientists. Then one of the first dynamical models to describe the behaviour of a neuron's membrane potential is shortly explained: the conductance-based Hodgkin-Huxley model. Many neural models today are of this type, because of its accuracy, and so is the model used in this research. The different variables used in the conductance-based model given in [1], which is used in this research, can then be understood easily. Finally some initial information is given on bifurcation theory which is a theory within dynamical systems theory, which looks at the influence of parameters in dynamical systems on the behaviour of the solutions. This theory is used extensively in this research as well.

#### Applied mathematics versus classical neuroscience

Many people will wonder why we should use mathematical models and theories to analyse neuronal behaviour, while results from experiments on neurons in vivo/vitro should suffice to describe this? Some arguments will be given why mathematics can provide a useful and necessary tool to analyse the more dynamical behaviour of a neuron or a network of neurons.

As described in the previous section the neuron's variables as membrane potential, gating 'variables' and intracellular ion concentrations, all change in time and are often dependent on each other in their dynamics. When this dynamical behaviour is not taken into account and only static models of neurons are analysed, a fundamental flaw of traditional neuroscience is discovered: the dynamical behaviour of a neuron is often described in average values [7].

Some examples of other flaws of the traditional approach of neurons by certain biologists. The following is for example not even questioned by many biologists:

“Excitation increases firing rates and inhibition decreases them”

But chemical inhibitors are not merely an off switch for neurons, but more a kind of control knob that reduces or increases the amount of synchronization among sets of neurons [7].

Another flaw described in [3]:

“Knowing the membrane currents of a neuron suffices to determine what the cell is doing and why”

This is contradicted by cells which have similar membrane currents but quite different types of dynamical behaviour [3] (due to different bifurcation mechanisms described later).

When oscillations and synchronization between firing patterns within networks are discussed this time factor can definitely not be left out anymore. These phenomena are mathematically related to dynamical systems theory. When an accurate model of the specific network is defined, mathematical analysis of this model can give valuable information on for example phase relations between

the cells, and transitions between different types of spiking the neurons can go through [7].

There are many reasons why the mathematical analysis of an *accurate* dynamical model of a neuron, or network of neurons, can give a richer picture on the various types of behaviour the neuron or network can show. Also possible synchronization between neurons in networks can be found by such an analysis. Experiments performed on neurons often give a more limited view on aspects of *dynamical* behaviour.

### The conductance-based HH-model

The Hodgkin-Huxley model developed in the fifties to describe the dynamics of a neuron's behaviour as a system of coupled ODEs [10], was a revolutionary result *then* but is still used nowadays as one of the most accurate neuronal models. Because the STN-GPe-model described in [1] is such a HH-type of model, the basic concepts of these type of models will be shortly explained in this section.

The model is developed as a *single-compartment* model. This means that the spatial component is not taken into account in the model and the model therefore describes the dynamical behaviour of the neuron at a specific 'point'-location on the membrane. An infinitely small point of the membrane does not contain any channels of course, and the HH-model is therefore an approximation of a *small* area of the neuron's membrane. Assumptions are therefore:

1. The model describes  $V(t)$  at a *specific* location  $x = x_0$  on for example the axon.
2. At  $x = x_0$  it is assumed that  $V$  is constant along the membrane surrounding the axon.
3.  $dV/dt$  is related to *the net membrane current* in a infinitesimally small time interval  $dt$  at location  $x = x_0$ . The net membrane current is then given in unit of current per unit of area, like pA/ $\mu\text{m}^2$ .

The concepts will now be explained for the model of a simple neuron, with only channels permeable to sodium and potassium located in its membrane. Channels of both currents are voltage-gated,  $I_{Na+}$  is a transient current (the channels have activation and inactivation gates), and  $I_{K+}$  is a persistent current (with only activation gates). An ohmic leak current  $I_L$  (with its conductance independent on  $V$ ) is also present due to resting channels which are always in the open state.

An equivalent circuit of the membrane is shown in Figure 1.7. 'Outside' indicates the extracellular fluid and 'inside' the intracellular fluid.

Because the membrane of a neuron is a lipid bilayer, and the charge of the extracellular fluid differs from the intracellular one (resulting in the potential difference over the membrane), the membrane can be represented as a capacitor due to its separation of charge. An electrical field is present in the membrane. The capacitance  $C_m$ , is a measure of the amount of charge on each 'plate' (a layer of the membrane) for a given potential difference (in F):

$$C_m = \frac{Q}{V}$$

For neurons this capacitance is often normalized to 1.0 pF/ $\mu\text{m}^2$ , where the area of the membrane is included, just as in the currents. Due to this separation of

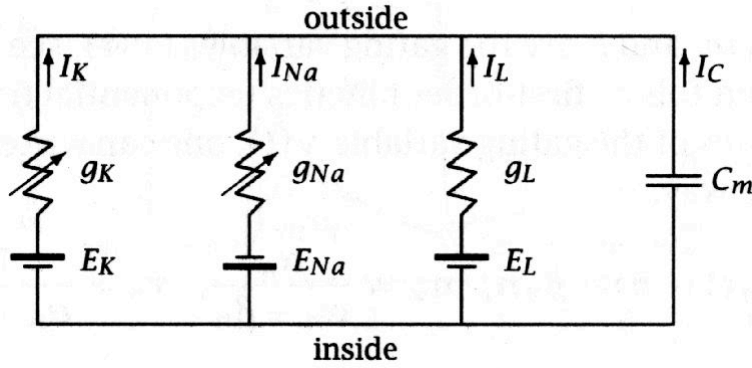


Figure 1.7: The membrane can be represented by an equivalent circuit. The membrane is presented as a capacitor with the inner and outer membrane being the conductors. The conductances are indicated as a (variable when dependent on  $V$ ) resistance, because they are inversely proportional to the resistance. The batteries, which provide the energy for the current, are the equilibrium potentials  $E_X$  for the currents of ion-type  $X$  and the capacitance  $C_m$  for the capacitive current.

charge a capacitive current

$$I_C = C_m \dot{V}$$

is therefore present next to the ionic currents. The current is dependent on  $\dot{V}$  because it takes time to charge the capacitor (membrane).

The total net current across the membrane is the sum of the individual currents:

$$I = C\dot{V} + I_{Na^+} + I_{K^+} + I_L$$

Rearranging the terms gives the HH-model of this simple neuron in (1.3). It relates the time derivative of the neuron's membrane potential to the currents flowing through the channels (in this case only two).

$$C\dot{V} = I - I_{Na^+} - I_{K^+} - I_L \quad (1.3)$$

$I \neq 0$  when sources or sinks are present (such as an applied current). The formula for  $I_{Na^+}$  is given by:

$$I_{Na^+} = g_{Na^+}(V - E_{Na^+})$$

With  $g_{Na^+}$  the membrane conductance with respect to  $Na^+$ -ions (dependent on  $V$ !),  $V$  the membrane potential and  $E_{Na^+}$  the equilibrium potential for  $Na^+$ .

$g_{Na^+}$  is given by:

$$g_{Na^+} = \overline{g_{Na^+}} m^a h^b$$

With:  $\overline{g_{Na^+}}$  the maximal conductance,  $a$  the number of activation gates,  $b$  the number of inactivation gates and  $m$  and  $h$  the probability of these gates to be in the open state. These gating variables  $m$  and  $h$  are dependent on the membrane potential, because the channels are voltage-gated. Only when  $h$  and  $m$  are nonzero ((partially) deinactivated and activated) a current is present.

When both are 1, the current is at its maximum ( $m^a h^b = 1$  and  $g_{Na^+} = \overline{g_{Na^+}}$ ). The ODEs for these gating variables  $m$  and  $h$  are given by ( $X \in \{m, h\}$ ):

$$\frac{dX}{dt} = \frac{X_\infty(V) - X}{\tau_X(V)}$$

In Figure 1.8 the steady-states  $m_\infty(V)$  and  $h_\infty(V)$  for  $m$  and  $h$  are plotted together.  $X_\infty(V)$  (with  $X \in \{m, h\}$ ) is the steady state (in)activation function, which gives the values for  $m$  and  $h$  for voltage values  $V$ , to which they will converge.  $\tau_X(V)$  is the time constant for the specific current. In regions of  $V$  where the time constant is small the (in)activation is fast, and where  $\tau_X$  is large the response to changes in  $V$  is slow.

The steady states together determine the voltage-range (yellow in Figure 1.8) in which the current is nonzero. Only in the voltage-range in which *both*  $h_\infty(V)$  and  $m_\infty(V)$  are nonzero a sodium-current is present.

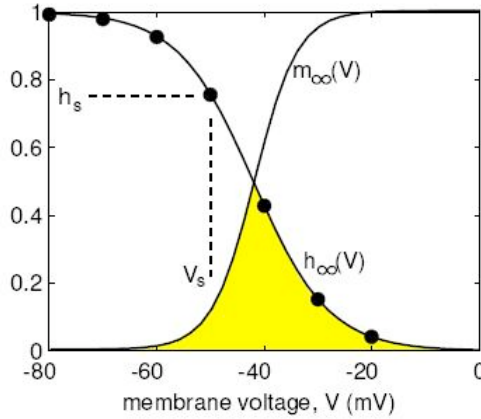


Figure 1.8: The steady state (in)activation functions for  $I_{Na^+}$  together determine the voltage-range in which  $I_{Na^+}$  is nonzero (yellow region).

Together this simple neuron already has a 4D coupled ODE-system with  $m$  and  $h$  the gating variables for  $I_{Na^+}$ ,  $n$  the gating variable for  $I_{K^+}$  and  $V$  the membrane potential, all four given by an ODE. Often it is assumed that  $m(V) = m_\infty(V)$  due to the fast activation of  $I_{Na^+}$  ( $\tau_m(V) \approx 0$  for all  $V$ ). This reduces the number of variables and thereby the complexity of the model. Most neurons consist of various types of channels, voltage- and ligand-gated, with their own speed of (in)activation. When all of the resulting currents would be included in the model, high-dimensional models would be the result. Difficult choices are therefore always which currents should at least be included in the HH-type of model of the neuron, to represent the neuron's behaviour as accurate as possible, while keeping the size of the model moderate.

### Bifurcation theory

Conductance-based models, in which parameters are still present can be analysed with a powerful mathematical tool called bifurcation theory. When certain

characteristics as conductances  $g_X$  or responses of a neuron to an applied current  $I_{app}$  are for example unknown, bifurcation analysis can give a detailed insight in the influence of the specific parameter on the dynamics of the system. The quality of the analysis of course depends drastically on the accuracy of the model.

When a codim-1 bifurcation analysis is applied to a model as in (1.3), with the parameter being varied the applied current  $I$  (often called  $I_{app}$ ) and the variables being  $V$ ,  $m$ ,  $h$  and  $n$ , the aim is to divide the parameter line for  $I$  in different regions in which System (1.3) behaves qualitatively different from other regions. This can be done by first looking at the equilibria of the system. The system is at an equilibrium when the right hand sides of all four ODEs are zero:

$$\begin{aligned}\dot{V} &= 0 \\ \dot{m} &= 0 \\ \dot{n} &= 0 \\ \dot{h} &= 0\end{aligned}$$

Such a 4D-solution to these equations, is one-dimensional (a curve) in  $\mathbb{R}^5$  due to the five unknowns (in the four equations). With two parameters the solution would be twodimensional (a surface) in  $\mathbb{R}^6$ . The projection of this curve on the IV-plane gives the IV equilibrium curve in a plane. Thus for every value of the parameter  $I$ , the values of the variables in the equilibrium have changed. Also more than one equilibrium can be present in one range of  $I$  while in another range only one is present. The eigenvalues of the equilibria determine the type of equilibrium (saddle, focus, node) and its stability. This will not be explained here, but the interested reader is referred to any introductory book on dynamical systems. The rest of the mathematics concerning codim-1 and codim-2 bifurcation theory can be found in the rest of the report and especially in Appendix C. What is of importance is that along this curve the stability of the equilibrium can change (because the eigenvalues change). A stable equilibrium can become unstable and this transition is called a bifurcation, because the behaviour of the system changes qualitatively. When the system analysed represents the behaviour of a neuron, the neuron would have been quiescent when the equilibrium was stable (in a certain range of applied current), and nonquiescent when the equilibrium had become unstable (in a different range). Codim-1 bifurcations of stable equilibria are of Hopf- or saddle-node type.

When a supercritical Hopf-bifurcation occurs the stable equilibrium loses its stability and a stable *limit cycle* is born. This means mathematically that the solution to the neural system will not converge to the equilibrium anymore (it is unstable in this new parameter region) but will converge to the stable limit cycle. For the behaviour of the neuron this means that before the Hopf bifurcation, for certain values of  $I$ , the neuron was quiescent, but for a somewhat stronger (or weaker) applied current  $I$  the membrane potential will spike repetitively with a certain amplitude and frequency.

This emerged limit cycle can bifurcate as well. The multipliers of the Poincaré map corresponding to the limit cycle determine its stability and type. The multipliers of this limit cycle vary dependent on the parameter  $I$ . When the stability of the limit cycle changes, or the limit cycle disappears, a bifurcation takes place. At such bifurcations extra limit cycles can emerge and surround

the original (possibly unstable one). This results in tori, and two instead of one frequency can be observed during spiking. When for example the stable limit cycle has become unstable, the neuron will stop spiking and converge to the stable equilibrium possibly present in this region of the parameter. The neuron's behaviour has thus qualitatively changed at a certain parameter value, the bifurcation point. Codim-1 limit cycle bifurcations are explained in Appendix C.1.2 and are encountered, and also discussed, in the analyses of the STN- and GPe-models.

The saddle-node type of codim-1 equilibrium bifurcation has not yet been explained. To show this type of bifurcation the analysis of a simple neural model is shown. A phase portrait of the system is shown in Figure 1.9, with the projection on the  $V, n$ -plane.

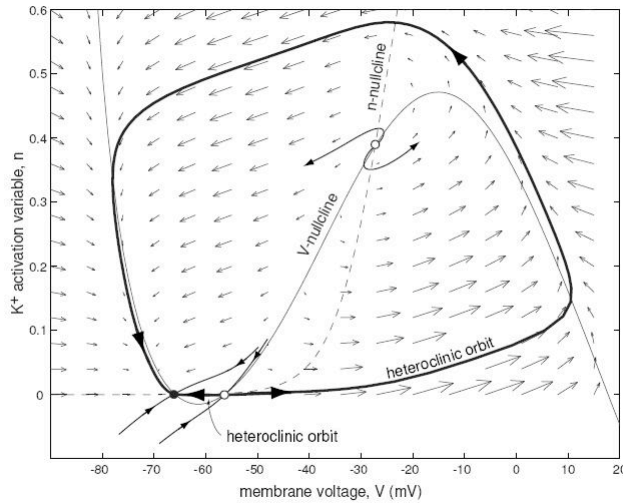


Figure 1.9: The phase portrait of the system with  $I < I_{bif} \approx 4.51$ . Two variables,  $V$  and  $n$ , are plotted on the  $x$ - and  $y$ -axis respectively. On the  $V$ -nullcline  $\dot{V} = 0$  and on the  $n$ -nullcline  $\dot{n} = 0$ . The intersections of these curves give the equilibria: two unstable equilibria (open dots) and one stable (black dot) one are present. A heteroclinic orbit connects the stable and an unstable node [3].

The activation variable  $n$  for the  $K^+$ -current is plotted on the  $y$ -axis and the membrane potential  $V$  on the  $x$ -axis. The  $V$ - and  $n$ -nullcline indicate where  $\dot{V} = 0$  respectively  $\dot{n} = 0$ . Where the two curves intersect the system is thus in equilibrium (both variables do not change in time). Three equilibria can be seen in Figure 1.9. Only the filled dot indicates a stable equilibrium (a node), the two open dots are unstable ones (focus and node saddles). An orbit connects the unstable and stable equilibrium, and is called a heteroclinic orbit. Due to the stable equilibrium, the neuron is quiescent in this region of the parameter line. This figure corresponds to the situation  $I < I_{bif}$  where  $I$  is the parameter and  $I_{bif}$  is the bifurcation value. The bifurcation has thus not yet occurred and the neuron is quiescent.

In Figure 1.10 the situation is drawn for  $I = I_{bif}$ . The  $V$ -nullcline has shifted

up. The stable and unstable equilibrium, which both were on the heteroclinic orbit, have coalesced and become one. The heteroclinic orbit has become a homoclinic one.

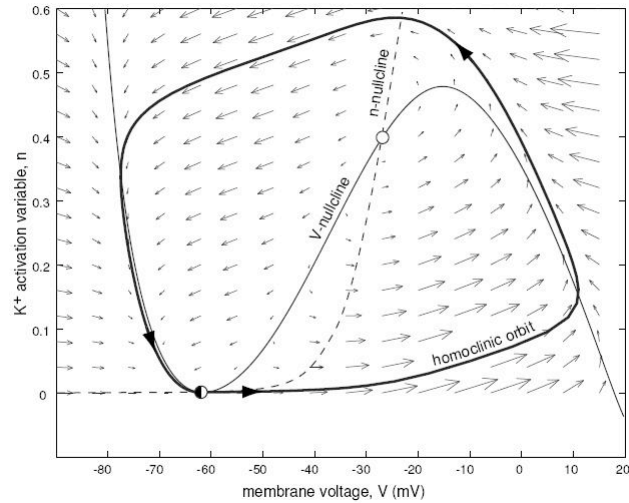


Figure 1.10: The phase portrait of the system for  $I = I_{bif} \approx 4.51$ . A stable and unstable equilibrium have coalesced on the invariant circle [3].

The situation for  $I > I_{bif}$  is shown in Figure 1.11 where the  $V$ -nullcline has shifted up even more, resulting in the total disappearance of the two equilibria.

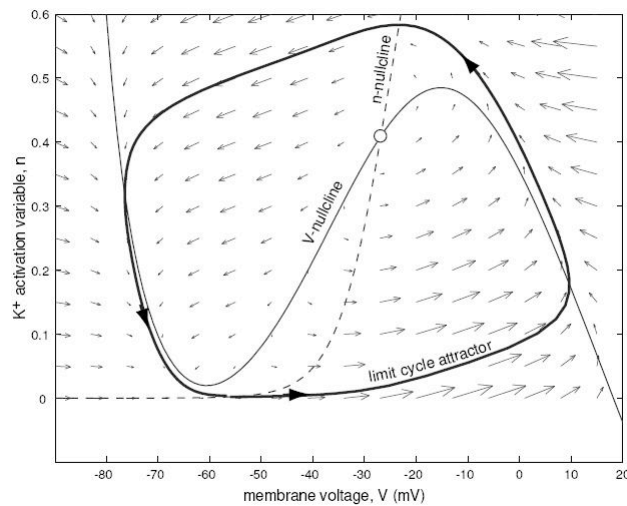


Figure 1.11: The phase portrait of the system for  $I > I_{bif} \approx 4.51$ . The stable and unstable equilibrium have disappeared and a stable limit cycle has been born from the invariant circle [3].

The invariant circle has become a limit cycle attractor. Due to the instability of the only equilibrium, the solution will converge to the stable limit cycle and the neuron will show spiking behaviour. The time diagram for  $V(t)$  is shown in Figure 1.12 which shows the dynamical behaviour of the membrane potential when  $I$  is gradually increased. It is clear that the behaviour of the system (and thus neuron) has qualitatively changed at the bifurcation value (from quiescent to spiking behaviour).

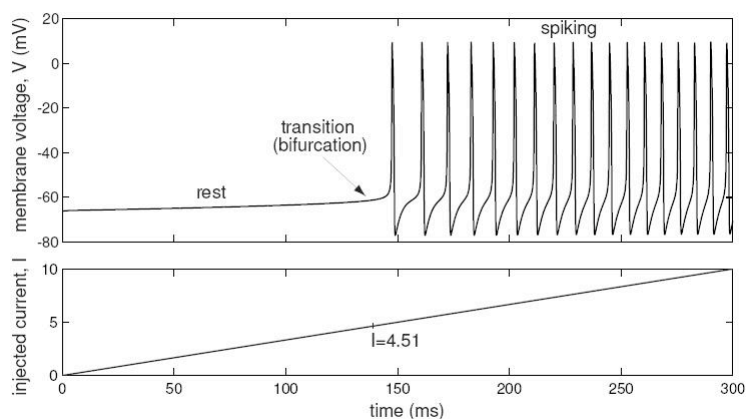


Figure 1.12: The time diagram for  $V(t)$  is shown when  $I$  increases gradually past the bifurcation value  $I_{bif}$ . For  $I < I_{bif}$  the neuron is quiescent (stable equilibrium). For  $I > I_{bif}$  the neuron spikes (stable limit cycle) [3].

Because bifurcation theory is such a powerful tool to really understand a neuron or network's behaviour this mathematical theory can hopefully give us more insight in the behaviour of the STN-GPe-network, such that the unanswered questions, described in the previous section, can be answered. Bifurcation analysis of course can only give much insight when good models are present for the STN-GPe-network. All the information given in this introduction then brings us to the motivation to conduct the research described in this report.

## 1.2 Motivation

After the description of some neurophysiological and neurodynamical concepts, the following unanswered questions on the behaviour of the STN-GPe-network can be listed from the above theory:

1. Concerning the synchronized correlated low-frequency firing seen in the parkinsonian STN-GPe-network:
  - Where does it originate? The thalamus, cortex or in the network itself?
  - What is the influence of the loss of SNC cells, and thereby the decrease in secretion of dopamine, on this synchronized behaviour?
  - What is the influence of the STN and GPe individually on these rhythms?

- How does the striatum exactly modulate these rhythms?
2. On DBS applied to the STN:
    - Does DBS excite the STN or inhibit it?
    - How does DBS eliminate this firing at tremor frequency when it possibly excites the STN-neuron even more?
    - What is the necessary amplitude and frequency of pulses necessary to eliminate the tremor frequency, and why these numbers?
  3. On the analysis of the network using bifurcation theory on a *good* STN-GPe network-model:
    - Are there accurate models for the STN-GPe-network which can be analysed using bifurcation theory? What are the main uncertainties in the model?
    - If yes: how can we use bifurcation theory in such a way that more understanding can be gained on the synchronization between the two nuclei? Which parameters should be chosen in the model, to give us more insight?
    - What type of architecture should be chosen in the model for the connections between the various neurons of the two nuclei? Is it known how the nuclei are connected?
    - Which other external nuclei should at least be included in the network-model to represent a situation of the STN-GPe-network which is comparable with reality?

The incentive to do this research lies in these various unanswered questions concerning the origin of the synchronized bursting behaviour seen in the various nuclei of the BG corresponding to Parkinson's Disease (PD) within the BG. Much is still uncertain in this area, while for proper treatment of PD-patients this knowledge is indispensable. Of course trying to answer all these questions might take years of study. Therefore a delimitation of the scope of the problem is necessary. This delimitation leads to the problem definition of this research, described in the next section.

### 1.3 Problem definition and approach

To use bifurcation theory to gain more knowledge on the STN-GPe-network, and to be able to answer some of the questions listed above somewhere in the future, first a conductance-based model of the network should be chosen. Because only one is present for the total *network* ([1, 9]) this one will be used for this research.

The global aim of this research, resulting from the considerations described in the previous section, is:

“To gain more knowledge on the behaviour of the STN-GPe-network by applying bifurcation theory to the network model given in [1], using the Matlab bifurcation software, MatCont. The different conductances between the nuclei should be taken as the parameters for the bifurcation analysis, just as in [1], to test the influence of the strength of the connections on the type of network behaviour. When larger networks are considered different architectures of connections between the neurons should be analysed. By varying the parameters

and architectures the parkinsonian behaviour of the network can possibly be seen and could give us more insight on the influence of the parameters and architectures on this generation of pathological rhythms. An extra aim is to make the figures in [1] which indicate the transition boundaries between various types of network-firing behaviour, more accurate and detailed.”

A delimitation of this global problem definition is necessary to make it suitable for a MSc-project, which consists of approximately six months of research. Unfortunately only a start can be made with the defined problem/aim which then hopefully can be finished by other researchers. The following subproblems should be solved during this research (using the same model from [1] and the bifurcation software MatCont):

**Analysis of the models of the individual neurons:** To compare the model-behaviour with experimental literature, simulations of the model need to be made. A bifurcation analysis of each neuron-model with the parameter being the applied current (simulating the synaptic current of the other nucleus), can give insight in the possible behaviour of each neuron and the influence of the other nucleus on this behaviour. Good evaluations of both models can then be made.

**The analysis of a small two-cell network:** A seemingly trivial network of one STN- and one GPe-neuron, reciprocally connected, should first be understood thoroughly before extensions to larger networks are possible. First the model synaptic connection chosen in [1] should be evaluated. A bifurcation analysis, with the two conductances taken as the parameters, should give more insight on the types of network behaviour possible in the various regions of the parameter plane. The influence of the strength of the connections on the type of behaviour of this small network can then be deduced.

## 1.4 Structure of the report

The report consists of three chapters and each has the same structure given below. The next two chapters, 2 and 3, describe the analysis of the STN- and GPe-models respectively (the first point of the two problems just above this section). Chapter 4 describes the analysis of the two-cell network consisting of one STN- and one GPe-cell (the last point of the problems above). Every chapter has the same structure:

1. Literature
  - (a) Experimental (and computational) results
  - (b) The model
2. Analysis
  - (a) Bifurcation analysis
  - (b) Simulations
3. Discussion

---

Simulations of both model-neurons (analysis part) are compared with experimental results (literature part) of the specific neuron. Experimental results for a two cell STN-GPe-network are not present. Therefore simulations of the two-cell model (analysis part) are compared to computational results from studies with similar, but larger, networks (literature part). The bifurcation analyses (codim-1 for the two individual neuron-models and codim-2 for the two-cell network) aims to give a detailed division of the parameter space in regions in which the neuron or neurons behave qualitatively different from other regions. The discussion at the end of each of the three chapters evaluates the results from simulations and the bifurcation analysis. In Chapter 5 the overall conclusion of the research can be found and in Chapter 6 recommendations for future research, extending this research and analysis to larger networks. The references and appendices finish the report where the appendices consist of the model constants from [1] (Appendix A), Matlab code (Appendix B), the possible codim-1 and codim-2 bifurcations with their characteristics (Appendix C), and the description of pulse-coupled models (Appendix D).



## Chapter 2

# The STN-neuron

This chapter discusses the STN-neuron by thoroughly analysing a mathematical model describing the dynamics of the STN-neuron's membrane potential and comparing the results with literature.

Section 2.1 describes experimental results for the STN-neuron and a specific dynamical model for the STN-neuron.

In Section 2.2 the results of *this* research will be presented, consisting of a detailed bifurcation analysis of the model described in Section 2.1 and various simulations. For this analysis and especially for the influence of the synaptic current  $I_{G \rightarrow S}$  on the model-neuron's behaviour, an applied current  $I_{app}$  is substituted for  $I_{G \rightarrow S}$  and worked with further on. In Section 2.2.1 the codim-1 bifurcations will be sought where the parameter is taken to be this applied current  $I_{app}$ , simulating the synaptic current from the GPe. These codim-1 bifurcations for equilibria and limit cycles indicate the ranges of applied current  $I_{app}$  in which the neuron spikes or is quiescent or where the system is bistable. The transitions between these states occur exactly at the found bifurcations. To illustrate the different types of behaviour of the model within these regions in parameter space, simulations of the model will be shown in Section 2.2.2. Initial conditions for the variables and parameter are taken from these regions. The different outcomes will be linked to the bifurcation diagram in Section 2.2.1. Also step- and pulse currents will be taken for  $I_{app}$  to record the neuron's response to fast and strong stimulation.

In Section 2.3 the results of the model, described in Section 2.2, will be shortly listed and discussed by comparing them with the experimental results. Possible differences between the model and experiments are evaluated and considerations for modelling are mentioned.

### 2.1 Literature

This section describes experimentally found results for the STN-neuron, and a specific conductance-based model which will be analysed in Section 2.2. In Section 2.1.1 the various spontaneous firing characteristics of the neuron are mentioned, as well as the neuron's reaction to various types of input. The currents measured through the membrane are listed at the end of the section. All results are found during experiments *in vitro* and *in vivo*. In Section 2.1.2 a

conductance-based model given in [1], is described. This model forms the basis for the analysis in Section 2.2.

### 2.1.1 Experimentally found results

This section will describe the electrophysiological properties of the neurons within the STN.

The STN is an oval-shaped small nucleus [11] which receives inhibitory and excitatory inputs from other neurons within the Basal Ganglia (as can be seen in Figure 1.6 on Page 10). Often various types of neurons can be found within a certain nucleus (see for example Section 3 on the GPe). Different types can be distinguished on the basis of electrophysiological characteristics. In contrast to the GPe, in which three totally different types of neurons occur, literature on STN-neurons seems to agree that within the STN only *two* electrophysiological types of neurons can be found which differ on only one characteristic: the ability of these neurons to generate plateau potentials (at the end of this section this phenomenon is explained). A subpopulation of STN-neurons is able to generate these plateaus while the rest is not. The ability to generate plateau potentials is the only characteristic on which these neurons seem to differ. For this reason the characteristics of *the* STN-neuron are described until the last section on hyperpolarizing input. In this section the generation of plateau potentials is discussed, and therefore a distinction should be made in this section between the two types. That distinction is not necessary during the discussion of the other characteristics.

When input to the STN-neuron is absent the neuron shows spontaneous spiking behaviour. The characteristics of this firing behaviour is described in the next section. The experimentally found responses of STN-neurons to de- and hyperpolarizing current injections will be described in the last two sections.

Experimentally found results can differ between articles because [12]:

- Experiments are done either in vivo or in vitro which give different results. In vivo other neurons are still present which can innervate the tested STN-neuron. In vitro the influence of other neurons can be limited.
- Different animals are tested: rats, primates and guinea pigs. Results from these animals are likely to differ.
- The results from in vitro experiments can differ because:
  - Results from experiments on brain slices where the other neurons and axons are still in tact, differ from acutely isolated neurons, which often only consist of the soma with the axon.
  - The preparation of the neurons makes a difference. The molecules of the preparation can transfer electrical energy and therefore influence the measured electrophysiological reaction of the tested STN-neuron.
  - Different recording techniques or stimulating techniques influence the results as well.

The experiments with STN-neurons, referred to in this section, are often in vitro instead of in vivo. The reason for this is that the STN is located very deeply in the brain and can not be reached easily [13]. When results of different articles differ too much, the method of experiments will be mentioned.

### Spontaneous spiking

When input to a STN-neuron is absent (in vivo this means: in awake-and-resting state), most STN-neurons *in vitro* show regular spontaneous single-spiking behaviour also called the resting oscillation. In vivo a more irregular firing pattern is observed where also doublet and triplet spikes are fired [14]. An example of a spontaneous firing STN-neuron in vitro can be seen in Figure 2.1. The most important characteristics of this spontaneous spiking behaviour are [14, 15]:

1. The depolarization phase ranges from  $\pm -60$  mV to  $\pm 45$  mV.
2. The spikes show a high level of *regularity*: the interspike interval is approximately constant after a while and the shape of the spikes does not change significantly.
3. The average interspike interval is approximately 500 ms which represents a firing frequency of 0–10 Hz. In vitro this frequency is approximately 10–30 Hz [14].
4. A *cycle* of a resting oscillation consists of (see Figure 2.2):
  - A single action potential, followed by:
  - A strong and long-duration afterhyperpolarization (AHP). This AHP consists of a *fast* one followed by a *longer*-lasting one. The long-lasting afterhyperpolarization is the cause of the low-frequency of the firing pattern. The AHP is followed by:
  - A slow-ramp depolarization, which brings the membrane potential near the threshold for firing another action potential. Mathematically this slow depolarization means that the trajectory (still on the cycle) follows the separatrix of a saddle, and stays close to the saddle for a while [3].

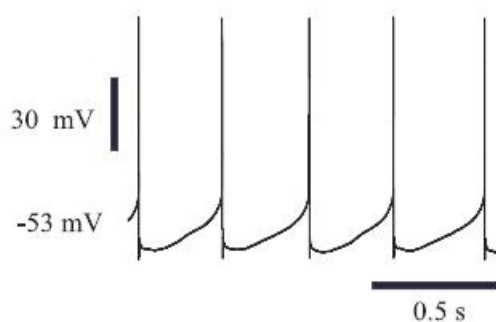


Figure 2.1: An example of a spontaneous firing STN-neuron [14].

### Depolarizing input

The STN-neuron receives excitatory input from the thalamus, cortex and the substantia nigra pars compacta (SNc) (see Figure 1.6). STN-neurons do not

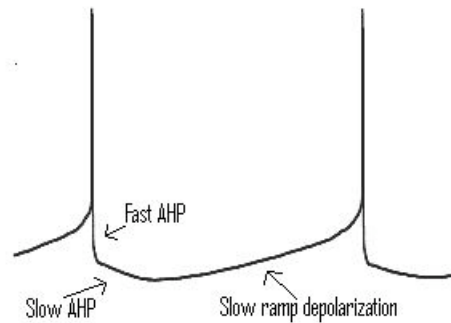


Figure 2.2: The fast and slow AHP and the slow depolarization ramp (figure is adjusted from [14]).

excite other STN-neurons (as we will see later on, this is different for the GPe-neurons) [14].

In Figure 2.3 the shape of an applied depolarizing current step is shown. Here  $a$  is the strength of the step (in  $\text{pA}/\mu\text{m}^2$ ) and  $b$  the duration of the step (in ms). For a depolarizing *applied* step it holds that  $a > 0$ .

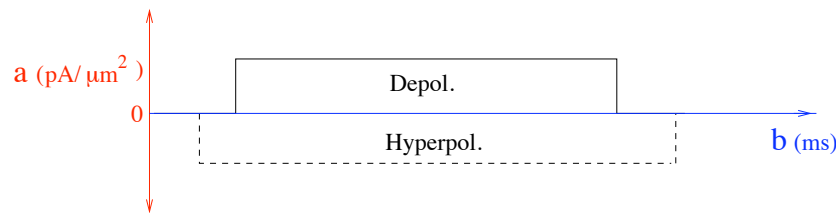


Figure 2.3: An example of a step current injection with  $a$  the strength of the step in  $\text{pA}/\mu\text{m}^2$  and  $b$  the duration in ms. Depolarizing:  $a > 0$  (shown in the figure), hyperpolarizing  $a < 0$ .

The *strength*  $a$  of an applied current-step influences *the frequency* of the generated action potentials. The larger  $a > 0$ , the higher the number of generated action potentials per time period. The STN-neuron fires at very low frequencies during spontaneous spiking but can reach up to 300–500 Hz when injected with a depolarizing current [14]. The increase in frequency of firing during the application of a depolarizing current step can be seen in Figure 2.4. A typical fI-curve of a STN-neuron, in which the frequency is plotted against the input current, can be seen in Figure 2.5. The curve looks sigmoidal and consists of three ranges. The secondary range is the sensitive range where a small increase in current strength gives the largest increase in frequency. The curve is often assumed linear up to 200 Hz [13] which seems not the case in Figure 2.5. In literature the slope of this ‘approximately linear’ part ranges from  $\pm 500 \text{ Hz/nA}$  (inferred from Figure 2.5 [14]) to  $900 \text{ Hz/nA}$  [13]. Both [13] and [14] use brain slices from the same type of rats for their experiments. The brain slices in [13] are somewhat thicker ( $100 \mu\text{m}$ ) than in [14] and the brain slices are kept in different solutions but these differences can not cause the large difference in slope. At very large applied currents the repetitive firing fails when the membrane potential fails to

repolarize sufficiently. The high-frequency firing is then replaced by a constant depolarized plateau. Although in Figure 2.5 the frequency of spontaneous firing (at  $I = 0$ ) seems to be zero, this is of course not the case. The spontaneous spiking frequency is in the order of 0–10 Hz and can therefore not be seen in the figure.

Although the frequency increases, the voltage range which is traversed by the STN-neuron should be approximately the same as during spontaneous firing [14]. At membrane potentials more depolarized than -30 mV, spike amplitude *does* seem to decrease with an increase in  $a$  [15].

Another consequence of an increase in the strength of the depolarizing step (with the duration kept constant) is that the afterhyperpolarization (AHP) after the break of the step lasts longer before spontaneous spiking takes over again. AHP-duration after the applied step thus increases smoothly with frequency [14].

The *duration* of an applied current-step influences the *spike-frequency adaptation*. The frequency of firing of the STN-neuron speeds up significantly during the first few intervals of applied current (not at the lowest firing rates). After that, slow spike frequency adaptation occurs, which gradually lowers the frequency [14]. This can be seen in Figure 2.6.

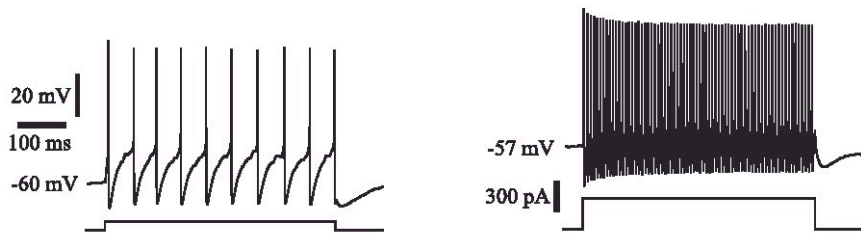


Figure 2.4: Influence of the strength of an applied depolarizing current-step on the firing rate of a STN-neuron [14].

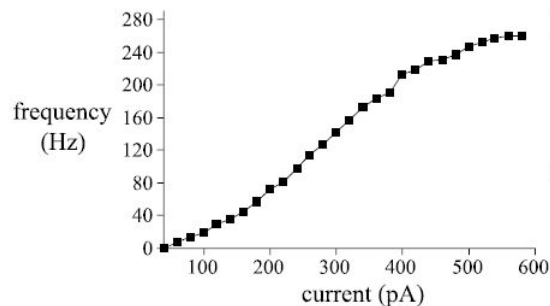


Figure 2.5: The typical sigmoidal shape of the  $fI$ -curve of a STN-neuron [14]. The offset is approximately zero.

### Hyperpolarizing input

As already mentioned in the introduction of this section, a distinction can be made within the STN between neurons which are *able* to generate plateau potentials and neurons which are *not able* to do so. The meaning of a plateau potential will be explained in this section. Only in this section it is necessary to make that distinction because it has a large influence on the various responses to hyperpolarizing stimuli. Both types of neurons react differently to these current injections. For a hyperpolarizing step,  $a$  in Figure 2.3 is smaller than zero.

The response of the STN-neuron to hyperpolarizing steps is not that clear yet. There are contradictory articles on the subject. What is definitely clear is that all STN-neurons become quiescent *during* the application of a sufficiently strong hyperpolarizing step current and that all neurons show rebound bursting behaviour *after* the break of the hyperpolarizing pulse. The two populations only differ in the decay of the rebound bursts. What exactly occurs *during* the application of a hyperpolarizing step (not sufficient to make the neuron quiescent), and which ion channels become active, is still unclear.

A subpopulation of the STN-neurons is able to generate voltage-dependent plateau potentials when they are more hyperpolarized than approximately  $-75$  mV and are innervated by glutamate receptor-mediated EPSPs [5, 11, 16, 13]. A plateau potential is a stable membrane potential more depolarized than the resting membrane potential. It is thus an increase in membrane potential often due to an applied de- or hyperpolarizing pulse and this increased potential does not disappear after the break of the pulse. The generation of a plateau potential requires the steady state IV-curve to cross the zero current line with a negative slope [16]. Because of the increase in membrane potential a plateau potential is often accompanied by the generation of a burst of action potentials. The depolarization necessary to generate a plateau potential is approximately  $10$  pA/ $\mu\text{m}^2$  [16]. The early phase of the plateau potential is resistant to membrane perturbations. When the membrane is not hyperpolarized sufficiently the plateau does not outlast the applied current pulse. The plateau-generating STN-neurons are also able to generate long-lasting rebound bursts after the break of an applied hyperpolarizing step of less than again  $-75$  mV [17, 16]. See Figure 2.6 for such rebound activity. After this burst the plateau potential shows a very slow decay [16] after which spontaneous spiking sets in again.

The rest of the STN-neurons, which do not have this plateau-generating ability, only show an increase in membrane potential during the application of the current pulse, which decays very fast after the break of the pulse. They show no difference in response when the potential is hyperpolarized more than  $-75$  mV. These neurons also respond with rebound bursting after the break of a hyperpolarizing step, but these bursts stop quite abruptly, with a fast decay of the membrane potential to resting potential [16].

The STN-neurons which are able to generate plateau potentials can also display burst firing when the membrane potential is sufficiently hyperpolarized according to [15]. See Figure 2.7 for an indication of this bursting. The STN-neuron then generates bursts of action potentials more than once. This claim is contradicted by the articles [16, 5], which state that rhythmic burst firing is seldom observed in STN-neurons *alone*, but only when the plateau-generating STN-neuron is present in a network with GPe-neurons. They claim that a short train of spikes in GPe-neurons can hyperpolarize the STN-neuron sufficiently to

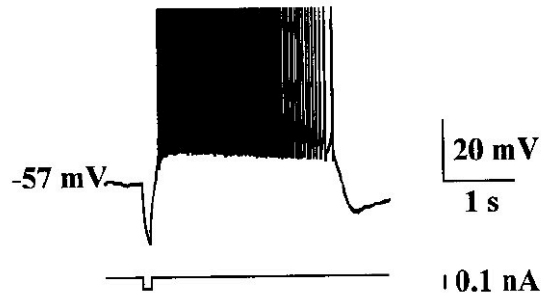


Figure 2.6: In a subpopulation of STN-neurons, long-lasting plateau potentials are the result of applications of de- or hyperpolarizing pulses [15].

cause rebound burst activity to occur, which can not be eliminated by GPe inhibition because the starting phase of the plateau potential is resistant to perturbations [16]. The methods of experiments of [15] are comparable to those of [16]. The type of rats from which brain slices are used and the thickness of the slices differ but this can not cause the opposite results of the two articles. [5] uses brain slices from rats with the cortex and striatum cultured. Results from these slices are therefore likely to differ. The cause for the contradicting results on bursting during hyperpolarization, is therefore unknown.

[17] claims that GPe-input by itself can not be sufficient to hyperpolarize the membrane enough. The equilibrium potential  $v_{G \rightarrow S}$  of the synaptic GPe-current is approximately  $-79$  mV [17], which is more negative than the threshold for rebound bursting. Therefore the only possibility to bring a STN-neuron into rebound burst activity, by only using the hyperpolarizing synaptic GPe-current is to have the GPe-neurons fire several barrages synchronically. During normal movement this is unlikely to occur because STN- and GPe-neurons fire asynchronously [17]. This characteristic of STN- and GPe-neurons shows that (rebound) bursting in STN-neurons is likely to be generated by the cortex and thalamus instead of by the GPe. The GPe input would then only *regulate* and time the STN-spikes [18].

A decrease in firing frequency is observed in STN-neurons with increasing strength of the applied hyperpolarizing current [14] which contradicts the bursting activity during the application of small hyperpolarizing stimuli. All STN-neurons terminate firing (become quiescent) with sufficient strength of the applied current [14] as can also be seen in Figure 2.7. After the break of such sufficient hyperpolarization, rebound bursting is observed. The rebound bursts firing modes are [17]:

- A short duration burst followed by:
  1. Spontaneous firing.
  2. A deep AHP (sometimes followed by second weaker rebound).
- Long duration rebound bursts.

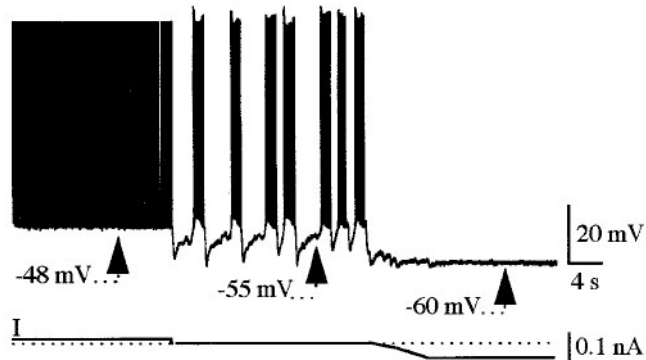


Figure 2.7: Switch from firing to pure bursting to quiescent mode by increasing the strength of the hyperpolarizing current injection [15].

### Currents

According to literature the STN-membrane consists of various channels, ligand- and voltage-gated, permeable to various types of ions. Due to the flow of ions through these channels, the membrane potential changes in time. The currents found experimentally will be listed in this section.

#### LEAK CURRENTS

In all neurons, thus also in the STN-neuron, an Ohmic leak current  $I_L$  is present due to open resting channels.

#### POTASSIUM ( $K^+$ ) CURRENTS

A persistent outward potassium current  $I_K$  is present which is activated by depolarization [19, 11]. This current restricts the action potential duration. The channels responsible for this type of current are of Kv3.1 type, which means the channels are activated at high thresholds and the kinetics are fast [19].  $I_K$  influences the repolarization of the plateau potential [16].

The ability of the STN-neuron to fire at very low frequencies (see Figure 2.5) shows the presence of a transient outward A-type potassium current  $I_A$  [20]. In the STN-model [11] this  $I_A$  is indeed included.  $I_A$  activates rapidly at low thresholds and inactivates slowly according to [20] although [11] has taken both the activation and inactivation to be fast. When a slow inactivation rate is taken for  $I_A$  in the STN-model, complex firing patterns, as periodic bursting, can occur in parameter regions.  $I_A$  opposes rebound bursting because it deinactivates during hyperpolarization resulting in a finite window of hyperpolarization from which the cell can only fire upon release [20, 11]. This is confirmed by [17] and [16] discussed in the previous section.  $I_A$  together with  $I_K$  influence the repolarization of the plateau potential [16].

A  $Ca^{2+}$ -dependent potassium current  $I_{AHP}$  has been recorded. It seems to be partly responsible for the slow part of the AHP [14]. It also limits the

excitability of the neuron for very strong depolarizing currents. Because the frequency of firing is very high for a strong depolarizing current, the internal concentration of  $\text{Ca}^{2+}$  increases extremely in a very short time. The result is a very large  $I_{AHP}$ . This of course limits the effect of the depolarizing input [14].  $I_{AHP}$  also influences the repolarization phase of the plateau potential [16].

#### SODIUM ( $\text{Na}^+$ ) CURRENTS

A transient inward sodium current  $I_{Na}$  has been recorded in STN-neurons [14].  $I_{Na}$  is responsible for the action potential generation: without  $I_{Na}$  spontaneous firing would be absent [14, 21].  $I_{Na}$  is slowly inactivating so the current is still present during the repolarizing phase after the spike [21].

Beside this transient sodium current, a persistent one has also been recorded [14, 21, 16]. This current has no influence on the plateau potential [11].

#### CALCIUM ( $\text{Ca}^{2+}$ ) CURRENTS

Various inward calcium currents have been recorded in STN-neurons. In general an inward calcium current of  $10 \text{ pA}/\mu\text{m}^2$  is *always* present in a STN-neuron, even at very hyperpolarized levels [14]. Four high-threshold currents (with the channels of N-, L-, Q- and R-type located in the soma) and one low-threshold-current (a T-type channel located in the dendrites near the GPE-synapses) [22] have been recorded. The high-threshold currents have a similar voltage dependence (activation curves have similar shapes but slightly different parameters). The N-type calcium current constitutes the largest part of the total calcium current. The R-type current has the lowest threshold together with the L-type [22]. All currents influence the plateau potential [13, 22, 16, 15, 21], the generation of rebound activities, the regulation of  $\text{Ca}^{2+}$ -dependent conductances (for  $I_{AHP}$  and the  $\text{Ca}^{2+}$ -dependent inward cation currents) [22], and bursting behaviour [15, 21].

But which  $\text{Ca}^{2+}$ -currents are mainly responsible for the characteristic behaviour of the STN-neuron? The long-lasting plateau potential is mainly mediated by the *L-type calcium current* [22, 16, 15]. The inactivation of this current influences the repolarization phase of the plateau potential [11]. This current is also explicitly included in the STN-model described in [11] with two inactivation variables, one dependent on the voltage, the other on the intracellular calcium concentration.

Beside the important L-type calcium current, the low-threshold T-type current  $I_T$  is responsible for the large increase in membrane potential after the break of a hyperpolarizing step.  $I_T$  is therefore essential for the rebound potential [21].

#### NON-SPECIFIC CATION CURRENTS

There are possibly also  $\text{Ca}^{2+}$ -dependent inward cation currents which regulate the duration of the plateau potential [16, 11, 15]. They may slow down the decay of a plateau potential [15].

The presence of a H-current  $I_H$  has been confirmed as well [16, 22, 11, 21]. It is a hyperpolarization-activated inward cation current. It deactivates very slowly [11]. It seems to be responsible for the depolarizing sag during hyperpolarization [21] thereby increasing the chance of rebound bursting. According to [11]  $I_H$  has no influence on the plateau potential while [21] claims that deactivation of  $I_H$  can regulate the repolarization phase of the plateau potential.

### 2.1.2 The STN-model

A mathematical single-compartment conductance-based model for the STN-neuron will be discussed in this section and analysed in the following ones. It is a HH-type of model describing the dynamics of the membrane potential as a function of the ion currents flowing through the neuron's membrane. It is developed by Terman et al. in 2002 [1] and it is given by Equation (2.1).

$$C_m \frac{dv_s}{dt} = -I_L - I_K - I_{Na} - I_T - I_{Ca} - I_{AHP} - I_{G \rightarrow S} \quad (2.1)$$

Here  $v_s$  is the membrane potential of a specific STN-neuron in mV, and  $C_m$  the membrane conductance (normalized to  $1 \text{ pF}/\mu\text{m}^2$ ). The currents (in  $\text{pA}/\mu\text{m}^2$ ) are given by Equations (2.2).

$$I_L = g_L(v_s - v_L) \quad (2.2a)$$

$$I_K = g_K n^4 (v_s - v_K) \quad (2.2b)$$

$$I_{Na} = g_{Na} m_\infty^3 (v_s) h (v_s - v_{Na}) \quad (2.2c)$$

$$I_T = g_T a_\infty^3 (v_s) b_\infty^2 (r) (v_s - v_{Ca}) \quad (2.2d)$$

$$I_{Ca} = g_{Ca} s_\infty^2 (v_s) (v_s - v_{Ca}) \quad (2.2e)$$

$$I_{AHP} = g_{AHP} (v_s - v_K) \frac{[Ca]_i}{[Ca]_i + k_1} \quad (2.2f)$$

$$I_{G \rightarrow S} = g_{G \rightarrow S} (v_s - v_{G \rightarrow S}) \sum_j s_j \quad (2.2g)$$

The currents chosen in this model will be described shortly in the following subsections, assuming that the reader is familiar with the Hodgkin-Huxley type of models (see Section 1.2 for a short introduction). The parameter values can be found in Appendix A.

There are not many other mathematical models present at the moment to describe the membrane dynamics of a STN-neuron accurately. Another conductance-based model is the model developed by Otsuka et al. in 2004 [11], which includes more currents than the one described above. Some of the *type* of currents chosen there to influence the membrane's potential are of the same type but are often *described* in a totally different manner. Beside this difference, the constant parameters have totally different values as well.

Model (2.1) is 5-dimensional with ODE's for the variables  $v_s$  in mV,  $n$ ,  $h$ ,  $r$  and  $[Ca]_i$  in mmol. A further explanation of these ODE's and the currents can be found in the sections below.

#### The gating variables

All currents given in (2.2) have a maximal conductance to their specific ion, given by  $g_X$  (in  $\text{nS}/\mu\text{m}^2$ ), with  $X$  the ion-type, and equilibrium potentials specific for that ion given by  $v_X$ . The (in)activation variables are given by  $n$ ,  $h$ ,  $r$ ,  $s$ ,  $m$  and  $a$ . These will be shortly discussed in this subsection.

Because the gating variables  $n$ ,  $h$  and  $r$  are slowly operating (in comparison to  $s$ ,  $m$ ,  $a$  which are taken to be instantaneous) they are given by the following equation (where  $X \in \{n, h, r\}$ ):

$$\frac{dX}{dt} = \phi_X \frac{X_\infty(v_s) - X}{\tau_X(v_s)}$$

This is just according to the HH-formalism (except that a constant  $\phi_X$  has been added which together with  $\tau_X(v_s)$  influences the speed of the variable dynamics. Variable  $X$ 's steady state  $X_\infty(v_s)$ , with  $X \in \{n, h, r, s, m, a\}$ , is given by Boltzmann equation:

$$X_\infty(v_s) = \frac{1}{1 + e^{-\frac{v_s - \theta_X}{\sigma_X}}}$$

$\theta_X$  is the half-activation voltage for variable  $X$  and  $\sigma_X$  the slope factor. The time-constants  $\tau_X(v_s)$  for the slow variables  $X \in \{n, h, r\}$ , are modelled by Equation (2.3).

$$\tau_X(v_s) = \tau_X^0 + \frac{\tau_X^1}{1 + e^{-(v_s - \theta_X^*)/\sigma_X^*}} \quad (2.3)$$

In (2.3) the minimum time constant for the specific variable  $X$  is given by

$$\frac{\tau_X^0}{\phi_X}$$

and the maximum time constant by

$$\frac{\tau_X^0 + \tau_X^1}{\phi_X}$$

$\theta_X^*$  is the voltage at which the time constant is midway between its maximum and minimum values and the slope factor for the voltage-dependence of the time constant is  $\sigma_X^*$ .

The leak-, sodium- and potassium-currents given in (2.2a), (2.2b) and (2.2c) are the standard currents included in every conductance-based model of spiking neurons. These will therefore not be discussed. For a description of these currents see Section 1.2. The calcium-currents on the other hand are rarer and also very important for the STN-neuron as was described in Section 2.1.1. These are discussed in the next subsection.

### The calcium currents $I_{Ca}$ and $I_T$

Two calcium currents  $I_{Ca}$  and  $I_T$  are included in the model (see Equations (2.2d) and (2.2e)).  $I_T$  is a low-threshold inward ( $I_T < 0$ ) current, as can be seen in Figure 2.8. In this figure  $r$  is taken to be equal to its steady state  $r_\infty$ .  $I_{Ca}$  is a high-threshold inward current (see Figure 2.9). Both calcium currents are essentially always inward because the extremely high equilibrium potential of calcium (155 mV) is never reached.  $I_{Ca}$  is active during spontaneous spiking while  $I_T$  is not.

The inactivation for  $I_T$  is not just  $r$ , the inactivation gating variable, but a function of  $r$ ,  $b_\infty(r)$ . The function is given by:

$$b_\infty(r) = \frac{1}{1 + e^{\frac{r - \theta_b}{\sigma_b}}} - \frac{1}{1 + e^{\frac{-\theta_b}{\sigma_b}}}$$

According to [1] this function accounts for the rebound potentials characteristic for STN-neurons. In Section 2.2.2 it can be seen that the model is indeed able to rebound burst after the break of a hyperpolarizing step. In Figure 2.10  $b_\infty(r_\infty)$  is plotted together with  $r_\infty$ . The difference is subtle but has large consequences.

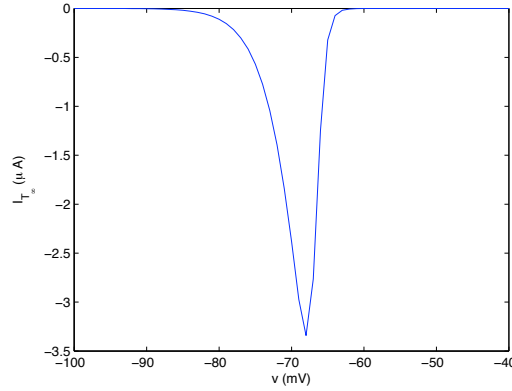


Figure 2.8: The inward low-threshold current  $I_T$  as function of the voltage  $v_s$  assuming instantaneous dynamics.

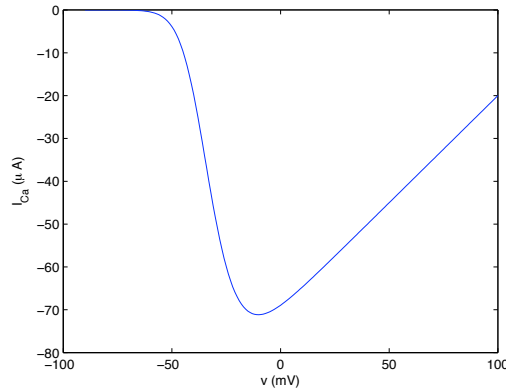


Figure 2.9: The inward high-threshold current  $I_{Ca}$  as function of the voltage  $v_s$ .

Because  $b_\infty(r)$  has a steeper decay from 1 to 0, the membrane just needs to be hyperpolarized a little for the T-current to be deinactivated. This results in an inward current during hyperpolarization, which increases the chance of rebound bursting.

### The $\text{Ca}^{2+}$ -dependent potassium current $I_{AHP}$

The outward  $\text{Ca}^{2+}$ -dependent potassium current is given by (2.2f). The current flows through ligand-gated channels, which can be seen by the absence of (in)activation variables in the equation (they would indicate the presence of voltage-gated channels). The conductance of these ligand-gated channels to  $\text{K}^+$   $I_{AHP}$  is given by

$$g_{AHP} \frac{[Ca]_i}{[Ca]_i + k_1}$$

where  $[Ca]_i$  is the intracellular calcium concentration. When  $k_1$  (the dissociation constant) is zero  $I_{AHP}$  is just an Ohmic current with the maximum constant

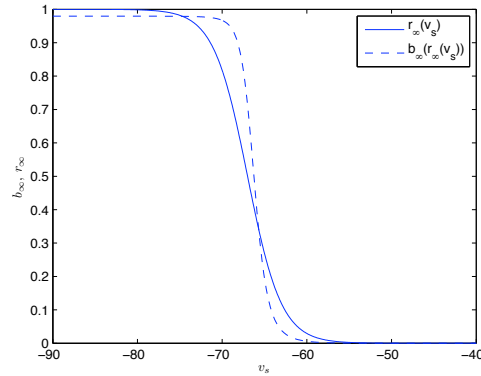


Figure 2.10:  $b_\infty(r_\infty(v))$  plotted together with  $r_\infty(v)$ .

conductance,  $g_{AHP}$ . A positive  $k_1$ , causes the current to become non-Ohmic and dependent on the intracellular calcium concentration which changes in time due to the calcium currents. A positive  $k_1$  limits the conductance significantly for small  $[Ca]_i$  but approaches the maximal conductance for larger  $[Ca]_i$ .

The dynamics of the intracellular calcium concentration  $[Ca]_i$  are given by Equation (2.4) with  $\epsilon$  a small constant parameter and  $[Ca]_i'$  the time derivative of  $[Ca]_i$ .

$$[Ca]_i' = \epsilon (-I_{Ca} - I_T - k_{Ca}[Ca]_i) \quad (2.4)$$

When  $I_{Ca}$  and  $I_T$  are nonzero, they both increase the internal calcium concentration (see (2.4)), because they are essentially always inward (and thus negative). The term  $k_{Ca}[Ca]_i$  indicates the clearance mechanisms of  $Ca^{2+}$  by channel pumps with  $k_{Ca}$  the calcium pump rate constant. An indication of the current  $I_{AHP}$  for various membrane potentials is given in Figure 2.11 assuming  $[Ca]_i' = 0$ . Clearly:

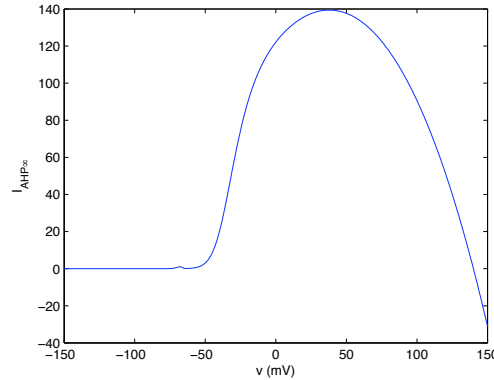


Figure 2.11: The outward current  $I_{AHP}$  as a function of the voltage  $v_s$  assuming instantaneous dynamics for  $[Ca]_i$  and  $r$ .

$$I_{AHP} > 0 \quad \text{for } v_s > -50 \text{ mV}$$

This current thus opposes the upstroking character of the action potential and

repolarizes the membrane potential afterwards. Assuming  $[Ca]_i' = 0$  (for drawing Figure 2.11) implies that  $[Ca]_i$  has very fast dynamics, while the extremely small value for  $\epsilon$  shows this is not the case. This is thus a very strong assumption.

### The synaptic current $I_{G \rightarrow S}$

$I_{G \rightarrow S}$  is the synaptic hyperpolarizing current, being nonzero when the GPe-neurons are active, and is given by (2.2g). Because in this chapter one STN-neuron (model) is analysed, and couplings of one GPe-neuron to a STN-neuron will be discussed in Chapter 4, a detailed description about this current will be postponed to that chapter. In this chapter only an applied current  $I_{app}$  will be varied to simulate synaptic input (for example from a GPe-neuron) to a STN-neuron and to investigate the influence of various types of input on the STN's membrane potential's dynamics. When an applied current  $I_{app}$  is used for the further analysis instead of the synaptic current  $I_{G \rightarrow S}$ , which we cannot control, Model (2.1) becomes as in (2.5).

$$C_m \frac{dv_s}{dt} = -I_L - I_K - I_{Na} - I_T - I_{Ca} - I_{AHP} + I_{app} \quad (2.5)$$

As one can see in (2.5) the sign in front of  $I_{app}$  is positive (in contrary to the sign in front of  $I_{G \rightarrow S}$ ). This means that when a *depolarizing* step-current is simulated to be injected  $I_{app}$  should be taken a *positive* number (because  $v_s > 0$ ). For the same reason  $I_{app}$  is smaller than zero when a hyperpolarizing step-current is simulated to be injected. For synaptic currents the sign-convention for an inward, and thus depolarizing current is negative ( $I_{G \rightarrow S} < 0$ ) and for an outward and thus hyperpolarizing current it is positive ( $I_{G \rightarrow S} > 0$ ). Because the injection of a current is not accompanied by a flow of positive ions *through* the membrane, we can not speak of 'inward' and 'outward' current. Then the ordinary convention is taken into account that a depolarizing current is taken '+' because it increases the membrane potential and a hyperpolarizing current is taken '-' because it lowers the membrane potential.

In the next section Model (2.5) will be used for the codim-1 bifurcation analysis. The parameter which will be varied is  $I_{app}$ , simulating the synaptic input from afferents of the STN-neuron. A detailed analysis can give us valuable information on the changes in behaviour of the model and thus in some sense on a STN-neuron in vivo) dependent on the input to the neuron. It can give us exact information in which intervals of  $I_{app}$  the STN-neuron is always quiescent, always spiking (with some frequency) or can be both quiescent and spiking dependent on the initial conditions (the system is then bistable).

## 2.2 Analysis

### 2.2.1 Bifurcation analysis

This section will analyse Model (2.5) in detail by searching for the codim-1 bifurcations of the equilibria and limit cycles of the system. These bifurcations indicate boundaries of regions of the parameter  $I_{app}$ , in which the model behaves qualitatively different compared to the other parameter-regions. Knowing these bifurcations thus gives us full information on the influence of the applied current

$I_{app}$  (simulating in this case the synaptic input from the GPe  $I_{G \rightarrow S}$ ) on the firing behaviour of the model. Although a *model* of a neuron is never as accurate as the real neuron, this analysis can thus indirectly give us valuable qualitative information on the firing behaviour of the STN-neuron in vivo.

In Appendix C.1 the possible codim-1 bifurcations of equilibria and limit cycles are shortly explained for a general system. Knowing the limited number of possible equilibrium-bifurcations these can then be sought for our system (2.5). The equilibrium IV-curve for physiologically reasonable values of the membrane potential  $v_s$  is drawn. On this curve the system and thus the neuron is quiescent. The bifurcations of the equilibria are indicated on the curve when found by MatCont<sup>1</sup>. Figures of the eigenvalues of the equilibria are plotted to give more information on the found equilibrium bifurcations and the ones that MatCont missed. At the end of this section the regions for  $I_{app}$  are listed in which the equilibrium is stable or unstable. This already gives us an idea on the amount of input needed to make the model quiescent.

Because Hopf-bifurcations of equilibria indicate the emergence of limit cycles, and thus possible spiking behaviour of the model, the Hopf-point will be further analysed. The emerged limit cycle is followed to search for possible limit cycle bifurcations. At the end of the section a detailed picture can be made of the influence of different values of the input  $I_{app}$  on the firing behaviour of the model. For some intervals of  $I_{app}$  the neuron *is* or eventually *becomes* quiescent. That is independent of the initial conditions chosen. In other regions the neuron will always spike, where the frequency of spiking is dependent on the value of  $I_{app}$ . The last possibility is that the system is bistable for a certain parameter interval. The behaviour of the neuron in this case, is dependent on the initial conditions chosen.

To show these different types of behaviour time diagrams are drawn in Section 2.2.2 for some of the variables. The initial conditions are taken from the different regions presented in this section. In that section  $I_{app}$  will also be taken equal to various step- and pulse-currents to analyse the influence of such instant applications on the system's behaviour.

## Equilibrium bifurcations

The neuron is quiescent means that the total system is in rest. This means that the neuron does not fire any spikes and has a constant membrane potential. That means that all five of the variables should be constant in time. The following thus must hold for the gating variable  $n$ :

$$\dot{n} = 0 \Rightarrow \phi_n \frac{n_\infty(v_s) - n}{\tau_n(v_s)} = 0$$

The same holds for the other slow gating variables  $h$  and  $r$ . This then leads to the equilibrium values for  $n$ ,  $h$  and  $r$ , dependent on the membrane potential  $v_s$ ,

<sup>1</sup>MatCont is a toolbox developed for Matlab for doing numerical bifurcation analysis of all kinds of ODE-systems. For further information on MatCont see [23] for the numerical methods needed to calculate the various limit cycle continuations and equilibrium curves. See [24], [25], and the MatCont manual [26] for more information on the program itself

and denoted by the subscript *eq*:

$$n_{eq}(v_s) = n_{\infty}(v_s) \quad (2.6a)$$

$$h_{eq}(v_s) = h_{\infty}(v_s) \quad (2.6b)$$

$$r_{eq}(v_s) = r_{\infty}(v_s) \quad (2.6c)$$

For the intracellular calcium concentration  $[Ca]_i$  the following can be deduced:

$$[\dot{Ca}]_i = 0 \Rightarrow \epsilon(-I_{Ca} - I_T - k_{Ca}[Ca]_i) = 0 \Rightarrow -I_{Ca} - I_T - k_{Ca}[Ca]_i = 0$$

This gives (2.7) for  $[Ca]_{i_{eq}}$  still dependent on  $v_s$ .

$$[Ca]_{i_{eq}} = -\frac{I_{T_{eq}} + I_{Ca_{eq}}}{k_{Ca}} \quad (2.7)$$

The currents  $I_{T_{eq}}$  and  $I_{Ca_{eq}}$  in (2.7) are the calcium currents given by (2.2d) and (2.2e) with the variable  $r$  replaced by  $r_{eq}$ .

The same should be done for the equation for  $v_{eqs}$ :

$$C_m \dot{v}_s = 0 \Rightarrow \frac{-I_L - I_K - I_{Na} - I_T - I_{Ca} - I_{AHP} + I_{app}}{C_m} = 0$$

This gives the Equation (2.8) for  $I_{app_{eq}}$  (often indicated by  $I_{\infty}(v_s)$  in literature) for the input current needed to keep the system in the resting state, when all five coordinates are already at their steady state values.

$$I_{app_{eq}} = I_{L_{eq}} + I_{K_{eq}} + I_{Na_{eq}} + I_{T_{eq}} + I_{Ca_{eq}} + I_{AHP_{eq}} \quad (2.8)$$

In (2.8) the various currents are the equilibrium currents with the gating variables and  $[Ca]_i$  at their equilibrium states.

These formulae for the equilibria of the system are programmed in Matlab. In Listing 2.2.1 these various Matlab functions can be found. The equilibrium IV-curve can be directly made using `Bifdiagram(v)`. The other function names speak for themselves. The implementation of these functions can be found in Appendix B.

Functions for the five coordinate and parameter equilibrium values

```
function I=Bifdiagram(v)
function N=Ninf(v)
function H=Hinf(v)
function R=Rinf(v)
function Ca=CaConc(v)
```

For every  $v$  (or an array of  $v$ ) the functions calculate the values for the other variables and the parameter  $I_{app}$  for which the system is in rest. These values are needed to let `MatCont` continue a specific equilibrium. In Figure 2.12 this continuation of Matlab can be found. It is the equilibrium curve of the system for  $v_s$  and  $I_{app}$  within physiologically normal ranges. While drawing the curve, `MatCont` continuously calculates the equilibrium's five eigenvalues. While monitoring the eigenvalues, `MatCont` found various bifurcations, which can be seen in Figure 2.12 (the three red dots on the left side of the picture

are neutral saddles and the red dot with ‘H’ alongside it is the subcritical Hopf bifurcation). The values are given in Table 2.1 where  $S_i$  for  $i \in \{1, 2, 3\}$  are the neutral saddles. The values are rounded. These bifurcations occur on the center manifold of the system (2D for a Hopf and otherwise 1D). Off this center manifold the orbits behave according to the standard saddle (see the beginning of this section). From now on the center manifold will not be named explicitly every time a bifurcation is discussed.

As one can see two obvious saddle-node bifurcations have been missed by MatCont. MatCont would have denoted the points as fold-points labelling them as ‘LP’s’. Even with smaller stepsizes chosen, these points were missed by the program. Later when plots of the eigenvalues are investigated these limit points might become apparent.

Another observation is that  $I_\infty(v)$  (Figure 2.12 rotated 90 degrees counter-clockwise) is clearly non-monotonic. This allows for the STN-neuron to exhibit all four possible codim-1 bifurcations of an equilibrium.

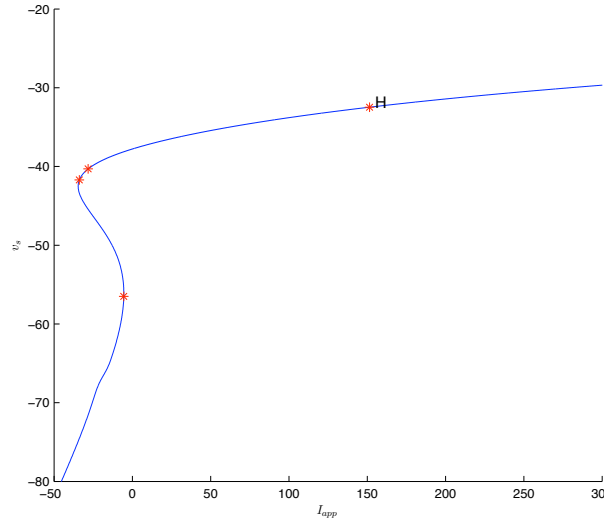


Figure 2.12: The equilibrium IV-curve for the STN-neuron. A subcritical Hopf-point is found for  $I_{app} \approx 150$ .

	Coordinates					Parameter	L. coeff.
	$v_s$	$n$	$h$	$r$	$[Ca]_i$	$I$	$l_1$
$H$	-32.47	0.485	0.108	0.000	1.843	151.52	$5.73e - 2 > 0$
$S_1$	-40.31	0.261	0.604	0.000002	0.845	-28.20	-
$S_2$	-41.64	0.231	0.701	0.000003	0.706	-33.70	-
$S_3$	-56.49	0.045	0.996	0.005	0.045	-5.45	-

Table 2.1: The values for the Hopf-bifurcation  $H$ , and the neutral saddles  $S_1$ ,  $S_2$  and  $S_3$  of equilibria of the STN-system.

The subcritical Hopf bifurcation (indicated in the table by  $H$ ), which takes place at a parameter value  $I_{app} \approx 151 \text{ pA}/\mu\text{m}^2$  (a depolarizing current injection) at a membrane potential of  $v_s \approx -32 \text{ mV}$ , is the most valuable one because a

transition between spiking and rest takes place there. The Lyapunov coefficient  $l_1$  at this point is positive, showing that the Hopf is indeed a subcritical one. That means that for increasing  $I_{app}$  the equilibrium becomes stable, and an unstable limit cycle emerges from the Hopf-point (to the right in the picture). The two eigenvalues which cross the imaginary axis are  $\lambda_{1,2} = \pm\omega_0 i = \pm 2.77538 i$ , so the period of the subthreshold oscillations are

$$T = \frac{2\pi}{\omega_0} = \frac{2\pi}{2.77538} \approx 2.2639 \text{ ms}$$

In Section 2.2.1 this limit cycle will be analysed further.

The other three ‘bifurcations’ (indicated in the table by  $S_i$  with  $i \in \{1, 2, 3\}$ ) are neutral saddles. The equilibrium does not undergo a qualitative change at those points, but the sum of two real eigenvalues becomes zero (as is the case for the purely imaginary eigenvalues for a Hopf-bifurcation) and is therefore recognized as a Hopf-point at first. The vectorfield does not change drastically at these points, and are therefore not bifurcation points.

Beside the knowledge that left of the Hopf-point the equilibria are unstable and to the right are stable (not knowing when this stability changes) the stability properties for the rest of the equilibrium curve Figure 2.12 are still unknown. Plots of the five eigenvalues for increasing  $I_{app}$  can give more information. In Figure 2.13 the real part of the five eigenvalues is plotted. The Matlab function  $[E,R,Im]=\text{EigenwaardenSN}(v)$  can be used for this purpose. The implementation can be found in Appendix B. These figures are made using the mat-file from MatCont.

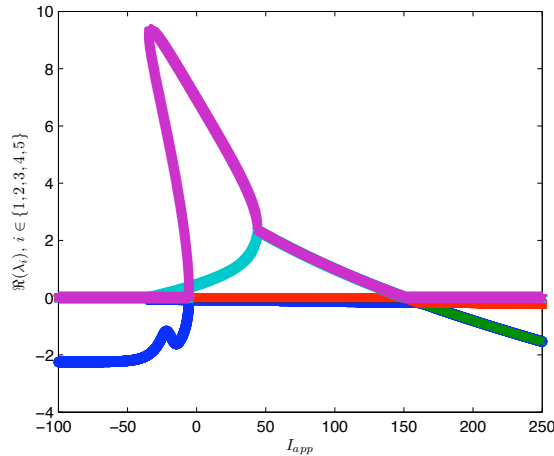


Figure 2.13: The real part of the five eigenvalues of the equilibria of the STN-system.

Some remarks about Figure 2.13: because in a region of  $I_{app}$  (between -50 and 0) several equilibria are present (see Figure 2.12) in this specific region it is very difficult to see which eigenvalues belong to which equilibrium in Figure 2.13. The choice for the large marks instead of a thin line between the eigenvalues was made because Matlab does not seem to order the eigenvalues everytime it calculates them. Therefore a smooth line can not be drawn between the points of one eigenvalue and marks has to be chosen. Also it seems that some of the

eigenvalues are approximately equal to zero. This is not the case though as can be seen in Figure 2.14 where only the very small (vertical) area around  $\Re\{\lambda\} = 0$  is plotted. The real parts are small but definitely nonzero.

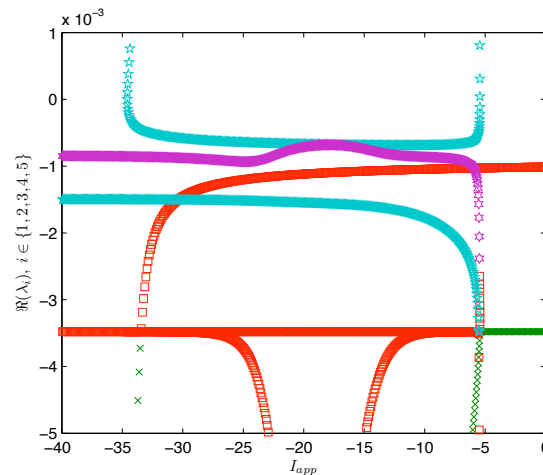


Figure 2.14: The real part of the five eigenvalues: zoom-in from Figure 2.13 with  $\Re\{\lambda_i\} \in [-0.005, 0.001]$ .

What can be seen from Figure 2.14 are the limit point bifurcations that MatCont missed. At these points the equilibrium is nonhyperbolic ( $\Re(\lambda_i) = 0$  and  $\Im(\lambda_i) = 0$  for some  $i$ ). At  $I_{app} \approx -5.43 \text{ pA}/\mu\text{m}^2$  and at  $I_{app} \approx -34.56 \text{ pA}/\mu\text{m}^2$  it can be seen in Figure 2.14 that the condition that the real part is zero, is met. Looking at Figure 2.15 where the imaginary parts of the eigenvalues are plotted, it can be seen that around these values for  $I_{app}$  the eigenvalues are indeed real. Saddle-node bifurcations thus occur for these, unfortunately *approximate*, values of  $I_{app}$ . The nondegeneracy conditions for a limit point should be checked as well.

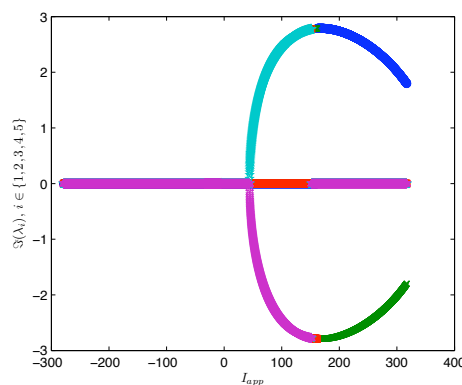


Figure 2.15: The imaginary parts of the five eigenvalues of the equilibria of the STN-system.

In Figure 2.16, where a small area around  $I_{app} = 150$  is plotted, the Hopf bifurcation can clearly be seen. The real part decreases to zero and looking

at the imaginary parts of the eigenvalues in Figure 2.15 one can see that the two eigenvalues are still imaginary, and thus purely imaginary at the Hopf point. Also it is clear from the figure that for smaller  $I_{app}$  than the bifurcation value the equilibrium is unstable and for larger values it is stable, indicating a *subcritical* Hopf-bifurcation.

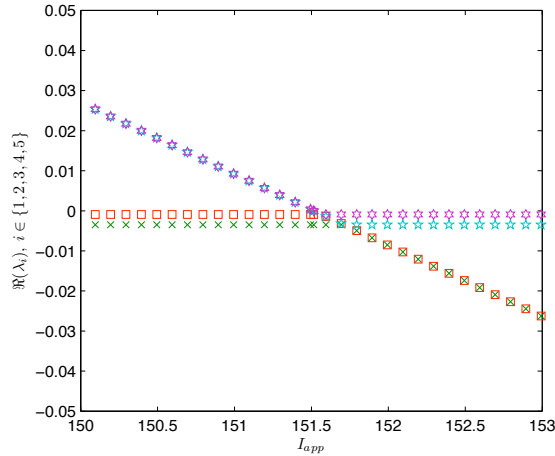


Figure 2.16: The real part of the eigenvalues: the subcritical Hopf occurs at  $I_{app} \approx 150$ .

Looking at Figures 2.13, 2.14 and 2.16 one can say that the equilibrium is stable in the following regions (follow the curve in Figure 2.12 starting at the right side of the Hopf bifurcation): The equilibrium on the right of the Hopf-point  $H$  is stable. Between  $H$  and the limit point (around  $I_{app} \approx -34$ ) the equilibrium is 2D unstable (two eigenvalues have crossed the imaginary axis). Between the two limit points the equilibrium becomes 1D unstable. After the last limit point the equilibrium is totally stable again. For  $I_{app}$  between approximately -34 and -5 the system has three equilibria from which only one is stable. Outside this region only a stable equilibrium is present. We will see in the next section whether the solution is always attracted to these equilibria when  $I_{app}$  is chosen in these regions, or that stable limit cycles are present as well to which the solution is drawn.

### Limit cycle bifurcations

Because not all equilibria are stable, the attraction domains of the stable ones do not attract the whole state space, and because we have observed that the STN-neuron can indeed spike (even without input), limit cycles are definitely present in the 6D variable-parameter space. In the previous section we saw that a subcritical Hopf bifurcation occurred for a parameter value of  $I_{app} \approx 151$  and a membrane potential of approximately -32 mV. for a large depolarizing input. An unstable limit cycle thus emerges. Orbits are therefore not attracted to this limit cycle. We are searching for stable limit cycles, which we can possibly find by continuing the unstable limit cycle emerged at the Hopf point.

In Figure 2.17 this continuation for increasing  $I_{app}$  can be seen. The continuation starts at the Hopf point in the left side of the figure, where  $v \approx -32$  mV

and  $n \approx 0.48$ . Clearly (unstable) limit cycles emerge with the starting amplitude approximately zero and increasing for increasing  $I_{app}$ . The bifurcations found during the continuation process can be found in Table 2.2. In Figure 2.17 the ‘NS’-marks at the left side (at the point of the hat) are the neutral saddles close to the Hopf bifurcation. They will not be discussed here because they do not indicate bifurcations.

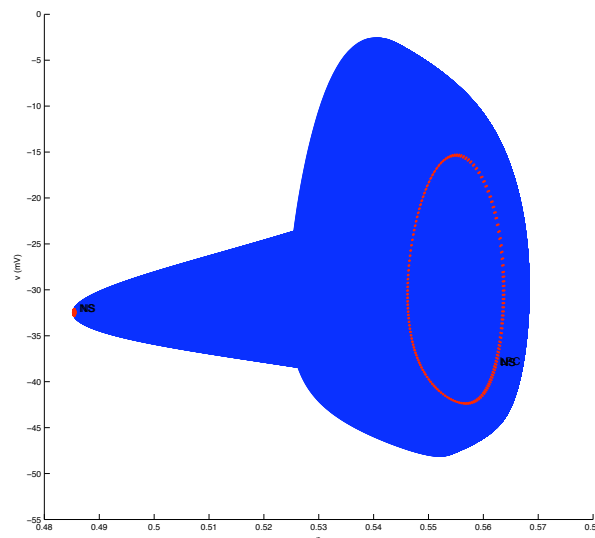


Figure 2.17: A subcritical Hopf occurs at  $(v, n) \approx (-32, 0.48)$ . For increasing  $I_{app}$  the unstable limit cycle grows in amplitude and finally coalesces with the stable limit cycle circling around it.

During the continuation MatCont finds very near to each other a Neimark-Sacker bifurcation (indicated by ‘NS’) and a limit point of cycles (indicated by ‘LPC’). The Neimark-Sacker bifurcation is found due to a numerical error. Using more discretization points limits the possibilities of numerical artifacts. The multipliers are real at the found NS so can never indicate a Neimark-Sacker bifurcation although the normal form coefficient is given by MatCont. In Figure 2.17 the red circle on the right indicates the fold bifurcation of limit cycles. The limit point of cycles is discussed. From the figure it is understandable that the fold bifurcation is also called a turning point bifurcation. A stable limit cycle surrounds the unstable one for  $I_{app} \in [151, 205]$ . They approach each other for increasing  $I_{app}$ , coalesce at the limit point and then disappear. Figure 2.17 looks like a pointed hat. The unstable cycles form the point, and the stable limit cycles the side flaps.

In Figure 2.18, the period of the limit cycle (in ms) is plotted against  $I_{app}$  which makes it clear as well that the period of the unstable limit cycle grows for increasing  $I_{app}$  (the lower branch of the figure), and that the period of the stable limit cycle, surrounding the unstable one, approaches infinity when  $I_{app} \rightarrow 0$ . The latter indicates the possible presence of a saddle homoclinic bifurcation or a saddle node on invariant circle bifurcation. Later we will find out which of

Type	Period $T$	Value of $I_{app}$	Normal form coeff.
NS <sub>1</sub>	2.263984	151.408	
NS <sub>2</sub>	2.264	151.6147	
LPC	2.771262	205.0175	0.1088715
NS <sub>3</sub>	2.776580	205.0175	
NS <sub>4</sub>	2.78622	205.0112	$-2.954137 \cdot 10^{-9}$

Table 2.2: The limit cycle bifurcations found by MatCont using a Hopf-limit cycle continuation.

the two occurs.

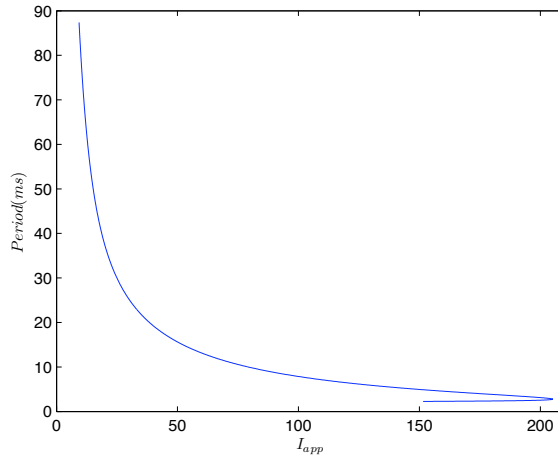


Figure 2.18: The period increases to infinity for  $I_{app} \rightarrow 0$  indicating the presence of a saddle homoclinic or SNIC bifurcation.

In Figure 2.19 the fl-curve is drawn which is related to the period ( $T$ ) drawn in Figure 2.18 by

$$f = \frac{1000}{T}$$

Because only the first part of Figure 2.19 (starting in approximately the origin and ending before the turning point) corresponds to the frequency of the stable limit cycle and thus the spiking behaviour of the model, this part is drawn again in Figure 2.20 next to the fl-curve which is drawn during experiments with STN-neurons.

The first observation that can be made from Figure 2.20 is the difference in  $I_{app}$  for which the model and experiments guarantee the neuron's spiking behaviour (the x-axis). According to the model the STN-neuron is unable to spike for  $I_{app} > 205 \text{ pA}/\mu\text{m}^2$  (past the limit point of cycles), because the unstable and stable limit cycles have coalesced and disappeared at  $I_{app} \approx 205 \text{ pA}/\mu\text{m}^2$ . A stable equilibrium (the upper branch in Figure 2.12) is present though in this parameter region. All solutions will converge to this equilibrium and the neuron will thus be quiescent for  $I_{app} > 205$ . Looking at the left figure in Figure 2.20 the neuron can be induced to fire at least up to  $I_{app} \approx 600 \text{ pA}/\mu\text{m}^2$  according to literature. The model-fl-curve (right in Figure 2.20) can thus only at best be

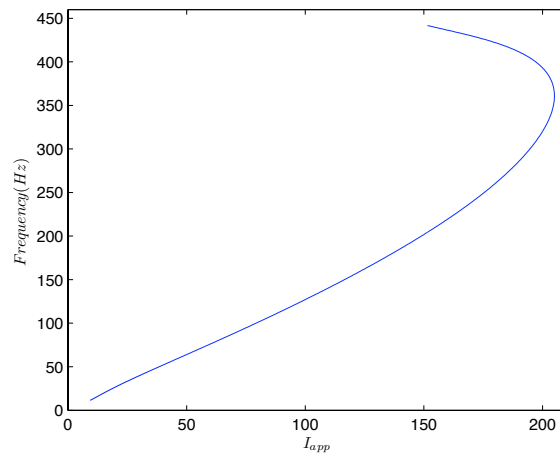
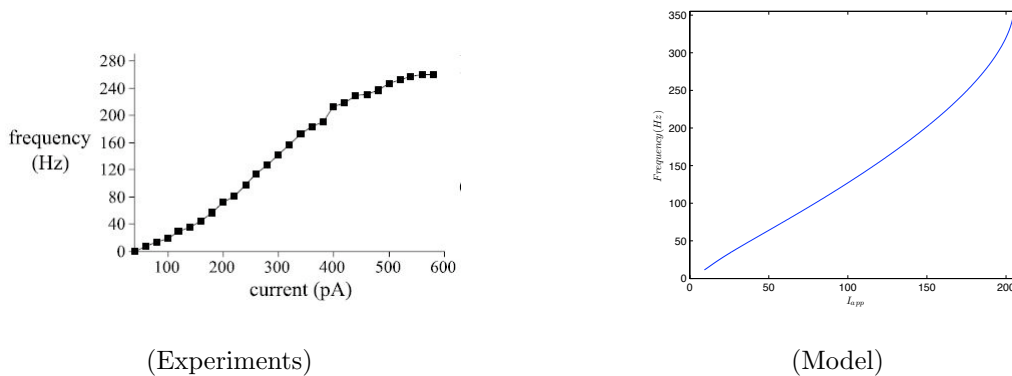


Figure 2.19: The fi-curve of the stable and unstable limit cycle.

Figure 2.20: The fi-plot from [14] (left) with  $I_{app} < 600$  compared to the fi-plot from model [1] (right) with  $I_{app} < 200$ .

compared to the first initial part (with  $f < 200\text{Hz}$ ) of the experimental fi-curve (left in Figure 2.20). The slope of the fi-curve for the model, up to 200 Hz, is approximately  $1350\text{ Hz/nA}$ . This is a significantly larger slope than claimed by [14] ( $500\text{ Hz/nA}$ ) or [13] ( $900\text{ Hz/nA}$ ). Because the fi-curves in experimental articles often plot the *averaged* frequency  $f_{av}$  over the total duration of the applied current step and the fi-curve of the model, drawn by MatCont, indicates the *asymptotic* frequency  $f_{as}$  of spiking for  $I_{app}$  to which  $f$  converges due to spike frequency adaptation, this may indicate that the slope of the model-fi-curve is not too large after all. But looking at the meaning of the average and asymptotic frequency it even makes things worse:  $f_{as}$  is practically always less than the average frequency  $f_{av}$ , due to the high initial frequency. Therefore the asymptotic frequency of the model  $f_{as} = 1350\text{ Hz/nA}$  is equivalent to an even higher  $f_{av}$  and thus is definitely too large.

The other observation can be made by looking at the frequencies reached (the y-axis) by the firing STN-neuron due to the injection of an applied current. The model is able to reach a firing frequency of about 300 Hz after the application of a current of approximately  $200\text{ pA}/\mu\text{m}^2$ . The application of this amount of

current in the experiments described in [14] results in a firing frequency of about only 60 Hz.

If the parameter only needs scaling (that the period over which the 300 Hz is traversed needs to be stretched up), there is still the problem of the shape of the fl-curve from the model. It has an inverse sigmoidal shape with steeper slopes in the first and third region compared to the second. In the experiments described in [14] and [13] the shape is simply sigmoidal.

After the analysis of the frequency of spiking of the model, the amplitude of the stable and unstable limit cycle will be plotted. In Figure 2.21 the minimum and maximum of the membrane potential  $v_s$  are plotted together with the equilibrium curve from the previous section. At the end of the simulation the period of the stable limit cycle became that large that it took too much time to draw more points than here indicated. When it is discussed whether a saddle homoclinic orbit bifurcation or a saddle node on invariant circle results, these last points of Figure 2.21 will be continued with larger stepsizes.

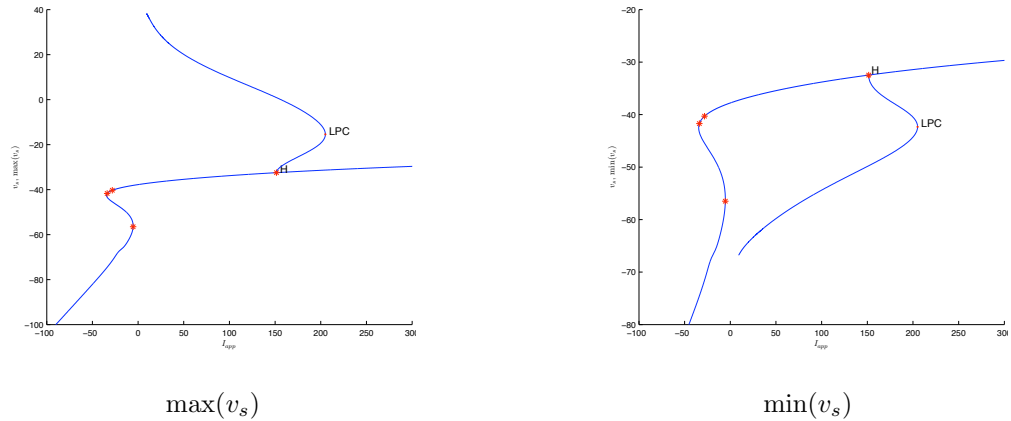


Figure 2.21: The maximum (left) and minimum (right) of the membrane potential on the (un)stable limit cycle is plotted together with the equilibrium curve.

An extension of Figure 2.17 can be seen in Figure 2.22. The unstable limit cycle is totally surrounded by the stable one and can thus not be seen anymore.

Because the period of the stable limit cycle tends to infinity while approaching  $I_{app} = 0$  this could indicate that the limit cycle will bifurcate according to a saddle node on invariant circle bifurcation (a SNIC bifurcation) or according to a saddle homoclinic orbit bifurcation. For a SNIC bifurcation a saddle and a node will both be on the limit cycle (the invariant circle) and will coalesce and disappear. This is only possible at the two limit points  $I_{app} \approx -5.43$  and  $I_{app} \approx -34.56$ . There a saddle and a node coalesce and disappear for increasing  $I_{app}$ . The limit cycle approaches the equilibrium curve for decreasing  $I_{app}$  indicating that in the case of a SNIC bifurcation a saddle and a node *appear* instead of *disappear*. When the oscillations continue for  $I_{app} < -5.54$  it is clear that  $T \rightarrow \infty$  does not indicate the presence of a SNIC bifurcation at this limit point. Then a saddle homoclinic orbit bifurcation is possible on the middle and top branch (saddle node homoclinic orbit bifurcation is a codim-2 bifurcation) or if this does not occur, a SNIC at the other limit point  $I_{app} \approx -34.56$ . In the case of the saddle homoclinic orbit bifurcation the stable and unstable manifolds

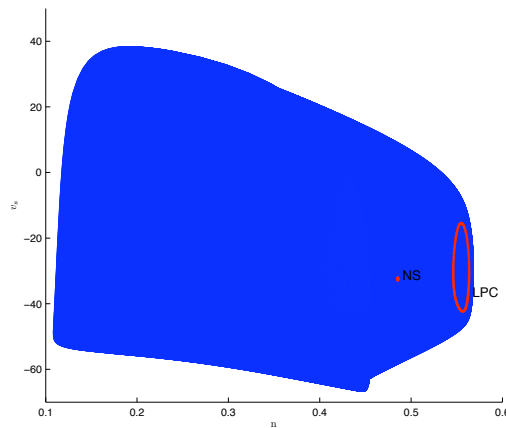


Figure 2.22: The stable limit cycle totally surrounds the unstable limit cycle (only a small part of this cycle was shown in Figure 2.17).

of a saddle of the system intersect (a homoclinic orbit results). In the case of this bifurcation the limit cycle bifurcates to this homoclinic orbit, resulting in oscillations with infinite period.

In Figure 2.23 it is shown that a SNIC bifurcation does not occur at the limit point  $I_{app} \approx -5.43$  because the limit cycle is still present after the limit point.

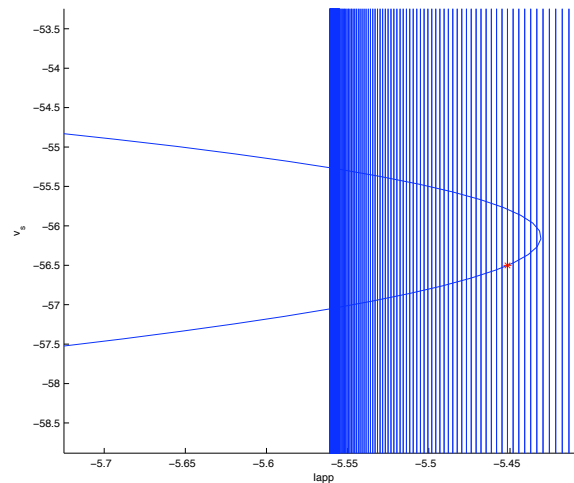


Figure 2.23: The limit cycle passes the first limit point  $I_{app} \approx -5.43$  without bifurcating.

As the limit cycle has passed the first limit point the cycle can undergo a saddle homoclinic orbit bifurcation on the middle and top branch (not the bottom branch because those equilibria only have stable manifolds). Because the limit cycles seem to converge far before the second limit point for decreasing  $I_{app}$  (see Figure 2.24) a SNIC bifurcation is unlikely to occur.

A saddle homoclinic orbit bifurcation has to be found: on which branch,

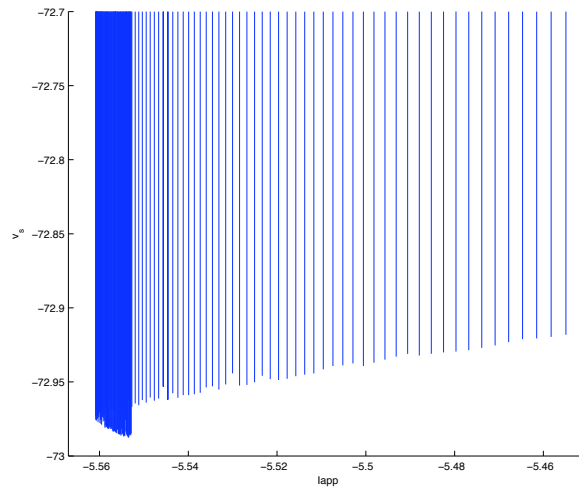


Figure 2.24: The convergence of the limit cycles far before the second limit point indicates a saddle homoclinic orbit bifurcation.

middle or top, will the stable and unstable manifolds of the saddle be joined by a homoclinic orbit? It is clear that the limit cycle will ‘hit’ the middle or top branch and this often occurs at the sharp corners of the cycles. The orbits converging to the limit cycle stay in the neighbourhoods of these corners, which are near saddles, for a long time resulting in the large period of the oscillation. In Figure 2.25 two sharp corners of the cycles can be seen.

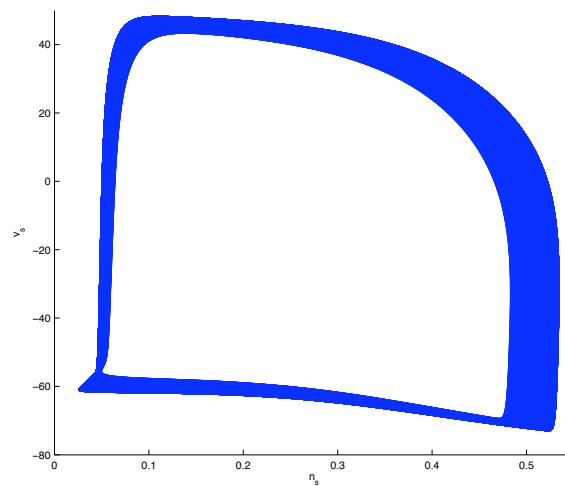


Figure 2.25: The lower left and right corner are sharp and can both indicate the homoclinic bifurcation occurring there.

By writing down the equilibrium values for the five coordinates for  $I_{app}$  be-

tween approximately  $-5.43$  (the limit points) and  $-6 \text{ pA}/\mu\text{m}^2$  it can easily be seen which corner is nearest to a saddle. Then it is also clear on which branch this saddle is and on thus on which branch the saddle homoclinic orbit bifurcation occurs. In this range for  $I_{app}$  two of the equilibrium values  $(v_s, n)$  on the top branch are around  $(v_s, n) \approx (-38.14, 0.317)$  and on the middle branch are  $(v_s, n) \approx (-55, 0.054)$ . Because the lower right corner of the limit cycles converges to  $(v_s, n) \approx (-75, 0.53)$  and the lower left corner to  $(v_s, n) \approx (-61, 0.025)$  it would indicate that the lower left corner converges to a saddle on the middle branch. This is confirmed by the 3D Figure 2.26.

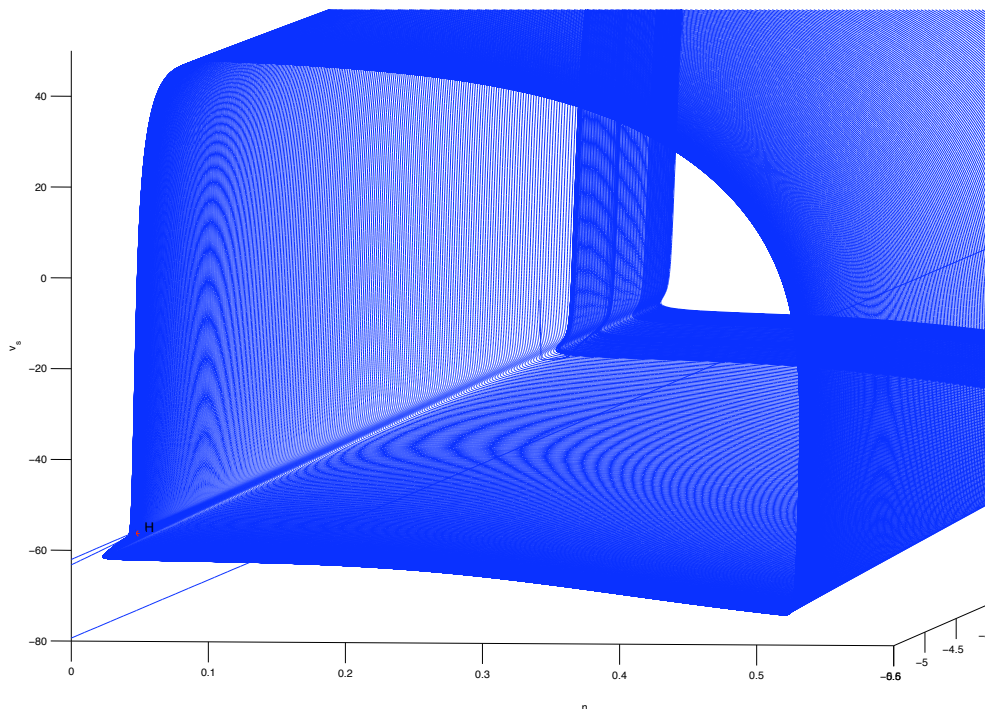


Figure 2.26: The lower left corner of the limit cycle converges to the middle branch of the equilibrium curve, also drawn in the figure.

Where the saddle homoclinic orbit bifurcation exactly occurs cannot be calculated explicitly by MatCont. The guess is that between  $I_{app} = -5.5$  and  $I_{app} \approx -6$ . After the bifurcation (thus for smaller values of  $I_{app}$ ) the limit cycle has disappeared.

### Qualitatively different parameter regions

Now we have drawn the equilibrium curve with its bifurcations, the different pictures for the unstable limit cycle that emerged from the subcritical Hopf bifurcation and the bifurcations of this limit cycle (fold- and saddle homoclinic), we can draw some initial conclusions about the model's behaviour for various values of  $I_{app}$ . In figure 2.27 the onedimensional parameter-region is drawn with the different bifurcations indicated on the line (a SHOB is a saddle homoclinic

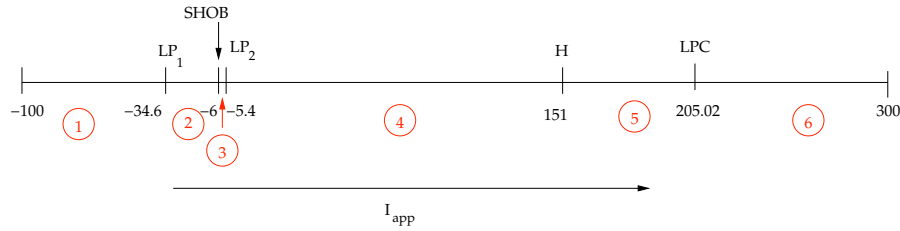


Figure 2.27: The qualitatively different regions in parameter space. For the values indicated in this figure draw a vertical line at these values in Figure 2.21.

orbit bifurcation). In the six parameter regions shown in the figure the model behaves differently, sometimes is even dependent on the chosen initial data for the coordinates, because the system is bistable.

The following numbered list gives the equilibria and limit cycles present in the various regions with the corresponding numbers with their stability properties. Also the behaviour of the STN-neuron will be guessed for all six regions.

1. In this region ( $I_{app} < LP_1 \approx -34.6$ ) only one stable equilibrium is present. Independent on the initial conditions taken for the coordinates, the solution to the system will converge to this equilibrium. For the neuron this means that it will be quiescent when  $I_{app} < -34$  where the right boundary of  $-34$  is approximate.
2. In this region ( $I_{app} \in [LP_1, SHOB] \approx [-34.6, -6]$ ) one stable equilibrium (the lower branch in Figure 2.21) is present and two unstable ones (1D on the middle branch and 2D unstable on the top branch). Numerically *all* solutions will converge to the stable equilibrium resulting in a quiescent neuron. When the initial data are chosen on the stable manifolds of the saddles the solution will in theory converge to the saddle, but this behaviour can never be captured by MatCont.
3. In this small region ( $I_{app} \in [SHOB, LP_2] \approx [-6, -5.4]$ ) the stable limit cycle has not yet disappeared (which has in region 2). Therefore in this region one stable and two unstable equilibria are present, together with a stable limit cycle. The system is thus *bistable*. It depends on the chosen initial data whether the solution will converge to the limit cycle (the neuron spikes), or will converge to the stable equilibrium (the neuron is quiescent).
4. In this region ( $I_{app} \in [LP_2, H] \approx [-5.4, 151]$ ) an unstable equilibrium is present (the top branch in Figure 2.21) and a stable limit cycle. The solution will converge to this stable limit cycle independent on the initial data chosen, when  $I_{app}$  is taken in this region. Because  $I_{app} = 0$  in this region, spontaneous spiking is guaranteed.
5. In this region ( $I_{app} \in [H, LPC] \approx [151, 205.02]$ ) the system is *bistable*. An equilibrium has become stable on the top branch due to the Hopf bifurcation. Beside this stable equilibrium a stable limit cycle is also present. The stable limit cycle circles around the unstable limit cycle. It thus depends on the chosen initial data whether the neuron will spike or become quiescent in this region.
6. In this region ( $I_{app} > LPC \approx 205.02$ ) only a stable equilibrium is present to which the solution will be attracted independent of the chosen initial

data. The neuron is therefore always quiescent when  $I_{app}$  is chosen in this region.

In the next section initial data within these various regions of parameter and phase space will be taken to verify whether the behaviour is indeed as described above. In regions of bistability it will be tested whether the neuron's state can be reset by a sufficient current pulse or step. Also it will be tested whether the model is capable of generating the behaviour described in literature (see Section 2.1.1).

## 2.2.2 Simulations

In the previous section Model (2.5) was analysed thoroughly using bifurcation theory, which resulted in a detailed picture of the possible behaviour of the model (Figure 2.27) for various intervals of the applied current  $I_{app}$ . In Section 2.2.2 System (2.5) will be simulated for  $I_{app}$  in the six different regions indicated in Figure 2.27 to check whether the neuron behaves in these regions as was guessed in the previous section. Especially the regions in which the system is bistable (regions 3 and 5) are interesting because the initial conditions chosen for the coordinates critically decide whether the model will fire or becomes quiescent. The simulations of the system for  $I_{app} = 0$  (in region 4) will be compared to experimental data for a spontaneous spiking STN-neuron described in Section 2.1.1. At the end of this section, the responses of the model to de- and hyperpolarizing steps and pulses will be tested in simulations. Specific stimulating steps and pulses for which experimental results are described (see Section 2.1.1) will be chosen for  $I_{app}$  to compare these model's responses with experimentally found responses to the same type of stimuli.

### Simulations in the different regions

In this section  $I_{app}$  will be assigned values in the six different regions from Figure 2.27. The initial data for the five coordinates  $v_s$ ,  $n$ ,  $h$ ,  $r$  and  $[Ca]_i$  will decide, in regions where the system is bistable (regions 3 and 5), whether the neuron will spike or not. In the other regions the initial data is taken arbitrarily because every orbit will converge to the only stable solution present in the region anyway.

#### REGION 1

In region 1 only a stable equilibrium is present to which all orbits converge independent on the initial data chosen. As can be seen in Figure 2.28 the orbit with initial data as in Table 2.3 converges to the stable equilibrium which is also indicated in Table 2.3 for  $I_{app} = -50$ .

	$v_s$	$n$	$h$	$r$	$[Ca]_i$	$I_{app}$
Initial data	-60	0.1	0.2	1e-5	1.5	-50
Stable equilibrium	-82.1	0.0019	1	0.995	0.0025	-50

Table 2.3: For  $I_{app}$  in region 1 ( $I_{app} = -50$ ), every orbit, independent of its initial data, converges to the stable equilibrium.

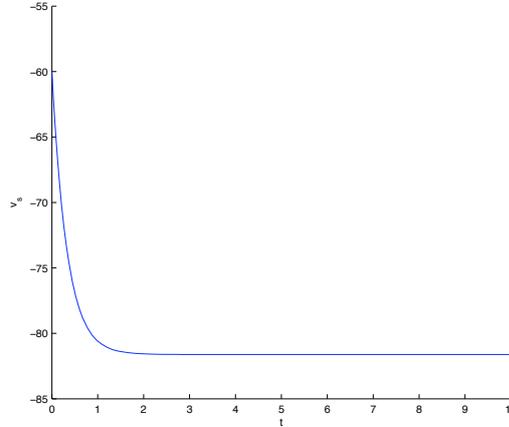


Figure 2.28: Every orbit with  $I_{app}$  in region 1 converges to the stable equilibrium.

The eigenvalues are all real and negative, thus indicating that the equilibrium is a stable *node*. Therefore no subthreshold oscillations are present.

#### REGION 2

For  $I_{app}$  in region 2, two unstable nodes are always present together with a stable node. The top branch in Figure 2.12 is 2D unstable and the middle branch in the same figure is 1D unstable. The stable nodes are on the lower branch. Independent on the initial data chosen for the five coordinates, the orbits converge to the stable equilibrium when  $I_{app}$  is chosen in this region. The convergence can be distorted though by the unstable manifolds of the saddles. The initial data chosen for the simulations are listed in Table 2.4 and are deliberately taken on the top- and middle-branch to show the slow convergence. For both initial data the stable equilibrium to which the orbit converges is listed directly below.

	$v_s$	$n$	$h$	$r$	$[Ca]_i$	$I_{app}$
Top-branch	-40	0.2689	0.5800	1.3710e-06	0.8791	-26.0971
Stable equilibrium	-70.3	0.0083	1	0.8389	0.1001	-26.0971
Middle-branch	-50	0.0953	0.9720	2.0343e-04	0.1720	-12.9428
Stable equilibrium	-64.1	0.0178	0.9997	0.1900	0.0116	-12.9428

Table 2.4: For  $I_{app}$  in region 2, the initial data for the coordinates are chosen on the top and middle branches which are saddles. The solution converges to the stable equilibrium on the lower branch.

The slow convergence to the slow equilibrium from the top-branch can be seen in Figure 2.29 and from the middle-branch in Figure 2.30.

The slow convergence is due to the stable (for Figure 2.30) and unstable (for Figure 2.29) manifolds of the saddle. No pictures are shown for other initial data but the solutions then converge more directly to the stable equilibrium.

#### REGION 3

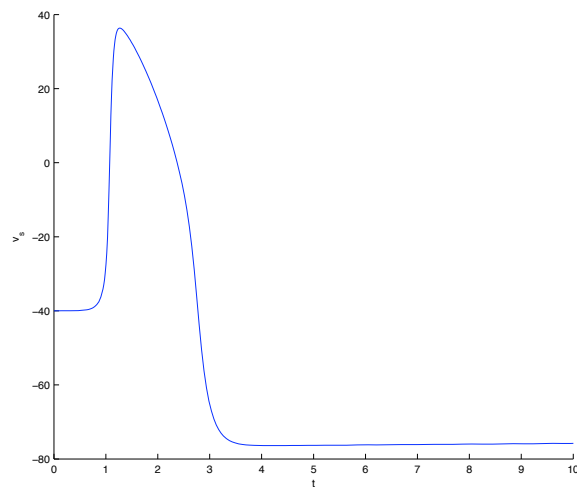


Figure 2.29: Starting in the 2D unstable node on the top branch the orbit eventually converges to the stable equilibrium on the lower branch.

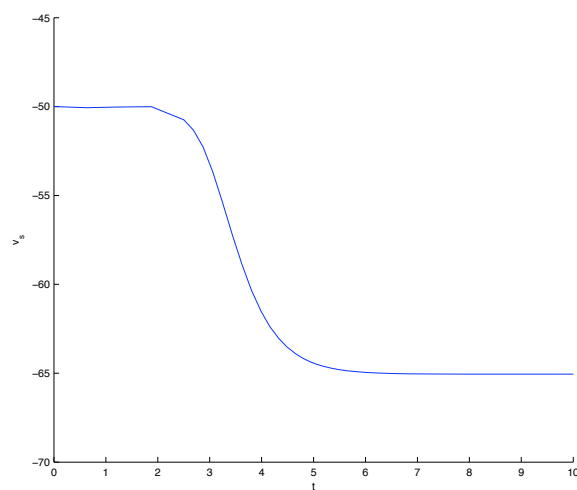


Figure 2.30: Starting in the 1D unstable node on the middle branch the orbit eventually converges to the stable equilibrium on the lower branch.

Region number 3 consists of few parameter values and they are all very close to the limit point bifurcation around  $I_{app} \approx -5.5$  and the saddle homoclinic orbit bifurcation value around  $I_{app} \approx -6$ . In this region a stable limit cycle is present (which is about to disappear) together with a stable node (on the lower branch) and 2D and 1D unstable nodes (on the top- and middle-branch respectively). The system is thus bistable.

In Table 2.5 the initial data of the different figures are listed. The bold numbers are the only changes from the data from the previous figure.

	$v_s$	$n$	$h$	$r$	$[Ca]_i$	$I_{app}$
Figure 2.31	-55.141	0.0525	0.9946	0.0027	0.0597	-5.6
Figure 2.32	-55.141	0.0525	0.9946	<b>1</b>	<b>0</b>	-5.6
Stable equilibrium	-57.183	0.0412	0.9972	0.0073	0.0382	-5.6

Table 2.5: The initial data for Figures 2.31 and 2.32. Also the coordinate values of the stable equilibrium are listed.

In Figure 2.31 the initial data are chosen on the middle branch (see Figure 2.12), thus in the 1D unstable node. After initiating a spike (see Figure 2.31) the solution eventually still converges to the stable equilibrium (not shown in the figure). Because it looks as convergence in 2D cross sections, but could be spiking with a large period ( $I_{app}$  is very near the saddle homoclinic orbit bifurcation value) the numerical data has to be checked whether in  $\mathbb{R}^5$  all five values of the equilibrium are approached. This is indeed the case. The initial spike can be due to a short convergence to the stable limit cycle after which it is drawn into the attraction domain of the stable equilibrium. This domain seems to be a large portion of the physiological range.

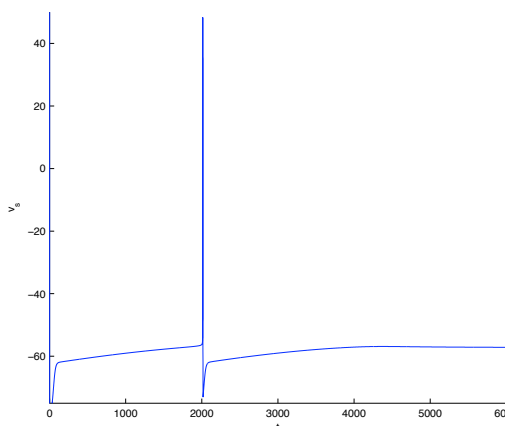


Figure 2.31: With initial data as on the first row in Table 2.5 the orbit is first attracted to the large-period stable limit cycle after which it converges to the stable node.

In Figure 2.32 the large influence of  $r = 1$  on the generation of rebound bursts can be seen. Although a stable limit cycle is present in this region, the solution does not converge to it. Sometimes initially it does (the system shows a few or a lot of rebound spikes), but eventually all orbits (with the initial data tested of course) tend to converge to the stable equilibrium.

#### REGION 4

In region 4 a stable limit cycle is present together with a 2D unstable node. Independent on the initial data chosen the solution will always converge to the stable cycle. This thus guarantees that the STN-neuron fires when  $I_{app} \in [-5.4, 151]$  so also with zero input ( $I_{app} = 0$ ). This agrees with experimental

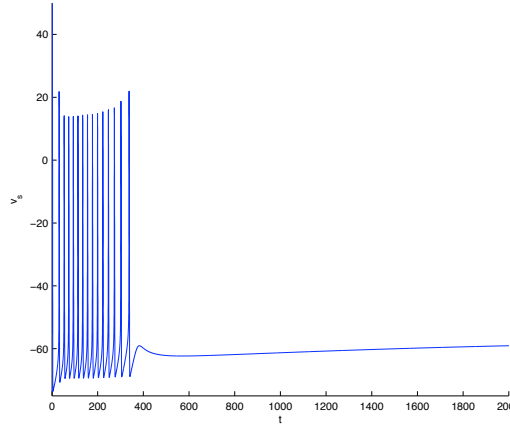


Figure 2.32: With  $r = 1$  and  $[Ca]_i = 0$  the orbit is initially attracted to the stable limit cycle, and the neuron spikes with a high frequency (rebound bursts). Eventually the solution again converges to the stable node.

results which claim that the STN-neuron is able to spontaneously spike. Only simulations for  $I_{app} = 0$  will be shown, to verify the various spontaneous firing properties of STN-neurons described in Section 2.1.1 with the model's behaviour. Time diagrams and some limit cycle cross sections are drawn.

All other values for  $I_{app}$  in this region will also show a convergence to the stable limit cycle, which for that value of the applied current, may have a different frequency and amplitude. The depolarizing range of region 4 will be shown in the following section when depolarizing values for  $I_{app}$  are taken with  $I_{app}$  not at its specific value initially: a step-current is taken for  $I_{app}$ .

The initial data for the five coordinates and the parameter are given in Table 2.6.

$v_s$	$n$	$h$	$r$	$[Ca]_i$	$I_{app}$
-55	0.2	0.5	0.5	1	0

Table 2.6: Initial data for spontaneous spiking

In Figure 2.33 the  $v_s, t$ -diagram of the model (right) is shown together with the same type of picture found in experimental literature (left). Spikes are shown for the stabilised system, when the orbit has already converged sufficiently close to the limit cycle.

Spike frequency adaptation can not be seen from Figure 2.33 because stabilisation has already occurred. In Figure 2.34 the initial spikes are shown and a decrease in the interspike interval towards a stable interval can be seen.

The average interspike interval approaches  $\pm 400$  ms which corresponds to a spike frequency of approximately 2.5 Hz. 3 Hz was claimed for this model in [1] and a spike frequency of 0–10 Hz is mentioned in literature. The interspike interval of 400 ms agrees with the 500 ms found by experiments and indicated in the left picture of Figure 2.33. The voltage range, which is traversed during spontaneous spiking, is approximately -70–40 mV, and the shape of the spikes

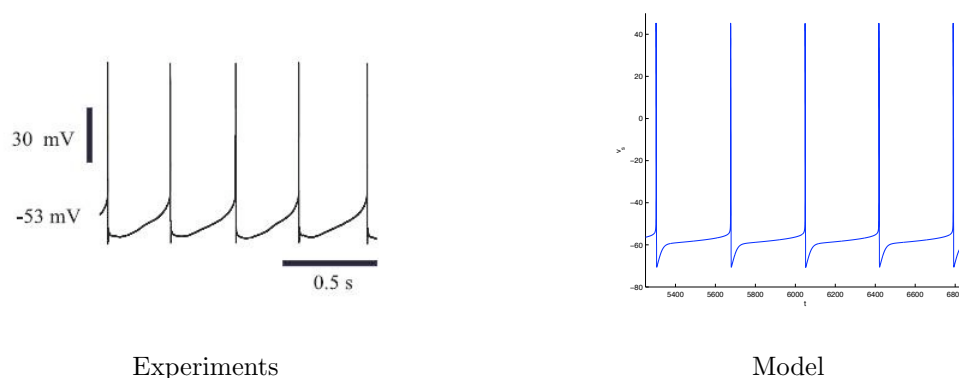


Figure 2.33: A spontaneous firing STN-neuron. Left: from experiments, right: from model.

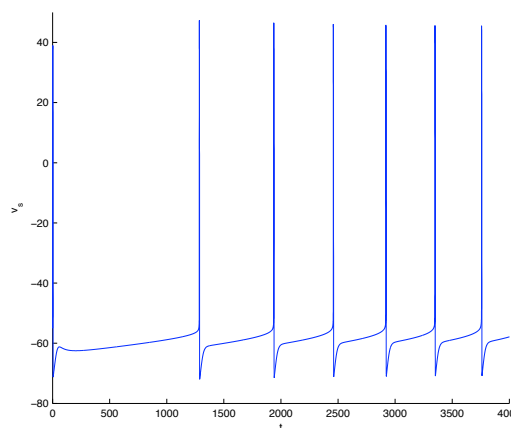


Figure 2.34: The initial spikes of spontaneous spiking show spike frequency adaptation: a decrease in interspike interval can be seen until it approaches a certain level.

hardly changes during spiking indicating a high level of regularity. This all agrees with the experimentally found results described in Section 2.1.1.

In the right picture of Figure 2.35 two spikes of Figure 2.33 are zoomed in and displayed together with the same type of curve from experiments for spontaneous spiking STN-neurons. One can clearly see in the right picture, that the duration of the action potential is very short whereas the AHP following the spike lasts quite long. The oscillation cycle of this model-neuron largely agrees with the cycle described in Section 2.1.1. The only difference is that the model does not have *two* phases of AHP (a slow and a fast one). Only a fast one is present. The fast AHP is directly followed by a slow depolarization.

In Figure 2.36 the intracellular calcium concentration  $[Ca]_i$  is plotted for increasing time  $t$ . The concentration clearly decreases with the exception of some small peaks, when  $v_s$  spikes. These small peaks could be due to the high-threshold calcium-current  $I_{Ca}$  which is activated during the peaks in  $v_s$ .

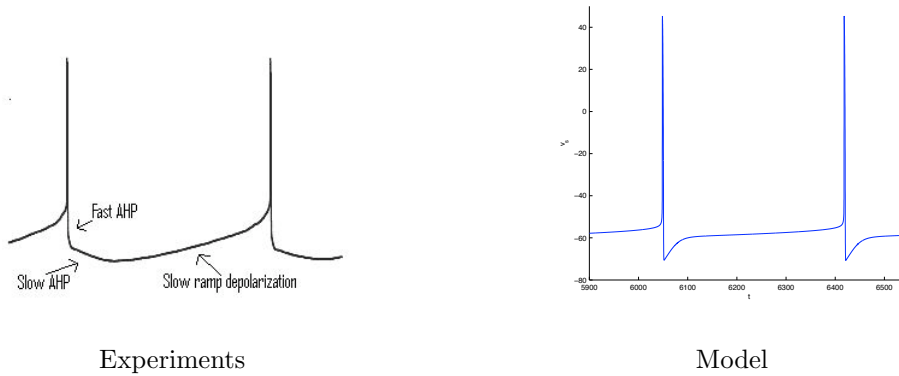


Figure 2.35: Left: two spikes of the left picture in Figure 2.33 zoomed in. Right: two spikes from the model simulation zoomed in.

Apparently during spontaneous spiking, the calcium clearance mechanism (denoted by  $-k_{Ca}[Ca]_i$  in (2.4)), exceeds the influx of calcium through  $I_{Ca}$  and  $I_T$ . The time diagrams of  $h$  and  $r$  are not shown here, but both show spiking

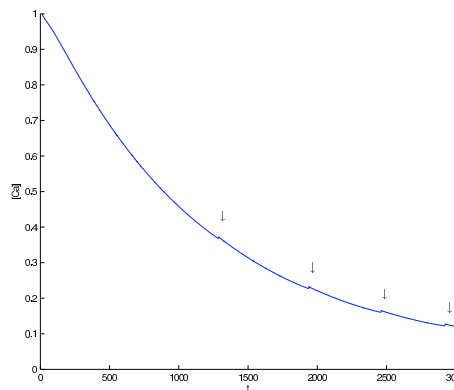


Figure 2.36: Decrease in intracellular calcium concentration during spontaneous spiking.

behaviour as  $v_s$  and  $n$  did. In Figure 2.37 the  $h, v_s$ -solution is plotted for a simulation time of 6000 ms. The solution approaches the stable cycle, which is shown in this 2D cross section of  $\mathbb{R}^5$ .

The initial point (indicated by ‘start’ in the figure) is not very near the stable cycle it finally approaches indicating spike frequency adaptation. The arrow in the figure indicates the direction of the solution. The ‘thick’ area is the limit cycle to which the solution is attracted.

As one can see from Figure 2.38 the intracellular calcium concentration starts around 1 and decreases during spontaneous spiking.

REGION 5

The system is also bistable in region 5 ( $I_{app} \in [H, LPC] \approx [151, 205.02]$ ) but the difference with region 3 is that there is a stable *focus* (instead of a stable *node*)

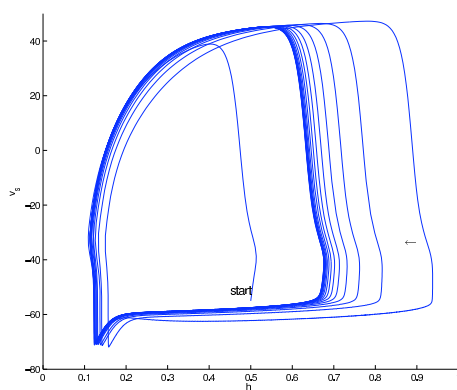


Figure 2.37: 6000 ms of spiking: a stable limit cycle is present.

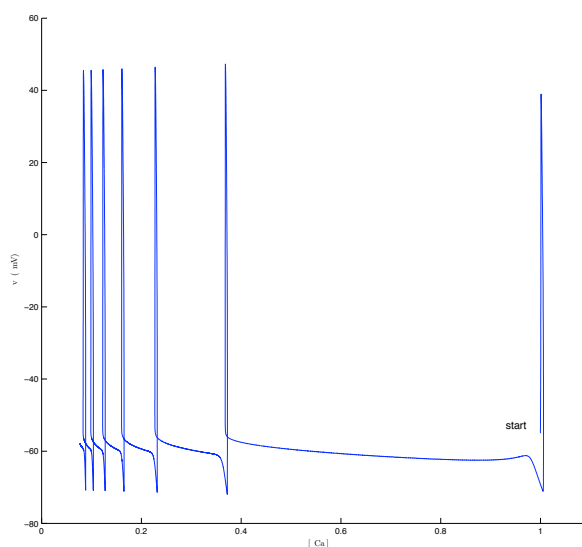


Figure 2.38: During spontaneous spiking of  $v_s$ , the intracellular calcium concentration decreases.

present together with the stable limit cycle. The stable focus is present on the top branch in Figure 2.12 together with an unstable (branch of  $\max(v_s)$  and  $\min(v_s)$  emerging from H in Figure 2.21) and a stable limit cycle (branch of  $\max(v_s)$  and  $\min(v_s)$  emerging from LPC and not from H in Figure 2.21).

In Figure 2.39 the initial data are as in the first row of Table 2.7. The solution converges to the stable focus which is also listed in the table. It is clear that it is a focus instead of a node because of the subthreshold oscillations which are present.

For the same applied current  $I_{app} = 170$  but different data for all coordinates except  $v_s$ , the solution converges to the stable limit cycle and thus shows spiking behaviour. This can be seen in Figure 2.40. These two figures clearly show that for the same applied current it depends on the initial data chosen for the coordinates whether the neuron will spike or becomes quiescent. The bistability

	$v_s$	$n$	$h$	$r$	$[Ca]_i$	$I_{app}$
To equilibrium (Fig 2.39)	-80	0	1	1	0	170
To limit cycle (Fig 2.40)	-80	1	0	0	1	170
Stable equilibrium	-32.053	0.498	0.096	2.58e-8	1.897	170

Table 2.7: The orbit starting in this point converges to the stable focus.

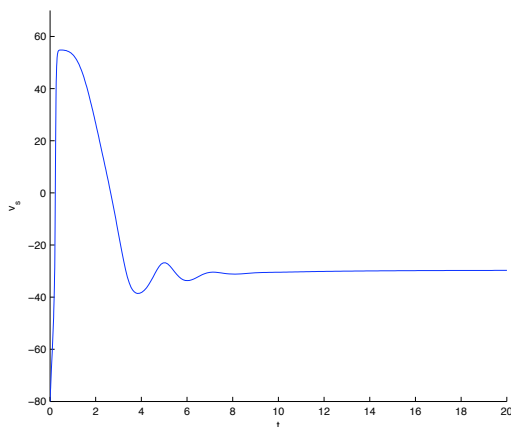


Figure 2.39: For the initial data as in the first row of Table 2.7 the solution converges to the stable focus (with values given in the last row of the same table).

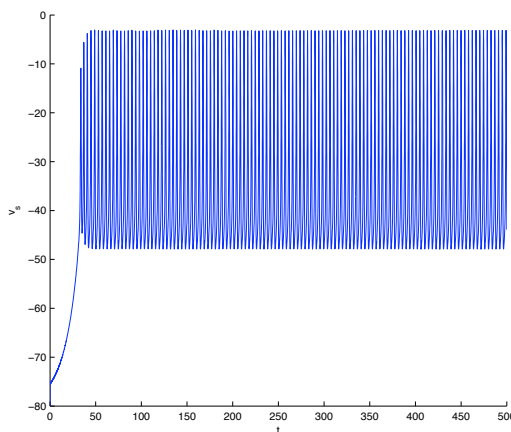


Figure 2.40: For the initial data as in the second row of Table 2.7 the solution converges to the stable limit cycle.

of region 5 is thereby shown.

#### REGION 6

In region 6 only a stable focus is present (on the top branch), which becomes

a stable node when the eigenvalues become real again (see Figure 2.15). Any solution will converge to this stable focus independent on the initial data chosen for the coordinates. In Figure 2.41 the initial data are as in the first row in Table 2.8.

	$v_s$	$n$	$h$	$r$	$[Ca]_i$	$I_{app}$
Figure 2.41	-40	0.8	0	0	1	210
Figure 2.42	-50	0	0	0	1	210
Stable focus	-31.23	0.5240	0.0754	1.7086e-08	2.0021	210

Table 2.8: The orbit starting in the points from row 1 and 2 converges to the stable focus listed in the last row, each in a different manner.

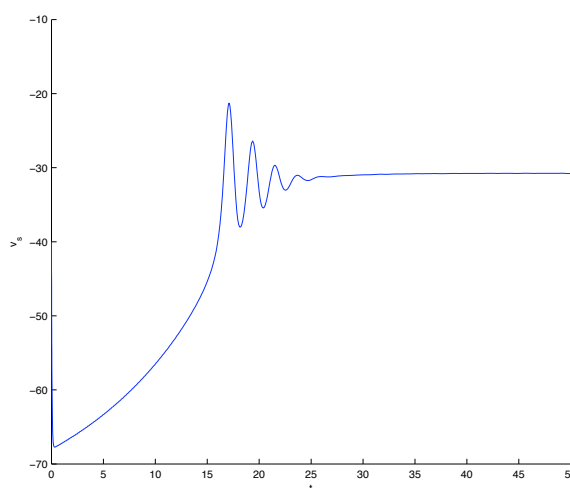


Figure 2.41: With the initial data as in row 1 of Table 2.8, the orbit oscillatory converges to the stable focus.

The orbit oscillatory converges to the stable focus. It is clear that the initial data are quite far away from the stable focus, causing the large spike in the beginning of the simulation. The values of this focus are given in the last row of Table 2.8. In Figure 2.42 the initial data are as in the second row of Table 2.8.

The oscillatory behaviour is less apparant in this figure. This is a different convergent behaviour compared to that shown in Figure 2.41.

### Responses to depolarizing steps and pulses

In the previous section simulations were shown for  $I_{app}$  in the different regions indicated in Figure 2.27. The spontaneous spiking behaviour of the model has already been compared to experimental results while discussing region 3. Other experimental results described in Section 2.1.1 involved the response of a STN-neuron to various types and amounts of de- and hyperpolarizing inputs. This section will therefore describe the response of the model to depolarizing current steps and pulses ( $I_{app} > 0$ ) (the next section deals with hyperpolarizing

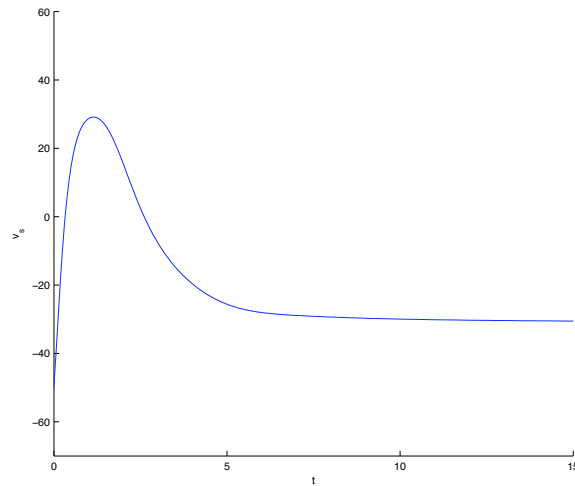


Figure 2.42: With the initial data as in row 2 of Table 2.8 the neuron converges more smoothly toward the focus than in Figure 2.41.

( $I_{app} < 0$ ) steps and pulses) and compare these responses to those described in Section 2.1.1.

Inputs can be ‘applied’ in three different ways [3]: through ramps, steps, and brief pulses. All three reset the initial data in a different way. Ramps are currents for which their strength increases linearly in time, starting with  $I_{app} = 0$  at  $t = 0$ . They are the currents used for continuations in MatCont. The limit cycle or equilibrium is followed for small changes in the applied current. The variables have time to follow the equilibrium or limit cycle so no change in the variables can be seen (the system is still quiescent or spikes). The system is not pushed in a completely different area of phase space evoking different behaviour. Ramps have been used in the bifurcation analysis of the model and are therefore dealt with already.

Steps will be discussed in this and the next section. They look like presented in Figure 2.3 (depolarizing). The strength  $a$  and duration  $b$  of the step can be varied, to verify whether the model reacts to these changes as it should. When the current is stepped the system changes instantly resulting in an instant change in the location and characteristics of the equilibria and limit cycles (if still present). The response of the orbit to this instant change depends on the timescales of the different variables. Slow variables as gating variables in this system do not have time to catch up with the instant change. Even if for example the stable equilibrium in which the system was, is only relocated, a spike is evoked due to the slow response of the system.

In the case of a brief current pulse the system is, as in the case of the step, instantly changed. Whether the neuron returns to its initial state (from before the application of the pulse) after the break of the pulse, depends on the possible bistability of the system. For example, the system in its stable equilibrium state before the application of the pulse, can be ‘pushed in’ the attraction domain of a stable limit cycle (the system is thus bistable) during the pulse application

and will not return to its resting state after the break of the pulse. Because experimental results with pulses have only been recorded for already hyperpolarized STN-membranes, the depolarizing pulse will be mentioned in the section on the hyperpolarizing step.

See Section 2.1.1 to compare the responses of the model to a depolarizing step with the experimentally found responses. The step equation used for  $I_{app}$  is as in (2.9), with  $a$  the strength of the step in  $\text{pA}/\mu\text{m}^2$  and  $b = b_2 - b_1$  the duration of the step in ms (see Figure 2.3).  $H(t)$  is the heaviside stepfunction.  $a > 0$  in this section, for a depolarizing step. The initial conditions for the five variables are taken as in Table 2.6.

$$I_{app} = a(H(t - b_1) - H(t - b_2)) \quad (2.9)$$

In Figure 2.43 a step with  $a = 10 \text{ pA}/\mu\text{m}^2$ , and  $b = 1000 \text{ ms}$  ( $b_1 = 2000 \text{ ms}$  and  $b_2 = 3000 \text{ ms}$ ) is simulated. Indeed an increase in frequency can be seen during the application of the step. In Figure 2.44  $a = 50 \text{ pA}/\mu\text{m}^2$  with the same values for  $b$ ,  $b_1$  and  $b_2$ .

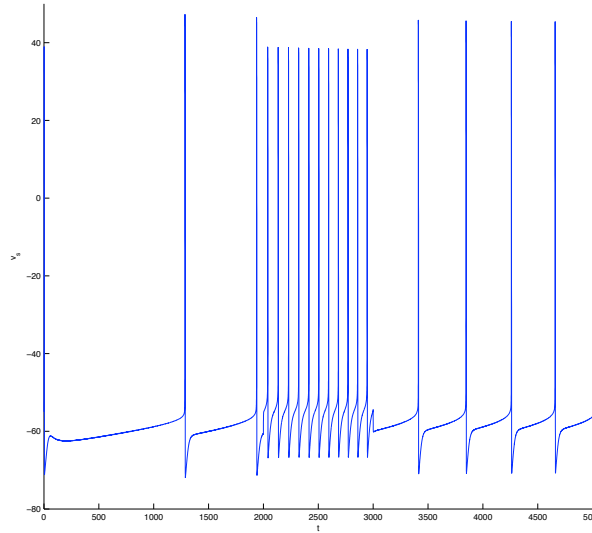


Figure 2.43: A step of amplitude  $10 \text{ pA}/\mu\text{m}^2$  is applied between  $t = 2000 \text{ ms}$  and  $t = 3000 \text{ ms}$ .

The frequency of spiking clearly increases with the strength of the applied step which agrees with experimental results listed in Section 2.1.1. What does not agree with literature, is the voltage range, which is traversed during the application of the step. The voltage range is clearly smaller, which can also be seen in Figure 2.45. During the step-application the solution is attracted to a *smaller* limit cycle (showing the decrease in traversed voltage range). The speed in which the solution approaches this limit cycle is clearly larger (showing the increase in frequency). The latter can not be seen from Figure 2.45 but can be seen from the timediagrams in Figure 2.43 and 2.44.

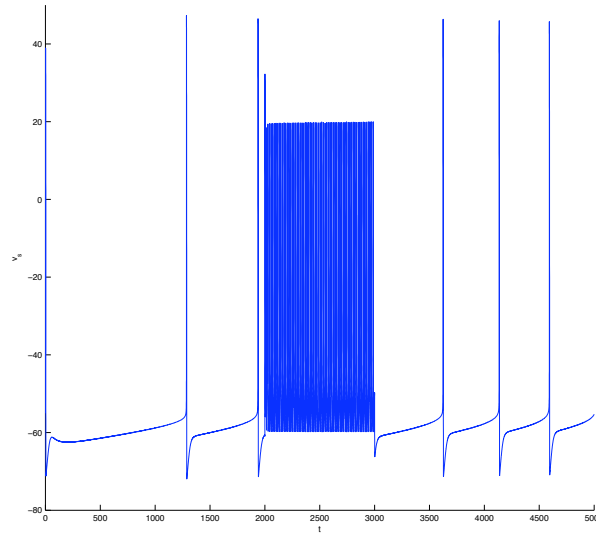


Figure 2.44: A step of amplitude  $50 \text{ pA}/\mu\text{m}^2$  is applied between  $t = 1000 \text{ ms}$  and  $t = 1500 \text{ ms}$ .

Experiments have also shown that the duration of the AHP after the break of the step, increases smoothly with frequency and thus with applied current. Whether they mean the total interspike interval following the application of the step or only the repolarization phase (so not the depolarization phase) is unclear. Both increase in duration after the step break which can be seen by comparing this interval in Figure 2.43 with that in Figure 2.44. A small increase in the duration of the repolarization phase can be seen as well an increase in interspike interval. Both are small but present.

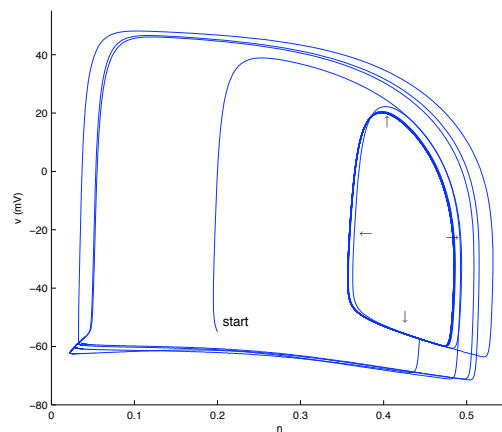


Figure 2.45: During the depolarizing step application the solution is attracted to a smaller limit cycle (see arrows).

Spike frequency adaptation which is observed in experiments during the application of a depolarizing step, is more difficult to show in static plots, but as can be seen in the figure of the limit cycle (Figure 2.45) the solution is drawn to another limit cycle than it traverses before the step is applied. As is intuitive, the longer the step is applied, the closer the solution gets to this new limit cycle and the frequency of the spikes will converge to a constant level. This is not possible when the step duration is too short. Therefore indeed the duration of the step influences this spike frequency adaptation.

The fI-curve of the model (based on applied current ramps) was already compared with an experimentally found fI-curve in Section 2.2.1. The slope of the model fI-curve was more than twice the largest slope found in literature and could even be larger if not the asymptotic frequency but the average frequency had been plotted.

### Responses to hyperpolarizing steps and pulses

This section is dedicated to compare the responses of the model to hyperpolarizing steps and pulses with the responses registered in experiments and described in Section 2.1.1. It is especially interesting to know if the model represents a plateau-generating STN-neuron or one which is not able to do so. For the analysis of networks with STN- and GPe-neurons this ability can make a large difference in network behaviour.

As was described in Section 2.1.1 contradictory results can be found in literature how a STN-neuron behaves during the application of hyperpolarizing currents. According to [15] the neuron shows bursting behaviour while this behaviour is never observed in other experiments with STN-neurons *alone*. Some articles agree on certain aspects of the response, so the focus will lie on testing those responses. They will be repeated here for the sake of convenience.

When the model is able to generate plateau potentials (approximately half of all STN-neurons) it should have the following firing characteristics:

- When the neuron is more hyperpolarized than approximately -75 mV, it should react to a depolarizing pulse of at least  $10 \text{ pA}/\mu\text{m}^2$  by generating a plateau potential often accompanied by the generation of action potentials.
- When the neuron is strongly hyperpolarized it should become quiescent.
- When a hyperpolarizing step is applied more hyperpolarizing than -75 mV, long-lasting rebound bursting should occur, which ends with a slow decay of the membrane potential to resting potential.

, When the model is not able to generate plateau potentials (approximately the other half of all STN-neurons):

- Independent on the hyperpolarization level of the neuron it responds to a depolarizing pulse by an increase in membrane potential during the application of the pulse. After the break of the pulse the membrane potential repolarizes rapidly.
- When the neuron is strongly hyperpolarized it should become quiescent.
- After the break of a hyperpolarizing step rebound bursting should occur, which ends with a fast decay of the membrane potential to resting potential.

What exactly happens during the application of a hyperpolarizing step which not yet makes the neuron quiescent is unclear. It could burst according to some articles or just spike at lower frequencies. See Section 2.1.1 for more details.

Now the model will be simulated and hyperpolarizing steps will be applied with a strength of  $a \text{ pA}/\mu\text{m}^2$  during a timeperiod of  $b \text{ ms}$  (see Figure 2.3. A hyperpolarizing step means that  $I_{app} < 0$  in (2.5) with (2.9) still used as formula for  $I_{app}$  but with  $a < 0$ . The initial data for the other variables are as in Table 2.6.

In Figure 2.46 a hyperpolarizing step with a strength of  $a = -4 \text{ pA}/\mu\text{m}^2$  is applied for a duration of  $b = 2000 \text{ ms}$ . During the application of the ramp between  $t = 2000 \text{ ms}$  and  $t = 4000 \text{ ms}$  the neuron still evokes a spike. The frequency of spiking is thus decreased but not yet terminated. Bursting is not observed.

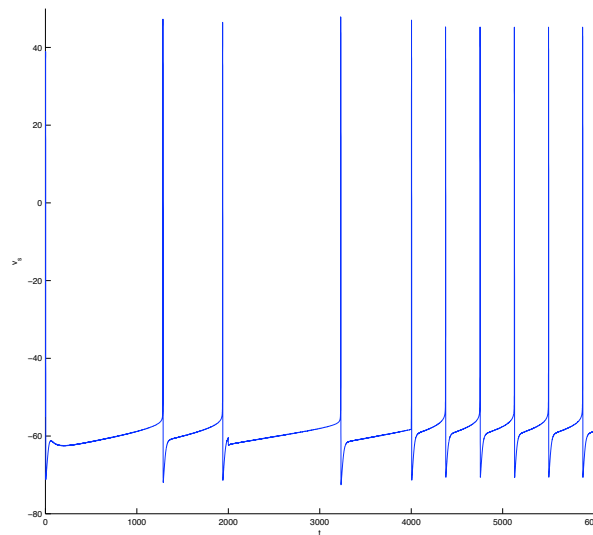


Figure 2.46: Hyperpolarizing step with  $a = -4 \text{ pA}/\mu\text{m}^2$  applied between  $t = 2000 \text{ ms}$  and  $t = 4000 \text{ ms}$ : the frequency decreases.

When  $a$  decreases from  $-4 \text{ pA}/\mu\text{m}^2$  to  $-10 \text{ pA}/\mu\text{m}^2$  (with the same duration of  $b = 2000 \text{ ms}$ ) the neuron is not able to spike anymore during the application of the step. This can be seen in Figure 2.47. The step is not that strong that rebound bursts are evoked after the step breaks. Spontaneous spiking continues after the break of the step. In Figure 2.48 the strength of the applied hyperpolarizing step has decreased even more ( $a = -50 \text{ pA}/\mu\text{m}^2$ ) with the same duration of  $b = 2000 \text{ ms}$ . During the step application the neuron is quiescent as before. Now the neuron *does* evoke rebound bursts after the step breaks. The rebound bursting stops quite abruptly with a short AHP and returns to spontaneous spiking behaviour very fast. This could indicate that the STN-neuron represented by the model is not able to generate plateau potentials. A plateau-generating neuron would have shown a slow decay after rebound bursting. This can only be checked by applying a short pulse when the membrane is hyperpolarized below

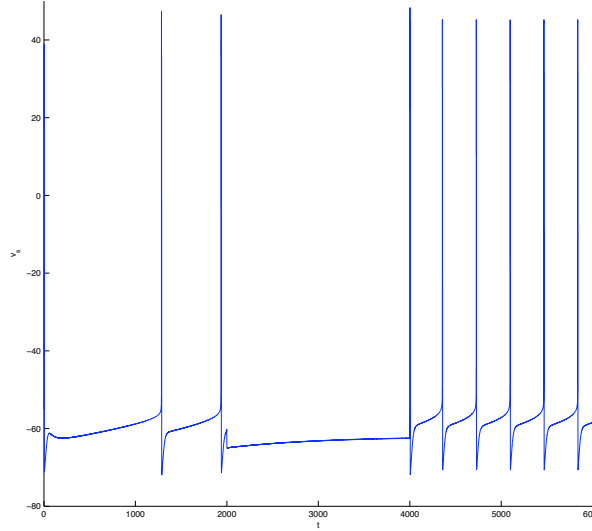


Figure 2.47: Hyperpolarizing step with  $a = -10 \text{ pA}/\mu\text{m}^2$  applied between  $t = 2000 \text{ ms}$  and  $t = 4000 \text{ ms}$ : it lowers the resting potential but evokes no rebound bursts.

-75 mV. This is not possible in simulations because this has to mean kicking the neuron out of its *stable* equilibrium state around -75 mV (or lower). Limit cycles are absent in this region (region 1). Also applying a hyperpolarizing step during which the pulse is applied does not work because after the break of the pulse the system still receives the hyperpolarizing step, therefore not giving the neuron the chance to generate a plateau potential. Unfortunately this characteristic of plateau-generating STN-neurons can therefore not be tested.

According to the second and third items of the list presented at the beginning of this section, this model seems to represent a neuron which is not able to generate plateau potentials because the decay to resting potential after the rebound bursts is too fast. It still has to be tested though whether a sufficiently hyperpolarized neuron is able to generate a plateau potential in response to a depolarizing pulse of at least  $10 \text{ pA}/\mu\text{m}^2$  (the first item). Because the plateau potential did not occur during rebound bursting, the chance of this happening appears to be quite small. Bursting during the application of the hyperpolarizing step has also not been observed (only a decrease in the frequency of firing) which confirms [16] and [5] and contradicts [15]. A STN-neuron which is not able to generate plateau potentials can exist but is the least interesting neuron in the STN, to analyse. The model described in the model [11] is a plateau-generating one.

The most realistic simulation of hyperpolarization of the STN-neuron would have been a spiking  $I_{app}$ , because the GPe-neuron will fire barrages of spikes instead of a step or pulse. A train of current pulses can be a nice simulation for a realistic  $I_{app}$  and therefore for the synaptic current  $I_{G \rightarrow S}$ . This has not been done here.

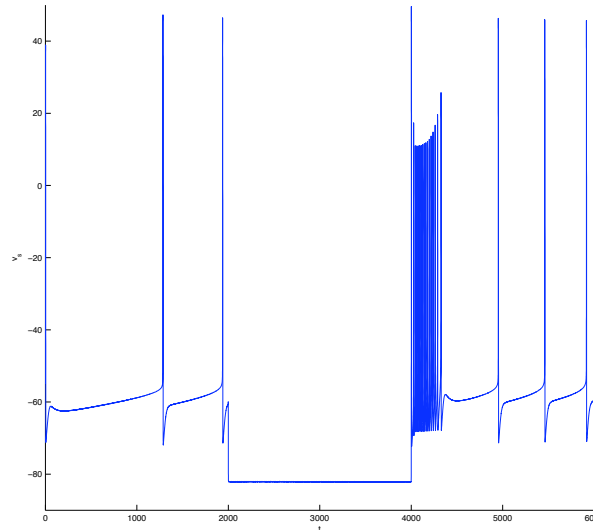


Figure 2.48: Rebound bursts occur after the break of a hyperpolarizing step with strength  $a = -50 \text{ pA}/\mu\text{m}^2$  and application between  $t = 2000 \text{ ms}$  and  $t = 4000 \text{ ms}$ .

## 2.3 Discussion

This section will summarise the different results which were derived from the analysis of the model and described in Section 2.2.1 and 2.2.2. The agreements and differences between the behaviour of the model and the experimentally found behaviour of STN-neurons (described in Section 2.1.1) will be concisely listed and discussed. It should be taken into account that [1] from which the model is derived, already states that the STN-model (and the GPe-model) is a simplified version of the STN-neuron.

This discussion and evaluation of the results of the model should first take into account the objectives for the model by the authors of [1]. Otherwise the model is criticized or complimented on characteristics of the model on which the development was not even aimed. The STN-model is developed together with the model for the GPe-neuron in [1]. The article mainly focuses on the analysis of different types of networks of these two neurons. The focus does therefore not lie on the analysis of the STN-neuron alone, as *is* the case in this chapter. Choices always have to be made during the development of a model, especially when large networks are considered. A balance has to be sought between a perfectly accurate model (if possible with the limited data available), which is less practical because of the CPU-time it takes to simulate the model, and a really fast but not accurate model, which therefore does not represent the neuron well enough. Concessions therefore always have to be made in the accuracy to keep the model ‘fast’. Whether these concessions made in the model by Terman et. al. in 2002 have still preserved the most important characteristics known for the STN-neuron in their model, will be discussed in this section. The model is

already fast enough for simulations for one neuron alone. The speed therefore does not have to be increased.

Beside the objectives of the model the validity of the experiments with which the results are compared should be taken into account during the evaluation. It should not be the case that the behaviour found during an experiment is directly the *true* behaviour of the STN-neuron. As already mentioned in Section 2.1.1 the results in experiments are dependent on the type of animal on which the tests are exhibited, the preparation of the brain slice, the recording method and other external factors [12]. When ‘several’ articles claim to have observed a certain firing characteristic of the STN-neuron under various circumstances, this characteristic will be assumed to be a *real* characteristic of the neuron. Contradictory results on a certain aspect of the neuron, are not expected to be represented by the model.

Taking all these things into account, the important discrepancies between the model and experiments will be discussed thoroughly and considerations for modelling, for example using other currents or a different description of the present currents, mentioned.

### 2.3.1 Summary of the results

This section will shortly list the results from the bifurcation analysis of the model and the simulations made of the model. The observed differences and agreements between the model and experiments are listed objectively as well. Because Section 2.1.1 divided the characteristic firing behaviour of the STN-neuron in characteristics of spontaneous firing (with a zero applied current to the STN-neuron), and characteristics of the neuron in response to de- and hyperpolarizing applied currents, this differentiation in characteristics will also be made in this section.

The bifurcation analysis of the model showed us in detail how the model-neuron behaves for different values of the parameter  $I_{app}$ . Regions for  $I_{app}$  for which the neuron behaves qualitatively different from other regions are bounded by the bifurcation points of the equilibria and limit cycles. In some regions the model-neuron appears to be sometimes with some subthreshold oscillations due to the convergence to this equilibrium. In others the neuron is always spiking (with different amplitudes and frequencies dependent on the exact value for  $I_{app}$ ). This quiescence and spiking behaviour are both independent on the initial data chosen. In two other regions the system is bistable and it therefore *does* depend on the initial data chosen whether the neuron becomes quiescent or will spike. In Figure 2.49 the picture of the regions is repeated for convenience sake.

Comparison of our system with experimental results shows the following:

- The specific regions and boundaries of these regions can not be checked with experiments because these have not been found that accurately.
- Experiments showed that with a ‘sufficiently’ large hyperpolarizing current the neuron can be made quiescent. This is indeed also the case for the model for  $I_{app} < -6$ . Only the value for which the model-neuron can be made quiescent is too small (approximately -75 mV was claimed in literature). Later we will see that other values in the depolarizing range of  $I_{app}$  need to be ‘stretched up’ as well in the model.
- Some experiments have shown (contradicted by others) that for a small

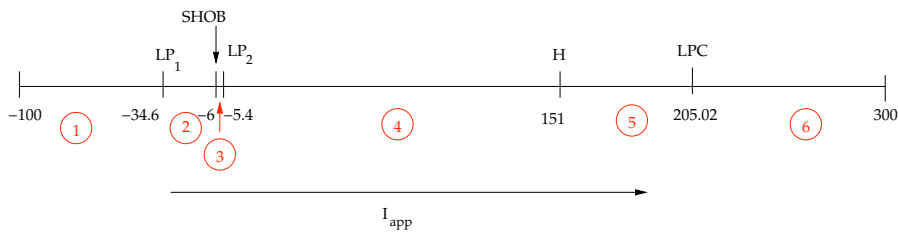


Figure 2.49: The qualitatively different regions in parameter space. See the last part of Section 2.2.1 for an extensive explanation.

applied hyperpolarizing current the neuron continues firing but at a lower frequency. This agrees with region 3 where the frequency of an already spiking neuron can approach zero, while approaching the SHOB-bifurcation value for  $I_{app}$ . It is a bistable region for the model, thus hyperpolarizing the model-neuron might make it quiescent as well.

- Experiments have shown that most STN-neurons show spontaneous spiking behaviour. Because the model has a large region in which  $I_{app} = 0$  is enclosed (region 3), and in which only a stable limit cycle is present, the spontaneous spiking of the model-neuron is guaranteed. Later the characteristics of the spontaneous spiking behaviour of the model will be compared with the characteristics listed in Section 2.1.1.
- The small bistable regions found for the model, have not been described in literature. Either the neuron was found quiescent for a certain applied current or spiking.
- The quiescence of the model-neuron for  $I_{app} > 205.02$  is not mentioned in experimental literature. Articles talk about saturation in the high-frequency range. More applied current can not increase the frequency even more, but spiking is still present. The disappearance of spiking for a large applied current has not been described.
- The stable limit cycle is present for  $I_{app} \in [-6, 205.02]$ . This limit cycle will be analysed later, by looking at its fl-curve and comparing this with the one made during experiments.
- When a stable focus is present for a certain value of  $I_{app}$  subthreshold oscillations can be seen due to the oscillatory convergence to the focus.

### Spontaneous spiking

Simulations of the model for  $I_{app} = 0$  (in region 4) showed the following characteristics:

- As can be seen in Figure 2.50, the spikes have a fast action potential, a fast AHP and a slow depolarization phase, in agreement with literature on spontaneous spiking. The slow AHP is the only phase missing, which can be seen by comparing the left and right picture in Figure 2.50.
- The asymptotic frequency during spontaneous spiking of the model is approximately 2.5Hz, which agrees with the claim of 0–10Hz in literature.
- The voltage range which is traversed during spontaneous spiking is -70–40 mV.

- Spike frequency adaptation occurs.
- The spikes show a high level of regularity (the shape of the spikes hardly change during spiking).

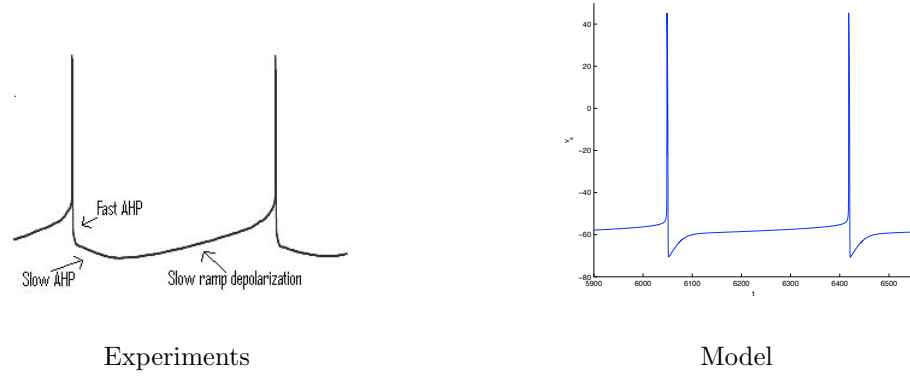


Figure 2.50: Left: two spikes of the left picture in Figure 2.33 zoomed in. Right: two spikes from the model simulation zoomed in.

### Response to depolarizing input

The frequency of the stable limit cycle, which is present in the range  $I_{app} \in [-6, 205.02]$  (on the left side of the region the cycle bifurcates into a homoclinic orbit before it disappears and right the cycle coalesces with an unstable cycle at a fold bifurcation), can be plotted for values of  $I_{app}$  in this region. In Figure 2.51 the model-fI curve is plotted next to an experimental fI curve again.

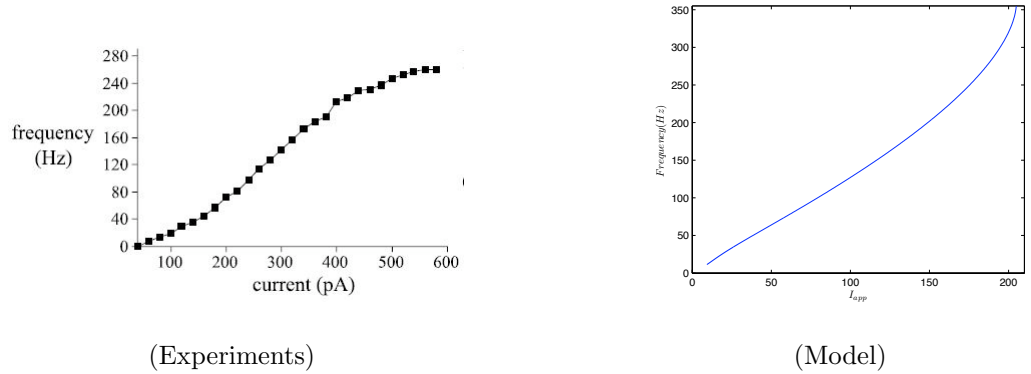


Figure 2.51: The fI-plot from [14] (left) with  $I_{app} < 600$  compared to the fI-plot from model [1] (right) with  $I_{app} < 200$ .

The differences between the model fI-curve and the experimental one are as in Table 2.9:

The first row states that according to experiments applied currents up to  $600 \text{ pA}/\mu\text{m}^2$  can still induce spiking at higher frequencies, whereas the bifurcation analysis of the model showed that right to the LPC and left to the SHOB the stable limit cycle has disappeared, causing the spiking behaviour to be absent

	Experiments	Model
$I_{app}(\text{pA}/\mu\text{m}^2) \in \dots$	$\approx [-6, 205.02]$	$\approx [0, 600]$
Slope of first part (Hz/nA)	500 [14]–900 [13]	$\approx 1350$
Shape curve	Sigmoidal	Inverse sigmoidal

Table 2.9: The differences between the model fI-curve and the experimental fI-curve

outside  $[\text{SHOB}, \text{LPC}] \approx [-6, 205.02]$ . These ranges differ a lot. Approximately the same range of frequencies is traversed for these different ranges of applied current. This results in the large difference in slope of the first part of the curve (up to 200Hz) between the two curves. Up to 200Hz the fI-curve is assumed to be linear. The slopes of these parts are compared in the second row of Table 2.9. Because the asymptotic value of the frequency (plotted in the fI-curve of the model) is in nearly all cases lower than the averaged frequency (plotted in the fI-curve of experiments), due to the high initial frequency, the found asymptotic frequency of approximately 1350 Hz/nA is definitely too large (the translation of this number to the average frequency would even be larger). ‘Only’ the range for  $I_{app}$  seems to differ from experimental results, but unfortunately a ‘simple’ scaling of the parameter  $I_{app}$  will not do the trick. The shape of the model fI-curve is also inverse sigmoidal, showing the steeper parts in the first and third segment, instead of in the second segment. According to various experiments [14, 13] this should be the other way around, a sigmoidal shape. This is mentioned in the third row of the table.

Beside these differences the model fI-curve agrees with literature on other things:

- The model shows an increase in frequency due to an increase in applied current.
- The frequencies which can be reached by the model agree with the frequency ranges described in literature.
- The STN-neuron is able to fire at very low frequencies. Due to the SHOB which occurs around  $I_{app} \approx -6$  the period of the oscillation tends to infinity in close surroundings of this bifurcation value. Extremely low frequencies can therefore be reached. This can also be seen in the fI-curve of the model in Figure 2.51.

Simulations of the model before and during the application of a depolarizing step, show other differences and agreements:

- The voltage range which is traversed during the application of the depolarizing step is clearly smaller than during spontaneous spiking. This contradicts experimental results, which state that this traversed range hardly changes.
- The duration of the AHP which occurs after the application of the step, increases with an increase in strength of the applied step. Whether the increase in AHP is smooth, as claimed in literature, can not be seen from the simulation pictures.
- Spike frequency adaptation seems to occur during the application of the step current, which agrees with experimental results.

### Response to hyperpolarizing input

Experimental results on the response of STN-neurons to hyperpolarizing current steps. Simulations of the model during and after the application of hyperpolarizing current steps show the following results:

- The model shows a decrease in frequency of firing during the application of a small hyperpolarizing current.
- The model-neuron becomes quiescent but does not show rebound bursts after the break of a stronger hyperpolarizing current, which lowers the membrane potential to approximately  $-75$  mV. This voltage agrees with experimental results.
- After the application of an even stronger hyperpolarizing current the model-neuron still becomes quiescent but shows rebound bursts after the break of the step. This rebound burst showed a fast decay after returning to spontaneous spiking.
- Because the rebound bursts did not show a slow decay which would have indicated the generation of a plateau potential, the model seems to represent a STN-neuron which is not able to generate plateau potentials. This is not an error of the model because two types of STN-neurons are indeed present in the nucleus. The plateau-generating neuron on the other hand is the more interesting one for analysis of STN-GPe-networks.
- The bursting during the application of a small hyperpolarizing current, claimed by [15] is not confirmed by the model's behaviour. The model thus follows [16] and [5].

### 2.3.2 Evaluation

Model [1] is a single-compartment model, meaning that the neuron is modelled as a point. This is an assumption made by all HH-models and thus also in the STN-model [11]. Multi-compartment models have been developed for the STN-neuron as well such as the model presented in [27]. Multi-compartment models are of course more accurate because delays between for example the generation of an EPSP in the dendrite of the neuron and the generation of an action potential as a consequence of this EPSP is taken into account. Because multi-compartment models take the spatial component into account, the distribution of the channel-types over the various compartments can be altered, for testing their influence. Because the channels for the low-threshold calcium current  $I_T$  are mainly located in the dendrites of the STN-neuron (the other channels are located in the membrane of the soma), a multi-compartment model could shine a light on the influence of the distance between these channels and the trigger region, on the firing behaviour of the neuron. Multi-compartment models are large, consisting of many spatial derivatives next to time derivatives as well, and because only the low-threshold calcium channels are not present in the soma, the spatial distribution of the channels over the soma-membrane does not make the model that more accurate, that the increase in variables is a small disadvantage compared to that. Multi-compartment models on the other hand are recommendations for future modelling of the STN-neuron, when more information is available on the morphology of the neuron and the density and distribution of the various channels over the membrane. Model [27] gives a good idea for this

multi-compartment modelling. A difference is made between active and passive properties of the STN-membrane.

### Model characteristics

What can be concluded from the previous summary of the results is that the model behaves quite well for the limited number of (gating) variables chosen. It unfortunately represents a STN-neuron which is not able to generate plateau potentials. This does not contradict experimental results because indeed two types of STN-neurons are present in the nucleus. The plateau-generation might be an interesting phenomenon of the STN for further analysis, and could therefore be added to the model as was done in [11].

Especially the characteristics of the spontaneous spiking behaviour agree well with experimental results. Aspects as frequency of spiking and traversed voltage range agree well, except for the slow AHP which misses after the action potential and fast AHP.

For the response of the model to de- and hyperpolarizing steps and pulses it can be said that the parameter  $I_{app}$  mainly needs scaling. The range in which all essential events takes place is simply too small. The hyperpolarizing current which is needed to make the neuron quiescent is too small compared to literature and the depolarizing current which is needed to make the model-neuron fire at for example 300Hz is less than half the current needed in experiments. Beside this scaling problem the response of the model to de- and hyperpolarizing currents largely agrees with literature. The frequency of spiking of the model is able to approach the zero-level due to the saddle homoclinic orbit bifurcation and the frequency of spiking increases with an increase in  $I_{app}$ . The range of frequencies which can be reached by the model agrees as well. For depolarizing input on the other hand the slope of the  $\text{fl}$ -curve is too large (still due to the scaling problem), and the shape of the  $\text{fl}$ -curve is inverse sigmoidal, which contradicts results from experiments. Also the voltage range which is traversed during the application of the depolarizing step is smaller than during spontaneous spiking. According to experiments this range should remain constant. The disappearance of the limit cycle for a certain depolarizing value for  $I_{app}$ , which in the model occurs for  $I_{app} \approx 205 \text{ pA}/\mu\text{m}^2$ , has not been observed in experiments. The quiescence of the neuron for larger values of  $I_{app}$ , shown for the model, is therefore also disputable.

### Model improvement

The model thus mainly shows the right STN-behaviour, but can of course be improved in such a way that the neuron generates plateau potentials, the range for  $I_{app}$  becomes ‘stretched up’, that a slow AHP follows the fast one and that the shape of the  $\text{fl}$ -curve becomes sigmoidal. Each of these improvements could be separate subjects for study where everytime a trade-off must be made between accuracy and simulation time. Besides, some recommendations for modelling can be done but exact methods to for example ‘add a slow AHP’ is not known, and maybe even impossible.

The following changes for the model can be considered:

1. The constant values for various parameters as conductances and equilibrium potentials differ a lot between this model [1] and [11]. The values

for  $I_K$  in [11] are for example derived from [19], which is the only article on the type of channels of the voltage-gated potassium current and therefore quite valuable. The constants in [1] are derived from data-fitting procedures. Thus changing these values can possibly change some characteristics of the model.

2. Currents can be added to the model (with the disadvantage of having a larger and slower model) and the formulae for the currents in the model can be changed. All changes should significantly improve the behaviour of the model, to exceed the disadvantage of the extra variable(s). To really improve the model the possible currents which can be added, should activate and inactivate at the right timescales. When for example the activation is too slow in comparison to the activation of the existing variables, the behaviour of the extra variable is hardly dynamical and can be taken as a constant current. Certain currents can also be active in voltage-ranges which are never reached by the STN-neuron and can therefore be omitted from the model. There can be good reasons why currents have not been added to the model, with the best reason being the increase in complexity of the model, causing an increase in CPU-time while simulating the model. The currents which can be changed or added are:

- Because the model presented in [11] is a plateau-generating one the currents present in that model can be used in this model to add this plateau-generating characteristic. Because the L-type of calcium-current is the most important current for the plateau generation, this current ( $I_L$  in [11]) can replace the existing high-threshold calcium current  $I_{Ca}$ , which was possibly also intended as a L-type of calcium current. Other high-threshold calcium currents as the N-type can be of importance as well. This current is present in model [27] next to the L-type of calcium current.
- A  $\text{Ca}^{2+}$ -dependent inward nonspecific cation current  $I_{Ca_N}$  seems to be present in the STN-membrane and is not present in the model. This current can slow the decay of the plateau potential and therefore influence the duration of it. This current can thus increase the possibility of plateau generation.
- A delayed rectifier potassium current is included in model [27], next to the normal fast rectifier  $I_K$ . Because the timescales for this potassium current are too large for this single-compartment model, this current can not influence the model's behaviour significantly. In a multi-compartment model it can change behaviour.
- The persistent sodium current found in experiments [14] did not seem to influence the important characteristics of the STN-neuron (when blocked, nothing changed). Although this is the case, the persistent sodium current is used in model [27].
- A hyperpolarization-activated cation current  $I_h$  is recorded as well. It seems to generate the depolarization sag during hyperpolarization, thereby increasing the chance of rebound bursting activities after the break of the hyperpolarization. Because the rebound activities are already as they should be (due to  $I_T$  which has the same (in)activation characteristics as  $I_h$ ), this current is not as necessary as other currents. It is used in the model [27].

- The slow part of the AHP should have been present, although other experimental figures as in [11] do not show these slow parts. Because  $I_{AHP}$  ( $I_{Ca-K}$  in [11]) is partly responsible for the slow part of the AHP, the dependency of the current on  $[Ca]_i$  should possibly be altered. The formulation of this current in [11] can also be used.
- During the application of the depolarizing step, in which the frequency increased according to literature, a smaller voltage range was traversed than during spontaneous spiking. This should have been the same. Which current can change this behaviour is not known.
- The transient potassium current  $I_A$  is measured in experiments and needed to have the STN-neuron fire at very low frequencies. Because the model is already able to fire at very low frequencies this current does not need to be added to the model. When complex firing patterns as periodic bursting is proven to occur in STN-neurons alone, this current can be considered as well. At the moment the bursting behaviour of the STN-neuron is discutable.  $I_A$  is included in the model by Otsuka et al. [11] although other activation dynamics are assumed there than given in [20].

### Model comparison

Model [11] also shows a fi-curve with a slope, which is too steep. The range for  $I_{app}$  is too small for the frequency range reached. The slow AHP is also missing, but not necessary for STN-neurons shown with experimental pictures. Model [11] on the other hand is able to generate plateau potentials during and after the application of a current pulse. The inactivation of the L-type of calcium current plays a large role in the plateau generation according to [11]. Although the model [11] has some similar errors with regard to the behaviour of the >stn-neuron, both models can be combined in some way to have the benefits of both. The fi-curve then still needs adjustments with addition and change in currents mentioned above.

[8] discusses the validity of model [9] and [1]. The article questions the usefulness of computational models as a tool to give insight in the Parkinsonian and normal behaviour of the Basal Ganglia. The article does not discuss the validity of the model of the STN-neuron alone but of the model of the total network of the Basal Ganglia described in [9]. According to the article the total model is too complex and not robust with respect to small perturbations in the parameters. Besides, time-delays miss in the model because every neuron is modelled as a point in space and synaptic connections or relay points do not include time delay functions. The models [27] and [1] have been cited rarely according to this article, showing the low scientific importance of models on explaining phenomena in the Basal Ganglia. During testing of the models the authors of [8] experienced the same problems as we did during the testing of the STN-model. Some results mentioned in [9] from the model described in the same article, differed to some degree with the results found during testing by the authors of [8]. We experienced the same type of problems during testing of the STN-model alone. In [1] it is for example claimed that the voltage range which is traversed during the application of a depolarizing step current, is the same as during spontaneous spiking behaviour. This is not the case according to the test of the model with MatCont.

Sensitivity analysis of the STN-model is a recommendation because parameters between this model and [11] already differ so much that the hope is that small perturbations in these parameters (due to the inaccuracy of the values) do not have large effects on the behaviour of the model-neuron. If this somehow *is* the case, the model can give less reliable predictive information and therefore becomes almost useless.

### Model analysis

A general conclusion can be made about the method used to analyse the model, the bifurcation analysis using MatCont. This method can be applied to any model, possibly better than this one, to give a more detailed idea on the behaviour of the neuron in various parameter regions. Provided the accuracy of the analysed model is sufficient, this bifurcation analysis then can give a good idea on the firing behaviour of the STN-neuron in vitro, in response to various amount of input. Because it is a mathematical analysis the physiological reality should be taken into account: the disappearance of a limit cycle at a certain parameter value might not be that instant in real life. The physiological range for  $I_{app}$  should also be checked, because nice mathematical phenomena might occur for values of  $I_{app}$  which will never be reached in vitro. Because MatCont is a program which is still being developed some bifurcation points were missed during continuations. The output of the improved program might be more reliable than the current output. The nice thing about bifurcation analysis is that the analysis can give more insight in the model and that it can be used to change the model. For example a certain transition between spiking and rest exists for the model but is not seen in experiments. By changing the model this bifurcation point can be ‘erased’ or, when needed, moved to a different value of  $I_{app}$ .

## Chapter 3

# The GPe-neuron

The GABAergic external Globus Pallidus (GPe) is a nuclei within the Basal Ganglia, and is innervated by the glutamatergic STN, the GABAergic striatum and the dopaminergic Substantia Nigra pars compacta (SNc). The GPe on its turn inhibits the STN, the striatum and the output nuclei of the Basal Ganglia, the Substantia Nigra pars reticulata (SNr) and the internal segment of the Globus Pallidus (the GPi) [4].

The previous chapter compared the *in vivo/vitro* properties of the STN-neuron with the [1]-model-STN's properties. This section will do the same for the [1]-model-GPe-neuron by first presenting the GPe-model as described in [1] and then comparing the choices made with experimental results for the GPe-neuron, by looking at the bifurcation analysis of the model.

### 3.1 Literature

#### 3.1.1 Experimentally found results

Unfortunately less is known for the GPe- neuron, resulting in a much shorter GPe-discussion compared to the one for the STN-neuron. Beside the little information available on the GPe-neuron the few published articles also often give contradictory information. The possible reasons for these discrepancies between articles can be found in [12] and were already listed at the beginning of Section 2.1.1. Another disadvantage is that the GPe-model presented in [1] is the *only* mathematical GPe-model at the moment, so a comparison between models as was done for the STN-neuron, is not possible here.

On some aspects of GPe-neurons the different articles are very clear. Certain neuron types are for example encountered far more often during experiments than others and are therefore 'typical' GPe-neurons. These neurons also project to the STN and other nuclei within the Basal Ganglia (in comparison to interneurons which do not) and are able to burst in some cases. The latter is necessary for the GPe-neurons because they appear to be the cause of the rebound bursting in STN-neurons [28]. The bursting of GPe-neurons is not essential for rhythmic population activity though [1].

According to [1] the model-GPe-neuron matches the characteristics of three types of GPe-neurons described in different articles, which are similar in a lot of characteristics. Different neurons belong to a type based on their electrophysi-

ological properties (instead of for example their morphological properties). The three types are the *type 2* described in [29], the type A described in [12] and the repetitive firing neuron described in [28]. The reader is referred to these articles for the definitions of these types. Only 37% of the tested neurons were of this type according to [29]. In [12] this was 63% and more than 70% in [28]. Looking at these numbers, the choice for this type of GPe-neuron as the ‘typical’ GPe-neuron in the [1]-model seems justified. The three articles also found two other types. These were often assumed to be interneurons which do not project to other nuclei in the Basal Ganglia, or cholinergic neurons. The characteristics of this ‘typical’ GPe-neuron are described below. When the three types differ too much on a certain aspect, it will be noted.

### Spontaneous spiking

The ‘typical’ GPe-neuron seems to be able to spontaneously spike. The characteristics of this spiking behaviour are somewhat uncertain:

- The resting membrane potential of the neuron is  $-59 \pm 9$  mV [29].
- In vitro the neuron fires spontaneously at the resting membrane potential [29, 12, 30]. The neuron can be quiescent as well at resting membrane potential [12].
- The firing frequency during spontaneous spiking is approximately 200 Hz according to [29]. This is a significant difference with the 2–40 Hz mentioned in [28] supported by the 10–15 Hz claimed in [30].
- The GPe-neuron is also able to autonomously discharge at high-frequency, interrupted by pauses [12, 30]. According to [30] this can only occur in vivo at resting membrane potential. According to [12] it only occurs during the application of weak hyperpolarizing currents and is very common in fast-spiking neurons such as interneurons so not in projection neurons we consider.
- The afterhyperpolarization consists of a fast and a slow part [28, 12].
- A slow depolarization occurs after the AHP [28]. Mathematically this slow depolarization means that the trajectory follows the separatrix of a saddle, stays close to the saddle for a while after eventually converging to the stable cycle [3].
- When the membrane is depolarized, sodium-dependent subthreshold oscillations occur with a frequency of 20–100 Hz [29].

### Depolarizing input

The reaction of this type of GPe-neuron to depolarizing current injections are:

- The neuron fires in frequencies up to 350 Hz [12]. According to [28] the maximum firing rate is only about 100 Hz because of the occurrence of spike accommodation. The fI curve looks as in Figure 3.1.
- Spike accommodation occurs according to [28], which is contradicted by [30].
- Spike frequency adaptation occurs [28].
- When the membrane is kept at a hyperpolarized level it reacts to de- and hyperpolarizing input in a ramp-like manner [28].

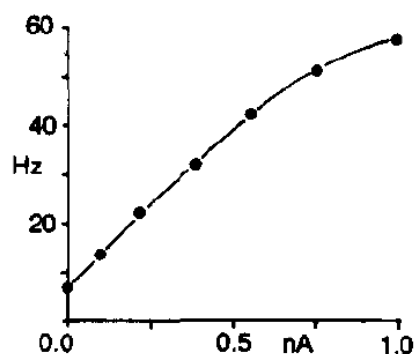


Figure 3.1: The firing frequency of the repetitively firing neuron as a function of the input [28]

### Currents

The following currents are described for the ‘typical’ GPe-neuron:

- A low-threshold calcium current ( $I_T$ ) is present [29, 12].
- A voltage-dependent inward rectifier ( $I_h$ ) is observed [12].
- Fast and slow  $\text{Ca}^{2+}$ -dependent  $\text{K}^+$ -currents have been identified. These cause the slow and fast parts of the afterhyperpolarization [28].
- A slowly in- and deactivating delayed rectifier  $\text{K}^+$ -current has been recorded in the GPe-neuron. Also a rapidly deactivating  $\text{K}^+$ -current is present. The ratio between the number of fast deactivating channels and slowly deactivating ones is approximately 1.5 [31].
- Two types of A-type potassium currents have been observed: a low- and high-threshold one [31].
- Slowly deactivating hyperpolarization-activated cation channels (HCN) are important for the discharge rate and the regularity of autonomous firing. The currents have a fast and slow component, due to two different channels. The currents are activated by striatal inhibition which takes place at the GPe-dendrites and reset the rhythmic discharge. The currents are activated during the foot of  $\text{Na}^+$ -activation curve (around -55 mV in GPe-neurons) therefore prohibiting the sodium-current to become inactive [30].

### Synaptic connections

In experiments the amount of GPe-neurons innervated by other nuclei have been tested. Also the number of GPe-neurons which send their axons to these nuclei have been counted. The results can be of use for the analysis of the possible architecture of the STN-GPe-network.

The results are as follows: 75% of the GPe-neurons are innervated by STN-neurons and half of the GPe-neurons send their axons to STN-neurons. These neurons had latencies of STN-stimulation of only 1 ms, which agrees with the fast inhibition of STN-neurons by GPe-firing. One third of the GPe-neurons are inhibited by striatal input. This specific inhibition is capable of resetting the pacemaking mechanism in GPe projection neurons [28].

### 3.1.2 The GPe-model

The GPe-model is as follows [1]:

$$C_m \dot{v}_g = -I_L - I_K - I_{Na} - I_T - I_{Ca} - I_{AHP} - I_{S \rightarrow G} \quad (3.1)$$

As one can see the GPe-model (3.1) is similar to the STN-model discussed in the previous chapter. (3.1) differs somewhat from the original GPe-model described in [1]. The additional current  $I_{G \rightarrow G}$ , present in [1], has been omitted in (3.1) because in this small network no input from other GPe-neurons is taken into account (see Figure 4.1). Also the input from the striatum (in the article called  $I_{app}$ ) to the GPe-neuron, as included in the original model is left out. The reason for this is that all external input (such as input from the striatum) to the two-cell network is ignored for the moment (see Figure 4.1). The reduced GPe-model (3.1) includes the same type of currents (and thus equations) as the STN-model, which together influence the dynamics of the GPe-neuron's membrane potential. Beside the agreements between the type of currents included, the constant variables as for example conductances, half-activation voltages and timeconstants differ of course.

$I_{S \rightarrow G}$  has exactly the same form as  $I_{G \rightarrow S}$ , with appropriately renamed synaptic parameters. As was done for the STN-model for the further analysis the synaptic current  $-I_{S \rightarrow G}$  is replaced in the model by an applied current  $+I_{app}$ . See the text above (2.5) for the explanation of this replacement. Model (3.2) will be analysed in Section 3.2.

$$C_m \dot{v}_g = -I_L - I_K - I_{Na} - I_T - I_{Ca} - I_{AHP} + I_{app} \quad (3.2)$$

From all the currents in (3.2) only  $I_T$  takes a simpler form than in the STN-model. The formula for  $I_T$  becomes:

$$I_T = g_T a_\infty^3(v_g) r (v - v_{Ca})$$

Comparing this  $I_T$ -equation with (2.2d) it is clear that no 'inactivation *function*' but just the inactivation *variable*  $r$  is included. According to [1] this choice reduces the posthyperpolarization rebound in GPe-cells compared to the rebound in STN-cells. Whether reducing rebound bursting in GPe-neurons and assuming the similarity between the models for two different neurons, is justified, is now discussed.

## 3.2 Analysis

This section analyses the GPe-model using MatCont for the bifurcation analysis, just as was done for the STN-model. First the equilibrium bifurcations will be sought, and possible Hopf-bifurcations will be analysed further in the section on limit cycle bifurcations of the GPe-system. Because the GPe-system also has one parameter ( $I_{app}$ ) and five coordinates ( $v_g$ ,  $n_g$ ,  $h_g$ ,  $r_g$  and  $[Ca]_{i_g}$ ) the possible equilibrium and limit cycle bifurcations are the same codim-1 bifurcations as mentioned in the beginning of Section 2.2.1. The center manifold theorems still need to be applied to derive the dimension of the center manifold on which all essential events of the bifurcation occur. See the beginning of Section 2.2.1 for more details. The aim is to give a detailed division of the parameter line for

$I_{app}$ , such that the behaviour of the model-GPe-neuron can be predicted within the different regions for  $I_{app}$ . Some simulations will be made as well, to compare certain characteristics of the model's behaviour with experimental results.

### 3.2.1 Bifurcation analysis

#### Bifurcations of equilibria

The GPe-system is in an equilibrium state when the five time derivatives of the coordinates are equal to zero. This means that the three gating variables  $n_g$ ,  $h_g$  and  $r_g$  are at their steady states  $n_{\infty_g}(v_g)$ ,  $h_{\infty_g}(v_g)$  and  $r_{\infty_g}(v_g)$ . For  $[Ca]_{i_g}$  in an equilibrium the following must hold (the derivation is analogous to the derivation for  $[Ca]_{i_s}$ , see Section 2.2.1):

$$[Ca]_{i_g} = \frac{I_T + I_{Ca}}{k_{Ca}}$$

Where  $I_T$  and  $I_{Ca}$  are at their equilibrium levels (with the gating variables at their steady states and  $v_g$  as the independent variable).

With the three gating variables and the internal calcium concentration at their constant levels, the potential's time derivative also needs to be equal to zero in an equilibrium. This then gives an equation for the applied current  $I_{app}$  as a function of  $v_g$  (for the derivation again see Section 2.2.1) (3.3):

$$I_{app} = I_L + I_K + I_{Na} + I_T + I_{Ca} + I_{AHP} \quad (3.3)$$

With again the currents only dependent on  $v_g$ , because for the other four variables their constant values are substituted in  $I_T$  and  $I_{Ca}$ .

Plotting (3.3) gives the equilibrium-curve of the model-GPe-neuron and is shown in Figure 3.2.

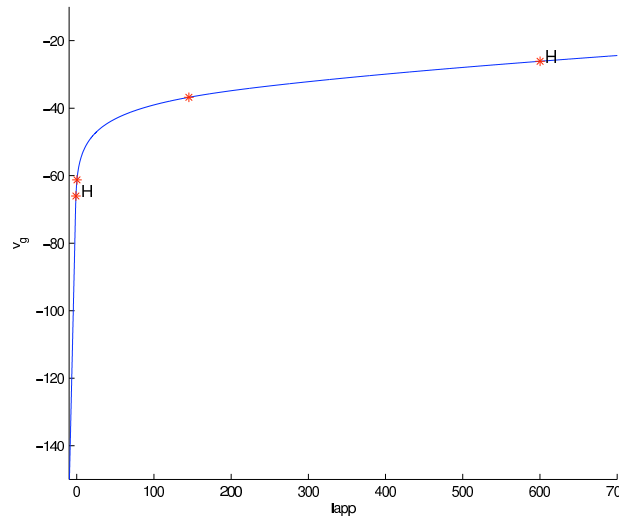


Figure 3.2: The monotonic equilibrium curve with a sub- and supercritical Hopf-bifurcation. Notice the steep increase in  $v_g$  for  $I_{app}$  around zero.

As can be seen the equilibrium curve, projected on the 2D  $I_{app}, v_g$ -space, is monotonically increasing for increasing  $I_{app}$ . This means that limit point bifurcations are not possible (as was possible for the STN-neuron). The only codim-1 equilibrium bifurcations possible are therefore the Andronov-Hopf bifurcations, and both types are indeed found.

The bifurcations found by MatCont during the drawing of the equilibrium curve are listed in Table 3.1. Here  $H_1$  corresponds to the point with the letter ‘H’ most left in Figure 3.2 and  $H_2$  to the point with the letter ‘H’ most right in the figure. The other points indicated in the figure are neutral saddles (in these points the sum of two eigenvalues is zero), and are not bifurcation points.

	$v_g$	$n_g$	$h_g$	$r_g$	$[Ca]_{i_g}$	$I_{app}$	L. coeff	$\omega_0$
$H_1$	-66.03	0.241	0.661	0.121	1e-6	-1.031	7.923e-3	0.173
$H_2$	-26.10	0.847	0.066	0.000	1.071	6.000e+2	-1.159e-2	4.979

Table 3.1: The equilibrium bifurcations of the GPe-model

For  $H_1$  the Lyapunov coefficient  $l_1 > 0$  which corresponds to a subcritical Hopf-bifurcation. For decreasing  $I_{app}$  (the equilibrium was continued by MatCont for decreasing parameter values) the unstable focus regains its stability while simultaneously an unstable limit cycle appears. Thus for  $I_{app} > -1.031$  an unstable focus is present and for  $I_{app} < -1.031$  a stable focus and an unstable limit cycle coexist.

Because for  $H_2$  the Lyapunov-coefficient  $l_1 < 0$ , a supercritical Hopf-bifurcation takes place there. For decreasing  $I_{app}$  this means that a stable focus turns unstable while a stable limit cycle emerges. Thus for  $I_{app} > 600$  a stable focus is present, which is unstable for  $I_{app} < 600$ . For  $I_{app} < 600$  a stable limit cycle is present next to the unstable focus.

In Figure 3.3 the real parts of the five eigenvalues of the system in the equilibrium are plotted for  $I_{app} \in [-10, 1000]$  pA/ $\mu\text{m}^2$ .

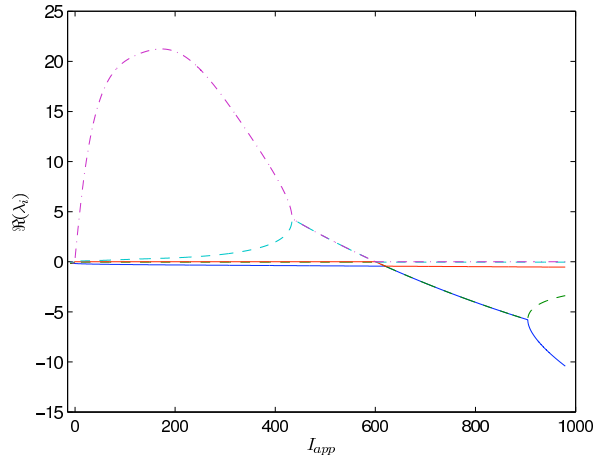


Figure 3.3: The real part of the five eigenvalues of the system at the equilibrium are plotted for  $I_{app} \in [-10, 1000]$  pA/ $\mu\text{m}^2$ .

It is already clear from this figure that a supercritical Hopf-bifurcation takes

place around  $I_{app} \approx 600 \text{ pA}/\mu\text{m}^2$ . This is even more clear when this region is zoomed-in as has been done in Figure 3.4.

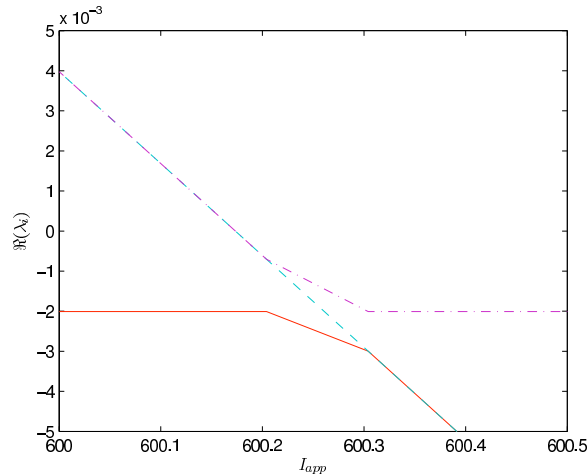


Figure 3.4: Around  $I_{app} = 600$  a supercritical Hopf-bifurcation takes place: the focus becomes stable for increasing  $I_{app}$ . Compare with Figure 3.5.

In Figure 3.5 the parameter region around  $H_1$  is focused on where it is clear that the stable focus loses its stability for *increasing* values of  $I_{app}$ .

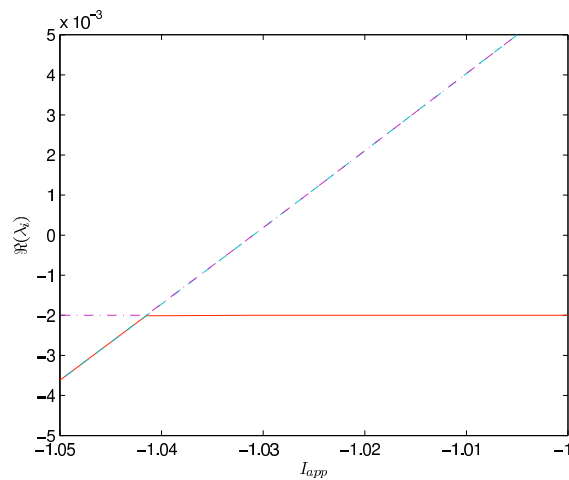


Figure 3.5: Around  $I_{app} = -1.031$  a subcritical Hopf-bifurcation takes place: the focus loses its stability for increasing  $I_{app}$ . Compare with Figure 3.4.

Not only the real part of the eigenvalues should be zero at the Hopf-bifurcation but the imaginary parts of the eigenvalues should be nonzero at the bifurcation point. When these conditions are both satisfied the eigenvalues are purely imaginary at the bifurcation point and a Hopf-bifurcation indeed occurs. In Figure 3.6 the imaginary parts of the five eigenvalues of the system at the equilibrium are plotted. The vertical lines around  $I_{app} = 600 \text{ pA}/\mu\text{m}^2$  are caused by the lack of

arrangement of the five eigenvalues within Matlab, and should be ignored by the reader. It is then clear that around  $I_{app} = 600 \text{ pA}/\mu\text{m}^2$  at least two eigenvalues are imaginary and because the real parts of these two eigenvalues become zero at this point, the eigenvalues are purely imaginary for a specific value of  $I_{app}$ .

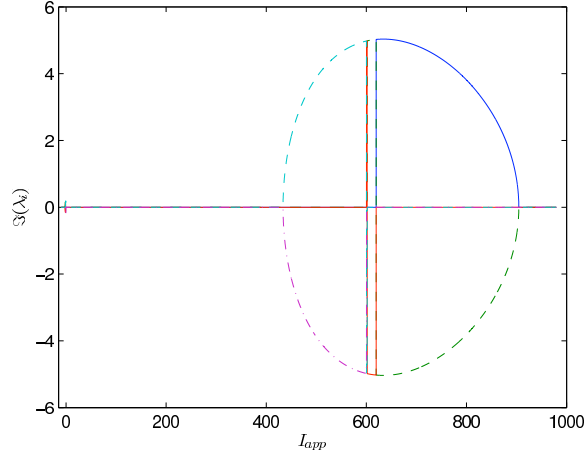


Figure 3.6: The imaginary parts of the five eigenvalues: around the second Hopf-bifurcation the eigenvalues are indeed not all real.

The same can be seen in Figure 3.7 for the imaginary parts of the five eigenvalues around  $I_{app} = -1.031 \text{ pA}/\mu\text{m}^2$ . The vertical lines can be ignored for the same reasons as mentioned above. The imaginary parts of at least more than two eigenvalues are indeed nonzero around the bifurcation value.

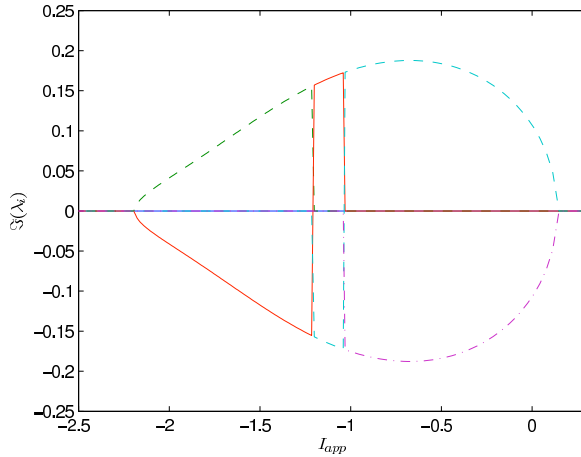


Figure 3.7: The imaginary parts of the eigenvalues around  $H_1$ : the eigenvalues are indeed not all real.

For the equilibrium it can be said in which regions of  $I_{app}$  the equilibrium is stable: for  $I_{app} < H_1 \approx -1.031 \text{ pA}/\mu\text{m}^2$  the focus is stable and becomes a stable *node* for  $I_{app}$  approximately smaller than  $-2.2 \text{ pA}/\mu\text{m}^2$  (see Figure 3.7). For  $I_{app} \in [H_1, H_2] \approx [-1.031, 600] \text{ pA}/\mu\text{m}^2$  the equilibrium is unstable. Close

to the two Hopf-points the equilibrium is an unstable focus (see Figure 3.6 and 3.7), but in the area in between, the equilibrium is an unstable node. For  $I_{app} > H_2 \approx 600 \text{ pA}/\mu\text{m}^2$  a stable focus is present which becomes a stable node around  $I_{app} \approx 900 \text{ pA}/\mu\text{m}^2$ . The area  $I_{app} \in [H_1, H_2]$  in which the system only has an unstable equilibrium is large. The GPe-neuron will therefore not be quiescent for a large range of applied current. For a very large applied current and for hyperpolarizing current stronger than approximately  $-1 \text{ pA}/\mu\text{m}^2$  the neuron *is* quiescent though. Because  $0 \in [H_1, H_2]$  and a stable limit cycle is present in this range as well, the model-neuron will indeed spontaneously spike which agrees with experimental results for the types of GPe-neurons represented by the model.

### Bifurcations of limit cycles

In this section the limit cycles, unstable and stable, emerging from the two Hopf-points found in the previous section will be continued by MatCont. Limit cycle bifurcations found during the continuation process will be listed and discussed. For the possible codim-1 limit cycle bifurcations see the beginning of Section 2.2.1. From the two global bifurcations only a saddle homoclinic orbit bifurcation (SHOB) is possible. A saddle-node on invariant circle bifurcation (a SNIC) is not possible due to the monotonic character of the equilibrium curve of the GPe-model.

Unfortunately both continuation processes became unreliable in the neighbourhood of the steep part of the equilibrium curve (see Figure 3.2). The stable limit cycle, which emerges from the Hopf-point around  $I_{app} \approx 600 \text{ pA}/\mu\text{m}^2$  remains stable up to at least  $I_{app} \approx 0 \text{ pA}/\mu\text{m}^2$  but during the continuation for negative  $I_{app}$  the multipliers of the limit cycle oscillate too much, to really trust the result. The multiplier, which should remain 1 during the continuation, begins oscillating extremely around  $I_{app} \approx 0 \text{ pA}/\mu\text{m}^2$ , even with a large decrease in stepsize. Unfortunately a possible change in stability or disappearance of the stable limit cycle can therefore not be known for certain.

The 1D unstable limit cycle emerging from the Hopf-point around  $I_{app} \approx -1.031 \text{ pA}/\mu\text{m}^2$  bifurcates to a 2D unstable limit cycle at a limit point of cycles (a turning point). This unstable cycle approaches the steep part of the equilibrium curve from the opposite side than the stable limit cycle did. The continuation of this 2D unstable limit cycle becomes unreliable close to the equilibrium curve as well, as the multipliers of the fixed point of the Poincaré map corresponding to the cycle, start to oscillate extremely.

The results which can be trusted will be listed here, and guesses about possible global bifurcations will be drawn. At the end of this section limited conclusions will be drawn on the behaviour of the model-GPe-neuron in the different regions of the 1D  $I_{app}$ -space.

#### CONTINUATION OF $H_1$

In Table 3.2 the limit cycle bifurcations are listed, which were found by MatCont during the continuation of the *first* Hopf-point ( $H_1 \rightarrow I_{app} \approx -1.031 \text{ pA}/\mu\text{m}^2$ ). The first LPC is found for increasing  $I_{app}$  and corresponds to the disappearance of the limit cycle at the Hopf-point. The second is a *real* turning point. At this LPC the 1D unstable limit cycle becomes 2D unstable. Mathematically it is a nice phenomenon but physiologically the solution of the system will

not change drastically. The neuron will still be attracted to either the stable equilibrium present in this range ( $v_g \approx -66.87$  mV), or the stable limit cycle originated around  $I_{app} = 600$  pA/ $\mu\text{m}^2$ , which is possibly still present around  $I_{app} \approx 0$  pA/ $\mu\text{m}^2$ . The latter will be discussed in the next section on the continuation of  $H_2$ .

Type	$I_{app}$	Period (ms)	Normal form coeff.
LPC	-1.030974	36.236	0.30605
LPC	-1.1698	51.64	1.659e-2

Table 3.2: The limit cycle bifurcations found during the continuation of  $H_1$ .

In Figure 3.8 and 3.9 the maximum and minimum values for the membrane potential  $v_g$  are plotted for a very small region of  $I_{app}$  in which the essential events near the LPC take place. The LPC is clearly a turning point. The 2D and 1D unstable limit cycles coalesce for decreasing parameter values and disappear.

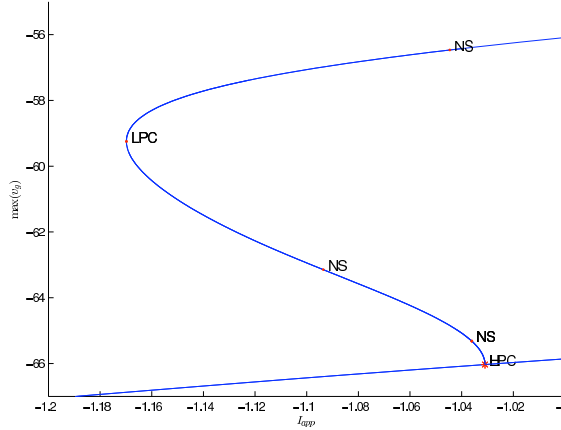


Figure 3.8: The maximum value of  $v_g$  for the two unstable limit cycles around  $I_{app} = -1$  pA/ $\mu\text{m}^2$ .

For  $I_{app} > -1$  pA/ $\mu\text{m}^2$ , when the limit cycle approaches the steep part of the equilibrium curve, the results become unreliable. The difficulty during the calculation could indicate that the limit cycle will become a homoclinic orbit with a saddle on the equilibrium curve. This guess is strengthened by the sharp corner in the limit cycle, which is present close to the equilibrium curve (see Figure 3.10). This then would indicate a SHOB. As can be seen in Figure 3.10 the corner in the limit cycle, at which the saddle will be located, lies on the top half of the cycle.

Figure 3.10 was plotted for  $I_{app} \approx -1.07$  pA/ $\mu\text{m}^2$ . This is on the left side of the equilibrium curve. The equilibrium value for this value of  $I_{app}$  therefore lies on the stable part of the equilibrium curve, ‘below’  $H_1$ . The value of the equilibrium is  $(v_g, n_g) = (-66.26, 0.2384)$ . This point lies below the corner of the limit cycle (see Figure 3.10). With a further increase in  $I_{app}$  the corner will approach this equilibrium, because the equilibrium curve is monotonically increasing. At a certain point the equilibrium will be ‘above’  $H_1$  and therefore unstable. The corner will not move too much as can be seen in Figure 3.13

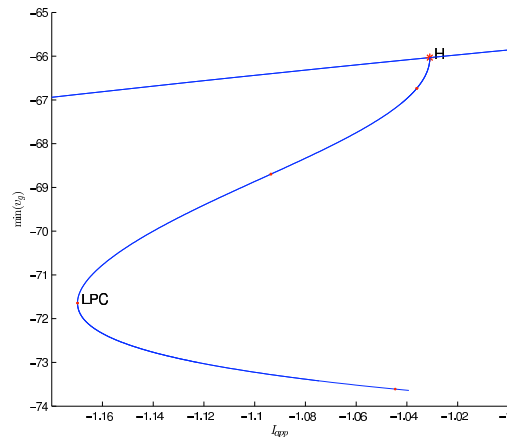


Figure 3.9: The minimum value of  $v_g$  for the two unstable limit cycles around  $I_{app} = -1 \text{ pA}/\mu\text{m}^2$ .

from the slow increase in maximum value of  $v_g$  (the corner is at the maximum value). My guess is that a SHOB will take place close to, but ‘above’,  $H_1$ . The limit cycle is then right to the steepest part of the equilibrium curve, thus for  $I_{app} > -1.031 \text{ pA}/\mu\text{m}^2$  ( $H_1$ ). Further analysis needs to be done to verify this.

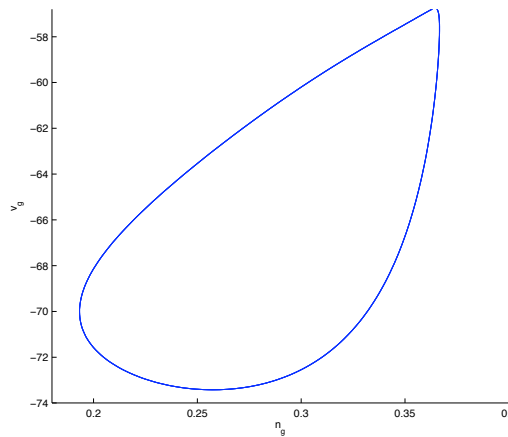


Figure 3.10: The shape of the last reliable 2D limit cycle (for  $I_{app} \approx -1.07 \text{ pA}/\mu\text{m}^2$ ) could indicate that the limit cycle will bifurcate into a homoclinic orbit: a SHOB.

In Figure 3.11 and 3.12 the period and frequency of the two unstable limit cycles, circling around each other, are plotted for the same small range of  $I_{app}$ . In Figure 3.11 the curve beneath the LPC corresponds to the 1D unstable limit cycle, which bifurcated directly from  $H_1$  and the top curve to the 2D unstable limit cycle. The top curve is the most interesting one because the period should tend to infinity when near the SHOB. Unfortunately this task has not been succeeded yet, due to numerical errors. To be sure a SHOB indeed occurs, the

period curve needs to be extended.

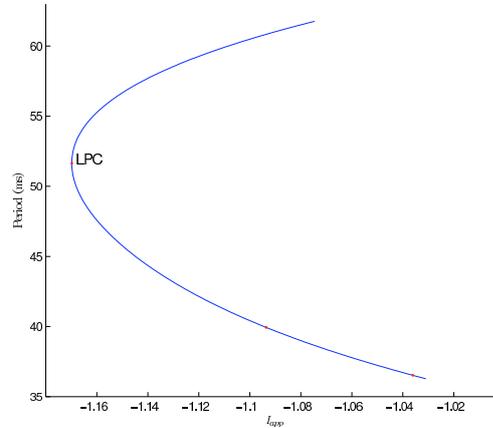


Figure 3.11: The period of the two unstable limit cycles around  $I_{app} = -1 \text{ pA}/\mu\text{m}^2$ . Beneath the LPC corresponds to the period of the 1D unstable limit cycle and above the LPC to the 2D unstable one.

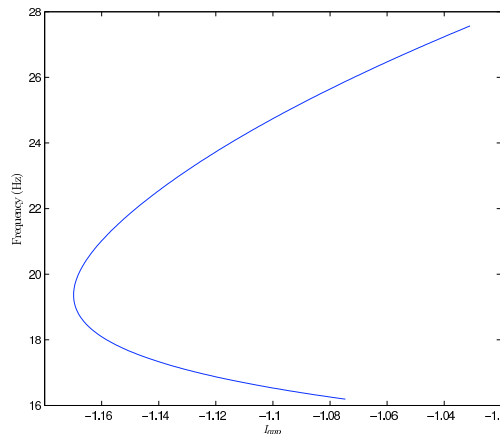


Figure 3.12: The frequency of the two unstable limit cycles around  $I_{app} = -1 \text{ pA}/\mu\text{m}^2$ . The top-curve corresponds to the frequency of the 1D unstable limit cycle and the lower curve to the 2D unstable one.

The frequency thus decreases for both cycles and the frequency of the 2D unstable cycle is smaller than that of the 1D unstable one. Therefore the top-curve in Figure 3.12 corresponds to the 1D unstable cycle and the lower curve to the 2D unstable one. With a SHOB the frequency should approach 0 Hz when near the bifurcation point. The fl-curve thus needs to be extended to find out whether such a bifurcation takes place.

#### CONTINUATION OF $H_2$

The Hopf-point around  $I_{app} = 600 \text{ pA}/\mu\text{m}^2$  gives rise to a stable limit cycle. During the continuation of this cycle, no bifurcations were found. When the

cycle, circling around the top-branch of the equilibrium curve, approaches the more vertical part of the curve ( $I_{app} \approx 0 \text{ pA}/\mu\text{m}^2$ ) MatCont has trouble continuing the cycle. For negative values of  $I_{app}$  the results are therefore unreliable. This is unfortunate while this region is the most interesting one, for a possible bifurcation of the stable limit cycle.

During the continuation only two branching points of cycle (BPC) were found. See Table 3.3 for the values.

Number BPC	$I_{app}$	Period (ms)
BPC <sub>1</sub>	562.6	1.447
BPC <sub>2</sub>	525.4	1.522

Table 3.3: The values of the branching points of cycle.

Branching points are not bifurcation points but are points found during the continuation process and indicate that the curve satisfying the continuation problem intersects itself. See chapter 10 in [32] for more information.

In Figure 3.13 and 3.14 the maximum and minimum values of  $v_g$  are plotted for  $I_{app} \in [0, 600] \text{ pA}/\mu\text{m}^2$ . The values are of the stable limit cycle emerging for decreasing  $I_{app}$  around  $I_{app} = 600 \text{ pA}/\mu\text{m}^2$ . As can be seen in Figure 3.14 the curve ‘stops’ very near the steep part of the equilibrium curve. After this point the part of the curve drawn by MatCont cannot be trusted, as the multiplier, which should stay close to 1 at all times, begins to oscillate extremely. Unfortunately this problem is not yet solved.

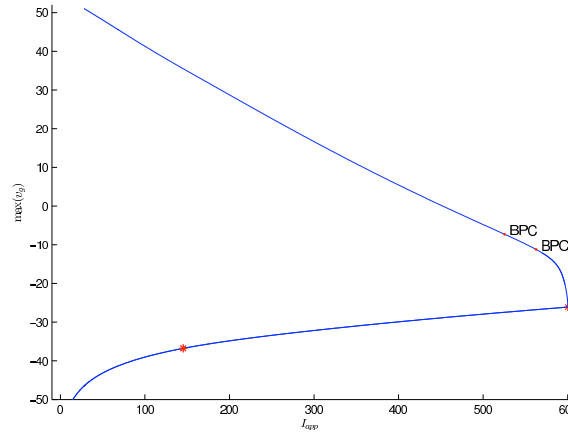


Figure 3.13: The maximum value for  $v_g$  of the stable limit cycle which emerges from the Hopf-point around  $I_{app} = 600 \text{ pA}/\mu\text{m}^2$ .

As for  $H_1$  a disappearance of the cycle through a SHOB needs to be considered. In Figure 3.15 the stable limit cycle is drawn for  $I_{app} \approx -0.39 \text{ pA}/\mu\text{m}^2$ , and a sharp corner can be seen, at  $(v_g, n_g) \approx (-70, 0.2)$ . The cycle is still on the right side of the equilibrium curve because the equilibrium values for  $v_g$  and  $n_g$  when  $I_{app} = -0.39 \text{ pA}/\mu\text{m}^2$  are  $-63.2 \text{ mV}$  and  $0.2803$  respectively located left to the corner. For a decrease in  $I_{app}$  the equilibrium will decrease as well, and very fast due to the steep decay. For the SHOB to actually occur the coalescence between the equilibrium and the cycle, needs to occur for  $v_g > -66 \text{ mV}$  ( $H_1$ )

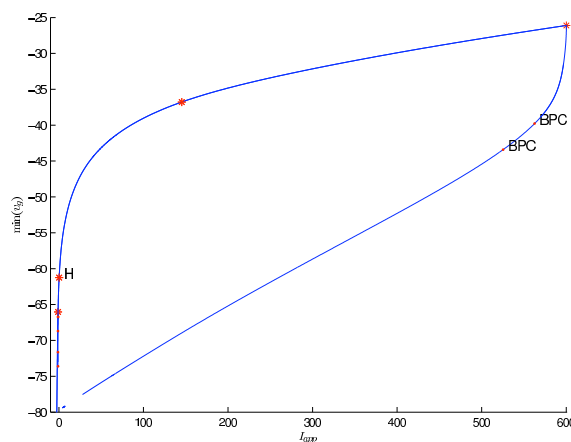


Figure 3.14: The minimum value for  $v_g$  of the stable limit cycle which emerges from the Hopf-point around  $I_{app} = 600 \text{ pA}/\mu\text{m}^2$ .

and therefore, due to the steepness of the equilibrium curve, has to take place after a very short decrease in  $I_{app}$ . The values of  $v_g$  and  $n_g$  of the corner then also need to increase a bit. The limit cycle is then still on the right side of the steepest part of the equilibrium curve. Whether these conditions are all met needs to be tested but all signs point to a SHOB.

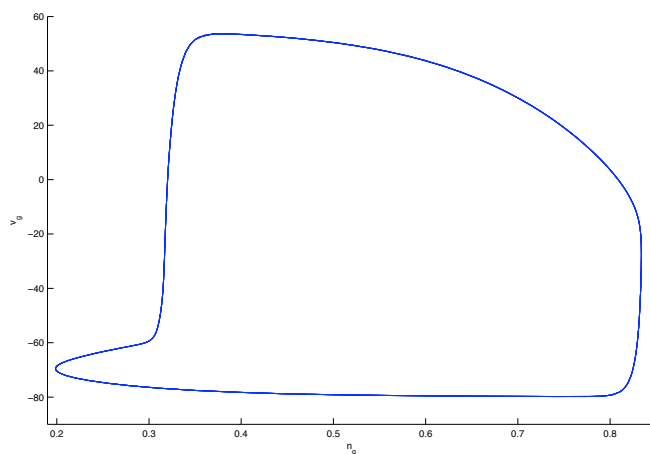


Figure 3.15: The stable limit cycle for  $I_{app} \approx -0.39 \text{ pA}/\mu\text{m}^2$ . A sharp corner near the unstable equilibrium  $(v_g, n_g) = (-63.2, 0.2803)$  could indicate the nearness to a SHOB.

In Figure 3.16 and 3.17 the period and frequency of the stable limit cycle are plotted for  $I_{app} \in [0, 600] \text{ pA}/\mu\text{m}^2$ . An almost linear fit-curve can be seen. Because the period of the stable limit cycle seems to decrease exponentially for increasing  $I_{app}$ , this could as well as the sharp corner, indicate the presence of a SHOB in the neighbourhood of  $I_{app} = -1$ . The presence of a SHOB is a guess and has not (yet) been shown by MatCont because around  $I_{app} = -1$  the output of

MatCont became unreliable.

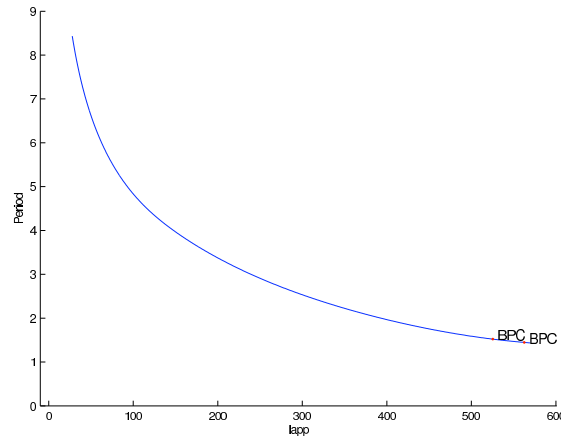


Figure 3.16: The period (in ms) of the stable limit cycle which emerges from the Hopf-point around  $I_{app} = 600 \text{ pA}/\mu\text{m}^2$ . The exponential decrease in period of the cycle for increasing  $I_{app}$  could indicate the presence of a SHOB around  $I_{app} = 0$ .

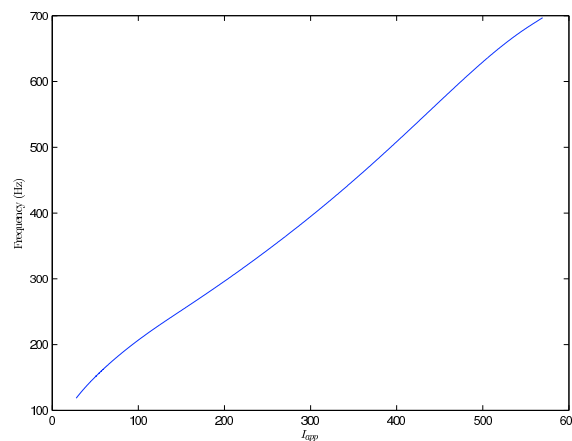


Figure 3.17: The frequency (in Hz) of the stable limit cycle which emerges from the Hopf-point around  $I_{app} = 600 \text{ pA}/\mu\text{m}^2$ . An almost linear relation between the frequency and the applied current is present.

It is also possible that the stable limit cycle and the 2D unstable limit cycle will meet, because both SHOB's occur close to, and above,  $H_1$ .

### Qualitatively different parameter regions

Some guesses can be made on the model's behaviour in the various regions, although the two saddle homoclinic orbits are not verified yet. Assuming these two SHOB's *do* occur, the model-neuron will behave as in the following list. The abbreviations correspond to the ones in Figure 3.18:  $H_1$  and  $H_2$  are the

Hopf-points, LPC the limit point of cycles for the unstable limit cycle, SHOB<sub>*i*</sub> the SHOB for the limit cycle emerging from  $H_i$ . In the figure the SHOB's are located randomly in the interval  $[H_1, \text{SHOB}_2] \approx [-1.031, -0.39] \text{ pA}/\mu\text{m}^2$ . Only when the neuron behaves qualitatively different this will be noted as a different region.

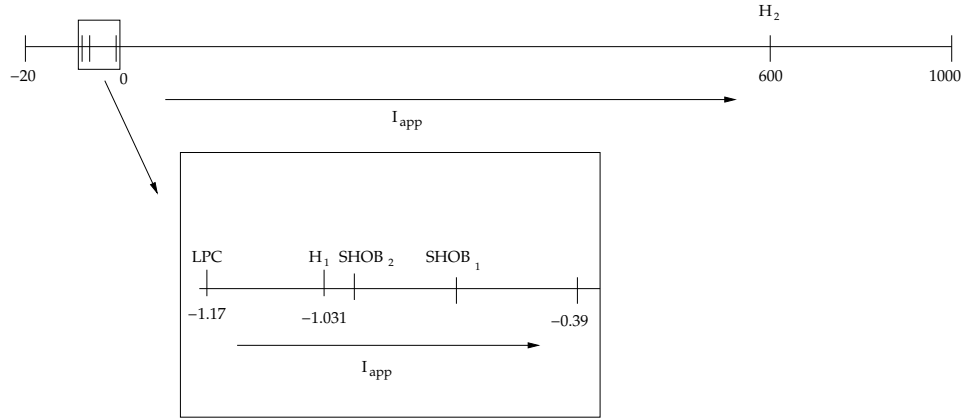


Figure 3.18: The different bifurcations for the GPE-model indicated on the parameter ( $I_{app}$ ) line. The SHOB-bifurcations are not verified yet. These bifurcations give rise to four, possibly three qualitatively different regions for the model-neuron.

1. For  $I_{app} < H_1 \approx -1.031 \text{ pA}/\mu\text{m}^2$  the neuron will be quiescent due to the presence of the stable equilibrium. For the subregion  $I_{app} \in [\text{LPC}, H_1] \approx [-1.17, -1.031] \text{ pA}/\mu\text{m}^2$  a 1D and a 2D unstable limit cycle are present next to the equilibrium. A possibly slower convergence to the stable equilibrium can be seen in this region, but the neuron will still become quiescent.
2. For  $I_{app} \in [H_1, \text{SHOB}_2]$  where the location of the SHOB-bifurcation of the stable limit cycle ( $\text{SHOB}_2$ ) is still uncertain, no stable state is present (right to  $H_1$  the equilibrium is unstable and the stable limit cycle has disappeared through  $\text{SHOB}_2$ ). This is physiologically unreasonable, meaning that this region should be very small and the SHOB-bifurcation of the stable limit cycle should be located very close to  $H_1$ .
3. For  $I_{app} \in [\text{SHOB}_2, H_2]$  ( $H_2$  corresponds to  $I_{app} \approx 600 \text{ pA}/\mu\text{m}^2$ ) the neuron will spike due to the presence of the stable limit cycle. The equilibrium is unstable in this range.
4. For  $I_{app} > H_2 \approx 600 \text{ pA}/\mu\text{m}^2$  the neuron is quiescent due to the disappearance of the stable limit cycle at the Hopf-point and the regaining of stability by the equilibrium.

### 3.2.2 Simulations

This section will shortly compare some results described in Section 3.1.1 with the same type of results for the GPE-model. As was described in the previous section for  $I_{app} = 0$  only a stable limit cycle is present thus the GPE-neuron will

indeed spontaneously spike. This agrees with experimental results. The characteristics of the model's spontaneous spiking behaviour will be compared with the characteristics observed during experiments. Also the reaction of the model-GPe-neuron to depolarizing input, represented in the fl-curve of the model, will be compared with the one given in [28].

The equilibrium corresponding to  $I_{app} = 0$  (the resting membrane potential RMP) is approximately  $v_g = -62$  mV. This agrees with the resting membrane potential of  $v_g = -59 \pm 9$  mV [29].

In Figure 3.19 and 3.20 a time diagram is shown for  $v_g$  with the initial data chosen as in Table 3.4. Figure 3.20 is a zoom-in of Figure 3.19. As can be seen in Figure 3.19 the initial point is far away from the stable limit cycle, because the convergence to the stable limit cycle is initially slow, and speeds up while approaching the cycle. In Figure 3.20 two spikes from Figure 3.19 are zoomed-in, to look at the AHP and slow depolarization phase of the spiking. The fast AHP and slow depolarization phase are clearly present. It also seems as if the model-GPe-neuron indeed has a phase which appears to be a slow AHP-phase. It does not fit in the fast AHP part or in the depolarization phase. It is more a 'constant' phase but comes closer to a slow AHP than any of the phases of the STN-neuron do.

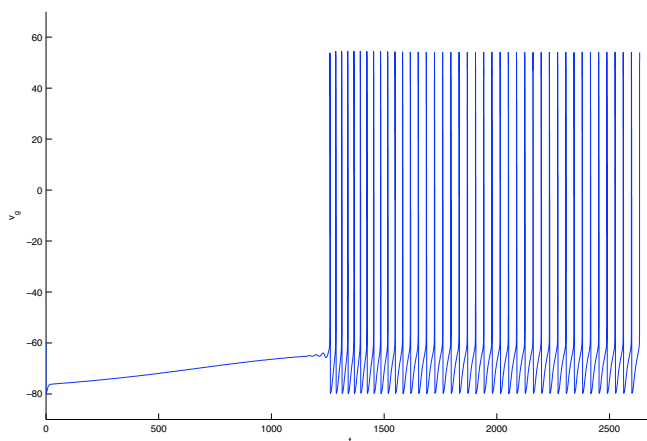


Figure 3.19: With the initial data as in Table 3.4 the neuron shows spiking behaviour, which is spontaneous because  $I_{app} = 0$ .

$v_g$ (mV)	$n_g$	$h_g$	$r_g$	$[Ca]_{i_q}$ (mmol)	$I_{app}$ (pA/ $\mu\text{m}^2$ )
-60	0.8	0.1	0	0.6	0

Table 3.4: The initial data for the spontaneous spiking Figures 3.19 and 3.20.  $I_{app} = 0$  pA/ $\mu\text{m}^2$  for spontaneous spiking.

Because it was claimed in [1] that for a small hyperpolarizing current ( $I_{app} = -0.5$  pA/ $\mu\text{m}^2$ ) the GPe-neuron would show bursting behaviour, we tested this as well and indeed, as can be seen in Figure 3.21 the GPe-neuron shows bursts of spiking followed by a short period of quiescence.  $I_{app} = -0.5$  pA/ $\mu\text{m}^2$  is

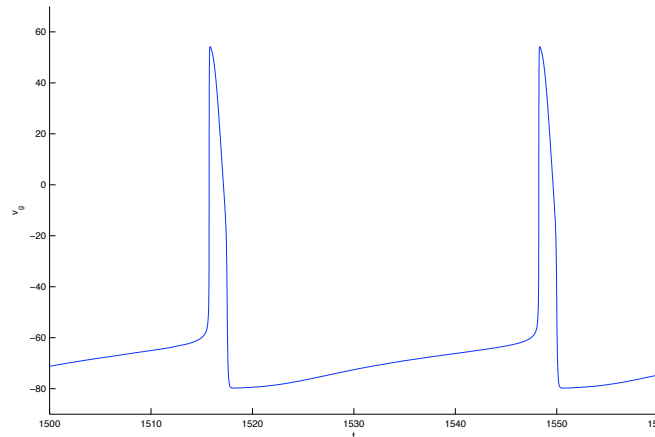


Figure 3.20: A zoom-in of Figure 3.19 to show the AHP after and the depolarization phase before the action potential.

located in the region where the stable limit cycle has not yet disappeared but which will bifurcate into a homoclinic orbit for a somewhat smaller  $I_{app}$ . The orbit therefore converges to the stable limit cycle, and during the convergence comes close to the sharp corner, close to the equilibrium which is still stable for  $I_{app} = -0.5 \text{ pA}/\mu\text{m}^2$ . The orbit spends some time in this region (the quiescent phase) due to the attraction to the equilibrium as well, until it is attracted to the stable limit cycle again. The quiescent phase is at approximately  $v_g = -70 \text{ mV}$  and the sharp corner is indeed located there. According to literature the GPe-neuron is indeed able to discharge at high frequencies interrupted by pauses, indeed after a weak hyperpolarization [12] although [30] claims the neuron only shows this type of behaviour at RMP.

In Figure 3.22 the fl-curve from experiments [28] and the fl-curve from the GPe-model [1] are plotted together to make a good comparison. The following differences and agreements between the figures can be noticed:

- The firing frequency during spontaneous spiking is in the order of 50 Hz. Because the continuation of the stable limit cycle could not be finished in the neighbourhood of  $I_{app} = 0$  this value of 50 Hz comes from a simple extrapolation. The real value for the frequency around  $I_{app} = 0$  can therefore differ from the 50 Hz. Because the frequency ranges differ between articles (10–15 Hz [30], 2–40 Hz [28] (see left picture in Figure 3.22) and in the order of 200 Hz [29]) the model's spontaneous firing frequency can not be verified. Assuming the lower frequencies from literature to be correct the model-neuron spontaneously fires at the right frequency.
- The shape of the two curves differs. The model fl-curve does not have a clear decreasing slope as the experimental fl-curve has. The model fl curve remains approximately linear with a tendency to the inverse sigmoidal shape also seen in the model fl-curve of the STN-neuron.
- The steepness of the approximately linear part of the curves (up to approximately  $600 \text{ pA}/\mu\text{m}^2$ ) differs by a large factor. The steepness of this

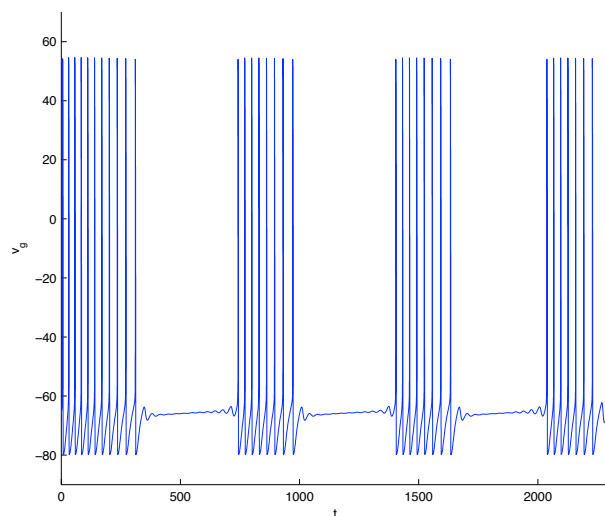


Figure 3.21: For  $I_{app} = -0.5 \text{ pA}/\mu\text{m}^2$  the GPe-neuron shows bursting behaviour.

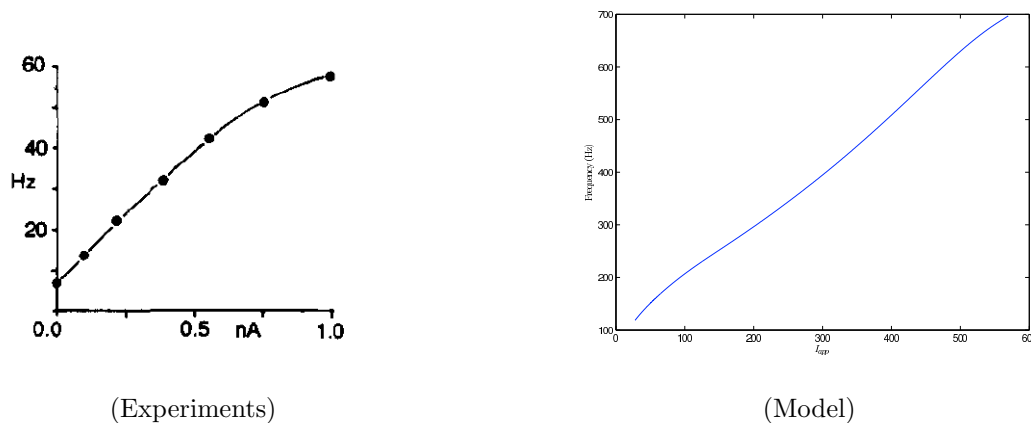


Figure 3.22: The model fI-curve (right) has a 25-fold steepness compared to the fI-curve from experiments [28] (left).

part of the curve for the experimental curve is approximately  $0.07 \text{ Hz/nA}$  and for the model-curve it is  $1.17 \text{ Hz/nA}$ . The slope of the model fI-curve is therefore almost 25 times too large.

These differences between the two fI-curves are based on the little information available on GPe-neurons in general and their responses to depolarizing input in particular. Therefore more experimental data is needed to really make a good comparison between model and experiments. Unfortunately this is the only information available at the moment. Therefore the conclusion can be drawn that the model-neuron behaves quite well, assuming the little information on GPe-neurons available, is correct. Only the steepness of the model fI-curve is too large, and should be reduced. Possible model-changes can be sought in

the parameter values of the model, the description of the model-currents and addition of other currents to the model which are described in Section 3.1.1.

### 3.3 Discussion

The bifurcation analysis of the GPe-model presented in [1] showed the following: although the two saddle homoclinic orbit bifurcations have not been verified to really take place, and the exact location of these possible bifurcations is for now unknown, the analysis showed that the model represents a GPe-neuron which almost always spikes when not inhibited. In the Basal Ganglia this of course is not the case as the GPe-neurons inhibit each other. In the small network of only one STN- and one GPe-neuron, discussed in the next section, the GPe-neuron is not inhibited though. For  $I_{app} < H_1 \approx -1.031 \text{ pA}/\mu\text{m}^2$  and  $I_{app} > H_2 \approx 600 \text{ pA}/\mu\text{m}^2$  the model-neuron is always quiescent. The SHOB of the stable limit cycle, if present, is assumed to occur close to  $H_1 \approx -1.031 \text{ pA}/\mu\text{m}^2$ , because otherwise the system would have no stable states between  $H_1$  and this SHOB. This is mathematically but not physiologically possible. By assuming this, the system is monostable with a stable limit cycle for:

$$I_{app} \in [\text{SHOB}_2, H_2] \approx [H_1, H_2] \approx [-1.031, 600] \text{ pA}/\mu\text{m}^2$$

The model-neuron will therefore always spike in this region, also when no current is applied ( $I_{app} = 0 \text{ pA}/\mu\text{m}^2$ ). This indeed agrees with experimental results which state the spontaneous spiking behaviour of the GPe-neuron.

When the SHOB's do not take place a totally different division of the parameter line for qualitatively different regions can be made. Therefore either these bifurcation points need to be found or ruled out as possibilities. Future versions of MatCont might be able to locate global bifurcations as well and be more accurate in the neighbourhood of such a bifurcation. If the SHOB of the stable limit cycle occurs, a region exists where the system does not have any stable states to which it can converge. No matter how small this region, it exists and does not agree with the physiological reality and should be adjusted. A neuronal model should always have at least one stable solution for every value of the parameter.

The simulations of the spontaneous spiking model-neuron showed a correct fast AHP and slow depolarization. A 'constant' phase follows the fast AHP and approximates the slow AHP in a better way than the model for the STN-neuron does. The resting membrane potential of the model agrees with the one measured in experiments. The fI-curve of the model is approximately linear up to  $600 \text{ pA}/\mu\text{m}^2$  which agrees with the fI-curve presented in [28]. For  $I_{app} > 600 \text{ pA}/\mu\text{m}^2$  the stable limit cycle could not be continued any further. Therefore frequencies are missing in that range. Whether the slope decreases for larger  $I_{app}$  as it does in the experimental fI-curve can therefore not be concluded. The slope of the linear part of the model fI-curve is 25 times the slope of the experimental fI-curve. Although this is the only experimental fI-curve with which the model is compared, reducing the slope might approach reality more.

Because little information is available on the different neurons within the GPe, it is difficult to compare the model-behaviour with the neuronal behaviour measured in experiments. With the limited articles available on the GPe it can be

---

concluded to some extent that the model indeed represents the behaviour of the three types of GPe-neurons described in Section 3.1.1. For future modelling of GPe-neurons more experimental data is necessary for data-fitting of the formulae and for comparing the behaviour of the model with experiments. Because the model behaves quite well and the differences between model and experiments are based on little information, no drastic changes to the GPe-model are suggested. Besides [1] already mention in their discussion that the models for both the STN- and GPe-neurons are simplified representations of reality. Possible reduction in the slope of the fI-curve and a more pronounced slow AHP can be achieved by adding currents described in Section 3.1.1 or changing descriptions of currents present in the model now.

The final remark which can be made by looking at the bifurcation analyses of the GPe- and STN-model, is that the GPe-model might consist of the same type of currents as the STN-model but the differences in parameters account for a qualitatively different behaviour of the two model-neurons.



# Chapter 4

## The STN-GPe network

The previous chapters discussed the two neurons present in the STN-GPe-network in the Basal Ganglia. In this chapter a network of only one STN- and one GPe-neuron will be analysed thoroughly in the sections following. A schematic view of this specific network can be seen in Figure 4.1.

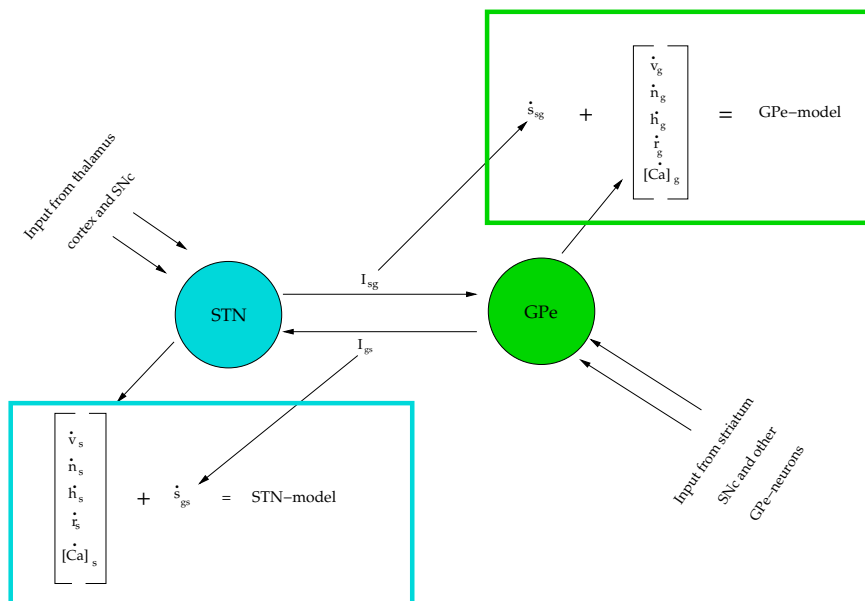


Figure 4.1: The STN- and GPe model are coupled, resulting in two extra variables

Before analysing this model-network, some results from literature will be presented in Section 4.1. First the synaptic coupling of the two neurons in our network is discussed by looking at the mathematical description of these chemical synapses in articles by Destexhe et al. [33] and [34]. Mathematical and experimental articles discuss the coupling of an excitatory to an inhibitory neuron, and analyse these types of synaptically coupled networks by for example looking at their ability to phase-lock, synchronize and cluster. One or

two articles specifically discuss the STN-GPe-network and their characteristics. By first describing and critically evaluating these results, the two-cell-model-network can be more easily analysed. The model of the two-cell network will be presented at the end of Section 4.1 where the variables mentioned in Figure 4.1 become clearer.

After the description of the model and its expected network behaviour, the model-network is analysed in Section 4.2 using MatCont. Because two parameters ( $g_{G \rightarrow S}$  and  $g_{S \rightarrow G}$ ) are present in the model, *codim-1* and *codim-2* bifurcations can occur, giving rise to interesting phase portraits in different regions of the parameter-plane. The goal is to produce a detailed picture of the parameter-plane, with clear bounded regions in which the neurons behave qualitatively different. These bifurcation boundaries indicate the transition between these regions. The final emphasis lies on the physical interpretation of this picture. What do the boundaries, regions and phase portraits imply for the behaviour of the two neurons in the network?

The bifurcation method used in Section 4.2 to analyse this small network in detail, can be applied to larger STN-GPe networks consisting of several STN- and GPe-neurons. Networks as in [1] can then be analysed, using this method. More detailed bifurcation pictures as the ones presented in [1] can then be made. Because GPe-neurons innervate each other (in contrary to STN-neurons) an additional parameter  $g_{G \rightarrow G}$ , representing the conductance of the GPe-neuron for the synaptic GPe-current, is present in these models. More difficult *codim-3* analysis is therefore also possible which was not the case for this small network consisting of only one GPe-neuron. Because the architecture of a real STN-GPe-network is still largely unknown, the influence of different architectures on the firing pattern of the neurons in the network can then also be tested. As can be seen in Figure 4.1 inputs of other nuclei to the two neurons are not included in the model-network for the moment. These might be added with substantial effort. See [9] for an example of coupling of the cortex, thalamus and striatum to the STN-GPe-network.

All results presented in this chapter of course only apply for the *model-network*, where the models for the two neurons and the synaptic connections are the ones presented in [1]. In Section 4.3 it is therefore discussed to what extent the results found for the model-network can be linked to the same two-cell-network *in vitro/vivo*. Of course this specific network, where all input to the two cells is ignored, is not present *in vivo*. It could give us some insight on the behaviour of larger networks of STN- and GPe-neurons.

## 4.1 Literature

This section will present relevant results from experiments and computational studies for small networks of excitatory and inhibitory neurons in general and the STN-GPe network in particular. Experiments for this type of two-cell network are of course not present and computational studies also often want to simulate more realistic and larger networks of STN- and GPe-neurons. Relevant results from literature for this small network are the results for the tightly and reciprocally connected (although larger) networks of excitatory and inhibitory neurons.

### 4.1.1 Computational and experimental results

In contrast to the GPe- and STN-neuron, there are results from computational studies of STN-GPe-networks and many mathematicians have tried to describe the behaviour of a network of inhibitory and excitatory neurons in general [35, 36, 37, 38]. Therefore not only relevant experimental results for our two-cell network are listed but also computational results. In Appendix D general concepts often used in articles on neurodynamics are explained and mathematical results on the transformation of a HH-model to a pulse-coupled model (revealing more on the dynamics of the phases of the neurons) are described. Because such a transformation unfortunately does not exist for our network (the network should only consist of class I excitable neurons), the still interesting results can be found in the appendix instead of here.

#### Computational results

This section will describe some computational results for specifically the STN-GPe-network. In [1] the results are presented from simulations of larger STN-GPe-networks using the models presented in this report. The ‘tightly reciprocally connected network’ has the most similarities with the two-cell network which will be analysed in the next section. The two cells are also reciprocally connected. The results for this ‘tight’ network presented in [1] will be shortly listed to get an idea on the possible behaviour of the two-cell network.

The results for the tightly connected network are all graphically presented in Figure 4.2. The differences between our small network-model and their (larger) network model are:

1. The conductance for the synaptic current between the GPe-neurons,  $g_{G \rightarrow G}$ , is varied in [1] while in our network with one GPe-neuron and thus no inhibition by others,  $g_{G \rightarrow G}$  is set to  $0 \text{ nS}/\mu\text{m}^2$  corresponding to the  $x$ -axis in Figure 4.2.
2. An applied current  $I_{app}$  is also included in the GPe-models of the network.  $I_{app}$  is an applied current which simulates the inhibiting influence of the striatum on the GPe-neuron and thus on the network. The aim of this research does not lie on the investigation of the influence of the striatum on the behaviour of the STN-GPe-network as *was* a part of the aim in [1]. For this reason  $I_{app} = 0 \text{ pA}/\mu\text{m}^2$  in our model (no input from the striatum) but is  $-1.2 \text{ pA}/\mu\text{m}^2$  in the results presented below.
3. In [1]  $g_{G \rightarrow S} = 1.0 \text{ nS}/\mu\text{m}^2$  for all simulations while in our network it is one of the two bifurcation parameters. The other one is  $g_{S \rightarrow G}$  and is also a varying parameter in [1].

The results are (following the  $x$ -axis in Figure 4.2 from left to right):

- When  $g_{S \rightarrow G}$  is small the neurons hardly influence each other and the STN-neuron shows its slow pacemaker activity.
- When  $g_{S \rightarrow G}$  is somewhat larger, episodic pattern firing can be seen. Every cell spikes repetitively, separated by periods of silence. These episodes are repeated at frequencies of 1–2 Hz. There may be little synchrony between individual spikes generated by different cells [39].
- When  $g_{S \rightarrow G}$  is above a certain boundary, the continuous mode sets in:

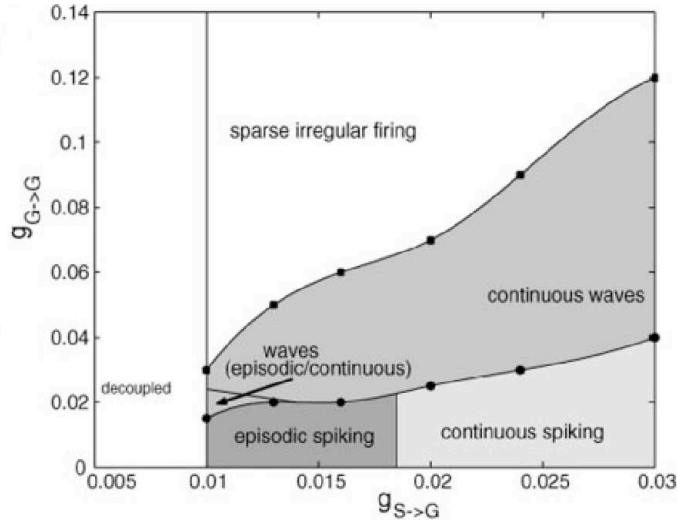


Figure 4.2: Results from [1] for a tightly connected network.  $g_{G \rightarrow S} = 1.0 \text{ nS}/\mu\text{m}^2$  and  $I_{app} = 1.2 \text{ pA}/\mu\text{m}^2$ .  $g_{S \rightarrow G}$  and  $g_{G \rightarrow G}$  are varied. The  $x$ -axis ( $g_{G \rightarrow G} = 0 \text{ nS}/\mu\text{m}^2$ ) corresponds to our network: the absence of other GPe-input to our one GPe-neuron.

the STN- and GPe-cell spike tonically. With further increase in  $g_{S \rightarrow G}$  the frequency increases to approximately 25Hz.

The maximal conductance for the synaptic current flowing through the  $\text{GABA}_A$ -receptor channels ( $g_{G \rightarrow S}$ ) is assumed to be in the range of 500 pS per synapse [40], which is approximately  $0.5 \text{ nS}/\mu\text{m}^2$ . The fixed value of  $1.0 \text{ nS}/\mu\text{m}^2$  for  $g_{G \rightarrow S}$  in [1] seems quite correct, knowing that the 500 pS is an approximate value. For all maximal synaptic conductances beside the  $\text{GABA}_A$ - and  $\text{GABA}_B$ -gated synaptic currents, the maximal conductances are often set to 200 pS per synapse [40], thus also for glutamate-gated synaptic currents. The range of variation for  $g_{S \rightarrow G} \in [0.005, 0.03] \text{ nS}/\mu\text{m}^2$  therefore seems justified.

Because the maximal conductances are all far more smaller than 1, these  $g_{G \rightarrow S}$  and  $g_{S \rightarrow G}$  play the role of  $\epsilon$  in the weakly connected networks (see previous section) and then the STN-GPe-network is indeed a weakly connected network as it should be (see Appendix D for the definition of weakly coupled networks).

Some other results for the STN-GPe-network [39] are:

- Clustered patterns are shown when clusters of cells synchronize. With a tight network, clustered patterns are unlikely to occur.
- In a network of one STN- and one GPe-neuron the neurons can trigger each other to burst by their spontaneous spiking behaviour. This bursting behaviour stops due to the activation of the outward current  $I_{AHP}$  in the GPe-neuron, which becomes activated due to the calcium build-up with each additional spike. Due to this outward current, on a certain moment the GPe-neuron will not be able to respond to a spike of the STN-neuron and the GPe-neuron will terminate its spiking behaviour. The STN-neuron will fire one rebound burst as a response to the last GPe-spike and stops firing as well.

- The time duration *between* the events (such as bursts or spikes) is determined by the  $I_{AHP}$  in STN-neurons. The calcium build-up in these neurons is fast due to the rapid firing of action potentials. When the event then terminates, a prolonged AHP can be seen in the STN-cell due to  $I_{AHP}$ . After this prolonged AHP regular spiking returns and a new event can be initiated.
- The time duration of an event is dependent on:
  1. The calcium build-up rate in GPe-neurons. The higher this rate the faster  $I_{AHP}$  is activated and makes the GPe-neuron quiescent. This build-up rate depends on the synaptic connectivity strength  $g_{S \rightarrow G}$ .
  2. The duration of rapid spiking of STN-neurons, which is dependent on the inactivation rate of  $I_T$ .

When larger networks of STN- and GPe-cells are modelled in the future it becomes more difficult to choose which neurons to connect with each other. This architecture of connections within the STN-GPe-network is still uncertain. For this reason various architectures have been tested in [1] to investigate their influence on the network firing behaviour. There has been some evidence that different parts of the network might oscillate separately from each other (some in-phase some out-of-phase for example) [39]. When random connections are present between the cells (no structured arrangement), efficient spreading of activity through the network occurs. In Figure 4.3 from [39] the influence of the strength of the connections between the different nuclei on the level of synchrony is indicated. A moderate connection strength between the GPe-neurons and strong connections between the other nuclei seems to promote synchronous firing of the STN- and GPe-neurons, whereas the strength of the connection strong between the GPe-neurons and moderate between the other nuclei promotes asynchronous solutions [39].

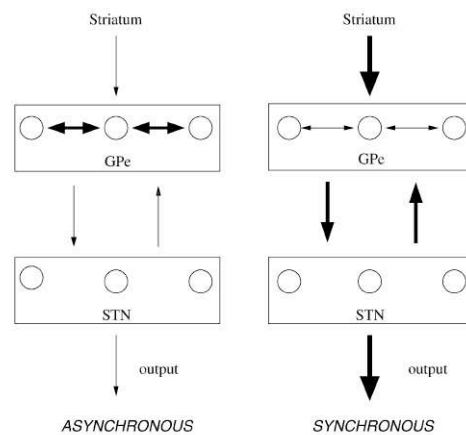


Figure 4.3: The strength of the connection between the GPe-neurons seems to have a large influence on the level of synchrony between the two nuclei and within the nuclei [39].

As has been shown in [5] the possible cause of the tremor frequency present in PD-patients, could lie in the STN-GPe-network which is able to generate syn-

chronized bursts which are modulated by striatal inhibition. Many of the computational studies done on the STN-GPe-network, from which two have been described here, have been aimed on finding the origin of the synchronized bursting behaviour in this network. There are indications that the origins can be found in the intrinsic properties of the network itself, but new sounds are heard that the cortical (external) rhythmic input to the network might influence the tremor frequency [4]. In a dopamine-depleted state the STN- and GPe seem to be more sensitive to the cortical rhythm of approximately 1Hz [4].

### Experimental results

The following results on bursting behaviour (possibly synchronized) of the STN-GPe-network, come from experimental studies with preparations of STN- and GPe-neurons in vitro (and sometimes in vivo) where the connections between the two nuclei are kept intact:

- The STN and GPe form a central pacemaker generator (CPG) which is a feedback system which can be active without external input. The STN-GPe-network is modulated by striatal inhibition which is directed at the GPe [5]. Both nuclei can burst synchronically at low frequencies of 0.4 Hz, 0.8 Hz and 1.8 Hz [5]. Some of these frequencies correlate with the tremor frequency according to [5]. These frequencies are lower than observed in conscious patients with PD [4]. It states that higher frequencies are assumed to be present in vivo [4]. It is clear that the synchronized behaviour of the network has been acknowledged to be possible, but the various characteristics of the synchronized firing are still uncertain.

The network behaves differently in normal and Parkinsonian states:

1. In normal/healthy states the information is processed by the STN and GPe using complex spatiotemporal patterns of firing [4]. These same uncorrelated patterns can be seen in the output nuclei of the Basal Ganglia.
  2. In Parkinsonian states the STN and GPe show more correlated, synchronous and rhythmic patterns of activity [4], which can again be seen in the Basal Ganglia output nuclei as well. Because correlated activity is possibly a less efficient coding mechanism of the Basal Ganglia, the symptoms of PD can partly be explained [1]. The correlated rhythmic bursts have frequencies in two ranges: 4–10 Hz and 15–30 Hz. The correlation between the nuclei can be seen in a wide spectrum of phase relations which exist between and within the nuclei.
- The GPe is crucial for the generation of synchronized bursting in the network. Input of GPe-neurons to STN-neurons is primarily responsible for the temporal organization of STN-activity. It hardly influences the frequency of firing of STN-neurons [5].
  - Oscillatory bursts are less often encountered in the GPe than in the STN and the strength of bursting of GPe-units is less than that of STN-units [5].

The firing of GPe-neurons has a large influence on the timing of firing of the innervated STN-neurons and thus on the phase of the oscillation [4, 18]:

- The principal permeant ion of the  $GABA_A$ -receptor is chloride  $Cl^-$ . The equilibrium potential of this  $GABA_A$ -current is therefore approximately -80 mV. Due to this relatively low equilibrium potential several IPSPs can lower the STN membrane potential by 10–20 mV under the lowest possible membrane potential a STN-neuron can reach during spontaneous spiking.
- Small IPSPs do not change the interspike interval of STN-neurons significantly, regardless of the phase at which the IPSP is evoked. Phase-independent delays in firing can therefore be the result, which can lead to desynchronization.
- As the magnitude of the IPSP increases, the effectiveness in prolonging the interspike interval is related more strongly to the phase of the oscillation at which the IPSP occurs, than to. Thus large IPSPs reset the oscillatory cycle and are likely to lead to synchronization.
- The effect of multiple IPSPs is that they can produce a sufficient hyperpolarization to activate a rebound depolarization in the STN-neuron which can restore rhythmic spiking, reduce or prevent action potential generation and/or can generate a burst of activity. The pattern and rate of IPSPs stipulates the response in the STN-neuron.

#### 4.1.2 The two-cell model

Because both the STN- and GPe-neuron have been described in detail in the previous chapter, only the synaptic coupling of both neurons in the two-cell network needs to be discussed. First the different models which can be used for synaptic coupling in networks are described and discussed. Then the chosen model for the synaptic connection in the STN-GPe-network in [1], and used for our analysis, is compared with the just described models in literature. At the end of this section the two-cell network model consisting of 12 ODEs is presented.

##### The synaptic connection in literature

This section will discuss and verify the model equations chosen in [1] for the two synaptic currents  $I_{G \rightarrow S}$  and  $I_{S \rightarrow G}$  and the corresponding ODE's for the fractions of open channels  $s_{G \rightarrow S}$  and  $s_{S \rightarrow G}$ .

As has been described in Section 1.1.1 and graphically shown in Figure 1.4a presynaptic neuron (for the STN-neuron this is the GPe-neuron and vice versa) projects to a postsynaptic neuron (the 'receiving' neuron). An action potential in the presynaptic cell causes the cell to release certain neurotransmitter molecules (the STN-neuron releases glutamate (excitatory) and the GPe-neuron  $GABA_A$  (inhibitory)) in the synaptic cleft. These molecules bind to receptor channels for this neurotransmitter in the membrane of the postsynaptic cell. A fraction of these receptor channels open and dependent on the neurotransmitter and type of channel an EPSP or IPSP is generated in the postsynaptic cell. But how to model the relation between the action potential in the presynaptic cell and the gating of the receptor channels in the postsynaptic cell?

Destexhe et al. have written various articles on, among other subjects, modelling synaptic currents and other gating kinetics of neurons. The following information is deduced from [33] and [34] on kinetic models of synaptic transmission. The results are for *one* axon of the presynaptic neuron projection on a certain location on the postsynaptic cell (see Figure 4.4), where a high concen-

tration of receptor channels is available. The model by Terman et al. can be used for several GPe-neurons projecting to one STN-neuron and vice versa. Therefore the results presented here need to be extended to the general case. This will be done in the next section.

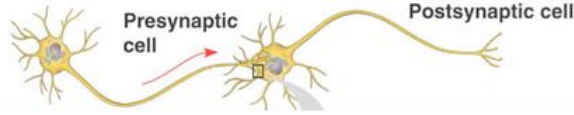


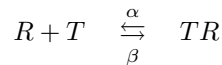
Figure 4.4: The presynaptic neuron fires an action potential, releases neurotransmitter in the synaptic cleft (between end axon presynaptic cell and soma postsynaptic cell), which binds to the receptor channels in the membrane of the postsynaptic cell. This triggers a postsynaptic potential.

Often the synaptic conductance  $g_{syn}$  is modelled as a waveform which varies in time and is dependent on the frequency of presynaptic release events. The most common one is the  $\alpha$ -function:

$$g_{syn}(t) = \frac{t - t_0}{\tau} \exp[-(t - t_0)/\tau], \quad \text{for } t \geq t_0$$

Here  $t_0$  is the time of transmitter release and  $\tau$  is a certain time constant. With multiple events at the presynaptic synapse the total conductance at a certain time instant is the sum of these individual waveforms. There are several disadvantages to this approach of the synaptic current such as inaccuracy, inefficiency of the calculation and the absence of a representation of saturation of the conductance. A kinetic model is the more logical approach to the synaptic current, but needs numerical integration which is computationally expensive. [34] shows some reasonable biophysical assumptions which results in a strongly reduced kinetic model which can be solved analytically and is still very accurate. Saturation of synaptic conductance is also taken into account.

When  $R$  is the postsynaptic receptor channel to which the neurotransmitter has not yet bounded. If  $T$  are the neurotransmitter molecules released by a presynaptic terminal after the arrival of an action potential, and  $TR$  is the bounded version of the receptor channel. This then is a two-state ligand-gated channel with the two states the open (bound) and closed (unbound) state. The reaction is given by:



$\alpha$  and  $\beta$  are the forward and backward rate constants for transmitter binding which can be seen as the transition probability (as in Markovian systems) from state  $R$  to state  $TR$  and vice versa [33].

When  $s$  is the fraction of the receptors which are *bound*, due to the release of the neurotransmitter molecules by the presynaptic neuron the change in time of this fraction is given by (4.1)

$$\frac{ds}{dt} = \alpha[T](1 - s) - \beta s \quad (4.1)$$

With  $[T]$  the concentration in the synaptic cleft of the neurotransmitter released by the presynaptic neuron. There is evidence that  $\frac{d[T]}{dt} = \infty$  during the rising

phase, after the release of the neurotransmitter molecules in the synaptic cleft by the presynaptic neuron. Also  $\frac{d[T]}{dt} = -\infty$  during the binding of the molecules to the receptor channels at the postsynaptic cell and due to the fast clearance mechanism by the presynaptic cell after release. Because the rise and fall of  $[T]$  seems to be extremely fast,  $[T]$  is assumed to change as a block pulse in time. In this case (4.1) can be solved analytically:

During a pulse ( $t_0 < t < t_1$ ),  $[T]$  is at its maximum value  $T_{max}$ . Then the solution to (4.1) is given by (4.2):

$$s(t - t_0) = s_\infty + (s(t_0) - s_\infty) \exp[-(t - t_0)/\tau_s] \quad (4.2)$$

With the equilibrium value ( $t \rightarrow \infty$ ):

$$s_\infty = \frac{\alpha T_{max}}{\alpha T_{max} + \beta} \quad (4.3)$$

And the time constant  $\tau_s$  given by:

$$\tau_s = \frac{1}{\alpha T_{max} + \beta}$$

*Directly* after a pulse ( $t > t_1$ ), due to the assumption that the fall of the concentration is infinitely fast,  $[T] = 0$  and the solution to (4.1) is almost trivial:

$$s(t - t_1) = s(t_1) \exp[-\beta(t - t_1)] \quad (4.4)$$

Assuming that binding of the neurotransmitter directly gates the opening of the associated receptor channel, then the total conductance through all receptor channels of the synapse is  $s\bar{g}_{syn}$ . When only one presynaptic neuron of a specific type adds to the synaptic current  $I_{syn}(t)$  in the postsynaptic cell, the formula for  $I_{syn}(t)$  is then given by (4.5).

$$I_{syn}(t) = \bar{g}_{syn} (V_{syn}(t) - E_{syn}) s(t) \quad (4.5)$$

With  $V_{syn}(t)$  the postsynaptic membrane potential and  $E_{syn}$  the synaptic equilibrium potential. Saturation of the response of the postsynaptic cell is implemented in this model when  $s \rightarrow 1$  (all channels reach the open state). In the next section it is shown that the kinetic model developed by Destexhe et al. in 1994 is used in the model [1] for the synaptic connections between the STN- and GPe-neuron.

### The model synaptic connection

The previous section discussed some accurate and computationally efficient results for the modelling of the relation between the membrane potential of *one* presynaptic cell and the gating of the receptor channels in the part of the membrane of the postsynaptic cell, to which the presynaptic cell projects. These results have been used in model [1] as well, but are generalized for larger networks of STN- and GPe-neurons. Let's take the model for the STN-neuron as an example (the results are analogues for the GPe-neuron). The time course of the STN-model is given by:

$$C_m \frac{dv_s}{dt} = -I_L - I_K - I_{Na} - I_T - I_{Ca} - I_{AHP} - I_{G \rightarrow S}$$

With  $I_{G \rightarrow S}$  the *total* synaptic current from *all* GPe-neurons projecting to this particular STN-neuron. Although the STN-neuron is modelled as a single-compartment and not many synapses can therefore end on this ‘point’-neuron, the physiological reality is that many synapses of GPe-neurons can end on a STN-neuron. This  $I_{G \rightarrow S}$  thus consists of the sum of the  $n$  individual synaptic currents through the STN-membrane, due to the release of neurotransmitter by the  $n$  different GPe-neurons. In equation form this becomes (4.6).

$$I_{G \rightarrow S} = I_{G_1 \rightarrow S} + I_{G_2 \rightarrow S} + I_{G_3 \rightarrow S} + \dots + I_{G_n \rightarrow S} \quad (4.6)$$

Because every  $I_{G_i \rightarrow S}$  (for  $i = 1 \dots n$ ) is given by (4.5), with appropriately renamed parameters, (4.6) becomes (4.7).

$$\begin{aligned} I_{G \rightarrow S}(t) &= \left[ \bar{g}_{G \rightarrow S} (v_s(t) - v_{G \rightarrow S}) s_{G_1 \rightarrow S}(t) \right] + \left[ \bar{g}_{G \rightarrow S} (v_s(t) - v_{G \rightarrow S}) s_{G_2 \rightarrow S}(t) \right] \\ &+ \dots + \left[ \bar{g}_{G \rightarrow S} (v_s(t) - v_{G \rightarrow S}) s_{G_n \rightarrow S}(t) \right] \\ &= \left[ \bar{g}_{G \rightarrow S} (v_s(t) - v_{G \rightarrow S}) \sum_i s_{G_i \rightarrow S}(t) \right] \end{aligned} \quad (4.7)$$

The reason that only  $s_{G_i \rightarrow S}(t)$  is dependent on the index  $i$  is because the GPe-neurons are assumed to be identical. This causes the maximal conductance  $\bar{g}_{syn} = \bar{g}_{G \rightarrow S}$  and the synaptic reversal potential  $E_{syn} = v_{G \rightarrow S} = -85$  mV to be constant for every GPe-neuron with index  $i$ . Beside this assumption, the postsynaptic membrane potential  $V_{syn}(t) = v_s(t)$  is assumed the same for every presynaptic GPe-neuron  $i$ , which is a reasonable assumption when the STN-neuron is modelled as a single compartment. When multi compartments would have been used the postsynaptic membrane potential would have varied between the different compartments and  $v_s(t)$  could not have been independent of the index  $i$ . The fraction of open receptor channels  $s_{G_i \rightarrow S}(t)$  at synapse  $i$  corresponding to GPe-neuron  $i$ , on time  $t$ , differs between the various GPe-neurons because the chance that  $v_{g_i}(t) = v_{g_j}(t)$  for  $i \neq j$  on time  $t$  is very small. Because  $v_{g_i}(t)$  on time  $t$  influences  $s_{G_i \rightarrow S}(t)$  directly,  $s_{G_i \rightarrow S}(t) \neq s_{G_j \rightarrow S}(t)$  for  $i \neq j$  on time  $t$  as well.

(4.7) is indeed chosen for the synaptic current  $I_{G \rightarrow S}$  for the STN-neuron. In the following,  $\alpha$  and  $\beta$  are the forward and backward rate constant for transmitter binding (see previous section).  $\theta_g$  is the ‘threshold’ above which the GPe membrane potentials  $v_{g_i}$  must rise before they release neurotransmitter and can influence the postsynaptic membrane potential  $v_s$  by generating an IPSP in the STN-neuron.  $\theta_g$  is taken as a constant and equal for all GPe-neurons projecting to this STN-neuron.  $H(v)$  is the heaviside function, which is defined as:

$$H(v) = \begin{cases} 0 & \text{if } v < 0 \\ 1 & \text{if } v \geq 0 \end{cases}$$

The dynamics of  $s_{G_i \rightarrow S}(t)$ , the fraction of open receptor channels at the

location at which GPe-neuron  $i$  projects, is then given by (4.8).

$$\begin{aligned} \frac{ds_{G_i \rightarrow S}}{dt} &= \alpha H(v_{g_i} - \theta_g)(1 - s_{G_i \rightarrow S}) - \beta s_{G_i \rightarrow S} \\ &= \begin{cases} -\beta s_{G_i \rightarrow S} & \text{if } v_{g_i} < \theta_g \\ \alpha(1 - s_{G_i \rightarrow S}) - \beta s_{G_i \rightarrow S} & \text{if } v_{g_i} \geq \theta_g \end{cases} \end{aligned} \quad (4.8)$$

Equation (4.1) from [34] is indeed used in [1]. There are two differences between (4.8) and (4.1):

1. The concentration of neurotransmitter in the synaptic cleft is called  $[T]$  in (4.1) and for this case is  $[GABA_A]$ . The dynamics of  $[GABA_A]$  are assumed to behave according to a pulse (see previous section), and thus only the values 0 and  $GABA_{A_{max}}$ , are assigned to  $[GABA_A]$ . Looking at (4.8) this  $GABA_{A_{max}}$  is apparently normalized to 1 in [1].
2. The heaviside function in (4.8) can not be used for computational purposes due to the infinitely large derivative of  $H$  at  $v_{g_j} = \theta_g$ . Therefore the Heaviside function  $H(v)$  is approximated in [1] by  $H_\infty(v)$  and is given by:

$$H_\infty(v) = \frac{1}{1 + \exp[-(v - \theta_g^H) / \sigma_g^H]}$$

This is the same type of function as is taken for the steady state voltage dependence for the gating variables in the models.  $\theta_g^H$  is the half-activation voltage and  $\sigma_g^H$  is the slope factor. Together they determine the speed in which  $H_\infty(v)$  steps from 0 to 1, which is less than  $\infty$  as was the speed for  $H(v)$ . Because of this finite speed, we are able to actually use the STN- and GPe-models in numerical programs as Matlab.

The solutions to the two ODE's (4.8) were already given in the previous section. (4.2) is the solution to the first ODE, when  $v_{g_i} > \theta_g$ , GPe-neuron  $i$  releases neurotransmitter in the synaptic cleft and  $[GABA_A] \rightarrow GABA_{A_{max}} = 1$  infinitely fast (replace  $T_{max}$  by 1 in (4.2)). The equilibrium value for  $s_{G_i \rightarrow S}$  when the concentration neurotransmitter remains maximal for a time period  $t \rightarrow \infty$ . This equilibrium value is given by (4.3) and is in this normalized case:

$$(s_{G_i \rightarrow S})_\infty = \frac{\alpha}{\alpha + \beta}$$

The solution to the second ODE is given by (4.4) when  $v_{g_i} < \theta_g$ , GPe-neuron  $i$  stops releasing neurotransmitter and the concentration of neurotransmitter in the synaptic cleft drops to 0 infinitely fast.

Analogues to the above the synaptic current from the presynaptic STN-neurons to the postsynaptic GPe-neurons,  $I_{S \rightarrow G}$ , is given by:

$$I_{S \rightarrow G} = \left[ \bar{g}_{S \rightarrow G} (v_g(t) - v_{S \rightarrow G}) \sum_j s_{S_j \rightarrow G}(t) \right]$$

$v_{S \rightarrow G} = 0$  mV and the dynamics of the fraction of open receptor channels in the GPe-membrane at the location where STN-neuron  $j$  projects, is given by (4.9):

$$\begin{aligned} \frac{ds_{S_j \rightarrow G}}{dt} &= \alpha H(v_{s_j} - \theta_s)(1 - s_{S_j \rightarrow G}) - \beta s_{S_j \rightarrow G} \\ &= \begin{cases} -\beta s_{S_j \rightarrow G} & \text{if } v_{s_j} < \theta_s \\ \alpha(1 - s_{S_j \rightarrow G}) - \beta s_{S_j \rightarrow G} & \text{if } v_{s_j} \geq \theta_s \end{cases} \end{aligned} \quad (4.9)$$

The values for  $\alpha$ ,  $\beta$ ,  $\theta_g$ ,  $\theta_g^H$  and  $\sigma_g^H$  are different for both neuron-models.

In the chapter on the STN-neuron and the section on the GPe-neuron the synaptic currents  $I_{G \rightarrow S}$  and  $I_{S \rightarrow G}$  were replaced by an applied current  $I_{app}$ , which became the parameter for the codim-1 bifurcation analysis. For this network the two synaptic conductances  $g_{G \rightarrow S}$  and  $g_{S \rightarrow G}$ , which are largely unknown in literature, will be taken as the parameters for the codim-2 bifurcation analysis in Section 4.2.

In the following section, results from literature on behaviour of networks of excitatory and inhibitory neurons will be listed. This is done to list the possible reactions of the two neurons to the synaptic coupling. Phase-locking, synchronization and other common network phenomena are explained as well. The results come from a variety of studies, experimental and computational. Because less is known for the STN-GPe network behaviour, a good comparison between the network behaviour shown in experiments and the model-network-behaviour is unfortunately very difficult.

### The total model

Adding the synaptic connection to the models of the two cells gives the total two-cell model (4.10) where the subscripts  $\kappa$  and  $\zeta$  are elements of  $\{s, g\}$ , and  $\kappa \neq \zeta$  holds. It is a coupled system due to the two synaptic currents. The formulae of the currents are given in (4.11). When no  $\kappa$  or  $\zeta$ -subscript hangs under a constant, it has the same value for both neurons. See Appendix A for the values of all constants.

$$C_m \frac{dv_\kappa}{dt} = -I_{L_\kappa} - I_{K_\kappa} - I_{Na_\kappa} - I_{T_\kappa} - I_{Ca_\kappa} - I_{AHP_\kappa} - I_{\zeta \rightarrow \kappa} \quad (4.10)$$

$$I_{L_\kappa} = g_{L_\kappa} (v_\kappa - v_{L_\kappa}) \quad (4.11a)$$

$$I_{K_\kappa} = g_{K_\kappa} n_\kappa^4 (v_\kappa - v_K) \quad (4.11b)$$

$$I_{Na_\kappa} = g_{Na_\kappa} m_{\infty_\kappa}^3 (v_\kappa) h_\kappa (v_\kappa - v_{Na}) \quad (4.11c)$$

$$I_{Ca_\kappa} = g_{Ca_\kappa} s_{\infty_\kappa}^2 (v_\kappa) (v_\kappa - v_{Ca_\kappa}) \quad (4.11d)$$

$$I_{AHP_\kappa} = g_{AHP_\kappa} (v_\kappa - v_K) \frac{[Ca]_{i_\kappa}}{[Ca]_{i_\kappa} + k_{1_\kappa}} \quad (4.11e)$$

$$(4.11f)$$

The low-threshold T-current differs between the two cells. For the STN-neuron the following description holds:

$$I_{T_s} = g_{T_s} a_{\infty_s}^3 (v_s) b_{\infty_s}^2 (r_s) (v_s - v_{Ca_s})$$

With  $b_{\infty_s}(r_s)$  is an inactivation ‘function’ of the inactivation variable  $r_s$ .

For the GPe-neuron the following more simple formula for  $I_T$  is given:

$$I_{T_g} = g_{T_g} a_{\infty_g}^3 (v_g) r_g (v_g - v_{Ca_g})$$

The synaptic currents are given by ( $\kappa$  and  $\zeta$  still in  $\{s, g\}$ ):

$$I_{\kappa \rightarrow \zeta} = g_{\kappa \rightarrow \zeta} (v_\zeta - v_{\kappa \rightarrow \zeta}) \sum_j s_{\kappa_j \rightarrow \zeta}$$

(4.10) defines two ODEs. For the six gating variables  $n_\kappa$ ,  $h_\kappa$  and  $r_\kappa$  the ODE is given by ( $X \in \{n, h, r\}$ ):

$$\frac{dX_\kappa}{dt} = \phi_{X_\kappa} \frac{X_{\infty_\kappa}(v_\kappa) - X_\kappa}{\tau_{X_\kappa}(v_\kappa)}$$

With  $X_{\infty_\kappa}(v_\kappa)$  the steady-state (in) activation function.

For the internal calcium concentration two additional ODEs are given:

$$[Ca]_{i_\kappa}' = \epsilon_\kappa (-I_{Ca_\kappa} - I_{T_\kappa} - k_{Ca_\kappa} [Ca]_{i_\kappa})$$

Due to the synaptic coupling two extra (synaptic) variables, and thus two extra ODEs are added to this model.

$$\frac{ds_{\kappa_j \rightarrow \zeta}}{dt} = \alpha_\zeta H(v_{\kappa_j} - \theta_\zeta)(1 - s_{\kappa_j \rightarrow \zeta}) - \beta s_{\kappa_j \rightarrow \zeta}$$

In total the system consists of 12 variables (and thus 12 ODEs) and 2 conductances as parameters. The system is thus  $\mathbb{R}^{12} \times \mathbb{R}^2$ -dimensional.

## 4.2 Analysis

This section is devoted to the analysis of (4.10) by looking at its equilibrium bifurcation analysis in Section 4.2.1 and by plotting the time diagrams of  $v_s$  and  $v_g$  in different physiologically reasonable regions of the parameter plane. The equilibrium bifurcation analysis of this small network differs from the codim-1 bifurcation analyses for the STN- and GPe-neuron in the previous chapters. Because two parameters instead of one are present in the two-cell model (4.10), Hopf- and fold-*curves*, instead of these bifurcation *points*, can be drawn in the parameter plane. Codim-2 bifurcation *points* can then be found on *these* curves. In chapter 8 of [32] the detailed definition and characteristics of these two types of curves and codim-2 bifurcation points can be found. For easy reference the possible codim-2 bifurcations are listed in Appendix C.2 as well, with the curve on which they can be encountered. The qualitative characteristics are mentioned as well.

In the following section the equilibrium bifurcations of the system are continued in the two parameters  $g_{S \rightarrow G}$  and  $g_{G \rightarrow S}$  of the system using MatCont. Fold- and Hopf-curves divide the 2D parameter space in different regions, which will be shown in a figure. The codim-2 bifurcations found by MatCont along the curves are shown as well and the coordinate and coefficient values of the point will be listed in a table. The stability of the equilibrium in the various regions is also indicated.

Because only the equilibrium of the system is analysed, possible bifurcations of the limit cycles which emerge from the Hopf curves, can not be seen from this figure. In addition, curves often ‘emerge’ from codim-2 bifurcation points which can divide parameter space in even more regions. These are often curves at which limit cycles also bifurcate. The figure presented in the next section thus gives a limited view into the behaviour of the network. The bifurcation analysis of the equilibria of the two-cell network, is just the beginning of a detailed analysis of this small network, and indirectly thus for a larger network. Such a detailed analysis with equilibrium and limit cycle bifurcations, as was done

for the GPe- and STN-neuron in the previous chapters, can give us a detailed division of, in this case, 2D parameter space. In the different regions it can be predicted how the network will behave. This can unfortunately not be done with an equilibrium analysis alone.

For only one parameter the total analysis is much easier than for two. This has various reasons. When the curves emerging from the codim-2 bifurcation points of equilibria are drawn as well as the codim-2 limit cycle bifurcation curves (for which a lot is unknown according to chapter 9 in [32]) it will be a chaotic picture with a large number of regions. Complex solutions to the system will bifurcate at these various boundaries. Because of the incomplete descriptions of the codim-2 limit cycle bifurcations, the difficulty in drawing the curves from the generalized- and double-Hopf points with MatCont, and due to the limited time left available for this MSc-project, the addition of these curves to the equilibrium bifurcation figure, will be added to the recommendation list at the end of the analysis-section.

For larger networks the same method for finding the equilibrium bifurcations can be used, but an extra parameter  $g_{G \rightarrow G}$  is added to the system when additional GPe-neurons are included in the network. Beside the codim-2 analysis described in this section, codim-3 analysis is then also possible, and more complicated as well. As was done in [1] one parameter can then be fixed to a certain value to keep it a codim-2 analysis.

In Section 4.2.2 time diagrams of the two membrane potentials  $v_g$  and  $v_s$  can already give an idea on the behaviour of the two neurons in the network although the parameter plane have not been divided accurately enough. The two time diagrams will be plotted together to see the dynamics of their phase difference  $|\phi_{GPe} - \phi_{STN}|$  as well. In Section 4.2.2 some results from literature described in 4.1.1 will be checked for this small network.

### 4.2.1 Equilibrium bifurcation analysis

This section describes the different bifurcations the equilibria of the two-cell system (4.10) undergo for different combinations of the two parameters in a physiologically relevant region of the parameter plane. The limit cycles which emerge from the many Hopf-points are not followed, and their presence or stability in the parameter plane is therefore unknown. Of course guesses can be made about the presence and stability of the emerged limit cycle in the close surroundings of the Hopf-curve. There may be many limit cycle bifurcation curves, emerging from the various codim-2 equilibrium bifurcation points (as the GH-points), present in the parameter plane in addition to the equilibrium bifurcation curves. Simulations in the relevant regions, shown in the next section, might give some insight on the presence of the *stable* limit cycles. A thorough limit cycle bifurcation analysis is therefore necessary to give a detailed picture of the parameter plane with the various regions in which the two-cell system behaves qualitatively different from the other regions.

In Figure 4.5 the 2D parameter space is divided into various regions by five Hopf-curves and one fold-curve. This figure will be discussed very shortly as the ranges taken for both conductance parameters  $g_{G \rightarrow S}$  and  $g_{S \rightarrow G}$  are physiologically not very interesting. Conductances are always positive thus only the first quadrant of the plane is useful to us. Beside this the values for the conductances are relatively small (in nS/ $\mu\text{m}^2$ ). Later this physiologically reasonable

region will be analysed further.

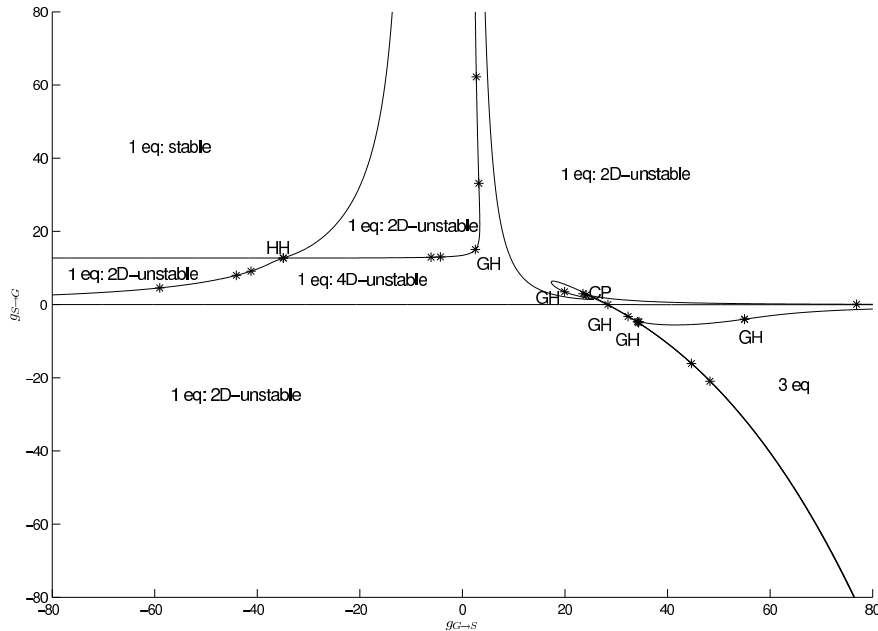


Figure 4.5: A large (physiologically unreasonable) region of the parameter plane is shown with 5 Hopf-curves and one fold-curve, dividing the plane in various regions. The number of equilibria is indicated in these regions with their stability. The region in which three equilibria coexist is larger than can be shown here.

As can be seen a stable equilibrium is only present for very negative values of  $g_{G \rightarrow S}$  and positive values of  $g_{S \rightarrow G}$ . If negative values for conductances would have been possible, and no stable limit cycles are present in this region, the STN- and GPe-neuron will be quiescent in this region independent on the chosen initial data for the twelve variables. In the figure it is indicated that only in the region in the lower right corner (the region does not stop at the nearest boundaries of the region) more than one equilibrium is present. In all other regions only one equilibrium of the system exists and its stability is indicated in the various region.

Looking at Figure 4.5 it is clear that around  $g_{S \rightarrow G} = 0 \text{ nS}/\mu\text{m}^2$  and  $g_{G \rightarrow S} \in [10, 60] \text{ nS}/\mu\text{m}^2$  many bifurcation curves come together and it can not be seen quite clearly how these curves are located relative to each other. A close-up of the fourth quadrant of Figure 4.5 is therefore shown in Figure 4.6. There are three curves (curves 1 and 3 are Hopf curves and curve 2 is a fold curve) very close to one another with their tails (downward) almost on top of each other. Number 4 is an almost straight Hopf-curve.

The red dots with a 2-letter abbreviations indicated in Figure 4.5 and 4.6 represent codim-2 bifurcation points. A GH indicates a generalized-Hopf/Bautin point, a HH a double-Hopf point and a CP a cusp-point (see Appendix C.2 for more details on these bifurcations). The values of the potentials, parameters, and possible frequency are listed in Table 4.1. The coefficients of the points,

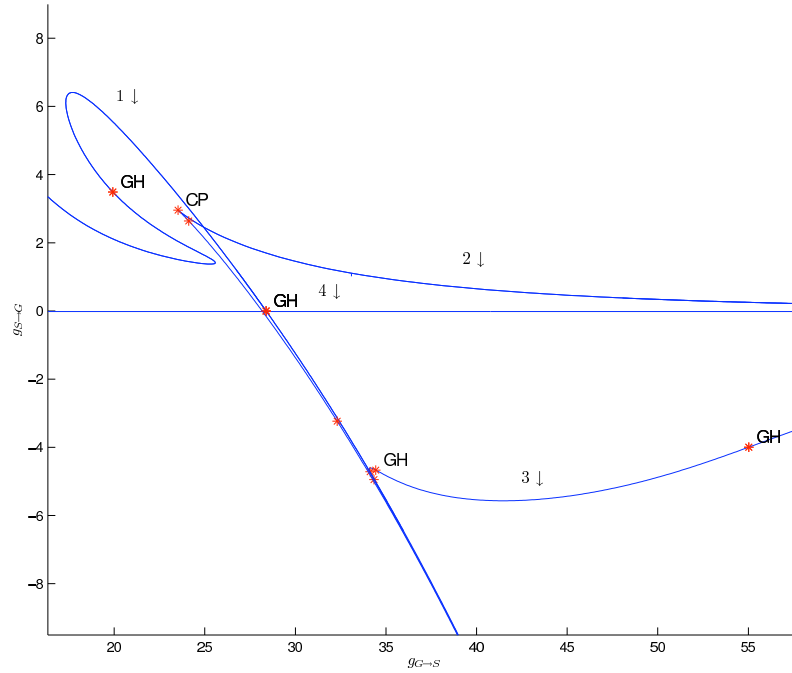


Figure 4.6: A zoom-in of a part of the fourth quadrant of Figure 4.5. Curves 1, 3 and 4 are Hopf curves and curve 2 is a fold curve. Curves 1, 2 and 3 overlap on the vertical downward parts of their curves.

which define their types are listed in Table 4.2.

Type	$v_s$ (mV)	$v_g$ (mV)	$g_{G \rightarrow S}$ (nS/ $\mu\text{m}^2$ )	$g_{S \rightarrow G}$ (nS/ $\mu\text{m}^2$ )	$\omega^2$
GH <sub>1</sub>	-40.186	-30.518	2.536	15.066	19.693
GH <sub>2</sub>	-56.083	-61.956	28.384	0.000	0.000
GH <sub>3</sub>	-49.709	-53.179	19.926	3.491	0.000
GH <sub>4</sub>	-54.280	-66.921	55.023	-3.996	0.071
GH <sub>5</sub>	-56.376	-63.420	34.438	-4.668	0.052
HH <sub>1</sub>	-27.194	-30.496	-34.922	12.717	20.668
CP <sub>1</sub>	-53.052	-59.000	23.524	2.955	-

Table 4.1: On the Hopf-curves five GH-bifurcations and one HH-bifurcation was found. On the fold-curve a CP-bifurcation was detected. The coefficients are listed in Table 4.2

The double-Hopf point is mathematically very interesting but is present in a nonphysiological region. For the interested mathematicians, the type of the HH is a type V of the difficult cases ( $p_{11}p_{22} = -1$ ) because  $\theta < 0$ ,  $\delta < 0$  and  $\theta\delta = 0.9705 < 1$ . See Section 8.6 in [32] for the parametric portraits of this nice codim-2 bifurcation type.

The fold-curve will now be looked at more thoroughly because it bounds a region in which three equilibria coexist. Outside this region only one equilibrium of the system is present. On the two boundaries, divided by the cusp bifurcation point, two equilibria coalesce and then disappear. These equilibria are different

Type	Coefficient	Value
GH <sub>1</sub>	$l_2$	-3.147e-3
GH <sub>2</sub>	$l_2$	-68.484
GH <sub>3</sub>	$l_2$	-7.919e-5
GH <sub>4</sub>	$l_2$	-1.193e-3
GH <sub>5</sub>	$l_2$	0.194
HH <sub>1</sub>	$p_{11}p_{22}$	-1
	$\theta$	-0.1043
	$\delta$	-9.305
	$\Theta$	9.272
	$\Delta$	-7030
CP <sub>1</sub>	$c$	2.666e-5

Table 4.2: The coefficients of the codim-2 equilibrium bifurcations listed in Table 4.1

for both boundaries. In Figure 4.7 only the fold-curve is drawn in the same lower right corner as in Figure 4.6.

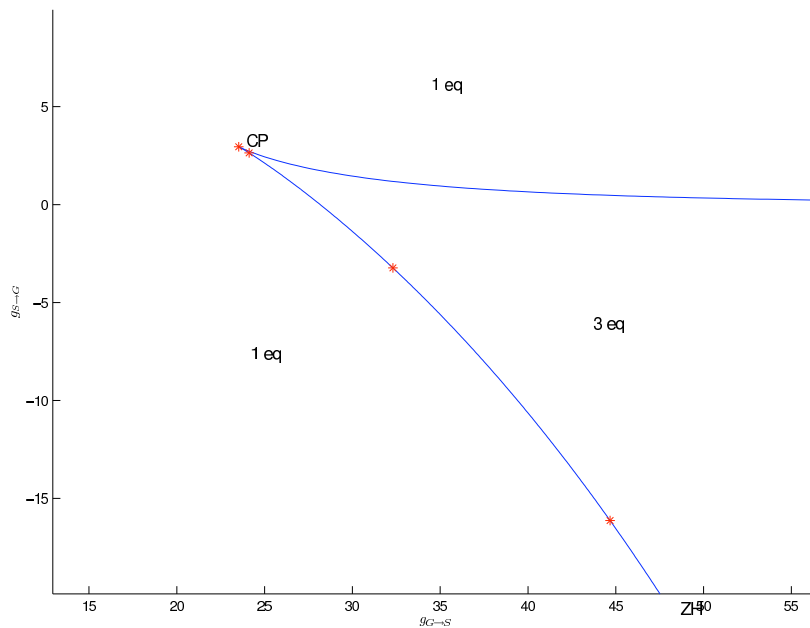


Figure 4.7: The lower right corner of Figure 4.5 with only the fold-curve is drawn. A cusp-bifurcation point (indicated with CP) separates the two fold curves on which different equilibria coalesce and disappear.

To indicate what exactly happens at the fold-curve and at the cusp-point our semicubic parabola from Figure 4.7 is sketched in Figure 4.8 (in the middle of the figure). In the squares the situation in the different regions is schematically presented on the equilibrium curve. For our system we of course have an equilibrium *surface* but projecting this on, in this case, the plane  $\{g_{G \rightarrow S} = 0\}$  (see  $x$ - and  $y$ -axis within the squares) shows the projection curve of the equilibrium

surface. The equilibrium surface and thus also equilibrium projection is clearly folded in this region which is the reason for the presence of the fold-curve.

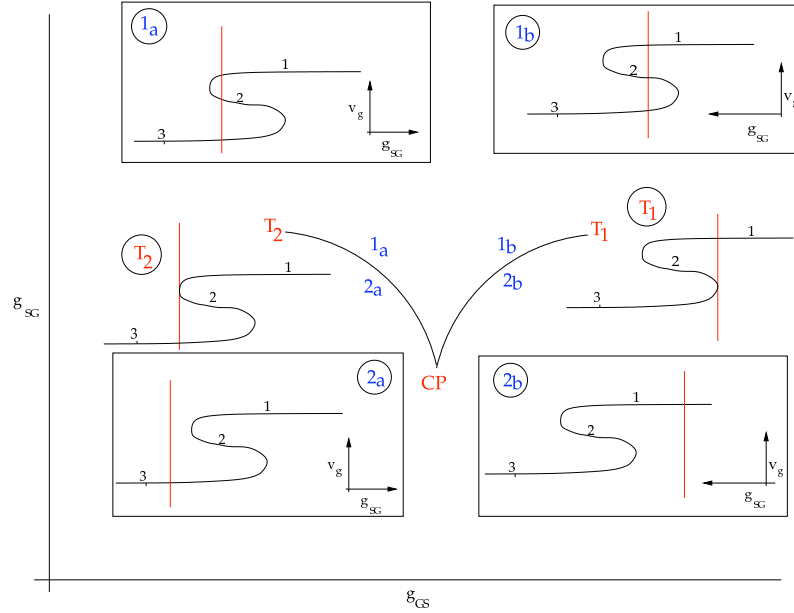


Figure 4.8: A schematic presentation of the influence of the fold-curve and cusp bifurcation point on the equilibria of the two-cell system.

For parameter values within the wedge (region 1a and 1b) three equilibria are present. When only moving vertically downward ( $g_{S \rightarrow G} \downarrow$  while  $g_{G \rightarrow S}$  remains constant) from region 1a to 2a, equilibrium 1 and 2 coalesce at  $T_2$  and only equilibrium 3 persists in region 2a. The same happens for equilibrium 2 and 3 which coalesce at  $T_1$  when moving ‘downward’ from region 1b to region 2b. Only equilibrium 1 persists in region 2b. Remember Figure 4.8 only gives a sketch of the situation because in reality the folded equilibrium surface (and thus also the projection curve) changes shape when moving in the parameter plane. In Figure 4.8 this shape is drawn the same in every region, causing trouble for the interpretation at the cusp point. The equilibrium curve becomes more ‘compact’ within the wedge for decreasing values of  $g_{S \rightarrow G}$  (nearer to the cusp-point). This means that the two fold points approach each other (as indeed can be seen in the decreasing distance between the branches  $T_1$  and  $T_2$ ). At the cusp-point the distance between the fold-points is zero, meaning that the three equilibria collide when crossing the fold-curve at exactly the cusp point and that only one persists in region 2. Because outside the wedge the equilibrium surface becomes more compact as well for decreasing  $g_{S \rightarrow G}$ , the initially different equilibria in regions 2a and 2b, become the same one after the total ‘stretch-out’ of the equilibrium-surface for  $g_{S \rightarrow G}$  below the cusp-point. Although in this explanation the two fold curves were crossed for a constant value of  $g_{G \rightarrow S}$  this is not necessary to notice the phenomena described here.

In Figure 4.9 the parameter plane for positive conductances is drawn. Part of two Hopf-curves and part of the fold-curve are present in this region. Three generalized Hopf-points and the cusp-point are present as well. Four of the five

regions in which the system will be simulated are indicated in Figure 4.9. The small fifth one (indicated by R.5) can be seen in a close-up in Figure 4.10.

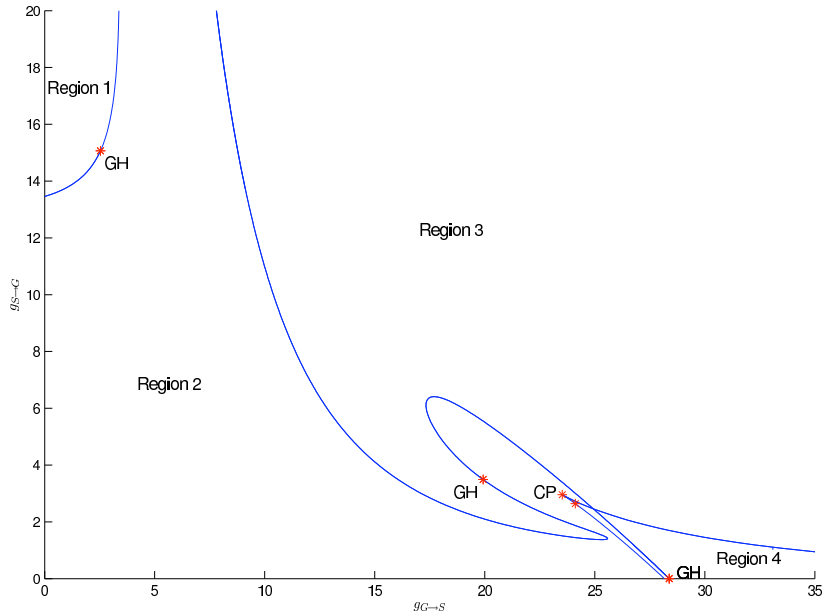


Figure 4.9: The part of the parameter plane which is physiologically relevant consists of parts of two Hopf-curves and the fold curve. Three generalized Hopf-points and the cusp point are present. Four regions in which the system will be simulated, are indicated. The fifth can be seen in Figure 4.10 (indicated by R.5).

As can be seen values of  $30 \text{ nS}/\mu\text{m}^2$  and  $20 \text{ nS}/\mu\text{m}^2$  for the conductances are still visible. Although values as  $g_{G \rightarrow S} = 30 \text{ nS}/\mu\text{m}^2$  and  $g_{S \rightarrow G} = 20 \text{ nS}/\mu\text{m}^2$  are very large for synaptic conductances (see Section 4.1.1) they are not *impossible* (as negative conductances are), because we saw in the chapters on the STN- and GPe-neuron that the parameter regions for both models needed to be ‘stretched up’ by a possible scaling. When this is needed the value of  $30 \text{ nS}/\mu\text{m}^2$  or  $20 \text{ nS}/\mu\text{m}^2$  in the *model* might not be that large.

Because part of the fold-curve is present in this region the hysteresis phenomenon so common and interesting in neurodynamical models, can possibly be seen in the regions around the fold-curve (all but region 1).

By continuing and following the three equilibria within the wedge, using MatCont, the following can be said about their stability in the different regions (the numbers of the list refer to the regions and the numbers of the equilibria refer to the equilibrium numbers in Figure 4.8). Starting in region 1 with equilibrium one we follow this equilibrium in the clockwise direction, following the numbers of the regions. The emergence of limit cycles at Hopf-points and their stabilities are noted as well. How they persist or bifurcate in this parameter plane is unfortunately unknown.

1. Only equilibrium 1 is present here, which is 2D unstable. Somewhat to the left this equilibrium was stable and lost its stability at another Hopf-curve.

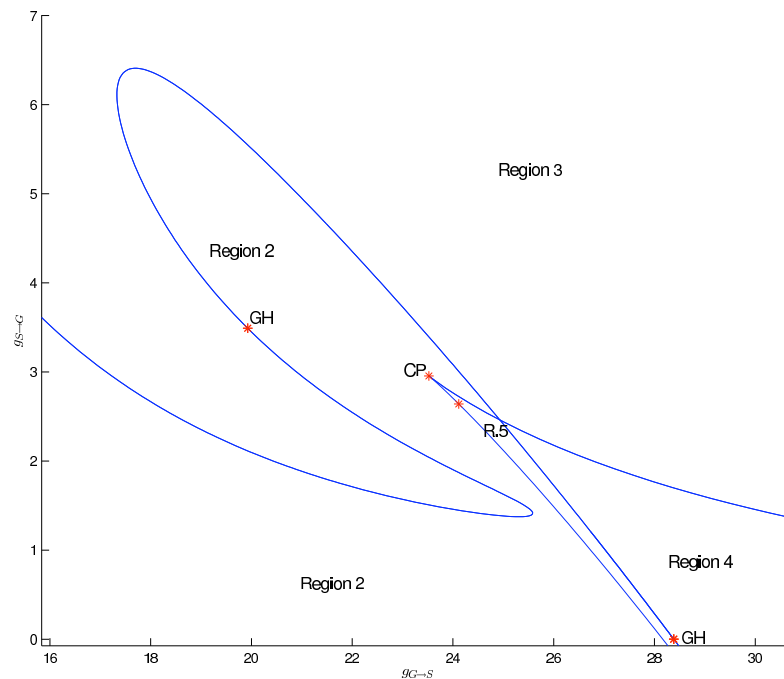


Figure 4.10: A close-up of Figure 4.9 to show the small fifth region indicated by R.5 between the Hopf and fold-curve.

Possibly the stable limit cycle which emerged from this Hopf-point, is still present in this region.

2. Only equilibrium 1 is present, which now has become 4D unstable. A stable limit cycle exists at least initially.
3. Still only equilibrium 1 is present (the equilibrium surface is still flat in this part of the parameter plane). It has become 2D unstable again, due to a subcritical Hopf-bifurcation. An unstable limit cycle at least initially is present in this region.
4. In this region, the system is inside the wedge and three equilibria are therefore present. Their stability is (the numbers refer to the equilibrium number in Figure 4.8):
  - (a) 2D unstable
  - (b) 3D unstable
  - (c) 4D unstable
5. The system is still inside the wedge but equilibrium 1 has become 4D unstable due to a supercritical Hopf-bifurcation. A stable limit cycle is at least initially present in region 5. The stability of the three equilibria is:
  - (a) 4D unstable
  - (b) 3D unstable
  - (c) 4D unstable

Travelling from region 5 to region 2 again, equilibrium 1 and 2 have coalesced and disappeared. Only equilibrium 3 persists in region 2 and is still 4D unstable.

Notice that equilibrium 1 and 3 indicate the same equilibrium in region 2 (as well as in region 1 and 3), but are different ones in regions 4 and 5. This is due to the compacting of the equilibrium surface near the cusp point. Here the hysteresis phenomenon can clearly be seen. Starting in region 1, 2 or 3 at equilibrium 1 which in these regions is the same as equilibrium 3, and moving to region 4 in a *clockwise* manner, brings you to equilibrium 1. Equilibrium 1 in region 4 is for example on the top surface of the folded equilibrium surface as in Figure 4.8. Starting in the same equilibrium (1 = 3) at the same point in the parameter plane, but going to region 4 in a *counterclockwise* manner puts the system at equilibrium 3 (on the lowest surface in Figure 4.8). In region 4 it is clear that equilibrium 1 and 3 are not equal anymore. Thus the system can end up in a completely different state by changing its path from its initial state to a state within region 4.

In the next section some simulations will be shown of the two-cell system within the physiologically relevant parameter plane. The three equilibria are unstable or nonexisting (for two out of three) in all five regions, showing that the two neurons will not be quiescent, at least not both at the same time, in the physiologically relevant region of the parameter plane. Stable limit cycles, possibly more than one should therefore be present in all five regions.

### 4.2.2 Simulations

When more stable limit cycles (or tori) coexist in a region, the initial data chosen for the 12 coordinates, decide to which cycle/torus the orbit converges. Without the knowledge on the presence and stability of the cycles, the initial data can only be chosen randomly. Also values for the two parameters need to be chosen randomly, because the boundaries in Figure 4.9 do not indicate a qualitative change in firing behaviour of the two neurons. The already unstable equilibria just bifurcate at these boundaries. Although everything is chosen randomly for the simulations it is expected that the firing of the neurons near the cusp-point might slow down (due to the many unstable manifolds) and that a stable limit cycle bifurcates at a limit point of cycle curve near a generalized Hopf-point. During simulations (for fixed values) a LPC or other limit cycle bifurcation can unfortunately not be found.

The initial data for the 12 coordinates, which are used for *all* the simulation figures shown in this section, are listed in Table 4.3. Here the membrane potentials  $v_s$  and  $v_g$  are in mV, the internal calcium concentrations  $[Ca]_{i_s}$  and  $[Ca]_{i_g}$  in mmol. The time  $t$  in all figures is in ms. In the time diagrams the top figure always corresponds to the STN membrane potential  $v_s$  and the bottom figure to the GPe membrane potential  $v_g$ .

$v_s$	$n_s$	$h_s$	$r_s$	$[Ca]_{i_s}$	$s_{G \rightarrow S}$	$v_g$	$n_g$	$h_g$	$r_g$	$[Ca]_{i_g}$	$s_{S \rightarrow G}$
-55	0.01	0.65	0.001	0.1	0.25	-65	0.2	0.5	0.1	0.1	0.3

Table 4.3: The initial data chosen for the twelve variables of the two-cell model for simulation purposes.

In Figure 4.11 a simulation is shown for  $g_{G \rightarrow S} = 1 \text{ nS}/\mu\text{m}^2$  and  $g_{S \rightarrow G} = 16 \text{ nS}/\mu\text{m}^2$ , which is located in region 1 of Figure 4.9. Due to the high conductance of the synaptic current from the STN- to the GPe-neuron, relative to

the conductance backward, the GPe-neuron is highly sensitive to the firing of the STN-neuron. As can be seen the STN-neuron is not able to fire due to the almost-spontaneous bursting of the GPe-neuron, because  $g_{G \rightarrow S} = 1.0 \text{ nS}/\mu\text{m}^2$  seems small relative to the  $16 \text{ nS}/\mu\text{m}^2$  but is a significant conductance [40].

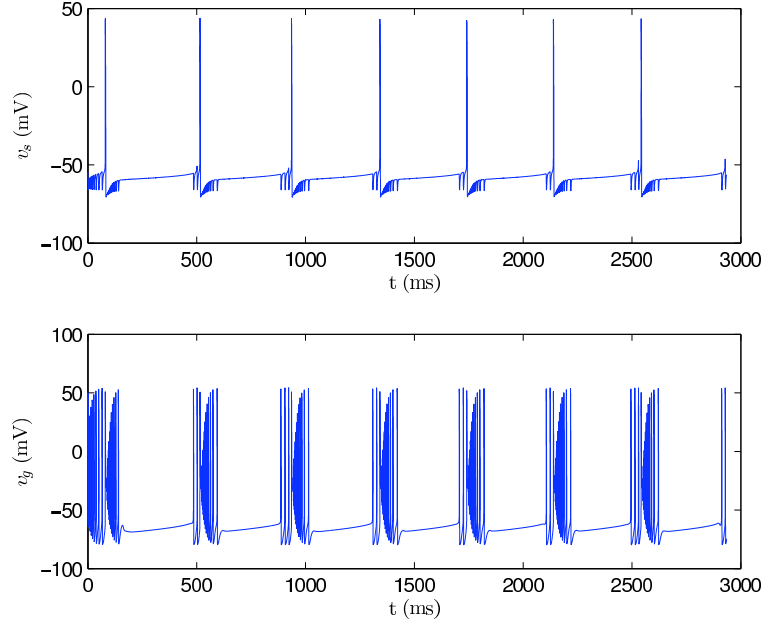


Figure 4.11: For  $g_{G \rightarrow S} = 1 \text{ nS}/\mu\text{m}^2$  and  $g_{S \rightarrow G} = 16 \text{ nS}/\mu\text{m}^2$  (region 1 in Figure 4.9) the STN-neuron shows a tonic spiking behaviour (top) and the GPe-neuron bursts (bottom).

In Figure 4.12 two bursts of the GPe-neuron and two spikes of the STN-neuron are zoomed-in. It is clear that the STN-neuron is only able to spike (one time) in a short quiescent period in the bursting of the GPe-neuron. The bursts of the GPe-neuron consist of two parts, one in which the amplitude of spiking and frequency remains approximately the same and one in which bursting starts at an almost zero amplitude, at a high frequency, which grows smoothly (with a decrease in frequency) to the same voltage range which was traversed during the first part of the burst. It seems as if the STN-spike pushes the GPe-neuron out of its quiescent and stable state, due to the high  $g_{S \rightarrow G}$ , in the attraction domain of the stable limit cycle to which it converges (showing the increase in amplitude and decrease in frequency). Because the interspike interval of the GPe-spikes in the first part of the burst is larger than in the second, the STN-neuron has more time to repolarize (increase) its membrane potential after a GPe-spike. This is not possible due to the almost constant inhibition by the GPe-neuron in the second part of the burst. That is possibly the reason that the STN-neuron does not regain its spontaneous spiking behaviour during the long quiescent period of the GPe-neuron. It can also be the case that the STN-system is at a stable equilibrium and can not be pushed-out of it very easily. This is my guess. When this is the case, the spike-response of the STN-neuron to an *inhibiting* spike shows the resonant character of the STN-neuron. The break of

the GPe-event is caused by the calcium build-up in the GPe-neuron during its spiking.  $I_{AHP}$  is activated and finally stops the firing.

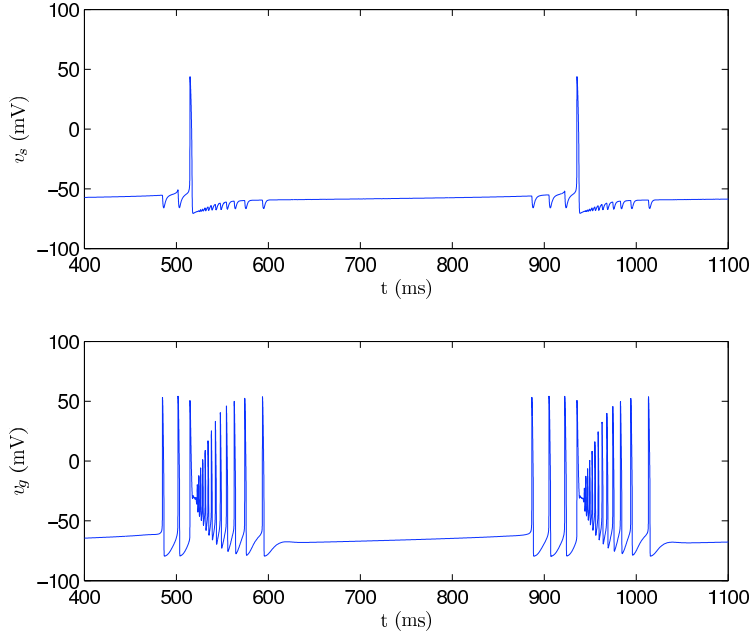


Figure 4.12: Two bursts (GPe) and spikes (STN) of Figure 4.11 are shown in a close-up. Clearly the bursts of the GPe-neuron consist of two phases, while the STN-neuron is almost always quiescent except during a short silent phase in bursting of the GPe-neuron.

In the first part of Section 4.1.1 results from [1] were described for tightly connected networks of 8–12 STN- and GPe-cells. The  $x$ -axis in Figure 4.2 agrees the most with our system. On this  $x$ -axis  $g_{G \rightarrow G} = 0 \text{ nS}/\mu\text{m}^2$ , which means that the GPe-neurons in the network are not inhibited by other GPe-neurons. Our GPe-neuron in the two-cell network is indeed not inhibited by other GPe-neurons (because they are absent), and therefore the results in Figure 4.2 on the line  $\{g_{G \rightarrow G} = 0 \text{ nS}/\mu\text{m}^2\}$  correspond the most the possible results for our network. Because only  $g_{S \rightarrow G}$  is varied along this zero-GPe-conductance line in [1], with  $g_{G \rightarrow S}$  set to a constant value of  $1 \text{ nS}/\mu\text{m}^2$ , in the following simulations the same range of values for  $g_{S \rightarrow G}$  are taken together with the constant value for  $g_{G \rightarrow S}$ . Because the striatal inhibition  $I_{app} = -1.2 \text{ pA}/\mu\text{m}^2$  in the results of [1], and we do not have striatal inhibition in our small network ( $I_{app} = 0 \text{ pA}/\mu\text{m}^2$ ), the question is how this striatal inhibition affects the results. Discrepancies between our and their simulations might be the result of this inclusion of the striatal input. Also the larger size of the network in [1] might result in differences between our simulations and theirs.

In Figure 4.13  $g_{G \rightarrow S} = 1 \text{ nS}/\mu\text{m}^2$  and  $g_{S \rightarrow G} = 0.006 \text{ nS}/\mu\text{m}^2$  which lies in the ‘decoupled’ range on the  $g_{S \rightarrow G}$ -axis in Figure 4.2. As can be seen in Figure 4.13 the neurons indeed hardly influence each other. The GPe-neuron inhibits the STN-neuron, which can be seen in the small hyperpolarization of  $v_s$  during spiking of  $v_g$ . Because  $g_{G \rightarrow S} = 1 \text{ nS}/\mu\text{m}^2$  is quite large ( $0.5 \text{ nS}/\mu\text{m}^2$  is

often chosen for the synaptic current through GABA<sub>A</sub>-gated receptor channels), the inhibition can clearly be seen. This inhibition does not change the pattern of tonic spiking of the STN-neuron though. The firing of  $v_g$  also does not show any change in pattern or firing rate at spiking moments of  $v_s$ . Indeed our simulations show that for  $g_{G \rightarrow G} = 0 \text{ nS}/\mu\text{m}^2$ ,  $g_{G \rightarrow S} = 1 \text{ nS}/\mu\text{m}^2$  and  $g_{S \rightarrow G} = 0.006 \text{ nS}/\mu\text{m}^2$  both neurons behave as if they were decoupled. This agrees with the results from [1]. In the simulations of [1] the GPe-neurons were mainly quiescent for these parameter values, and nonbursting as in our simulations. This difference can be attributed to the inhibition of the GPe-neurons by the striatum in their simulations. This inhibition misses here, and GPe-neurons can therefore spike without being stopped.

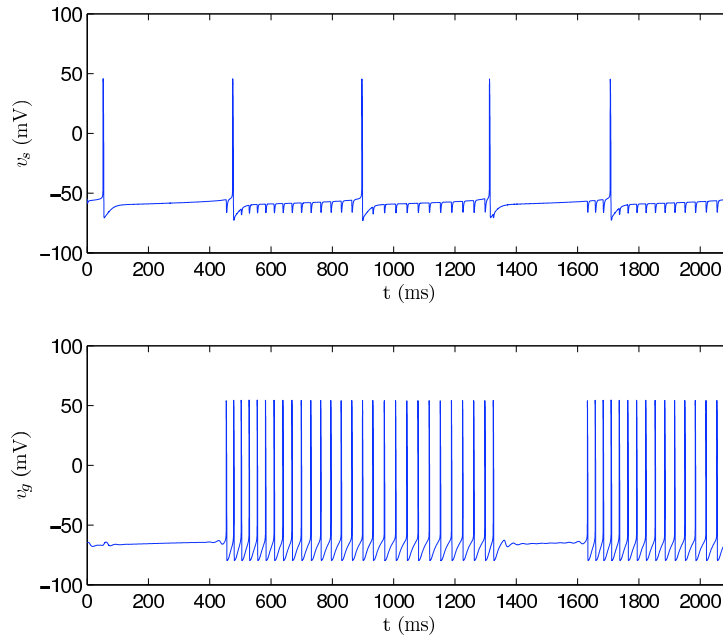


Figure 4.13: For  $g_{G \rightarrow S} = 1 \text{ nS}/\mu\text{m}^2$  and  $g_{S \rightarrow G} = 0.006 \text{ nS}/\mu\text{m}^2$  both neurons behave as if they were decoupled. This agrees with Figure 4.2 from [1].

In Figure 4.14  $g_{G \rightarrow S} = 1 \text{ nS}/\mu\text{m}^2$  still and  $g_{S \rightarrow G} = 0.015 \text{ nS}/\mu\text{m}^2$ , which lies in the ‘episodic spiking’-range on the  $g_{S \rightarrow G}$ -axis in Figure 4.2. The neurons do not act as if decoupled (as was the case in Figure 4.13), because the start and break of their events are approximately the same. In [1] both neurons show events of repetitive spiking behaviour separated by periods of quiescence when the parameter values are taken in this ‘episodic spiking’-range. The events are repeated periodically at 1–2 Hz. In our simulations the STN-neuron does not show these events of repetitive spiking, assuming that a single spike does not satisfy conditions which define ‘repetitivity’ within an event. The events *are* separated by periods of quiescence and the events are repeated periodically at approximately 2.3 Hz. The GPe-neuron does spike repetitively during an event which is then followed by a period of quiescence. The events are repeated periodically at 4 Hz which is higher than the 1–2 Hz in [1]. This is probably also the result from the absence of striatal inhibition of the GPe-neuron in our simu-

lation. The GPe-neuron is therefore able to fire at a higher rate and apparently twice the rate it reaches with a striatal inhibition of  $I_{app} = -1.2 \text{ pA}/\mu\text{m}^2$ .

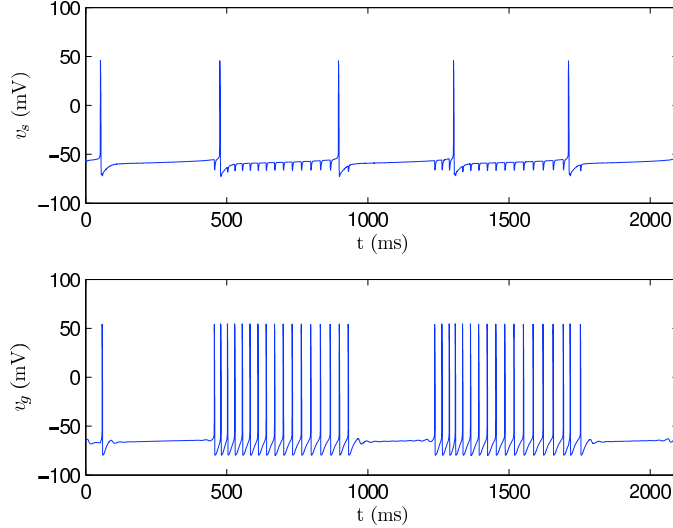


Figure 4.14: For  $g_{G \rightarrow S} = 1 \text{ nS}/\mu\text{m}^2$  and  $g_{S \rightarrow G} = 0.015 \text{ nS}/\mu\text{m}^2$  (in the ‘episodic spiking’-range of Figure 4.2) the STN-neuron does not show episodic spiking behaviour, which the GPe-neuron does. The firing frequency of  $v_g$  is twice the rate of that in [1] due to the absence of striatal inhibition in our simulations.

The simulation of the two-cell network with  $g_{S \rightarrow G}$  chosen in the ‘continuous spiking’-region on the  $g_{S \rightarrow G}$ -axis in Figure 4.2, is not shown here, because the firing behaviour of the two neurons is almost exactly the same as in the ‘episodic spiking’ region depicted in Figure 4.14. According to [1] the neurons should both spike tonically in this region, with their frequency rate increasing to approximately 25 Hz for increasing  $g_{S \rightarrow G}$  within this range. Figure 4.14 which also applies for the ‘continuous spiking’-region, does not show continuous spiking behaviour but episodes of bursts or single spikes. When inhibition of the GPe-neuron by the striatum would have been included in our simulation, the frequency rate of firing would decrease resulting in a decrease in the calcium build-up rate as well. When the interspike interval has increased to a certain level due to the striatal inhibition, that the calcium build-up during the spike is completely reduced by removal of calcium during the interspike interval following the spike, the GPe-neuron will indeed show continuous spiking behaviour, because spiking will simply not stop. When this is the case, the longer interspike intervals for the GPe-neuron will lead to less inhibition of the STN-neuron within the same time interval, which leads to an increase in firing rate of the STN-neuron. This leads to continuous spiking behaviour of the STN-neuron as well. Beside the influence of  $I_{app}$  on the difference in result, the large difference in size and architecture of our networks can of course lead to different results. The relation between the network architecture and results is more difficult to quantify.

In Figure 4.15  $g_{G \rightarrow S} = 24 \text{ nS}/\mu\text{m}^2$  and  $g_{S \rightarrow G} = 2.5 \text{ nS}/\mu\text{m}^2$ , which lies near the cusp-point (in the projection on the parameter plane of course, not

in  $\mathbb{R}^{14}$ ) in Figure 4.9. Both parameter values have increased in comparison to the simulation shown in Figure 4.14. The increase in  $g_{S \rightarrow G}$  can be seen by the increased influence of repetitive spiking of the STN-neuron on the firing of the GPe-neuron. After  $v_s$  elicits a spike the GPe-neuron becomes active again after a period of quiescence, and the rate of firing is high initially. This reduces to a constant rate until  $v_s$  spikes again and the rate increases to a large value again. The calcium builds up rapidly during these high rates (and in between) and the GPe-event stops at some time due to the activation of  $I_{AHP}$ . Due to the increase in rate of firing of  $v_g$  and thus in the rate of calcium build-up the duration of the GPe-events is shorter than in Figure 4.14. The increase in  $g_{G \rightarrow S}$  can be seen in the larger down-peaks in  $v_s$  when  $v_g$  spikes. Due to the rapid firing of  $v_g$  the STN-neuron is inhibited below a certain level that  $v_s$  polarizes (in a rebound manner) fast after the summation of a number of IPSPs. rebound polarization. This is due to the activation of  $I_T$ . Therefore two spikes (instead of one in Figure 4.14) are elicited by the STN-neuron.

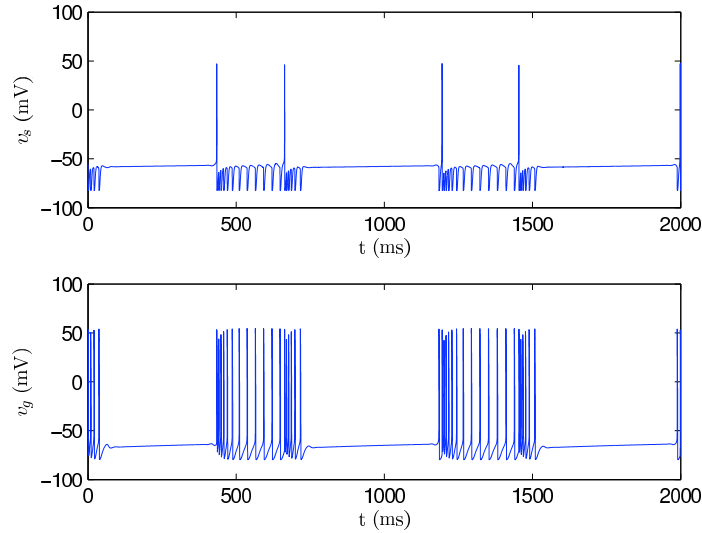


Figure 4.15: For  $g_{G \rightarrow S} = 24 \text{ nS}/\mu\text{m}^2$  and  $g_{S \rightarrow G} = 2.5 \text{ nS}/\mu\text{m}^2$  (close to the cusp-point in Figure 4.9) the two neurons have a large influence on each other. Both conductances have increased in comparison to Figure 4.14 leading to short-duration events and higher firing rates of both neurons.

In Figure 4.16  $g_{G \rightarrow S} = 27.5 \text{ nS}/\mu\text{m}^2$  and  $g_{S \rightarrow G} = 0.36 \text{ nS}/\mu\text{m}^2$  (in region 5 in Figure 4.9). One event of both neurons is shown in close-up to show the direct influence of the firing of each neuron on the firing of the other neuron. After a spike of  $v_s$ , the firing rate of  $v_g$  becomes somewhat larger (not that large as in Figure 4.15 due to the small value for  $g_{S \rightarrow G}$ ). The spikes of  $v_g$  lowers the STN membrane potential but due to the relatively large interspike interval of  $v_g$  the membrane potential repolarizes (increases) to a larger value than reached during the previous repolarization phase. Therefore a slow depolarization of the values of  $v_s$  just before the next spike sets in, can be seen. When the depolarization reaches a certain threshold the STN-neuron fires again and the process repeats itself.

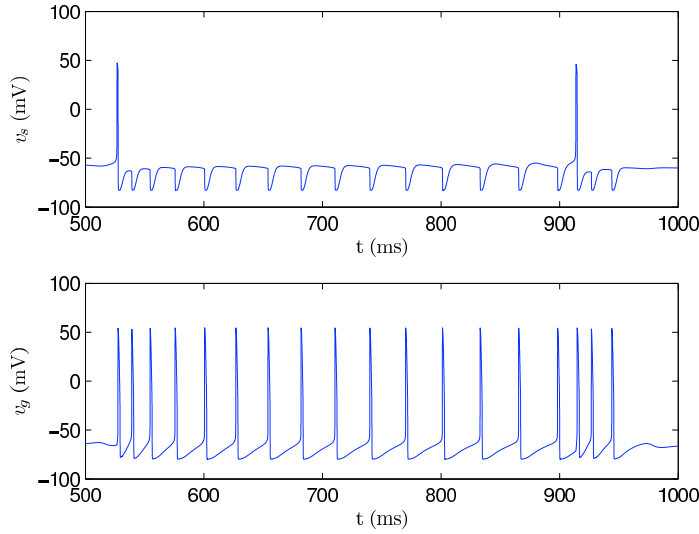


Figure 4.16: For  $g_{G \rightarrow S} = 27.5 \text{ nS}/\mu\text{m}^2$  and  $g_{S \rightarrow G} = 0.36 \text{ nS}/\mu\text{m}^2$  (in region 5 in Figure 4.9), a close-up of one event is shown, to indicate the direct influence of firing of the two neurons on each other.

### 4.3 Discussion

This chapter discussed the model of a small network of only one STN- and one GPe-neuron. The model for this two-cell network is given in (4.10) and consists of the two models for the individual neurons (discussed in previous chapters) with the addition of the synaptic currents  $I_{G \rightarrow S}$  (from GPe to STN) and  $I_{S \rightarrow G}$  (from STN to GPe).

Because the models of the individual neurons within the network are already evaluated in the previous chapters, only the synaptic connection between the two neurons needed discussion. The model of the synaptic connection between the two cells, described in [1], agrees with the model suggested in [33] and [34]. The model is optimized for simulation purposes by approximating the heaviside function using numerical programs as Matlab.

The two-cell network analysed in this chapter of course does not resemble the STN-GPe-network in vivo which receives external input. Such a network consists of many more cells, and two neurons are almost never reciprocally connected. Because two neurons are reciprocally connected, interesting phenomena as synchronization between neurons or phase-locking can not be observed. Although our small network hardly resembles the STN-GPe-network in vivo, and does not provide us with more knowledge on synchronization and other PD-related phenomena, it is a good network to start with. The equilibrium bifurcation curves in the parameter plane already gave rise to a complex hysteresis phenomenon (although stable equilibria were absent) and the simulations of both membrane potentials can easily be interpreted for different parameter combinations. Understanding the total bifurcation diagram (with codim-2 limit cycle bifurcation and equilibrium bifurcation curves) of such a small system is necessary to extend the network to larger sizes with different types of architecture.

Because in experimental studies either one cell or a large network of cells

(within a brain slice) is analysed, experimental results for the behaviour of this specific two-cell network could not be found. Due to the small size of the network the network behaviour can be guessed quite easily by looking at extreme values for the conductances, such as  $g_{G \rightarrow S} \gg g_{S \rightarrow G}$ .

In [1], from which this network model is derived, larger networks of STN- and GPe-neurons are analysed, for different types of architectures. The ranges of values which are chosen in [1] for the conductances can not be easily discussed because these are unknown or at least uncertain at the moment. In [40] values of  $0.5 \text{ nS}/\mu\text{m}^2$  for  $g_{G \rightarrow S}$  and of  $0.2 \text{ nS}/\mu\text{m}^2$  for  $g_{S \rightarrow G}$  are suggested. In [1] a constant value  $g_{G \rightarrow S} = 1.0 \text{ nS}/\mu\text{m}^2$  is assigned which is twice the value suggested in [40] but due to uncertainties the order of magnitude is of importance and thus seems correct.  $g_{S \rightarrow G}$  is varied within a range of  $[0.005, 0.03] \text{ nS}/\mu\text{m}^2$  and nicely surrounds the average value of  $0.2 \text{ nS}/\mu\text{m}^2$  suggested in [40]. The small average values of both conductances indicate that the neurons are weakly connected within the network. This means that firing of the presynaptic neuron does not change the shape of the action potential in the postsynaptic cell, but only influences the firing rate. See Appendix D for a more precise definition.

The ‘tightly connected network’ described in the article, resembles our small network the most, because some two-cell combinations are reciprocally connected within the larger network. The situation  $g_{G \rightarrow G} = 0 \text{ nS}/\mu\text{m}^2$  applies to our network as GPe-GPe-inhibition is absent with only one GPe-neuron. Because striatal inhibition is present in the simulations in [1] (which is not in our two-cell network) the results for this ‘tightly connected network’ differ somewhat from the simulations of our two-cell model when all other values of the conductances are taken equally.

A codim-2 equilibrium bifurcation analysis was conducted for this small network, showing the mathematically nice phenomena around a cusp bifurcation point. Because only in a nonphysiological range (for negative conductances) an equilibrium is stable, the mathematically nice transitions between the unstable equilibria can not be seen in the behaviour of the two neurons. The solutions to (4.10) will all converge to a stable limit cycle which is always present. Due to shortage in time and due to the difficulties of drawing codim-2 limit cycle bifurcation curves using MatCont, a limit cycle bifurcation analysis of the two-cell system has not been done yet. This is necessary (more than the equilibrium bifurcation analysis) to know for example the bistable regions. The limit cycle bifurcation curves indicate the possible emergence of tori or disappearance of cycles. A detailed description can *then* be given of the qualitatively different behaviour of the two neurons in the network. The codim-2 limit cycle bifurcation points which can be found on the curves, are unfortunately theoretically not completely understood.

## Chapter 5

# Conclusion

The motivation to conduct this neurodynamical research, described in the previous chapters, was to be able to predict the behaviour of the STN-GPe-network for different types of architectures and different connection strengths between the nuclei. This would possibly give us more information on the type of architecture and region in parameter space, for which the specific pathological type of behaviour occurs. Interpretation of these results could lead to more understanding on the origin of this synchronized and correlated behaviour in PD-patients. When this pathological behaviour had been encountered, models of DBS could then be used to analyse the effect different amplitudes and frequencies of DBS have on the behaviour of the network. Possibly the desynchronization between the nuclei can be seen. Interpretation of the conditions under which this desynchronization occurs could give us more information on the precise influence DBS has on the STN to which it is applied, and thereby on the STN-GPe-network.

Unfortunately these nice results have not yet been observed. Only a small part of this interesting field of research has been analysed in this research. The aim of this research was initially larger than described in Section 1.3. Analysing the two individual models showed more obstacles that needed to be understood, that fast extension of smaller networks to larger networks was not possible. Although larger networks are indeed necessary to grasp the synchronization phenomena of the original network, a thorough analysis of the model is to my opinion extremely important to be able to draw scientifically correct conclusions in the future on these larger network-models. The analysis of the individual models provided us with valuable information, which was not expected in advance.

The two aims of the research were:

**The analysis of the models of the individual neurons** To verify the model-behaviour with experimental literature, simulations of the model need to be made. A codim-1 bifurcation analysis of each neuron-model with an applied current (simulating the synaptic current of the other nucleus) as the parameter, can give insight in the possible behaviour of each neuron, for various amounts of input.

**The analysis of a small two-cell network** : this network consists of one STN- and one GPe-neuron. First the model synaptic connection chosen in [1] should be evaluated. Then a codim-2 bifurcation analysis with the two conductances taken as the parameters, should give more insight on

the types of network behaviour possible in the various regions of the parameter plane. The influence of the strength of the connections on the type of behaviour can then be deduced.

The problems defined in the problem definition are almost all solved (and analysed), except for the detailed division of the parameter plane into qualitatively different regions. This division could only have been made by the drawing of limit cycle bifurcation curves, because the performed equilibrium bifurcation analysis showed the instability of all equilibria in the physiologically relevant region of the parameter plane. Due to lack of time and difficulties drawing these limit cycle curves with MatCont, the limit cycle bifurcation analysis is not finished. All other analyses and evaluations have been done. The results of the analyses have been described in the three discussion-sections of the different chapters and will therefore not be repeated here. A summary of the results can be found in the abstract.

Although larger networks have not been analysed in this research the method of analysis, applied here to the two-cell network can be applied almost without adjustments to larger networks. When the extra parameter  $g_{G \rightarrow G}$  in larger network-models is taken equal to a constant, the analysis is *exactly* the same, namely codim-2. Thus the bifurcation method used here is a powerful one, which only depends on the number of parameters. MatCont is a program which is further developed and extended constantly. The limit cycle bifurcation curves can therefore be drawn more easily in the future, making it possible to indicate the bifurcation boundaries indicated in [1] more accurately.

The conductance-based network-model described in [1] can be used, after some small adjustments, for future research of larger networks of the subthalamic nucleus and the external part of the globus pallidus. Analysis of larger STN-GPe-network models with different architectures can give us more insight in PD-related phenomena as synchronized bursting, of the network. Bifurcation theory and its numerical implementation in MatCont, gives us a valuable tool for detailed analyses of networks. When MatCont, the bifurcation software in Matlab, is linked to Simulink the bifurcation analysis, described in this report, can be easily extended to larger networks.

## Chapter 6

# Recommendations

For future research in this field of the STN-GPe-network it would in general be helpful for the development of accurate models of this network, to be able to use more accurate (and more in general) experimental information. Accurate information leads to more accurate models, which can only then be analysed for predictive purposes.

For the improvement of the results of the research described in this report, the following is recommended:

- Improve the models of the individual neurons (especially the STN-model) by the recommendations given in the separate discussions. Improvements should be in such a way that simulations performed with these models are still fast but which show a slow AHP and a flatter fl-curve.
- For the bifurcation analysis of the individual models, the applied current can be set to a step current with a certain amplitude  $a$  and duration  $b$ . A codim-2 bifurcation analysis could then give us more detailed information, then the simulations with de- and hyperpolarizing input, on the exact influence of  $a$  and  $b$  on the firing properties of the neuron-models.
- For the two-cell network a limit cycle bifurcation analysis still needs to be performed to be able to divide the parameter plane accurately in qualitatively different regions. Limit point of cycle curves emerge from the various GH-points and can be drawn by MatCont very soon.
- When larger networks of STN- and GPe-neurons are considered, three parameters are present. A new result would be to draw a 3D parameter figure which consists of the different bifurcation boundaries. In [1] one parameter was always fixed to a certain constant value. Besides their analysis was 'approximate' which a bifurcation analysis is not.
- When the analysis of larger networks of only STN- and GPe-cells has been finished, the addition of models of other nuclei can be thought of. Especially the striatum appears to modulate the network's behaviour. But how exactly is unknown. The addition of the SNc, in which the cause of PD is located, is not added in the network-model of [9]. The addition of a good model of this dopaminergic nucleus, might give some indication of the influence of lack of dopamine on the synchronization properties of the STN-GPe-network.
- When the addition of extra nuclei to the STN-GPe network-model is con-

sidered and the models of the thalamus, GPI, striatum and the external stimulus DBS are used from [9], a good evaluation of each model, as has been done in this report for the STN-, and GPe-models, is recommended. [8] for example already states that the model for the thalamus in [9] is an extreme simplification of the real thalamus.

- When synchronization phenomena and correlated bursting are the interesting phenomena one tries to find during the analysis of a network-model, the question arises how these phenomena can be seen in a bifurcation diagram. What kind of transitions should be present or what kind of possibly complex and attracting cycles/tori should emerge from these bifurcation curves/surfaces.
- Whether it is possible or not it would be a complete and detailed analysis when the bifurcation boundaries in the 2D or 3D parameter space could be explicitly given by a function (when of course it *is* a well-defined function), such as:

$$g_{G \rightarrow G}(g_{S \rightarrow G}, g_{G \rightarrow S})$$

As was mentioned in the previous section of the conclusion, MatCont is a powerful tool to analyse neural models quite fast using bifurcation theory. Because the software is still under development, some aspects of the software can and hopefully will be improved:

- MatCont has not found any limit points of equilibria during the analysis of the three models, although they were clearly present in the STN- and network model. Fortunately a limit point can be easily noticed by staying present and alert during the continuation of the equilibrium. Although this is the case, one logically questions whether MatCont does not miss any other bifurcations, and whether the output of MatCont is reliable.
- For the two-cell network-model analysed in this research, introducing the model to network took some time already, by adding the subscripts for both type of cells to all constants, variables and ODEs. This is undoable for large-size networks. A link between Simulink and MatCont should be made possible and is to my knowledge under development. Simulink would be very handy for the addition of a certain type of neuron to the network.

# References

- [1] D. Terman, J.E. Rubin, A.C. Yew, and C.J. Wilson. Activity patterns in a model for the subthalamopallidal network of the Basal Ganglia. *The journal of Neuroscience*, 22(7):2963–2976, April 2002.
- [2] Eric R. Kandel, James H. Schwartz, and Thomas M. Jessell. *Principles of neural science*, pages 5–317, 853–867. McGraw-Hill, New York, 2000.
- [3] E.M. Izhikevich. *Dynamical systems in neuroscience: the geometry of excitability and bursting*. MIT-press, Cambridge, July 2007.
- [4] Mark D. Bevan, Peter J. Magill, David Terman, J. Paul Bolam, and Charles J. Wilson. Move to the rhythm: oscillations in the subthalamic nucleus-external globus pallidus network. *Trends in neuroscience*, 25(10):525–531, October 2002.
- [5] D. Plenz and S. Kitai. A Basal Ganglia pacemaker formed by the subthalamic nucleus and external globus pallidus. *Nature*, 400:677–682, 1999.
- [6] Xiao Jiang Feng, Brian Greenwald, Herschel Rabitz, Eric Shea-Brown, and Robert Kosut. Optimal deep brain stimulation of the subthalamic nucleus - a computational study. *Journal of computational neuroscience online*, May 2007.
- [7] Dana MacKenzie. Mathematical modellers help plumb mysteries of Parkinson’s Disease. Website, May 2003. <http://www.siam.org/news/news.php?id=322>.
- [8] Alejandro Pascual, Julien Modolo, and Anne Beuter. Is a computational model useful to understand the effect of deep brain stimulation in Parkinson’s disease? *Journal of integrative neuroscience*, 5(4):541–559, 2006.
- [9] J.E. Rubin and D. Terman. High frequency stimulation of the subthalamic nucleus eliminates pathological thalamic rhythmicity in a computational model. *Journal of computational neuroscience*, 16:211–235, January 2004.
- [10] A.L. Hodgkin and A.F. Huxley. A quantitative description of membrane current and its application to conduction and excitation in a nerve. *Journal of physiology*, 117:165–181, 1952.
- [11] T. Otsuka, Takafumi Abe, Takahisa Tsukagawa, and Wen-Jie Song. Conductance-based model of the voltage-dependent generation of a plateau potential in subthalamic neurons. *Journal of Neurophysiology*, 92:255–264, February 2004.

- 
- [12] A.J. Cooper and I.M. Stanford. Electrophysiological and morphological characteristics of three subtypes of rat globus pallidus neurone in vitro. *Journal of Physiology*, 527(2):291–304, 2000.
- [13] H. Nakanishi, H. Kita, and S.T. Kitai. Electrical membrane properties of rat subthalamic neurons in an in vitro slice preparation. *Brain research*, 437:35–44, 1987.
- [14] Mark D. Bevan and Charles J. Wilson. Mechanisms underlying spontaneous oscillation and rhythmic firing in rat subthalamic neurons. *Journal of neuroscience*, 19(17):7617–7628, September 1999.
- [15] Corinne Beurrier, Patrice Congar, Bernard Bioulac, and Constance Hammond. Subthalamic nucleus neurons switch from single-spike activity to burst-firing mode. *Journal of Neuroscience*, 19(2):599–609, January 1999.
- [16] Takeshi Otsuka, Fujio Murakami, and Wen Jie Song. Excitatory postsynaptic potentials trigger a plateau potential in rat subthalamic neurons at hyperpolarized states. *Journal of neurophysiology*, 86:1816–1825, 2001.
- [17] Mark D. Bevan, Charles J. Wilson, J. Paul Bolam, and Peter J. Magill. Equilibrium potential of GABA<sub>A</sub> current and implications for rebound burst firing in rat subthalamic neurons in vitro. *Journal of Neurophysiology*, 83(5):3169–3172, May 2000.
- [18] M.D. Bevan, P.J. Magill, N.E. Hallworth, J.P. Bolam, and C.J. Wilson. Regulation of the timing and pattern of action potential generation in rat subthalamic neurons in vitro by GABA<sub>A</sub> IPSPs. *Journal of Neurophysiology*, 87:1348–1362, March 2002.
- [19] Mark A. Wigmore and Michael G. Lacey. A Kv3-like persistent, outwardly rectifying, Cs<sup>+</sup>-permeable, K<sup>+</sup>-current in rat subthalamic nucleus neurons. *Journal of physiology*, 527:493–506, 2000.
- [20] Maureen E. Rush and John Rinzel. The potassium A-current, low-firing rates and rebound excitation in Hodgkin-Huxley models. *Bulletin of Mathematical Biology*, 57(6):899–929, 1995.
- [21] Corinne Beurrier, Bernard Bioulac, and Constance Hammond. Slowly inactivating sodium current ( $I_{NaP}$ ) underlies single-spike activity in rat subthalamic neurons. *Journal of Neurophysiology*, 83(4):1951–1957, April 2000.
- [22] Wen Jie Song, Yosuke Baba, Takeshi Otsuka, and Fujio Murakami. Characterization of CA<sup>2+</sup> channels in rat subthalamic nucleus neurons. *Journal of neurophysiology*, 84:2630–2637, 2000.
- [23] W. Govaerts. Numerical bifurcation analysis for ODEs. *Journal of computational and applied mathematics*, 125:57–68, 2000.
- [24] Willy Govaerts and Bart Sautois. Bifurcation software in Matlab with applications in neuronal modeling. *Computer methods and programs in biomedicine*, 77:141–153, 2005.

- [25] A. Dhooge and W. Govaerts. MatCont: a Matlab package for numerical bifurcation analysis of ODEs. *ACM transactions and mathematical software*, 29(2):141–164, June 2003.
- [26] A. Dhooge, W. Govaerts, Yu. A. Kuznetsov, W. Mestrom, A.M. Riet, and B. Sautois. *MatCont and CL\_MatCont: continuation toolboxes in Matlab*. University of Gent and Utrecht university, December 2006.
- [27] Andrew Gillies and David Willshaw. Membrane channel interactions underlying rat subthalamic projection neuron rhythmic and bursting activity. *Journal of neurophysiology*, 95:2352–2365, 2006.
- [28] H. Kita and S.T. Kitai. Intracellular study of rat globus pallidus neurons: membrane properties and responses to neostriatal, subthalamic and nigral stimulation. *Brain Research*, 564:296–305, 1991.
- [29] A. Nambu and R. Lliñas. Electrophysiology of globus pallidus neurons in vitro. *Journal of neurophysiology*, 72(3):1127–1139, 1994.
- [30] C. Savio Chan, Ryuichi Shigemoto, Jeff N. Mercer, and D. James Surmeier. HCN2 and HCN1 channels govern the regularity of autonomous pacemaking and synaptic resetting in globus pallidus neurons. *Journal of Neuroscience*, 24(44):9921–9932, 2004.
- [31] Gytis Baranauskas, Tatiana Tkatch, and D. James Surmeier. Delayed rectifier currents in rat globus pallidus neurons are attributable to Kv2.1 and Kv3.13.2 K<sup>+</sup>-channels. *Journal of Neuroscience*, 19(15):6394–6404, 1999.
- [32] Yuri A. Kuznetsov. *Elements of applied bifurcation theory*. Springer, New York, 1998.
- [33] Alain Destexhe, Zachary F. Mainen, and Terrence J. Sejnowski. Synthesis of models for excitable membranes, synaptic transmission and neuromodulation using a common kinetic formalism. *Journal of computational neuroscience*, 1:195–230, 1994.
- [34] A. Destexhe, Z.F. Mainen, and T.J. Sejnowski. An efficient method for computing synaptic conductances based on a kinetic model of receptor binding. *Neural computation*, 6:14–18, 1994.
- [35] J. Rubin and D. Terman. Geometric analysis of population rhythms in synaptically coupled neural networks. *Neural computation*, 12:597–645, 2000.
- [36] N. Kopell and G.B. Ermentrout. Mechanisms of phase-locking and frequency control in pairs of coupled neural oscillators. *Handbook of dynamical systems*, 3, 2003.
- [37] J. Rubin and D. Terman. Analysis of clustered firing patterns in synaptically coupled networks of oscillators. *Journal of mathematical biology*, 41:513–545, 2000.
- [38] Christoph Börgers and Nancy Kopell. Effects of noisy drive on rhythms in networks of excitatory and inhibitory neurons. *Neural computation*, 17:557–608, 2005.

- [39] D. Terman, J.E. Rubin, A.C. Yew, and C.J. Wilson. Synchronous rhythms in a model for the indirect pathway of the Basal Ganglia. *Neurocomputing*, 38–40(1–4):973–982, June 2001.
- [40] Christopher Koch and Idan Segev. *Methods in neuronal modeling, from ions to networks*. The MIT press, Cambridge, Massachusetts, 1998.
- [41] Eugene M. Izhikevich. Class I neural excitability, conventional synapses, weakly connected networks, and mathematical foundations of pulse-coupled models. *IEEE transactions on neural networks*, 10(3):499–507, 1999.
- [42] G.B. Ermentrout and Carson C. Chow. Modeling neural oscillations. *Physiology and behavior*, 77:629–633, 2002.
- [43] Eugene M. Izhikevich. Weakly pulse-coupled oscillators, FM interactions, synchronization, and oscillatory associative memory. *IEEE transactions on neural networks*, 10(3):508–526, May 1999.

## Appendix A

# Model constants

The values for the various constants used in the STN- and GPe-model are listed in table A.1.

Conductances  $g_X$  for  $X \in \{L, K, Na, T, Ca, AHP\}$  are in  $\text{nS}/\mu\text{m}^2$ . Equilibrium potentials  $v_L, v_K, v_{Na}, v_{Ca}$  and  $v_{G \rightarrow S}$  are in  $\text{mV}$ . The six parameters for the three timeconstants  $\tau_x^i$ , for  $x \in \{h, n, r\}$  and  $i \in \{0, 1\}$  are in  $\text{ms}$ . The unit of  $\epsilon, \alpha$  and  $\beta$  is  $\text{ms}^{-1}$ .

	<b>STN</b>	<b>GPe</b>
Parameter	Value	Value
$g_L$	2.25	0.1
$g_K$	45.0	30.0
$g_{Na}$	37.5	120.0
$g_T$	0.5	0.5
$g_{Ca}$	0.5	0.15
$g_{AHP}$	9.0	30.0
$v_L$	-60.0	-55.0
$v_K$	-80.0	-80.0
$v_{Na}$	55.0	55.0
$v_{Ca}$	140.0	120.0
$\tau_h^1$	500.0	0.27
$\tau_n^1$	100.0	0.27
$\tau_r^1$	17.5	
$\tau_h^0$	1.0	0.05
$\tau_n^0$	1.0	0.05
$\tau_r^0$	40.0	
$\tau_r$		30.0
$\phi_h$	0.75	0.05
$\phi_n$	0.75	0.05
$\phi_r$	0.2	1.0
$k_1$	15.0	30.0
$k_{Ca}$	22.5	20.0
$\epsilon$	3.75e-5	1e-4
$\theta_m$	-30.0	-37.0
$\theta_h$	-39.0	-58.0
$\theta_n$	-32.0	-50.0
$\theta_r$	-67.0	-70.0
$\theta_a$	-63.0	-57.0
$\theta_b$	0.4	
$\theta_s$	-39.0	-35.0
$\theta_h^\tau$	-57.0	-40.0
$\theta_n^\tau$	-80.0	-40.0
$\theta_r^\tau$	68.0	
$\theta_g^H$	-39.0	-57.0
$\theta_g$	30.0	20.0
$\alpha$	5.0	2.0
$v_{G \rightarrow S}$	-85.0	
$v_{G \rightarrow G}$		-100.0
$v_{S \rightarrow G}$		0.0
$\sigma_m$	15.0	10.0
$\sigma_h$	-3.1	-12.0
$\sigma_n$	8.0	14.0
$\sigma_r$	-2.0	-2.0
$\sigma_a$	7.8	2.0
$\sigma_b$	-0.1	
$\sigma_s$	8.0	2.0
$\sigma_h^\tau$	-3.0	-12.0
$\sigma_n^\tau$	-26.0	-12.0
$\sigma_r^\tau$	-2.2	
$\sigma_g^H$	8.0	2.0
$\beta$	1.0	0.08

Table A.1: The parameters of the STN- and GPe model from [1]

## Appendix B

### Some M-files

In this appendix some M-files for the calculation of equilibria (the first 5), their eigenvalues ( $[E,R,I]=\text{Eigenwaarden}(v)$ ) and for the simulation of time diagrams of the system (RHS and Main). These functions are for the STN-model but are also made for the other models. They show different equations but the same approach. In the comments of the files more is explained on the functions.

Listing B.1: M-file for the calculation of the bifurcation diagram

```
function Iinp_s = Bifdiagram(v_s)
%This function calculates the input Igs, such that the
%system is in an equilibrium. It first calculates
%the equilibrium values for the other four variables n,h,
5 %r, ca_conc_i_s ([Ca]), and then uses v'=0 to calculate
%the value for the synaptic current from a GPe neuron to
%a STN neuron

%Experimental constants
10 gca_s=0.5;
   gahp_s=9.0;
   gl_s=2.25;
   gk_s=45.0;
   gna_s=37.5;
15 gt_s=0.5;
   vna_s=55.0;
   vk_s=-80.0;
   vl_s=-60.0;
   vca_s=140.0;
20 theta_m_s=-30.0;
   theta_a_s=-63.0;
   theta_s_s=-39.0;
   theta_n_s=-32.0;
   theta_h_s=-39.0;
25 theta_r_s=-67.0;
```

```

sigma_m_s=15.0;
sigma_a_s=7.8;
sigma_s_s=8.0;
sigma_n_s=8.0;
30 sigma_h_s=-3.1;
sigma_r_s=-2.0;
theta_b_s=0.4;
sigma_b_s=-0.1;
k1_s=15.0;
35 kca_s=22.5;

%The steady states (n=ninf, h=hinf, r=rinf).
minf_s=1./(1+exp(-(v_s-theta_m_s)./sigma_m_s));
ainf_s=1./(1+exp(-(v_s-theta_a_s)./sigma_a_s));
40 sinf_s=1./(1+exp(-(v_s-theta_s_s)./sigma_s_s));
ninf_s=1./(1+exp(-(v_s-theta_n_s)./sigma_n_s));
hinf_s=1./(1+exp(-(v_s-theta_h_s)./sigma_h_s));
rinf_s=1./(1+exp(-(v_s-theta_r_s)./sigma_r_s));
binf_s=1./(1+exp((rinf_s-theta_b_s)./sigma_b_s)) ...
45 ... -1/(1+exp(-theta_b_s/sigma_b_s));

%The steady currents. Use the steady states:n,h,r
Il_s=gl_s*(v_s-vl_s);
Ik_s=gk_s*ninf_s.^4.*(v_s-vk_s);
50 Ina_s=gna_s*minf_s.^3.*hinf_s.*(v_s-vna_s);
It_s=gt_s*ainf_s.^3.*binf_s.^2.*(v_s-vca_s);
Ica_s=gca_s*sinf_s.^2.*(v_s-vca_s);

%ca_conc_i_s '=0
55 ca_conc_i_s=-(Ica_s+It_s)/kca_s;

%Iahp for the equilibrium value of ca_conc_i_s
Iahp_s=gahp_s*(v_s-vk_s).*(ca_conc_i_s/(ca_conc_i_s+k1_s));
60 %v'=0, gives this equation. Eq currents
Iinp_s=Il_s+Ik_s+Ina_s+It_s+Ica_s+Iahp_s;

```

Listing B.2: M-file for the calculation of the equilibrium value for  $n$ 

```

function ninf = Ninf(v)
%Function which calculates the equilibrium value for n
%(n'=0) when the potential v is given.
64 theta=-32;
sigma=8;

ninf = 1./(1+exp(-(v-theta)./sigma));

```

Listing B.3: M-file for the calculation of the equilibrium value for  $h$

```

function hinf = Hinf_s(v)
69 %Calculates the equilibrium value of h (h'=0), when the
   %potential is v

   theta=-39;
   sigma=-3.1;
74 hinf=1./(1+exp(-(v-theta)./sigma));

```

Listing B.4: M-file for the calculation of the equilibrium value for  $r$ 

```

function rinf = Rinf(v)
   %Function which calculates the equilibrium value for r
   %(r'=0) when the potential is equal to v
79 theta = -67;
   sigma = -2.0;

   rinf=1./(1+exp(-(v-theta)./sigma));

```

Listing B.5: M-file for the calculation of the equilibrium value for  $Ca$ 

```

function conc = CaConc(v)
84 %Experimental constants
   gt=0.5;
   gca=0.5;
   kca=22.5;
89 vca=140;
   theta_a=-63;
   theta_b=0.4;
   theta_s=-39;
   theta_r=-67;
94 sigma_a=7.8;
   sigma_b=-0.1;
   sigma_s=8;
   sigma_r=-2;

99 %The steady states
   ainf=1./(1+exp(-(v-theta_a)./sigma_a));
   sinf=1./(1+exp(-(v-theta_s)./sigma_s));
   rinf=1./(1+exp(-(v-theta_r)./sigma_r));
   binf=1./(1+exp((rinf-theta_b)./sigma_b))...
104     -1/(1+exp(-theta_b/sigma_b));

   %The equilibrium currents
   It=gt*ainf.^3.*binf.^2.*(v-vca);
   Ica=gca*sinf.^2.*(v-vca);
109 %The concentration at the equilibrium

```

---

```
conc = -(Ica+It)/kca;
```

Listing B.6: The calculation of the real and imaginary parts of the eigenvalues of the equilibrium

```

function [EIG,Real,Imag] = EigenwaardenSN(v0)
114 %This function calculates the eigenvalues for the
    %equilibria of the system for the STN-neuron. The
    %argument of the function is a vector of potentials.
    %For every entry of the vector the other four variables
    %in the equilibrium are calculated, together with the
119 %parameter values of Igs. The functions Ninf(v0),
    %Hinf(v0), Rinf(v0), CaConc(v0) and Bifdiagram(v0)
    %are used. When these vectors for the variables and
    %parameter are generated as well, the jacobian matrix
    %can be evaluated at all these equilibria. The derivatives
124 %of the right hand side of the ode-system are analytically
    %calculated using Maple. For every entry i of the vectors
    %the five eigenvalues of the jacobian are calculated.
    %These are put in column i of EIG. In Real(:,i)
    %(Imag(:,i)) the real (imaginary) part of EIG(:,i)
    %is written.
129 %Experimental constants
    gca_s=0.5;
    gahp_s=9.0;
    gl_s=2.25;
134 gk_s=45.0;
    gna_s=37.5;
    gt_s=0.5;
    vna_s=55.0;
    vk_s=-80.0;
139 vca_s=140.0;
    Cm_s=1;
    tau_n0_s=1.0;
    tau_n1_s=100.0;
    theta_n_tau_s=-80.0;
144 sigma_n_tau_s=-26.0;
    tau_h0_s=1.0;
    tau_h1_s=500.0;
    theta_h_tau_s=-57.0;
    sigma_h_tau_s=-3.0;
149 tau_r0_s=40.0;
    tau_r1_s=17.5;
    theta_r_tau_s=68.0;
    sigma_r_tau_s=-2.2;
    theta_m_s=-30.0;
154 theta_a_s=-63.0;
    theta_s_s=-39.0;
    theta_n_s=-32.0;

```

```

theta_h_s=-39.0;
theta_r_s=-67.0;
159 sigma_m_s=15.0;
sigma_a_s=7.8;
sigma_s_s=8.0;
sigma_n_s=8.0;
sigma_h_s=-3.1;
164 sigma_r_s=-2.0;
theta_b_s=0.4;
sigma_b_s=-0.1;
phi_n_s=0.75;
phi_h_s=0.75;
169 phi_r_s=0.2;
epsilon_s=0.0000375;
k1_s=15.0;
kca_s=22.5;

174 %Declaration of the length of input v0 and output matrices
N=length(v0);
EIG=zeros(5,N);
Real=zeros(5,N);
Imag=zeros(5,N);

179 %The equilibrium values for I, n, r, h and [Ca]
I0=Bifdiagram(v0); %Zie Bifdiagram.m
n0=Ninf(v0); %npunt is 0 als n=ninf
r0=Rinf(v0); %rpunt is 0 als r=rinf
184 h0=Hinf_s(v0); %hpunt is 0 als h=hinf
Ca0=CaConc(v0); %zie CaConc.m

%The calculation of the eigenvalues of the jacobian matrix
%evaluated at equilibrium [v0(i) n0(i) r0(i) h0(i) Ca0(i)]
189 for i = 1:N
    %The timeconstants are dependent on v
    tau_n_s=tau_n0_s+tau_n1_s/(1+exp(-(v0(i)-...
        theta_n_tau_s)/sigma_n_tau_s));
    tau_h_s=tau_h0_s+tau_h1_s/(1+exp(-(v0(i)-...
194     theta_h_tau_s)/sigma_h_tau_s));
    tau_r_s=tau_r0_s+tau_r1_s/(1+exp(-(v0(i)-...
        theta_r_tau_s)/sigma_r_tau_s));

    %The entries of the Jacobian matrix (the partial
199     %derivatives of the RHS of the ode-system) are
    %calculated using Maple. The RHS functions can be
    %found in RHS.m. The entries, named
    %Ci (for i = 1:14) are evaluated at the equilibrium
    %[v0(i) n0(i) r0(i) h0(i) Ca0(i)].

204     %In the following:
    %x=[n,h,r,[Ca],v]

```

```

%n'=N(x)
%h'=H(x)
209 %r'=R(x)
%ca'=CA(x)
%v'=V(x)

dNdn = -phi_n_s/tau_n_s;
214 dNdv = phi_n_s/(1+exp(-(v0(i)-theta_n_s)/sigma_n_s))...
      ^2/sigma_n_s*exp(-(v0(i)-theta_n_s)/sigma_n_s)/...
      (tau_n0_s+tau_n1_s/(1+exp(-(v0(i)-theta_n_tau_s)...
      /sigma_n_tau_s))) - phi_n_s*(1/(1+exp(-(v0(i)-...
      theta_n_s)/sigma_n_s))-n0(i))/(tau_n0_s+tau_n1_s...
219 /(1+exp(-(v0(i)-theta_n_tau_s)/sigma_n_tau_s))...
      ^2*tau_n1_s/(1+exp(-(v0(i)-theta_n_tau_s)/...
      sigma_n_tau_s))^2/sigma_n_tau_s*exp(-(v0(i)-...
      theta_n_tau_s)/sigma_n_tau_s);

dHdh= -phi_h_s/tau_h_s;
224 dHdv = phi_h_s/(1+exp(-(v0(i)-theta_h_s)/...
      sigma_h_s))^2/sigma_h_s*exp(-(v0(i)-theta_h_s)/...
      sigma_h_s)/(tau_h0_s+tau_h1_s/(1+exp(-(v0(i)-...
      theta_h_tau_s)/sigma_h_tau_s))) - phi_h_s*(1/...
      (1+exp(-(v0(i)-theta_h_s)/sigma_h_s))-h0(i))/...
229 (tau_h0_s+tau_h1_s/(1+exp(-(v0(i)-theta_h_tau_s)...
      /sigma_h_tau_s)))^2*tau_h1_s/(1+exp(-(v0(i)-...
      theta_h_tau_s)/sigma_h_tau_s))^2/sigma_h_tau_s*...
      exp(-(v0(i)-theta_h_tau_s)/sigma_h_tau_s);

dRdr = -phi_r_s/tau_r_s;
234 dRdv = phi_r_s/(1+exp(-(v0(i)-theta_r_s)/sigma_r_s))...
      ^2/sigma_r_s*exp(-(v0(i)-theta_r_s)/sigma_r_s)/...
      (tau_r0_s+tau_r1_s/(1+exp(-(v0(i)-theta_r_tau_s)...
      /sigma_r_tau_s))) - phi_r_s*(1/(1+exp(-(v0(i)-...
      theta_r_s)/sigma_r_s))-r0(i))/(tau_r0_s+tau_r1_s/...
239 (1+exp(-(v0(i)-theta_r_tau_s)/sigma_r_tau_s)))^2*...
      tau_r1_s/(1+exp(-(v0(i)-theta_r_tau_s)/...
      sigma_r_tau_s))^2/sigma_r_tau_s*exp(-(v0(i)-...
      theta_r_tau_s)/sigma_r_tau_s);

dCAdr = 2*epsilon_s*gt_s/(1+exp(-(v0(i)-theta_a_s)/...
244 sigma_a_s))^3*(1/(1+exp((r0(i)-theta_b_s)/...
      sigma_b_s))-1/(1+exp(-theta_b_s/sigma_b_s)))*...
      (v0(i)-vca_s)/(1+exp((r0(i)-theta_b_s)/...
      sigma_b_s))^2/sigma_b_s*exp((r0(i)-theta_b_s)/...
      sigma_b_s);
249 dCAcda = -epsilon_s*kca_s;
dCAadv = epsilon_s*(-2*gca_s/(1+exp(-(v0(i)-...
      theta_s_s)/sigma_s_s))^3*(v0(i)-vca_s)/...
      sigma_s_s*exp(-(v0(i)-theta_s_s)/sigma_s_s)-...
      gca_s/(1+exp(-(v0(i)-theta_s_s)/sigma_s_s))...
254 ^2-3*gt_s/(1+exp(-(v0(i)-theta_a_s)/...
      sigma_a_s))^4*(1/(1+exp((r0(i)-theta_b_s)/...
      sigma_b_s))-1/(1+exp(-theta_b_s/sigma_b_s)))^2*...

```

```

    (v0(i)-vca_s)/sigma_a_s*exp(-(v0(i)-theta_a_s)/...
    sigma_a_s)-gt_s/(1+exp(-(v0(i)-theta_a_s)/...
259    sigma_a_s))^3*(1/(1+exp((r0(i)-theta_b_s)/...
    sigma_b_s))-1/(1+exp(-theta_b_s/sigma_b_s)))^2);
dVdn = -4*gk_s*n0(i)^3*(v0(i)-vk_s)/Cm_s;
dVdh = -gna_s/(1+exp(-(v0(i)-theta_m_s)/sigma_m_s))...
    ^3*(v0(i)-vna_s)/Cm_s;
264 dVdr = 2*gt_s/(1+exp(-(v0(i)-theta_a_s)/sigma_a_s))...
    ^3*(1/(1+exp((r0(i)-theta_b_s)/sigma_b_s))-1/...
    (1+exp(-theta_b_s/sigma_b_s)))*(v0(i)-vca_s)/...
    (1+exp((r0(i)-theta_b_s)/sigma_b_s))^2/...
    sigma_b_s*exp((r0(i)-theta_b_s)/sigma_b_s)/Cm_s;
269 dVdca = (-gahp_s*(v0(i)-vk_s)/(Ca0(i)+k1_s)+...
    gahp_s*(v0(i)-vk_s)*Ca0(i)/(Ca0(i)+k1_s)^2)/Cm_s;
dVdv = (-gl_s-gk_s*n0(i)^4-3*gna_s/(1+exp(-(v0(i)-...
    theta_m_s)/sigma_m_s))^4*h0(i)*(v0(i)-vna_s)/...
    sigma_m_s*exp(-(v0(i)-theta_m_s)/sigma_m_s)-...
274    gna_s/(1+exp(-(v0(i)-theta_m_s)/sigma_m_s))...
    ^3*h0(i)-3*gt_s/(1+exp(-(v0(i)-theta_a_s)/...
    sigma_a_s))^4*(1/(1+exp((r0(i)-theta_b_s)/...
    sigma_b_s))-1/(1+exp(-theta_b_s/sigma_b_s)))...
    ^2*(v0(i)-vca_s)/sigma_a_s*exp(-(v0(i)-...
279    theta_a_s)/sigma_a_s)-gt_s/(1+exp(-(v0(i)-...
    theta_a_s)/sigma_a_s))^3*(1/(1+exp((r0(i)-...
    theta_b_s)/sigma_b_s))-1/(1+exp(-theta_b_s/...
    sigma_b_s)))^2-2*gca_s/(1+exp(-(v0(i)-theta_s_s)/...
    sigma_s_s))^3*(v0(i)-vca_s)/sigma_s_s*exp(-(v0(i)-...
284    theta_s_s)/sigma_s_s)-gca_s/(1+exp(-(v0(i)-...
    theta_s_s)/sigma_s_s))^2-gahp_s*Ca0(i)/...
    (Ca0(i)+k1_s))/Cm_s;

    %The Jacobian matrix
289 Jac = [dNdn  0  0  0  dNdv; ...
    0  dHdh  0  0  dHdv; ...
    0  0  dRdr  0  dRdv; ...
    0  0  dCAdr dCAdca dCAdv; ...
    dVdn dVdh dVdr dVdca dVdv];
294

    %For equilibrium(i)=[v0(i) n0(i) h0(i) r0(i) Ca0(i)]
    %the five eigenvalues of Jac are calculated and put
    %in column i of EIG
    EIG(:,i)=eig(Jac);
299 end;

    %The real and imaginary parts of EIG are calculated and
    %assigned to the other return variables Real and Imag.
    Real=real(EIG);
304 Imag=imag(EIG);

    %Various plots can be made. The axis at the end of the

```

```

%statement can be adjusted to zoom-in at certain areas
309 figure(1) %real part
plot(I0, Real(1,:), 'o', I0, Real(2,:), 's', I0, Real(3,:), 'x' ...
      , I0, Real(4,:), 'p', I0, Real(5,:), 'h');
      AXIS([100 200 -0.01 0.01]);
314 %legend('Re(\lambda_{1})$', ...
      % '$Re(\lambda_{2})$', '$Re(\lambda_{3})$', ...
      % '$Re(\lambda_{4})$', '$Re(\lambda_{5})$', ...
      % 'interpreter', 'latex', 'Location', 'East'); ...
      %title('The real parts of the five eigenvalues');
319 %figure(2) %imaginary part
%plot(I0, Imag(1,:), 'o', I0, Imag(2,:), 's', I0, Imag(3,:), 'x' ...
      , I0, Imag(4,:), 'p', I0, Imag(5,:), 'h'); ...
      % AXIS([-200,60,-1,1]); legend('Im(\lambda_{1})$', ...
324 % '$Im(\lambda_{2})$', '$Im(\lambda_{3})$', ...
      % '$Im(\lambda_{4})$', '$Im(\lambda_{5})$', ...
      % 'interpreter', 'latex', 'Location', 'East'); ...
      % title('The imaginary parts of the eigenvalues');

```

Listing B.7: For an initial value Main.m simulates the STN-neuron using RHS.m

```

%The main file solving the STN ode system for initial
%condition 'initial', and right hand side function RHS
329 %(RHS.m). The ode45 solver is used. Where the vector
%y=[n;h;r;[Ca],v] (with other names used in RHS.m):

%y(1)=n_s;
%y(2)=h_s;
334 %y(3)=r_s;
%y(4)=ca_conc_i_s;
%y(5)=v_s;

tspan = [0 10000];
339 initial = [0;0;0;1;-55];

[t,y]=ode45(@RHS,tspan,initial);

N=length(t);
344 plot(t,y(1:N,5)); %the 5th column represents v
title('Spontaneous_spiking_behaviour'); %when Igs=0
xlabel('t_(ms)');
ylabel('v_(mV)');

```

Listing B.8: RHS.m represents the timed derivatives of the five variables

```

function dydt = RHS(t,y)

```

```
349 | %The variables
      | n_s=y(1);
      | h_s=y(2);
      | r_s=y(3);
354 | ca_conc_i_s=y(4);
      | v_s=y(5);

      | %When Igs is a stepfunction or pulse the following
      | %variables have to be defined:
359 | %a=-2; %strength of the pulse/step (<0 when depolarizing,
      | %>0 when hyperpolarizing)
      | %dur = 9200; %duration of the pulse/step in ms
      | %b1=800; % start of the pulse/step in ms
      | %b2=b1+dur; % Break of the pulse/step (don't adjust)
364 | %Experimental constants
      | gca_s=0.5;
      | gahp_s=9.0;
      | gl_s=2.25;
369 | gk_s=45.0;
      | gna_s=37.5;
      | gt_s=0.5;
      | vna_s=55.0;
      | vk_s=-80.0;
374 | vl_s=-60.0;
      | vca_s=140.0;
      | Cm_s=1;
      | tau_n0_s=1.0;
      | tau_n1_s=100.0;
379 | theta_n_tau_s=-80.0;
      | sigma_n_tau_s=-26.0;
      | tau_h0_s=1.0;
      | tau_h1_s=500.0;
      | theta_h_tau_s=-57.0;
384 | sigma_h_tau_s=-3.0;
      | tau_r0_s=40.0;
      | tau_r1_s=17.5;
      | theta_r_tau_s=68.0;
      | sigma_r_tau_s=-2.2;
389 | theta_m_s=-30.0;
      | theta_a_s=-63.0;
      | theta_s_s=-39.0;
      | theta_n_s=-32.0;
      | theta_h_s=-39.0;
394 | theta_r_s=-67.0;
      | sigma_m_s=15.0;
      | sigma_a_s=7.8;
      | sigma_s_s=8.0;
      | sigma_n_s=8.0;
```

```

399 sigma_h_s=-3.1;
    sigma_r_s=-2.0;
    theta_b_s=0.4;
    sigma_b_s=-0.1;
    phi_n_s=0.75;
404 phi_h_s=0.75;
    phi_r_s=0.2;
    epsilon_s=0.0000375;
    kl_s=15.0;
    kca_s=22.5;
409
    %The steady states
    minf_s=1/(1+exp(-(v_s-theta_m_s)/sigma_m_s));
    ainf_s=1/(1+exp(-(v_s-theta_a_s)/sigma_a_s));
    sinf_s=1/(1+exp(-(v_s-theta_s_s)/sigma_s_s));
414 ninf_s=1/(1+exp(-(v_s-theta_n_s)/sigma_n_s));
    hinf_s=1/(1+exp(-(v_s-theta_h_s)/sigma_h_s));
    rinf_s=1/(1+exp(-(v_s-theta_r_s)/sigma_r_s));
    binf_s=1/(1+exp((r_s-theta_b_s)/sigma_b_s))-...
        1/(1+exp(-theta_b_s/sigma_b_s));
419
    %The time-constants
    tau_n_s=tau_n0_s+tau_n1_s/(1+exp(-(v_s-theta_n_tau_s)/...
        sigma_n_tau_s));
    tau_h_s=tau_h0_s+tau_h1_s/(1+exp(-(v_s-theta_h_tau_s)/...
424 sigma_h_tau_s));
    tau_r_s=tau_r0_s+tau_r1_s/(1+exp(-(v_s-theta_r_tau_s)/...
        sigma_r_tau_s));

    %The currents
429 Il_s=gl_s*(v_s-vl_s);
    Ik_s=gk_s*n_s^4*(v_s-vk_s);
    Ina_s=gna_s*minf_s^3*h_s*(v_s-vna_s);
    It_s=gt_s*ainf_s^3*binf_s^2*(v_s-vca_s);
    Ica_s=gca_s*sinf_s^2*(v_s-vca_s);
434 Iahp_s=gahp_s*(v_s-vk_s)*(ca_conc_i_s/(ca_conc_i_s+kl_s));
    %Igs=a*(heaviside(t-b1)-heaviside(t-b2)); %when Igs is a
    %step or pulse
    Igs=0; %A constant Igs (at the moment zero for spontaneous
    %spiking)
439
    %The differential equations
    dydt=zeros(5,1); % a column vector
    dydt(1)=phi_n_s*((ninf_s-n_s)/tau_n_s);
    dydt(2)=phi_h_s*((hinf_s-h_s)/tau_h_s);
444 dydt(3)=phi_r_s*((rinf_s-r_s)/tau_r_s);
    dydt(4)=epsilon_s*(-Ica_s-It_s-kca_s*ca_conc_i_s);
    dydt(5)=(-Il_s-Ik_s-Ina_s-It_s-Ica_s-Iahp_s-Igs)/Cm_s;

```

# Appendix C

## Possible bifurcations

This appendix describes the possible codim-1 and codim-2 equilibrium bifurcations and the possible codim-1 limit cycle bifurcations. This is of course not complete. The interested, more mathematically oriented, reader is advised to read more on bifurcation theory in [32] for the mathematical theory and for bifurcations in neurodynamical models, one is referred to [3].

### C.1 Possible codim-1 bifurcations

Because Model (2.5) presented in Section 2.1.2 has only one parameter, namely  $I_{app}$ , the number of possible codim-1 bifurcations of an equilibrium are limited to only four, independent on the phase dimension. For bifurcations of a limit cycle the number *is* dependent on the dimension of the system. These bifurcations will be shortly listed in the following section to make the analysis clearer. For the precise definitions of the bifurcations, together with an introduction to bifurcation theory in general, see Section 1.2.

#### C.1.1 Bifurcations of a stable equilibrium

The possible events that can happen in a dynamical system of any dimension with a stable equilibrium are: it can disappear (saddle-node type of bifurcation) or lose its stability (a Hopf type). In neuronal models the bifurcations often correspond to a transition between rest and spiking. Of course the equilibrium can also remain stable, which means that no change occurs.

The possible bifurcations from resting state to periodic spiking state are [3]:

1. Saddle-node (fold,tangent,limit point,turning point) bifurcation
2. Saddle-node on invariant circle bifurcation
3. Supercritical Andronov-Hopf bifurcation
4. Subcritical Andronov-Hopf bifurcation

When the steady-state IV-curve is monotonic, saddle-node bifurcations can not occur. Only Andronov-Hopf bifurcations are possible. When the curve is non-monotonic both bifurcations can occur. Also there is always bistability of the resting attractor and some other attractor near a subcritical Hopf-bifurcation and near a saddle-node bifurcation. This does not have to be the case in the other two cases [3].

Only the saddle-node and subcritical Hopf bifurcation are encountered for this specific system and will therefore be shortly explained qualitatively. For the more quantitative description see Section 1.2.

### Saddle-node bifurcation

In the case of a saddle-node bifurcation, two equilibria (a saddle and node) of the system, with one parameter and one coordinate, coalesce at the parameter's bifurcation value. Afterward no equilibria are present. One eigenvalue becomes zero, which means that the coalescence occurs on a one-dimensional manifold. The real negative eigenvalue, corresponding to the stable equilibrium, increases during the change of the parameter and becomes 0. The real positive eigenvalue, corresponding to the saddle, decreases and becomes zero. Beside the conditions that the bifurcation point should be an equilibrium and should have one eigenvalue real and equal to zero, there are two nondegeneracy conditions which should be satisfied. See [32] for these conditions.

When System (2.5) exhibits a saddle-node bifurcation this occurs in  $\mathbb{R}^5$ . But where in  $\mathbb{R}^5$  does this occur? How can we picture one saddle and one node to coalesce in  $\mathbb{R}^5$ ? Center manifold theories answer these questions, it simply states that the essential events near the bifurcation value still occur on a one-dimensional parameter-dependent invariant submanifold  $\mathcal{W}_\alpha^c$  (called the center manifold) of  $\mathbb{R}^5$ . The center manifold is attracting for all orbits when the other four eigenvalues all have negative real parts ( $n_- = 4$  and  $n_+ = 0$ ). Off the center manifold (in  $\mathbb{R}^4$ ) the system behaves as a standard saddle. Because the number of eigenvalues on the imaginary axis ( $n_0$ ) is one in this codim-1 case, the dimension of the center manifold is also one.

If we introduce a (parameter-dependent) coordinate system on  $\mathcal{W}_\alpha^c$  with the coordinate  $\eta \in \mathbb{R}^{n_0}$  (thus  $\eta \in \mathbb{R}^1$ ), the restriction of the system to  $\mathcal{W}_\alpha^c$  is locally topologically equivalent to the normal form for the saddle-node bifurcation ((C.1a).

Shoshitaishvili's theorem (1975) then claims that with  $v \in \mathbb{R}^{n_+ + n_-}$  the total system (in  $\mathbb{R}^5$ , not only on  $\mathcal{W}_\alpha^c \subset \mathbb{R}^1$ ) is locally topologically equivalent to (C.1):

$$\dot{\eta} = \alpha \pm \eta^2 \tag{C.1a}$$

$$\dot{v} = -v \tag{C.1b}$$

With the second equation the standard saddle equation. It is clear that these equations are decoupled. They can be looked at independently, one gives the behaviour of the system on the center manifold, on which all essential events near the bifurcation parameter value occurs. The other gives the trivial behaviour of the system off the center manifold, on the 4D-manifold. The computation of the center manifold for this system is not easy and will not be discussed here. The interested reader is referred to Section 5.4. in [32].

### Andronov-Hopf bifurcation

In the case of an Andronov-Hopf bifurcation two complex conjugate eigenvalues with negative real parts approach the imaginary axis from the left side and become purely imaginary ( $\lambda_{1,2} = \pm i\omega_0$ ). If certain nondegeneracy conditions are satisfied as well (see [32] for these conditions), a Hopf bifurcation takes

place. In this case the equilibrium loses its stability but does not disappear. The bifurcation occurs on a two-dimensional manifold because *two* eigenvalues become non-hyperbolic. The Lyapunov coefficient  $l_1$  decides whether the Hopf bifurcation is a sub- or a supercritical one. When  $l_1 > 0$  a *subcritical* Hopf bifurcation occurs. In this case an unstable equilibrium becomes stable and an unstable limit cycle emerges. When  $l_1 < 0$  a *supercritical* Hopf bifurcation occurs. In this case a stable equilibrium loses its stability and a stable limit cycle appears surrounding the unstable equilibrium. The Lyapunov coefficient is calculated by MatCont in Section 2.2.1. See [26] for the definition of  $l_1$  and [32] for the long formula of  $l_1$ .

Center manifold theories state that again the essential events near the bifurcation point occur in a two-dimensional parameter-dependent invariant submanifold of  $\mathbb{R}^5$  (*two*-dimensional because the number of eigenvalues on the imaginary axis  $n_0$  is two). The center manifold is again attracting for all orbits when the other three eigenvalues all have negative real parts ( $n_+ = 0$  and  $n_- = 3$ ).

When the Hopf-conditions and the nondegeneracy conditions are all met by the original system, we can restrict the system to  $\mathcal{W}_\alpha^c$ , on which the essential events of the Hopf bifurcation occur. Introducing a parameter-dependent coordinate system on  $\mathcal{W}_\alpha^c \subset \mathbb{R}^2$ , with the coordinate  $z$  being the complex variable  $\rho e^{i\phi}$ . The system restricted to  $\mathcal{W}_\alpha^c$  is then locally topologically equivalent to (C.2a). The whole of the five-dimensional original system is then locally topologically equivalent to (C.2) according to Shoshitaishvili's theorem with the last equation representing the standard saddle.

$$\dot{z} = (\alpha + i)z + \sigma z^2 \bar{z} \quad (\text{C.2a})$$

$$\dot{v} = -v \quad (\text{C.2b})$$

Where  $\sigma = \text{sign } l_1(0) = \pm 1$  and  $v \in \mathbb{R}^{n_+ + n_-}$  (thus  $v \in \mathbb{R}^3$ ).

For more precise mathematical definitions of these bifurcations see [3] and/or [32].

### C.1.2 Bifurcations of a stable limit cycle

In this section the codimension 1 bifurcations of limit cycle attractors on a phase plane will be discussed. These can also occur in higher dimensional spaces, as is the case for our model. The number of codim-1 limit cycle bifurcations for  $n$ -dimensional systems is not limited to only four as was the case for codim-1 equilibrium bifurcations. Additional bifurcations are possible. First the bifurcations possible in a planar case will be listed. Then two other interesting cases are discussed. They correspond to transitions from repetitive spiking to resting behaviour.

The bifurcations of a limit cycle attractor in  $\mathbb{R}^2$  are [3]:

1. Saddle-node on invariant circle bifurcation (SNIC bifurcation)
2. Supercritical Andronov-Hopf bifurcation
3. Fold limit cycle bifurcation
4. Saddle homoclinic orbit bifurcation

Because a limit cycle  $L_0$  of a  $n$ -dimensional continuous systems can be seen as a fixed point (stable if the limit cycle is stable) of the corresponding Poincaré map in the  $(n-1)$ -dimensional local cross section  $\Sigma$  to  $L_0$ , the multipliers of these fixed points can give us information on the possible bifurcations of the limit

cycles. This bifurcation of a limit cycle can occur in  $n$ -dimensional systems with  $n \geq 2$ , and center manifold theorems give us the submanifolds of for example 5D systems on which the essential events take place. These occur on a parameter-dependent invariant manifold  $W_\alpha^c \subset \Sigma$ . The Poincaré map is locally topologically equivalent to the suspension of its restriction to this submanifold by the standard saddle map. This is analogous to the center manifold theorems for equilibrium bifurcations in higher dimensional systems.

The first two bifurcations listed above have been discussed in the previous section. They now occur in opposite direction though, where the limit cycle disappears (in the case of the SNIC bifurcation) or loses its stability (in the case of the Hopf bifurcation), resulting in an equilibrium.

In the case of a fold limit cycle bifurcation a stable and an unstable limit cycle coalesce at the bifurcation, and after the bifurcation, the stable limit cycle has disappeared and a node is the result (often stable). At the point of annihilation there is a periodic orbit (called a fold). For the Poincaré map this means that an unstable and stable fixed point coalesce at the bifurcation point, corresponding to  $\mu_1 = 1$ . After the coalescence no fixed point is present anymore. Because (2.5) is a 5D continuous system, center manifold theorems should give us an idea where a fold bifurcation takes place in  $\mathbb{R}^5$ . The restriction of the Poincaré map to the invariant manifold  $W_\alpha^c$  is a one-dimensional map (because only one multiplier crosses the unit circle). The stability of the manifold is determined by the other 3 multipliers: when they all lie inside the unit circle the one-dimensional manifold is attracting for all orbits in the 5D vectorfield.

A saddle homoclinic orbit bifurcation is a global bifurcation (as is the SNIC) and also comes in two variants: a sub- and a supercritical one. In the following  $\beta(\alpha)$  is the split function and  $\sigma(\alpha)$  the saddle quantity. See Section 1.2 for definitions. At the bifurcation value for the parameter ( $\alpha = 0$ ) a saddle equilibrium exists ( $\lambda_1(0) < 0 < \lambda_2(0)$ ) and a homoclinic orbit connects the stable and unstable manifolds of this saddle. When  $\sigma(0) = \lambda_1(0) + \lambda_2(0) \neq 0$  and  $\beta'(0) \neq 0$ , then for small  $\alpha$  a unique limit cycle bifurcates from the homoclinic orbit. The cycle is stable and exists for  $\beta > 0$  if  $\sigma(0) < 0$  and is unstable and exists for  $\beta < 0$  if  $\sigma(0) > 0$ . This is a summary of a theorem by Andronov and Leontovich (1939). The first case is called a supercritical homoclinic orbit bifurcation and the latter one a subcritical. The supercritical case is more common in neuronal models than the subcritical one. The saddle homoclinic orbit bifurcation is only possible when the steady state IV-curve is non-monotonic (as is the case for the STN-model). As the split function  $\beta$  approaches its bifurcation value ( $|\beta| \rightarrow 0$ ) the limit cycle passes closer and closer to the saddle and becomes increasingly angled. Its period tends to infinity because a phase point spends more and more time near the equilibrium.

The flip (period-doubling) and Neimark-Sacker bifurcation can occur in  $n$ -dimensional systems with  $n \geq 3$ . Therefore they are not mentioned in the list above for bifurcations of limit cycles in  $\mathbb{R}^2$ . In the case of a flip bifurcation a real multiplier of the fixed point of the Poincaré map approaches the limit cycle ( $\mu_1 \rightarrow -1$ ). As the bifurcation value is approached by the parameter the stable fixed point of the Poincaré map loses its stability and a period-two cycle emerges. For the limit cycle in the continuous system this means that the limit cycle (say  $L_0$ ) loses its stability, and a stable limit cycle with approximately twice the period of  $L_0$  appears. The new cycle makes two big excursions near  $L_0$  before the closure. The essential events occur on a one-dimensional submanifold of  $\mathbb{R}^5$ .

The other 3 multipliers decide the stability of the manifold.

In the case of a Neimark-Sacker bifurcation the multipliers of the fixed point of the Poincaré map are complex and approach the unit circle ( $\mu_{1,2} = e^{\pm i\theta}$ , with  $0 < \theta < \pi$ ). The stable fixed point of the Poincaré map, corresponding to the stable limit cycle in the continuous system, loses its stability and an isolated closed invariant curve (corresponding to a torus in one dimension higher) surrounds the fixed point after the bifurcation. This curve is unique and stable. This is the supercritical case. A subcritical Neimark-Sacker bifurcation causes an unstable closed invariant curve to disappear and the stable fixed point to lose its stability during the bifurcation. Because a stable torus bifurcates from the limit cycle (in the supercritical case), two periods can be seen in the oscillations of the coordinates when the orbit converges to the 2D-torus. On a 2D parameter-dependent invariant submanifold off  $\mathbb{R}^5$  the essential events of this Neimark-Sacker bifurcation take place. The other two multipliers decide whether this manifold is stable or unstable.

For preciser mathematical definitions again see [3] and/or [32].

## C.2 Possible codim-2 equilibrium bifurcations

Because two parameters instead of one are present in the two-cell model (4.10), Hopf- and fold-*curves*, instead of these bifurcation *points*, can be drawn in the parameter plane. Codim-2 bifurcation *points* can then be found on *these* curves. In chapter 8 of [32] the detailed definition and characteristics of these two types of curves and codim-2 bifurcation points can be found. For easy reference the possible codim-2 bifurcations are listed in Appendix C.2 as well, with the curve on which they can be encountered. The qualitative characteristics are mentioned as well.

Let  $\dot{x} = f(x, \alpha)$  with  $x \in \mathbb{R}^{12}$  and  $\alpha \in \mathbb{R}^2$  for our system (4.10). Then the solution to the system of 13 equations in (C.3)

$$f(x, \alpha) = 0 \quad (\text{C.3a})$$

$$f_x(x, \alpha) = 0 \quad (\text{C.3b})$$

Defines a 1D manifold  $\Gamma \in \mathbb{R}^{14}$  when the nondegeneracy conditions for the fold bifurcation are satisfied as well. The first 12 equations in (C.3) denote the conditions for an equilibrium and the 13<sup>th</sup> equation is the fold-condition. The projection  $\pi : (x, \alpha) \mapsto \alpha$  maps  $\Gamma$  onto a curve  $\mathcal{B} = \pi \Gamma$  on the parameter plane. A fold-bifurcation takes place on this curve. The restriction of the system to the centre manifold  $\mathcal{W}^c$  of the fold-bifurcation is given by (C.4). The normal form coefficient  $a$  in this equation is nonzero at a nondegenerate fold bifurcation point, and thus defines a nondegeneracy condition. When this condition is violated a codim-2 bifurcation (Cusp) takes place, and is described below.

$$\dot{\xi} = a\xi^2 + \mathcal{O}(\xi^3) \quad (\text{C.4})$$

The solution to the system of 13 equations in (C.5)

$$f(x, \alpha) = 0 \quad (\text{C.5a})$$

$$\text{tr } f_x(x, \alpha) = 0 \quad (\text{C.5b})$$

Defines a 1D manifold  $\Gamma \in \mathbb{R}^{14}$  when the nondegeneracy conditions for the Hopf-bifurcation are satisfied as well. In (C.5b)  $\text{tr}$  is the sum of the diagonal matrix elements, and (C.5b) thus defines the sum of the eigenvalues. Each point on the curve specifies an equilibrium of the system with two purely imaginary eigenvalues.  $\mathcal{B} = \pi \Gamma$  with  $\pi$  the same projection map as before, defines the Hopf bifurcation boundary.

On a fold-curve one of the twelve eigenvalues is real and zero. On a Hopf-curve two of the twelve eigenvalues are purely imaginary. In specific points on these curves certain genericity conditions can be violated *or* other eigenvalues can cross the imaginary axis as well. A codim-2 bifurcation point has then been found. The possible codim-2 bifurcations for equilibria are listed below. The ones which are encountered in the next section are discussed more extensively than the others.

On a fold curve (where  $\Re(\lambda_1) = 0$ ), the following codim-2 bifurcations can be encountered, where the violated genericity conditions or eigenvalue demands are mentioned as well (the abbreviations for all bifurcations indicate the representation of the bifurcation in MatCont):

1. Bogdanov-Takens (BT): an additional real eigenvalue approaches the imaginary axis and becomes zero:  $\lambda_{1,2} = 0$ . The centre manifold  $\mathcal{W}^c$  becomes 2D instead of 1D. This bifurcation is also called a double-zero bifurcation.
2. Zero-Hopf (ZH): two extra complex eigenvalues approach the imaginary axis and  $\mathcal{W}^c$  becomes 3D:  $\lambda_1 = 0$  and  $\lambda_{2,3} = \pm i\omega_0$ . This bifurcation is also called fold-Hopf or Gavrilov-Guckenheimer bifurcation.
3. Cusp (CP): in addition to the fold-condition  $\lambda_1 = 0$  the normal form coefficient  $a$  in (C.4) becomes zero:  $\lambda_1 = 0$  and  $a = 0$ . This bifurcation defines a semicubic parabola, which divides the parameter plane into two regions: one where three equilibria coexist and one where only one exists. Exactly at the cusp bifurcation the three equilibria collide and one equilibrium persists. At the two lines, which meet at the cusp point, two equilibria collide and disappear. This bifurcation gives rise to the hysteresis phenomenon where solutions ‘jump’ to a different stable (when present) equilibrium at the two curves of the semicubic parabola. This hysteresis phenomenon is present in many neural models and also in ours. In the next section the found cusp-bifurcation will be analysed further and the semicubic parabola will be shown as well.

On a Hopf-curve (where  $\Re(\lambda_{1,2}) = 0$  and  $\Im(\lambda_{1,2}) \neq 0$ ) the following codim-2 bifurcations can be encountered [32]:

1. Bogdanov-Takens (BT): the two purely imaginary eigenvalues approach each other and collide in the origin of the complex plane. This means that  $\omega_0 \rightarrow 0$  with  $\lambda_{1,2} = \pm i\omega_0$ . This bifurcation is also called a double-zero bifurcation.
2. Zero-Hopf (ZH): in addition to  $\lambda_{1,2} = \pm i\omega_0$  a real eigenvalue becomes zero:  $\lambda_3 = 0$ . This bifurcation is also called a fold-Hopf or Gavrilov-Guckenheimer bifurcation.
3. Double-Hopf (HH): two extra complex-conjugate eigenvalues  $\lambda_{3,4}$  approach the imaginary axis and the essential Hopf-events will take place on a 4D centre manifold  $\mathcal{W}^c$  instead of a 2D one. Thus  $\lambda_{1,2} = \pm i\omega_0$  and  $\lambda_{3,4} = \pm i\omega_1$ . This bifurcation is also called a double-pair or Hopf-Hopf bifurca-

tion. This is a complex codim-2 bifurcation with various types divided into complex and simple, with each different type having a completely different bifurcation unfolding, sometimes extremely complex. Limit cycles, two- and three-dimensional tori can be encountered. The type of unfolding depends on various coefficients which are defined in [32] and will not be repeated here. Because MatCont gives the values of these coefficients when a HH is detected, from these values the type of HH can be deduced (even without the knowledge of the meaning of these coefficients). These types will not be discussed here, because the HH-point found for the two-cell network is mathematically very interesting but does not lie in a physiologically relevant region of the parameter plane. The type of unfolding will be mentioned though.

4. Generalized Hopf (GH): while  $\lambda_{1,2} = \pm i\omega_0$  remain simple the Lyapunov coefficient  $l_1 = 0$  at the generalized Hopf-point. A subcritical Hopf-bifurcation turns into a supercritical one. This bifurcation is also called a Bautin or degenerate-Hopf bifurcation. The second Lyapunov coefficient  $l_2$  is nonzero at the GH-point and decides the type of Bautin bifurcation to occur. With  $s = \text{sign } l_2 \neq 0$ , the topological normal form of the system near the Bautin bifurcation point, is given by (in polar coordinates) (C.6):

$$\dot{\rho} = \rho(\beta_1 + \beta_2\rho^2 + s\rho^4) \quad (\text{C.6a})$$

$$\dot{\phi} = 1 \quad (\text{C.6b})$$

With  $\beta_1 = 0$  defining the Hopf-curve and  $\beta_2$  being the first Lyapunov coefficient  $l_1$ . In Figure C.1 the parameters  $\beta_1$  and  $\beta_2$  are indicated for  $s = -1$ , and in the origin the GH-point is located. The trivial solution to (C.6b) for  $s = -1$  is of course  $\rho = 0$  which corresponds to the only equilibrium. There can be 0 (only an equilibrium), 1 (an equilibrium and a limit cycle) or 2 (an equilibrium and 2 limit cycles) positive solutions for (C.6b). Setting  $\rho^2$  to a variable  $\xi$  in (C.6) and calculating the discriminant, gives the curve (see Figure C.1):

$$T = \{(\beta_1, \beta_2) : \beta_2^2 + 4\beta_1 = 0, \beta_2 > 0\}$$

On which (C.6b) has *one* positive solution. *Above*  $T$  (region 3) the system has *two* positive solutions and *below*  $T$  (region 1) it has zero positive solutions and thus only an equilibrium. Beside the fold bifurcation of cycles on the  $T$ -curve for  $\beta_2 > 0$  a subcritical Hopf bifurcation occurs while crossing the  $\{\beta_1 = 0\}$ -line and for  $\beta_2 < 0$  a supercritical Hopf bifurcation takes place. In region 1 (left of the Hopf-curve and below the  $T$ -curve) only a stable equilibrium is present, which becomes unstable in region 2 (supercritical Hopf) and a stable limit cycle is present in region 2. From region 2 to 3 the equilibrium becomes stable again (subcritical Hopf), the stable limit cycle stays unchanged, and within this stable limit cycle an unstable limit cycle emerges (still a result from the subcritical Hopf bifurcation). These two cycles collide at the  $T$ -curve and disappear, leaving the stable equilibrium, stable and unchanged (region 1).

For the system which is topologically equivalent to (C.6) the Hopf-curve will be curved instead of straight ( $\beta_1$  and  $\beta_2$  are functions of the two

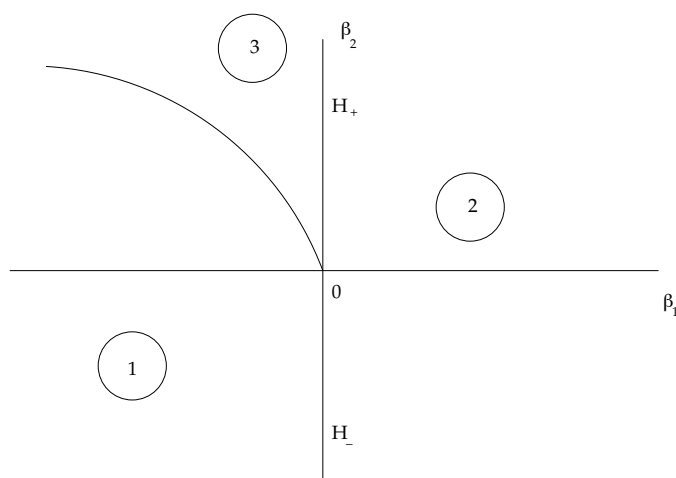


Figure C.1: A schematic picture of the behaviour of the topological normal form (C.6) for  $s = -1$  near a GH-point (at the origin). The vertical  $\beta_2$ -axis is the Hopf-‘curve’ and the value of  $\beta_2$  corresponds to the value of  $l_1$ . The  $T$ -curve is a limit cycle bifurcation curve, instead of an equilibrium one. It represents the ‘limit-point-of-cycles’ bifurcation curve on which a stable and unstable limit cycle collide and disappear.

parameters of the original system) and the GH-point will not be located in the origin. Also the line  $T$  branching from the GH point will not be such a nice parabola. But qualitatively these curves and phenomena can be expected in the neighbourhood of a GH-point. The GP-point indicates the beginning of the LPC-curve (the  $T$ -curve) and should be possible to make with MatCont. Unfortunately we have not yet succeeded in drawing this curve and because this curve is a limit cycle bifurcation curve belongs to this section.

## Appendix D

# Pulse-coupled models

General concepts of coupled networks will be first explained shortly to be able to understand the different results for coupled networks better. Then pulse-coupled canonical models, to which a Hodgkin-Huxley type of model can be transformed are presented. These models give a better insight in possible synchronization properties because the dynamics of the phases of the oscillation of the different neurons in the network are given instead of the dynamics of for example the potential.

The following definitions are derived from [41]:

- A *neural network model* is a HH-type of model which describes the dynamics of state variables as membrane potential, gating variables and ionic concentrations.
- A *pulse-coupled canonical network model* describes the dynamics of the phase  $\phi_i$  of the  $i$ th neuron. The simplest pulse-coupled 1D model is:

$$\phi_i' = \omega_i + (1 + \cos \phi_i) \sum_{j=1}^n s_{ij} \delta(\phi_j - \pi) \quad (\text{D.1})$$

The variables used are:

- $\phi_i(t) \in \mathbb{S}^1 = \{e^{i\phi} \in \mathbb{C}\}$  is the phase variable  $\in [-\pi, \pi]$  on time  $t$  that indicates where in the periodic cycle the state is. The period of the cycle differs between the neurons, but is scaled to  $2\pi$  for all  $T_i$ . The speed in which  $\phi_i$  cycles the unit circle preserves the value of  $T_i$ .  $\phi_i(t) = \pi$  indicates that the  $i$ th neuron fires and  $\phi_i$  is then reset to  $-\pi$ , where the periodic cycle starts over.  $\mathbb{S}^1$  is the unit circle. The  $i^{\text{th}}$  and  $j^{\text{th}}$  neurons are said to be *synchronized* when [42, 43]

$$\phi_j(t) - \phi_i(t) \rightarrow \chi_{ij}^*$$

With  $\chi_{ij}^*$  some constant. If  $\chi_{ij}^* = 0$  neuron  $i$  and  $j$  are *in-phase*. If  $\chi_{ij}^* = \pi$  neuron  $i$  and  $j$  are in *anti-phase*. For all other values for  $\chi_{ij}^*$  the neurons are out-of phase[43].

- $\omega_i > 0$  is the frequency of the  $i$ th neuron.
- The synaptic coefficient is a constant  $-1 < s_{ij} < 1$ .  $s_{ij} > 0$  indicates an excitatory synapse and  $s_{ij} < 0$  an inhibitory one.

- $\delta(x)$  is the dirac delta function. Thus  $\delta(\phi_j - \pi) = 1$  when  $\phi_j = \pi$  (the  $j$ th then fires an action potential). This caused an increment of  $\phi_i$  by  $(1 + \cos \phi_i)s_{ij}$ . The absolute and relative refractory period are taken into account because  $(1 + \cos \phi_i) \approx 0$  when  $\phi_i$  just fired (crossed  $\pi$ ).
- A neural network is called *weakly connected* when the amplitudes of post-synaptic potentials are much smaller than the amplitude of an action potential and/or are smaller than the mean EPSP size needed to have the postsynaptic silent cell to fire an action potential. A neural network is almost always called weakly connected because the size of the postsynaptic potential is about 0.1 mV and indeed much smaller than the size of an action potential (100 mV) or the needed EPSP-size of 20 mV to trigger a postsynaptic action potential. The shapes of the action potentials are not changed by the coupling but their timings are [43]. Weakly connected networks are described by:

$$\dot{X}_i = F_i(X_i, \lambda) + \epsilon G_i(X_1, \dots, X_n, \lambda, \epsilon)$$

With  $X_i$  the vector with state variables of neuron  $i$  and  $F_i(X_i, \lambda)$  describing the intrinsic membrane properties of neuron  $i$  dependent on a vector of parameters  $\lambda$ .  $\epsilon \ll 1$  is a dimensionless constant and indicates the weak connection. The function  $G_i$  indicates the influence on the state variables of neuron  $i$  of the state variables of the neurons projecting to it. It is plausible to have  $G_i$  to be the sum of the pairwise coupled forms:

$$G_i(X_1, \dots, X_n, \lambda, \epsilon) = \sum_{j=1}^n G_{ij}(X_i, X_j, \lambda) + \mathcal{O}(\epsilon) \quad (\text{D.2})$$

In the model used in this report [1] such a dimensionless  $\epsilon \ll 1$  is absent. The only dimensionless parameters are  $s_{G \rightarrow S}$  and  $s_{S \rightarrow G}$  but are not constant, their dynamics depend on a time varying membrane potential.

When:

1. The neural network is weakly connected, and:
2. The neurons within the network are class I excitable, meaning that they can generate action potentials with an arbitrarily small frequency. This on its turn then indicates that the neuron's activity is near a bifurcation from quiescent state to period spiking, which is of saddle-node type due to the necessity of the arbitrarily low frequency of firing directly after the transition. And:
3. The synapses between the neurons are conventional, thus axo-dendritic and/or axo-somatic and:
4. The synaptic transmission is slower than an action potential but faster than the interspike interval and:
5. The synaptic transmission can be considered negligible when the presynaptic neurons are at rest, meaning that their spontaneous release of neurotransmitter does not affect the postsynaptic neurons significantly.

Then the neural network model (HH-type) can be transformed to a canonical pulse-coupled form by a certain change of variables (see [41] for more information). This transformation can give more insight than the original model on

synchronization properties due to the explicit description of the dynamics of the phases of the neurons within the network. A disadvantage of the pulse-coupled model is that the change of variables is only valid in a small neighbourhood of the saddle-node bifurcation, thus for a small range of values of the parameter  $\lambda$  and in a range where the interspike interval is very large (close to the bifurcation).

When a network satisfies the conditions described above where a saddle-node bifurcation takes place for some  $\lambda = \lambda_0$ , each  $G_i$  has the pairwise connected form given in (D.2),  $\epsilon$  is small and  $\lambda$  is in a small neighbourhood of  $\lambda_0$  then a transformation exists to the canonical model (D.3):

$$\phi'_i = (1 - \cos \phi_i) + (1 + \cos \phi_i)r_i + \sum_{j=1}^n w_{ij}(\phi_i)\delta(\phi_j - \pi) + \mathcal{O}(\sqrt{\epsilon} \ln \epsilon) \quad (\text{D.3})$$

With  $r_i$  the new parameter (in the original network model it was  $\lambda$ ). The small remainder  $\mathcal{O}(\sqrt{\epsilon} \ln(\epsilon))$  can be set to zero due to  $\epsilon \ll 1$ .  $w_{ij}$  is the *phase resetting curve* (PRC):

$$w_{ij}(\phi_i) = 2 \arctan\left(\tan \frac{\phi_i}{2} + s_{ij}\right) - \phi_i$$

With  $s_{ij}$  a constant proportional to  $|G_{ij}|$ . In the simple pulse-coupled model (D.1)  $w_{ij}$  was simply taken to be equal to  $s_{ij}$ .  $w_{ij}$  is a *phase resetting curve* because when  $\phi_j \in \mathbb{S}^1$  crosses  $\pi$  (the  $j$ th neuron fires a spike) the value of  $\phi_i$  is incremented by  $w_{ij}(\phi_i)$ . This means:

$$\tan \frac{\phi_i^{\text{new}}}{2} = \tan \frac{\phi_i^{\text{old}}}{2} + s_{ij}$$

$\phi_i$  integrates many such inputs and fires itself when it crosses  $\pi$ . Because when  $s_{ij} > 0$ ,  $w_{ij} \geq 0$ , firing of  $\phi_j$  can only advance  $\phi_i$ . And an inhibitory synapse ( $s_{ij} < 0$ ) can only decrease  $\phi_i$ .

A weakly connected network of class I excitable neurons can be converted into (D.3) when  $|\lambda - \lambda_0| = \mathcal{O}(\epsilon^2)$  and into (D.4) when  $|\lambda - \lambda_0| \gg \epsilon/(\ln \epsilon)^2$  and both neurons have nearly identical frequencies. The latter means that the neurons become uncoupled. For the coupled STN- and GPe-neurons this means that they show pacemaker activity regardless of activities of the other neuron.

$$\phi'_i = \omega_i + \sum_{j=1}^n s_{ij}\mathcal{H}(\phi_j - \phi_i) \quad (\text{D.4})$$

With:

$$\mathcal{H}(\chi) = 1 - \cos \chi$$

For a network with an inhibitory and excitatory neuron reciprocally connected and satisfying the assumptions mentioned above, (D.5) holds (with  $\phi_{inh}$  the phase of the inhibitory neuron and  $\phi_{exc}$  that of the excitatory neuron):

$$\phi'_{exc} = (1 - \cos \phi_{exc}) + (1 - \cos \phi_{exc})r + w_{inh \rightarrow exc}(\phi_{exc})\delta(\phi_{inh} - \pi) \quad (\text{D.5a})$$

$$\phi'_{inh} = (1 - \cos \phi_{inh}) + (1 - \cos \phi_{inh})r + w_{exc \rightarrow inh}(\phi_{inh})\delta(\phi_{exc} - \pi) \quad (\text{D.5b})$$

Here  $w_{inh \rightarrow exc} \leq 0$  (inhibitory synapse) and  $w_{exc \rightarrow inh} \geq 0$  (excitatory synapse). If  $\phi_{inh} > \phi_{exc}$  then firing of  $\phi_{inh}$  advances  $\phi_{exc}$ . Because the firing of  $\phi_{inh}$

causes  $\phi'_{exc} < 0$  (see (D.5a)) the difference between  $\phi_{exc}$  and  $\phi_{inh}$  becomes even larger. And the firing of  $\phi_{exc}$  increases  $\phi_{inh}$  even more (see (D.5b)). Thus both synapses contribute to the instability of the in-phase synchronized solution in this one direction ( $\phi_{inh} > \phi_{exc}$ ). After a while  $\phi_{inh} \rightarrow \phi_{exc} + 2\pi$  and because  $\phi_{exc} + 2\pi \equiv \phi_{exc}$  the situation of  $\phi_{exc} > \phi_{inh}$  arises. In this case the phase difference will decrease. From this side the synchronized in-phase solution is therefore stable. It means that the pulse-coupled model is at a double limit cycle bifurcation. This only occurs because  $r$  is assumed to be equal for both neurons which is not generic. When  $r_{inh}$  is slightly different from  $r_{exc}$  then there is no synchronized solution when  $r_{exc} < r_{inh}$  and a nearly in-phase synchronized solution with a small phase shift when  $r_{exc} > r_{inh}$ . The phase shift increases though when  $r_{exc} - r_{inh}$  increases.